ALICE-UG-002

CERN-LHCC-2012-013 / LHCC-P-005
September 12, 2012

Upgrade of the Inner Tracking System Conceptual Design Report

The ALICE Collaboration*

Version: CDR-1

*See Appendix A for the list of collaboration members

Contents

Chapter 1

Introduction

1.1 Background

ALICE (A Large Ion Collider Experiment) is a general-purpose, heavy-ion detector at the CERN LHC. It is designed to address the physics of strongly interacting matter, and in particular the properties of the Quark-Gluon Plasma (QGP), using nucleus-nucleus collisions at high energies.

The ALICE detector consists of a central barrel and a forward muon spectrometer, allowing a comprehensive study of hadrons, electrons, muons, and photons produced in the collision of Pb–Pb nuclei. Pb–Pb measurements are accompanied by precision measurements with pp and p–Pb collisions to provide a quantitative base for comparison with results from Pb–Pb collisions. The ALICE scientific plans and organization for the approved program are defined in the ALICE Physics Performance Report Vol. I [1] (scientific program) and Memorandum of Understanding [2] (the sharing of resources and responsibilities). An updated description of the ALICE detector can be found in [3].

Prior to the start-up of the LHC heavy-ion programme, the nature of the QGP as an almost-perfect liquid emerged from the experimental investigations at CERN SPS and at BNL RHIC. ALICE has confirmed this basic picture, observing the creation of hot hadronic matter at unprecedented values of temperatures, densities and volumes, and exceeding the precision and kinematic reach of all significant probes of the QGP that had been measured over the past decade. These physics results, which are presented in around 30 publications in peer reviewed journals [4], have been achieved by ALICE after only two years of Pb–Pb running, demonstrating its excellent capabilities to measure high-energy nuclear collisions at the LHC. Despite this success there are several frontiers, as high precision measurements of rare probes at low transverse momenta, for which the current experimental setup is not yet fully optimized. Detector upgrades combined to a significant increase of luminosity could enhance the physics capabilities enormously.

The ALICE long-term physics goals, its experimental strategy and the general upgrade plans are discussed in [5]. The main physics topics addressed, which will be briefly discussed in Section 1.2, require the measurement of heavy-flavour hadrons, quarkonia, and low-mass dileptons at low transverse momenta. These measurements in Pb–Pb collisions are characterized by a very small signal-over-background ratio, which calls for large statistics. In addition, the large background makes the application of triggering techniques impossible or very inefficient. Besides a very large statistics, these measurements require also a significant improvement of the vertexing and tracking efficiency.

The upgrade strategy is formulated under the assumption that, after the second long shutdown in 2018, the LHC will progressively increase its luminosity with Pb beams eventually reaching an interaction rate of about 50 kHz, i.e. instantaneous luminosities of $L = 6 \times 10^{27}\,\mathrm{cm}^{-2}\mathrm{s}^{-1}$. In the proposed plan the ALICE detector is modified such to allow the readout of all interactions. ALICE will then be in

a position to accumulate $10\,\mathrm{nb}^{-1}$ of Pb–Pb collisions, recording about 10^{11} interactions. The planned upgrades, which will enhance the ALICE vertexing and tracking capabilities at low p_{t} and allow data taking at substantially higher rates, include:

- A new beampipe with smaller diameter;
- A new, high-resolution, low-material ITS;
- Upgrade of the TPC consisting in the replacement of the wire chambers with GEM detectors and new pipelined readout electronics;
- Upgrade of the readout electronics of TRD, TOF, PHOS and Muon Spectrometer for high rate operation;
- Upgrade of the forward trigger detectors;
- Upgrade on the online systems and offline reconstruction and analysis framework.

The present document addresses the question of how to upgrade the Inner Tracking System (ITS) detector to comply with the new requirements set by the ALICE upgrade strategy. In particular, this document will address the question of how to improve the performance for the detection of heavy-flavour hadrons, and of thermal photons and low-mass dileptons emitted by the QGP.

It will be shown that it is possible to build a new silicon tracker with greatly improved features in terms of: determination of the impact parameter (d_0) to the primary vertex, tracking efficiency at low p_{t} , and readout rate capabilities. These potential improvements are achievable owing to the spectacular progress made in the field of imaging sensors over the last ten years as well as the possibility to install a smaller radius beampipe.

Such a new silicon tracker will allow ALICE to measure charm and beauty production in Pb-Pb collisions with sufficient statistical accuracy down to very low transverse momentum, measure charm baryons and perform exclusive measurements of beauty production. These measurements are essential in order to understand the energy loss mechanism and thermalization of heavy quarks in the QGP state. The new ITS will also play a key role for the measurement of thermal photons and low-mass dileptons. This is crucial to assess the initial temperature and degrees of freedom of the QGP, as well as the chiral nature of the phase transition.

1.2 Scientific Scope of the Upgrade

The longterm goal of the ALICE experiment is to provide a characterization of the Quark-Gluon Plasma (QGP) state. A precise determination of its properties will be a major scientific achievement. These properties include initial temperature, degrees of freedom, speed of sound and general transport coefficients such as the shear viscosity over the entropy. Measuring such characteristics would go a long way towards a better understanding of QCD as a genuine multi-particle theory. To achieve this goal, high statistics measurements are required, as these will give access to the very rare physics channels needed to understand the dynamics of this condensed phase of QCD. As discussed in [5], in the central rapidity region the physics program will include the following main topics.

- Study of the thermalization of partons in the QGP, with focus on the massive charm and beauty quarks. Heavy-quark elliptic flow is especially sensitive to the partonic equation of state. Ultimately, heavy quarks might fully equilibrate and become part of the strongly-coupled medium.

- Study of the in-medium parton energy loss mechanism, which provides both a testing ground for the multi-particle aspects of QCD and a probe of the QGP density. The relevant observables are: jet structure, jet–jet and photon–jet correlations, jets and correlations with high-momentum identified hadrons plus heavy-flavour particle production. In particular, it is crucial to characterize the dependencies of energy loss on the parton species, mass, and energy.

- Study of the quarkonium dissociation and, possibly, regeneration pattern, as a probe of deconfinement and of the medium temperature.

- Study of the production of thermal photons and low-mass dileptons emitted by the QGP. This is to assess the initial temperature and degrees of freedom of the system, as well as the chiral nature of the phase transition.

The upgrade of the ITS to improve its resolution and readout rate capabilities is a fundamental cornerstone within such a physics program. The new measurements on charm and beauty production that will become possible with the ITS upgrade are listed below:

- Study of the thermalization of heavy quarks in the medium, in particular by measuring heavy flavour charmed and beauty baryons. The new improved silicon tracker at mid-rapidity will impact significantly the following measurements:
  - D mesons, including $\mathrm{D_s}$, down to zero p_t will be accessible for the first time.
  - Charm and beauty baryons, Λ_c and Λ_b. The latter will be measured via the decay $\Lambda_\mathrm{b} \rightarrow \Lambda_\mathrm{c} + \mathrm{X}$ and this will be accessible for the first time.
  - Baryon/meson ratios for charm ($\Lambda_\mathrm{c}/\mathrm{D}$) and for beauty ($\Lambda_\mathrm{b}/\mathrm{B}$), will also be accessible for the first time.
  - The elliptic flow of charmed and beauty mesons and baryons down to low transverse momentum will also be accessible for the first time.
- Study of the quark mass dependence of in-medium energy loss. This is done by measuring the nuclear modification factors R_AA of the p_t distributions of D and B mesons separately. The new detector will dramatically improve or make accessible for the first time the following measurements in Pb–Pb collisions:
  - Measurement of beauty via displaced $\mathrm{D}^0 \rightarrow \mathrm{K}\pi$, which will be accessible for the first time.
  - Measurement of beauty via displaced $\mathrm{J}/\psi \rightarrow \mathrm{ee}$, which will also be accessible for the first time.
  - Improve measurement of single displaced electrons.
  - Improve beauty decay vertex reconstruction, using any of the previous three channels plus an additional track.

In addition, the upgraded ITS will be extremely important for a detailed measurement of thermal electromagnetic radiation from the hot QGP, which is just in its infancy at the LHC. This will permit ALICE to characterize:

- Thermal radiation from the QGP.

- In-medium modifications of hadronic spectral functions as related to chiral symmetry restoration, in particular for the ρ meson.

In order to address new high precision measurements in a thorough and systematic way, the following design goals have to be met:

1. Coverage in transverse momentum to be as complete as possible, in particular down to very low momenta.

2. Very accurate identification of secondary vertices from decaying charm or beauty (D, J/ψ, Λ_c, Λ_b).

The recent progress in Si detector technology, an improved integration to reduce the distance between the interaction region and the first layer of the ITS and a minimized material budget make it possible for ALICE to improve the resolution on the charged track impact parameter by a factor of three. This improves the sensitivity to charm by one order of magnitude or more, depending on the transverse momentum range. This in turn implies a better signal-to-background ratio. Therefore fully reconstructed rarely produced heavy-flavour hadrons (including charm-strange and beauty-charm mesons, which should be exceedingly sensitive to parton re-combination effects) will become accessible.

In pp collisions, there is also a need to improve the understanding of the flavour dependence of multiparticle production. The precise measurement of both the total charm and beauty production cross sections, down to zero p_t , will be possible for the first time. Furthermore, heavy-flavour jet tagging will also be significantly enhanced.

Moreover, the improved readout rate capabilities of the new detector will allow the inspection of 50 kHz Pb–Pb and 2 MHz pp interactions. It should be however noticed that other ALICE central detectors. e.g. the TRD and the TOF, will presumably limit the readout of pp interactions at a maximum rate of about 200–400 kHz. The new readout strategy is to send the event related data of all interactions to the online systems (DAQ and HLT). The raw data will be processed and compressed by the online systems, based on clustering and tracking algorithms, but no event will be discarded. In order to achieve this, an upgrade of the Inner Tracking System (ITS) is necessary.

1.3 Current Detector Performance and Limitations

The present ALICE ITS consists of six cylindrical layers of silicon detectors placed coaxially around the beam pipe. They are located at radii between 39 mm and 430 mm and cover the pseudo-rapidity range $|\eta| < 0.9$ for vertices located within ± 60 mm with respect to the nominal interaction point (i.e. $\pm 1\sigma$ of the luminous region). Within the boundaries set by technological limitations and available funds, the number, position and segmentation of the layers were optimized to achieve a high precision in the determination of the charged particle impact parameter to the primary vertex and efficient track finding in combination with the TPC. Therefore, the inner radius is the minimum allowed by the radius of the beam pipe. The outer radius is determined by the necessity to match tracks with those from the TPC.

As will be illustrated in Chapter 3 optimizing the detector geometry to achieve the highest standalone tracking efficiency would lead to an alternative configuration including a larger number of layers and different radii. The first layer has a more extended pseudo-rapidity coverage ($|\eta| < 1.98$) which, together with the Forward Multiplicity Detectors (FMD), provides continuous coverage for the measurement of charged particle multiplicity.

As a result of the high particle density (the current system is designed for up to 100 particles per cm^2 for Pb-Pb collisions at $\sqrt{s_{NN}} = 5.5$ TeV), and in order to achieve the required impact parameter resolution, the first two layers of the ITS are made of Silicon Pixel Detectors (SPD) and the two middle ones are made of Silicon Drift Detectors (SDD). The two outer layers, where the track density has fallen to one particle per cm^2, are equipped with double-sided Silicon micro-Strip Detectors (SSD). The four outer

layers have analogue readout and therefore can be used for particle identification via dE/dx measurement in the non-relativistic ($1/\beta^2$) region. All detector elements were carefully optimized to minimize their radiation length, achieving $1.1\%X_0$ per layer, the lowest value among all the current LHC experiments.

The performance of the present ITS for tracking and identifying charged particles in pp and Pb-Pb collisions will be discussed in Chapter 3. The capabilities for heavy flavor detection will be shortly reviewed in Chapter 2. It will be shown in these that the precision of the present ITS in the determination of the track impact parameter is adequate to study the production of charm mesons in exclusive decay channels (e.g. $D^0 \to K\pi$ and $D^+ \to K\pi\pi$) at values of transverse momentum above 2 GeV/c. At lower transverse momenta, however, the statistical significance of the measurement is insufficient.

The situation is even worse for charm baryons. The most abundantly produced charm baryon (Λ_c) has a mean proper decay length ($c\tau$) of only 60 μm. This is lower than the impact parameter resolution of the present ITS in the transverse momentum range of the majority of its daughter particles. Therefore, charm baryons are presently not accessible by ALICE in central Pb-Pb collisions. For the same reasons outlined above, the study of beauty mesons, beauty baryons, or of hadrons with more than one heavy quark are also beyond the capability of the current detector.

A major limitation of the present ITS detector is given by its poor readout rate capabilities. As it will be illustrated in Chapter 3, the ITS can run up to a maximum read-out rate of 1 kHz (with 100 % dead time) irrespective of the detector occupancy. This rate limitation restricts ALICE to use only a small fraction of the full Pb–Pb collision rate of 8 kHz that the LHC presently can deliver and prevents the collection of required reference data in pp collisions. Clearly, the present ITS is inadequate to fulfill the required rate capabilities envisaged for the ALICE long-term plans discussed in the previous section.

Finally, the impossibility to access the present ITS detector for maintenance and repair interventions during the yearly LHC shutdowns represents another major limitation in sustaining a high data quality. In the context of an upgrade, the rapid accessibility to the detector will be set as a priority.

1.4 Detector Upgrade Concept

In this section, the key features of the ITS upgrade will be discussed and compared to the present ITS, following the considerations made in Sections 1.2 and 1.3.

- **First detection layer closer to the beam line**. At present the radial distance of the first layer from the beamline is 39 mm. On the basis of the first studies done by the LHC Beampipe Working Group and the ALICE Technical Coordination, the installation of a new beampipe with an outer radius of 19.8 mm is considered a realistic possibility. This will be discussed in Chapter 5.
  The installation of such a beampipe would enable the first detection layer to be located at a radius of about 22 mm. The baseline for the wall thickness of the beampipe in this document is 0.8 mm, although the possibility of a thinner wall (for example 0.5 mm) should be addressed with dedicated R&D.

- **Reduction of material budget**. Reducing the material budget of the first detection layer is particularly important for improving the impact parameter resolution. In general, reducing the overall material budget will allow the tracking performance and momentum resolution to be significantly improved. As will be shown in Chapter 4, the use of Monolithic Active Pixel Sensors (MAPS) will allow the silicon material budget per layer to be reduced by a factor of 7 in comparison to the present ITS (50 µm instead of 350 µm). A careful optimization of the analogue front-end timing specifications and readout architecture will allow the power density to be reduced by a factor of 2. At the same time this will increase the pixel density by a factor of 50.
  The lower power consumption and a highly optimized scheme for the distribution of the electrical

power and signals will allow the material budget of the electrical power and signal cables to be reduced by a factor of 5. Mechanics, cooling and other detector elements can also be improved when compared to the present ITS design. Combining all these new elements together, it should be possible to build a detector with a radiation length of 0.3% X_0 per layer or better.
An example of the feasibility of such a design is represented by the STAR HFT detector [6]. Achieving such a low material budget is particularly critical for the first detection layer, since it affects strongly the impact parameter resolution at low p_t where the resolution is mainly determined by multiple Coulomb scattering.
As will be illustrated in Chapter 4, hybrid pixels would allow the construction of detector layers with a slightly higher radiation length (0.5% X_0), but this would still represent a significant improvement of the performance as compared to the present ITS.

– **Geometry and segmentation**. The studies presented in this document are based on a detector consisting of seven concentric cylindrical layers covering a radial extension from 22 mm to 430 mm with respect to the beamline. The physics studies of the benchmark channels presented in Chapter 2 are based on the assumption that all layers are segmented in pixels with dimensions of $20 \times 20\,\mu$m. However, as will be illustrated in Chapter 3, the detector performance in terms of impact parameter resolution and standalone tracking efficiency will not change significantly, even if the outermost four layers would have a much lower granularity as can be achieved for example with the Silicon micro-Strip Detectors presented in Chapter 4.

– **Measurement of specific energy deposition**. The new detector will preserve PID capabilities by measuring the ionization in the silicon layers (dE/dx). As will be discussed in Chapter 3, in the case where all seven layers would be implemented with monolithic pixel technology, the performance of the detector would be slightly reduced with respect to the present one. Nevertheless it would maintain a $3\,\sigma$ separation power up to 600 MeV/c for pion to kaon and up to 1 GeV/c for proton to kaon.

– **Readout time**. As we have seen in Section 1.3, the present ITS features a maximum readout rate of 1 kHz. The new detector aims to read the data related to each individual interaction up to a rate of 50 kHz for Pb–Pb collisions and 2 MHz for pp collisions. The readout architectures that allows such rates to be achieved are presented in Chapter 4.

As will be shown in Chapter 3 a new silicon tracker featuring the characteristics listed above will enable the track position resolution at the primary vertex to be improved by a factor of 3 or larger. The standalone tracking efficiency would be comparable to what can be presently achieved by combining the information of the ITS and the TPC. The relative momentum resolution of the silicon tracker standalone would be about 2% up to 2 GeV/c and remain below 3% up to 20 GeV/c.

In summary, the baseline idea for the layout of the ITS upgrade is to replace the existing ITS detector in its entirety with three inner layers of pixel detectors followed by four outer layers of silicon strips, or pixel detectors with lower granularity.

Two basic technology choices are considered for the ITS pixel detector: hybrid silicon pixel detectors and Monolithic Active Pixel Sensors (MAPS). In Chapter 4 we demonstrate the key R&D areas for both pixel detector technologies, for the new Silicon micro-Strip Detector and for the system aspects. The new detector geometry, such as the number of layers, radial position, and segmentation, as well as the options of pixel or strips detectors for the outermost layers, are being evaluated with respect to their performance in terms of standalone tracking efficiency, momentum resolution and PID. However, other considerations related to space and integration issues, cost, etc., will also be taken into account in the definition of the layout of the new detector.

1.5 Physics Performance Studies

A detailed presentation of the performance studies for heavy-flavour detection with an upgraded ITS is the main topic of Chapter 2. We consider the following benchmark analyses and summarize the improvement attainable with an upgrade here:

- Charm meson production via $D^0 \to K^-\pi^+$: precise measurement down to $p_t = 0$.
- Charm and strangeness production via $D_s \to \phi\pi \to K^+K^-\pi^+$: extension of the momentum reach to low p_t.
- Charm baryon production via $\Lambda_c \to pK^-\pi^+$: first measurement in Pb–Pb collisions at LHC, study of the charmed baryon/meson ratio.
- Beauty production via $B \to D^0$ ($\to K^-\pi^+$): measurement of B production in Pb–Pb collisions.
- Production of low-mass dielectrons: measurement of QGP radiation and hadronic spectral functions.

For these studies, a fast simulation scheme has been employed. It is based on Monte Carlo productions including the detailed geometry and response of the current ALICE detector setup. The impact of the ITS upgrade is obtained by recomputing reconstructed track parameters by means of a scaling of the residuals of the impact parameters in $r\varphi$ and z, as well as of the transverse momentum, with respect to their true values. The latter are known from the generated particle kinematics. For the performance studies, the following baseline configuration for the upgraded ITS (see detailed description in Chapter 3) has been considered: 7 pixel layers with radii from 2.2 to 43 cm instrumented with pixel detectors with an intrinsic resolution $(\sigma_{r\varphi}, \sigma_z) = (4,4)$ µm, and with a radiation length of 0.3% X_0 per layer.

1.6 Competitiveness and Uniqueness of ALICE with an Upgraded ITS

In this section we point out the aspects that will make unique the heavy flavour physics program that can be carried out with heavy-ion collisions at the top LHC energy by ALICE with an upgraded ITS detector.

1.6.1 With respect to STAR at RHIC

With its new silicon Heavy Flavour Tracker (HFT) [6], the STAR experiment at RHIC is going to address a heavy flavour physics program similar to the one we propose. This project intends to study heavy quark propagation and thermalization in the QGP formed in Au–Au collisions at $\sqrt{s_{NN}} = 200$ GeV. This will be mainly done via the measurement of the D meson and Λ_c baryon nuclear modification factor and elliptic flow, and via beauty-decay electron tagging.

Charm and beauty production cross sections are expected, on the basis of NLO pQCD calculations [7], to be about 10 and 100 times, respectively, larger at the top LHC energy than at the top RHIC energy. Therefore at the LHC, the kinematic range over which charm and beauty production can be measured extends to much larger transverse momenta. This presents a unique opportunity for the study of the predicted colour-charge and mass dependencies of the parton–medium interaction with high energy c and b quarks, using in particular prompt and non-prompt D mesons, and non-prompt J/ψ mesons.

The intriguing open questions on heavy quark thermalization in the QGP, and the coalescence-induced baryon/meson effect in the charm sector have to be addressed in the very different energy regimes accessible at RHIC and the LHC. Indeed, these effects could vary between $\sqrt{s_{NN}} = 200$ GeV and 5.5 TeV, and their comparison would provide crucial information for the characterization of the QGP properties and their excitation energy function. For instance, the first measurements of global system features in Pb–Pb

collisions at $\sqrt{s_{\rm NN}} = 2.76$ TeV by ALICE [8–10] indicate that the hot and dense system formed at the LHC has three times larger energy density and two times larger volume than at RHIC energies.

1.6.2 With respect to CMS and ATLAS at the LHC

The ATLAS and CMS experiments have excellent capabilities for lepton triggering and reconstruction over a broad η acceptance. This is coupled to a precise track position and momentum measurement with silicon detectors in strong magnetic fields. Both these features make them ideally suited to study beauty production at high $p_{\rm t}$ using displaced leptons and displaced $\rm J/\psi$ mesons.

A comparison of the features of ALICE, ATLAS and CMS that are relevant for heavy-flavour measurements is presented in Table 1.1.

Table 1.1: Comparison of the features of the future ALICE, ATLAS and CMS trackers that are relevant for heavy-flavour measurements [11, 12]. The p range of the ALICE PID reported here refers to the combined PID information of ITS, TPC and TOF. However, it does not include the TPC PID in the relativistic rise.

	current ALICE	ALICE upgrade	ATLAS upgrade	CMS upgrade
innermost point (mm)	39.0	22.0	25.7	30.0
x/X_0 (innermost layer)	1.14%	0.3%	1.54%	1.25%
d_0 res. $r\varphi$ (μm) at 1 GeV/c	60	20	65	60
hadron ID p range (GeV/c)	0.1−3	0.1−3	–	–

An important advantage for ALICE in the low-momentum region is the small material budget of the silicon tracker, which with this ITS upgrade would become a factor 4 and 5 smaller than that of CMS and ATLAS respectively. This lower thickness results in substantially smaller multiple scattering for low-momentum particles and so a better impact parameter resolution and reconstruction efficiency. This is clearly crucial for low-$p_{\rm t}$ charm and beauty measurements. This is the case in particular for $\Lambda_{\rm c}$ reconstruction, where the decay protons have momenta well below 1 GeV/c and are strongly affected by multiple scattering (larger for heavier particles, due to the $1/\beta$ dependence).

Finally, hadron identification over a very broad momentum range, 0.1–3 GeV/c, will be preserved as one of the most unique features of ALICE and a very strong point in its competitiveness with respect to the other two large LHC experiments. This capability, provided by the TPC, the TOF, and the ITS, has already proven to be crucial for the measurement of D meson production in Pb–Pb collisions, with background reduction of a factor 2–3 in the low momentum region. It has also been crucial for the observation of the $\Lambda_{\rm c}$ signal in pp collisions. The simulation studies for $\Lambda_{\rm c} \to {\rm pK}\pi$ and $\rm D_s \to KK\pi$ reported in Chapter 2 indicate that the background is reduced by a factor up to 20–30 at low $p_{\rm t}$ by applying the π/K/p identification from ITS, TPC and TOF. The study of charm meson and baryon production and flow at low momentum would not be possible without good hadron identification capability.

1.7 Upgrade Timeline

The ALICE upgrade will require a long shutdown (LS) and, therefore, will naturally have to be in phase with the installation of upgrades for the other LHC experiments. These are planned as of today for the 2013/14 and 2017/2018 shutdowns. The ALICE upgrade targets the long LHC shutdown period in 2017/2018 (LS2). The R&D efforts for the ITS upgrade will continue until 2014, construction will take place in 2015/17 and then installation and commissioning in 2018. A more detailed discussion of the ITS upgrade timeline is given in 6.

1.8 Document Summary

The physics performance and limitations of the present ALICE detector in studying heavy flavour at mid-rapidity in Pb-Pb collisions, as well as the performance of the upgraded detector, are discussed in Chapter 2. Chapter 3 deals with the detector functional requirements and performance in terms of tracking and identification of charged particles. Chapter 4 reviews the technologies that are being considered for the detector implementation, with a particular focus on the key R&D activities. The aspects related to the integration of the new detector, the support mechanics, the cooling and the services will be presented in Chapter 5. Finally, Chapter 6 will present the project organization, timeline and cost estimate.

Chapter 2

Physics Motivation

2.1 Studying the QGP with Heavy Quarks and Low-mass Dileptons

The main physics motivation for the upgrade of the Inner Tracking System of the ALICE experiment is to perform new measurements on heavy flavour (charm and beauty) and thermal dilepton production in heavy-ion collisions, which address important questions about the QGP properties that cannot be answered with the present experimental setup.

Heavy quarks play a special role in heavy-ion physics because they constitute a tagged (identified) probe (from production to observation), which enables a unique access to their interactions in the QGP. This allows us to gain microscopic insights into the transport properties of the medium. Heavy-flavour particles may be thought of as "Brownian motion" markers, the kinematical distributions of which (especially in momentum and azimuthal angle) reflect their reinteraction history. The large mass makes complete thermalization very difficult, thus most likely preserving a "memory" of the interaction history. As an additional benefit, the large-mass limit allows for simplifications in the theoretical treatment via controlled approximations (such as potential approaches), which improves the accuracy in extracting microscopic information on QCD matter structure from experiment (for a review, see e.g. [13]). Moreover, in QCD as in QED, the interactions of non-relativistic and semi-relativistic particles in a medium are dominated by elastic collisions, while in the ultra-relativistic limit radiation takes over. At which momentum scale this transition occurs in QCD is currently an open, yet fundamental question, whose answer is required for a proper interpretation of hard- and heavy-flavour probes. In fact, heavy quarks provide a unique tool to map out the momentum scale of this transition, since they can be tagged throughout all momentum ranges, from low to intermediate, to high p_{t}.

The two main open questions concerning heavy-flavour interactions with the QGP medium —and the corresponding experimental handles— are:

- Thermalization and hadronization of heavy quarks in the medium, which can be studied by measuring the baryon/meson ratio for charm ($\Lambda_{\mathrm{c}}/\mathrm{D}$) and for beauty ($\Lambda_{\mathrm{b}}/\mathrm{B}$), the azimuthal anisotropy v_2 for charm mesons and baryons, and the possible in-medium thermal production of charm quarks.

- Heavy-quark in-medium energy loss and its mass dependence, which can be addressed by measuring the nuclear modification factors R_{AA} of the p_{t} distributions of D and B mesons separately in a wide momentum range.

These two topics are presented separately in the following. However, it is important to emphasize that they are closely related. The high-momentum heavy quarks quenched by in-medium energy loss are shifted towards low momentum and may ultimately thermalize in the system, through QCD interaction

mechanisms that are essentially the same as those responsible for the energy loss, and participate in the collective expansion dynamics. Therefore, the simultaneous experimental investigation and theoretical understanding of the thermalization-related observables and of the energy-loss-related observables constitute an unique opportunity for the characterization of the QGP properties, in particular of the flavour-dependent transport coefficients. In this scope, heavy quarks are particularly well suited, because they preserve their identity (mass, flavour, and colour charge) while interacting with the medium.

Presently, in the ALICE central barrel, the capability of studying yields and spectra of particles containing heavy quarks is mainly provided by the ITS. Charm production can be addressed through meson and baryon hadronic decays ($\mathrm{D}^0 \to \mathrm{K}^-\pi^+$, $\mathrm{D}^+ \to \mathrm{K}^-\pi^+\pi^+$, $\mathrm{D}_\mathrm{s}^+ \to \mathrm{K}^+\mathrm{K}^-\pi^+$, $\mathrm{D}^{*+} \to \mathrm{D}^0\pi^+$, $\mathrm{D}^0 \to \mathrm{K}^-\pi^+\pi^-\pi^+$, and $\Lambda_\mathrm{c}^+ \to \mathrm{pK}^-\pi^+$) via topological selection of secondary decay vertices displaced from the primary vertex. Particle identification is needed to reduce the very large backgrounds in heavy ion collisions. This is provided mainly by the TPC and TOF detectors. In addition, charm and beauty can be tagged in semi-leptonic decays $\mathrm{D,B} \to \mathrm{e} + \mathrm{X}$. Electron identification is provided by the TPC, TOF, TRD and EMCAL detectors. However, in order to obtain the B-decay electron yields, a residual component of electrons from charm decays has to be subtracted statistically, introducing a significant systematic uncertainty, especially in the low p_t region (below 5 GeV/c). Important physics topics such as the study of beauty baryons or of hadrons with more than one heavy quark are beyond the capability of the current detector, and the performance for charm baryons will be much worse than for charm mesons, given that the most abundantly produced baryon (Λ_c) has a mean proper decay length ($c\tau$) of only 60 μm, to be compared with the 120–300 μm of D mesons.

It is important to stress that in order to address new high-precision measurements in a thorough and systematic way, the following design goals have to be met:

1. Coverage in transverse momentum as complete as possible, in particular down to very low momenta.

2. Very precise reconstruction of secondary vertices from decaying charm or beauty particles (prompt D, D and J/ψ from B decays, Λ_c, Λ_b).

The measurement of low-mass dilepton production provides access to the bulk properties and the space-time evolution of the hot and dense QCD matter formed in ultra-relativistic heavy-ion collisions, and reveals microscopic properties such as the relevant degrees of freedom and the hadronic excitation spectrum in medium (see [14] for a recent review). Electromagnetic (EM) radiation is produced at all stages of the collision, and since leptons couple only weakly to the surrounding medium, their spectrum retains information of the entire system evolution. This is contrary to the measurement of final state hadrons which interact with the system until freeze-out, and therefore carry only indirect information on the early stages of the collision.

The fundamental questions to be addressed by a comprehensive measurement of low-mass dileptons in heavy-ion collisions at the LHC are the following:

– The generation of hadron masses is driven by the spontaneous breaking of chiral symmetry of QCD in the vacuum. Lattice QCD predicts that this fundamental symmetry is restored at finite T, leading to substantial modifications of the vector and axial-vector spectral functions. Such modifications, in particular of the ρ–meson, can be inferred from low-mass dilepton spectra, which constitute the only experimental observable proposed so far to characterize the chiral properties of hot QCD.

– Dilepton production is intimately related to the temperature of the system at all stages of the collision and encoded in the transverse momentum and invariant mass dependencies. Unlike transverse

momentum, invariant mass is not subject to blue-shift in collectively expanding systems and therefore most directly related to temperature. The study of low-mass dileptons allows also an estimate of real direct photon production which is complementary to real photon measurements from conversions and calorimetry, and less prone to physical backgrounds [15].

– The space-time evolution of the system, in particular its lifetime can be extracted from low-mass dilepton measurements. The potential to disentangle early from late contributions gives detailed access to the evolution of collectivity and the fundamental properties related to it, such as transport coefficients, viscosity, and the equation of state.

The upgrades of the ITS and the TPC as main tracking and PID devices in the ALICE central barrel enable a high statistics measurement of e^+e^- pairs in Pb–Pb collisions. Specifically, the measurement benefits from the low material budget and the enhanced low-p_t tracking capabilities of the upgraded ITS to extend the measurement into the relevant low pair-mass (M_{ee}) and low pair transverse momentum ($p_{t,ee}$) region, and to suppress combinatorial backgrounds from photon conversions and π^0 Dalitz decays. Moreover, the excellent secondary vertex resolution of the ITS will allow to separate contributions from semi-leptonic charm decays, which constitute a major physics background to the prompt radiation.

A new vertex detector with the capabilities described above will place ALICE in a unique position in comparison to the other LHC experiments, since for a number of heavy-flavour and dilepton measurements, the other experiments can only explore momenta above a certain threshold of a few GeV/c.

2.2 Physics Landscape and Impact of the ITS Upgrade

2.2.1 Heavy Flavour Thermalization, Coalescence, and Possible Thermal Production: Present Status and Further Measurements

Given the very large energy of the collisions at LHC, an abundant production of $c\bar{c}$ and $b\bar{b}$ pairs is expected in the initial hard-scattering processes (about 80 and 3, respectively, per central Pb–Pb collision at $\sqrt{s_{NN}} = 5.5$ TeV, using NLO QCD calculations [7] with nuclear PDF modification [16] and binary collision scaling).

Heavy quarks lose energy while traversing the hot and dense medium and, at sufficiently low transverse momentum, they can thermalize in the medium itself. Reinteractions will reflect in the p_t spectra and, in particular, in the azimuthal anisotropy in semi-central collisions.

At low momentum the azimuthal anisotropy is determined by the so-called elliptic flow, which provides the most direct evidence of the collective hydrodynamical behaviour of the medium. During the collision, the two nuclei overlap in an elliptically-shaped region, the short axis of which lies on the reaction plane. The expansion, under azimuthally anisotropic pressure gradients, translates the space asymmetry into a momentum anisotropy. This is detected by measuring the momentum-dependent azimuthal distribution $d^2N/dp_t d\Delta\varphi$ of the produced particles with respect to the reaction plane. The parameter describing the anisotropy is v_2, which is the second coefficient of the Fourier expansion of the azimuthal distribution.

The momentum distribution of heavy quarks at the moment of their creation is isotropic in azimuthal direction. Therefore, a non-zero v_2 value of heavy-flavour hadrons can only originate from interactions between light QGP constituents and the heavy quarks.

A preliminary measurement of the D^0, D^+ and D^{*+} azimuthal anisotropy coefficient v_2 in 30–50% central Pb–Pb collisions was obtained by ALICE using about 10^7 events from the 2011 run (see Figure 2.1) [17]: the result is very intriguing because, with a non-zero v_2 (3σ significance for D^0 in 2–6 GeV/c), it suggests that D mesons may take part in the flow.

Several models [18–20] that include heavy quark transport in the medium, with various implementations

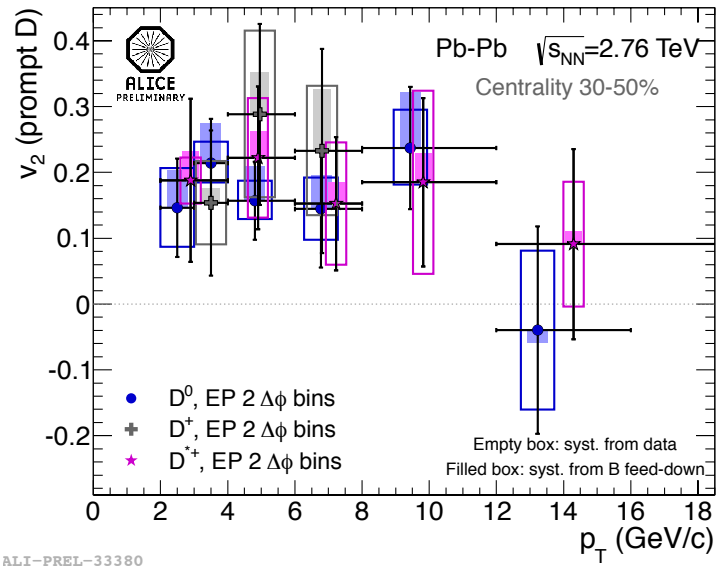

Figure 2.1: Preliminary measurement of D^0, D^+ and D^{*+} v_2 in 30–50% Pb–Pb collisions at the LHC by ALICE, with 10^7 events from the 2011 run [17].

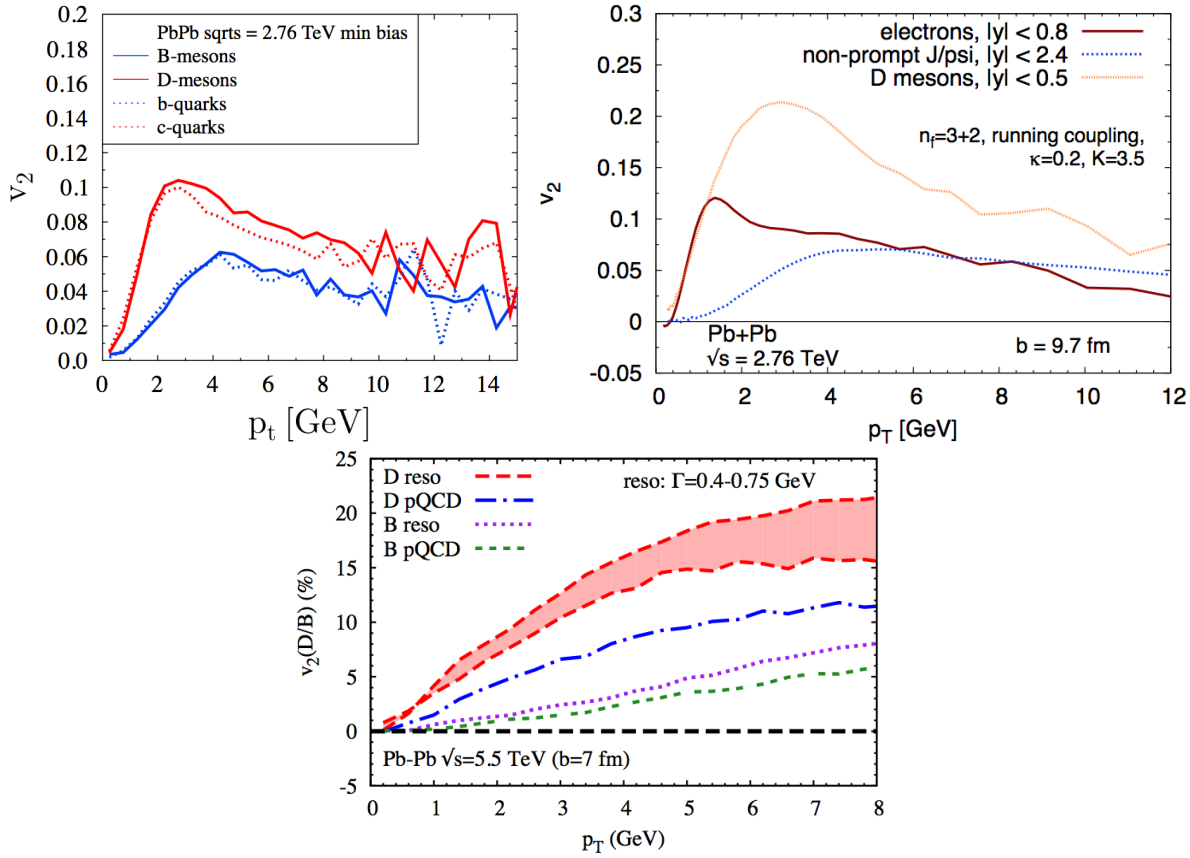

Figure 2.2: Model predictions for the azimuthal anisotropy parameter v_2 of D and B mesons (or J/ψ from B decays) in Pb–Pb collisions at LHC energies: top, from left to right [18, 19], bottom [20].

of the quark-medium interaction, predict a large v_2 (up to 0.2 in semi-central collisions) for D mesons at low momentum, as shown in Figure 2.2. At low p_t, v_2 for B mesons is predicted to be substantially smaller than for D mesons. This is a consequence of the smaller mass of charm quarks, which can more

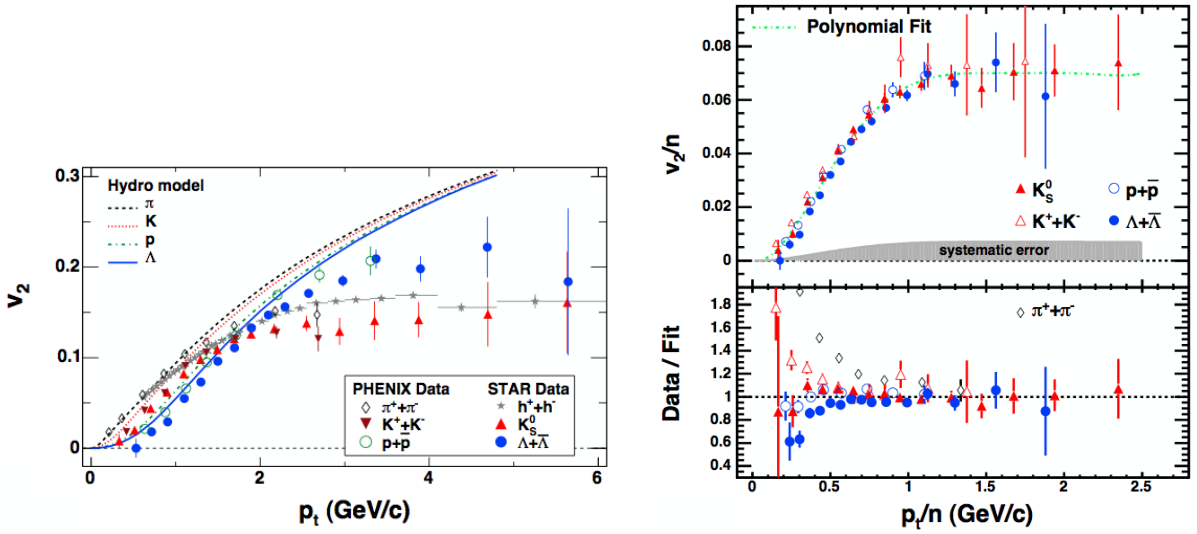

Figure 2.3: Constituent quark scaling of meson and baryon v_2 as measured by STAR in Au–Au collisions at $\sqrt{s_{\rm NN}} = 200$ GeV [21]. Left: v_2 vs. $p_{\rm t}$. Right: v_2/n_q vs. $p_{\rm t}/n_q$.

easily absorb the v_2 of the light plasma particles with which they collide during the expansion. This difference of v_2 between b and c quarks at intermediate $p_{\rm t}$ is inherent of the QCD interaction mechanisms and can, thus, serve as an important test of our understanding of these mechanisms in an extended QGP.

Measurements of the v_2 of D mesons and B mesons (or J/ψ and D from B decays) starting at $p_{\rm t} \approx 2$ GeV/c with absolute uncertainties well below 0.02 for D and of at most 0.05 for B are required in order to achieve sensitivity for the predicted difference between charm and beauty. On the basis of the results obtained for D mesons with 10^7 events from the 2011 Pb–Pb run, with absolute statistical uncertainties of about 0.10, we can expect to reduce the statistical uncertainties to about 0.06 with the data of the 2015–16 runs (3 times larger integrated luminosity). On the other hand, a measurement for beauty down to 2 GeV/c will not be possible, for ALICE due to the lack of statistics, for CMS due to the $p_{\rm t}$ cut of about 6 GeV/c for non-prompt J/ψ imposed by the muon trigger $p_{\rm t}$ threshold (see Section 2.2.2).

At RHIC, $v_2(p_{\rm t})$ or $v_2(m_{\rm t} - m_0)$ of identified particles scales with $m_{\rm t} - m_0$ for $p_{\rm t} < 2$ GeV/c [22]. The same behavior is observed also at LHC [23]. At higher $p_{\rm t}$, v_2 seems to scale with the number of constituent quarks n_q, so that v_2/n_q scales with $p_{\rm t}/n_q \simeq m_{\rm t}/n_q$. This is clearly visible in Figure 2.3, where the Λ and $\rm K^0_S$ data extend up $p_{\rm t} \approx 5$ GeV/c [21]. This observation suggests the presence of an initial partonic state. It can be naturally explained with a coalescence model [24] for hadronization, where the flow of constituent quarks add up, so that $v_2^{meson}(p_{\rm t}) = 2\,v_2^q(p_{\rm t}/2)$ and $v_2^{baryon}(p_{\rm t}) = 3\,v_2^q(p_{\rm t}/3)$. Preliminary results from ALICE on proton and pion v_2 up to $p_{\rm t} \approx 9$ GeV/c indicate that this scaling holds at LHC energies only within about 20% [25], thus challenging the interpretation based on coalescence models.

A very stringent test of the level of in-medium thermalization of c and b quarks would be to verify whether this universal scaling continues to hold also for heavy flavour mesons and baryons. This requires measuring the D meson and $\Lambda_{\rm c}$ elliptic flow in the range $2 < p_{\rm t} < 5$ GeV/c, where the baryon/meson (Λ/K) separation at RHIC is most pronounced.

The production of charm and beauty baryons has also a particular interest to assess the thermalization and the mechanisms of hadronization of heavy flavours in the medium, because it was predicted that their production could be significantly enhanced in nuclear collisions [30]. For light flavour and strange baryons, such an enhancement was indeed observed at intermediate transverse momenta at RHIC and at LHC [26, 27], as shown in Figure 2.4.

Within thermal models, it is assumed that heavy quarks, produced in initial hard scattering processes,

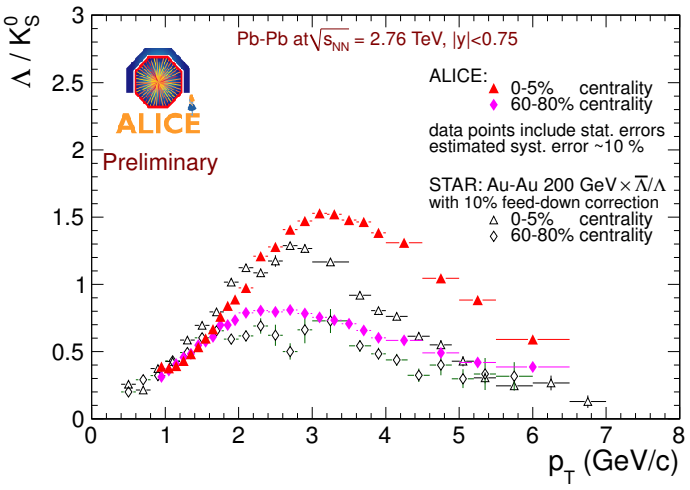

Figure 2.4: $\Lambda/\mathrm{K}^0_\mathrm{S}$ ratio vs. transverse momentum as measured by ALICE at LHC and by STAR at RHIC [26, 27].

reach the thermal equilibrium with the medium, charm and beauty hadrons are produced during the QGP hadronization and the relative abundances of hadron species with given heavy flavour depends only on their masses. At variance, within coalescence models, partons produced in hard scatterings can combine with quarks and anti-quarks in the QGP to form hadrons. The resulting hadrons will have momenta between those from the independent fragmentation and from the hadronization of the QGP. It was suggested that this could lead to a rather significant enhancement of the Λ_c with respect to thermal models [30], where the relative abundance of particles depends only on their masses.

Figure 2.5 shows the $\Lambda_\mathrm{c}/(\mathrm{D}^0+\mathrm{D}^+)$ ratio in central (0–10%) Pb–Pb collisions at $\sqrt{s_\mathrm{NN}} = 2.76$ TeV from a model with charm-quark transport in the QGP and hadronization via coalescence (based on [28]). The ratio reaches a maximum of 0.16 at p_t of about 4 GeV/c, and the enhacement with respect to pp collisions is of a factor about 1.5.

Some coalescence models consider also the possibility of recombination of a heavy quark with di-quarks present in the QGP, which would lead to larger enhancements. As an example of the size of the expected effect, we report in Figure 2.6 the $\Lambda_\mathrm{c}/\mathrm{D}^0$ and $\Lambda_\mathrm{b}/\overline{\mathrm{B}}^0$ enhancements as a function of transverse momentum for central Au–Au collisions at RHIC ($\sqrt{s_\mathrm{NN}} = 200$ GeV) [29]. The enhancement is of up to 7–10 for both baryon/meson ratios, and it is maximum at $p_\mathrm{t} \simeq 2$ GeV/c for charm and $p_\mathrm{t} \simeq 4$ GeV/c for beauty. For strange quarks (Figure 2.4) the position of the maximum is higher by about 0.5 GeV/c at LHC with respect to RHIC energy. Therefore, one can expect the maximum of $\Lambda_\mathrm{c}/\mathrm{D}^0$ to be at $p_\mathrm{t} \simeq 3$ GeV/c at LHC energy. This demands for a measurement of Λ_c production in central Pb–Pb collisions starting from $p_\mathrm{t} \simeq$ 2–3 GeV/c.

If coalescence occurs statistically at the hadronization temperature, there could be a chance that even two or three charm quarks coalesce together forming a multi-charm baryon. That can happen only if the quarks are close to thermalization because high momentum quarks hadronize independently, unless two or three correlated quarks are close together in momentum from the hard process (which is much less likely to occur). Thus, also an enhanced production rate of multi-charm baryons is a distinctive feature of thermalization of the medium produced in heavy ion collisions. The enhancement predicted by statistical models in case of hadronization by coalescence can reach a factor 10^3 for the Ω_ccc at LHC energies [31]. Thus, double and triple charmed baryons or charmed-beauty baryons could be observed (it has to be noted that states as the Ω_ccc are not yet observed even in elementary collisions).

From the experimental point of view, the main issue for the measurement of charmed baryons is their rather short lifetime: the $c\tau$ of the Λ_c is a factor of 2 smaller than that of the D^0. The charmed baryon mea-

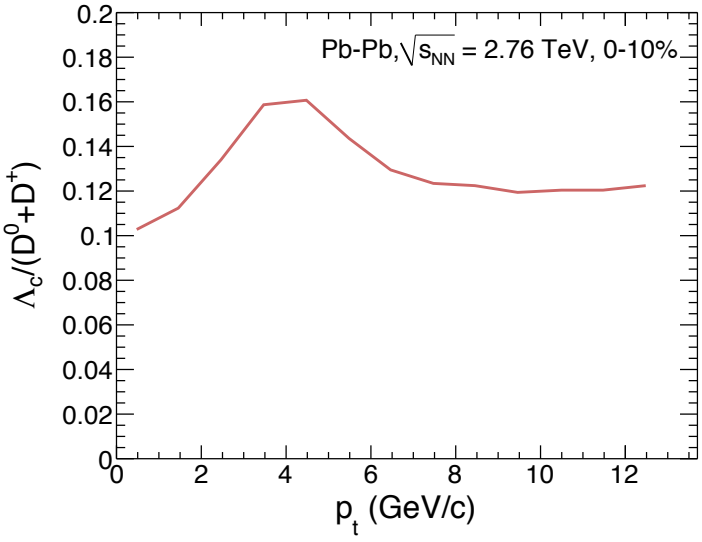

Figure 2.5: $\Lambda_c/(D^0+D^+)$ ratio in central Pb–Pb collisions at $\sqrt{s_{NN}} = 2.76$ TeV from a calculation with charm-quark transport in the QGP and coalescence (based on [28]).

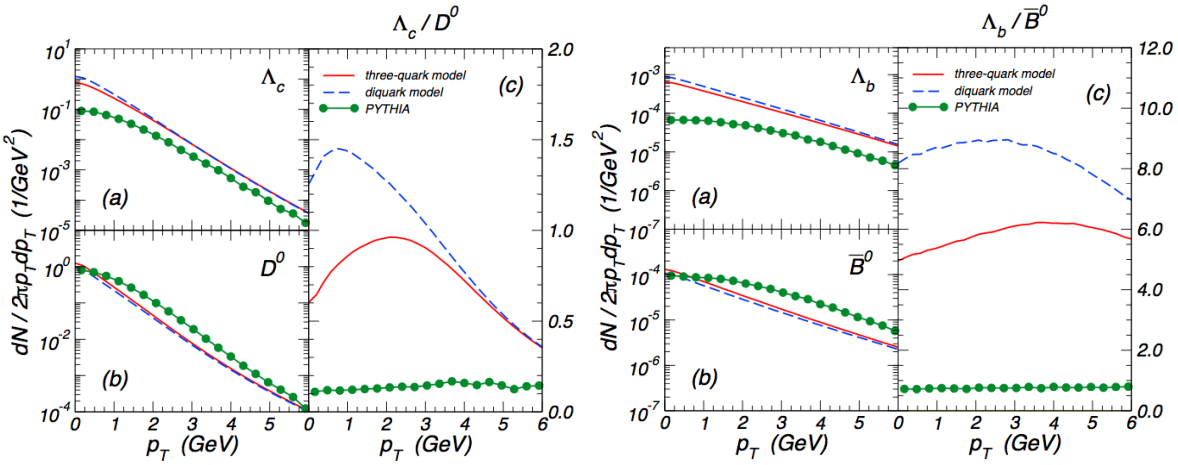

Figure 2.6: Heavy flavour baryon/meson enhancement as a function of p_t in Au–Au collisions at $\sqrt{s_{NN}} =$ 200 GeV [29]. Left: Λ_c/D^0. Right: $\Lambda_b/\overline{B}^0$.

surements require a very precise tracking and impact parameter resolution, because the decay tracks typically have displacements of a few tens of microns ($\sim c\tau$) from the primary interaction vertex. Presently, the Λ_c signal was observed by ALICE in the $pK^-\pi^+$ decay channel in pp collisions at $\sqrt{s} = 7$ TeV collected in 2010, as we show in one of the next sections. However, the statistical significance is relatively low (about 5 σ), as compared to the D meson signals. In Pb–Pb collisions, in particular down to low transverse momenta, the Λ_c measurement is beyond the capabilities of the present setup.

Complementary to the Λ_c measurement is the study of the production of the strange charm meson D_s^+. Due to the abundance of strange quarks in the QGP, D_s^+ production is expected to be enhanced at low momentum if charm hadrons form predominantly by in-medium hadronization of c quarks (see e.g. [28, 33, 34]). In particular, the enhancement of D_s^+/D in Pb–Pb vs. pp collisions quantifies how much of the strangeness content of the QGP is picked up by the charm; it is thus quantifying the coalescence contribution in c-quark hadronization. The maximal enhancement effect may reach up to a factor of 2, therefore an accuracy of at least 20–30% in the D_s^+ measurement is required for an evidence of the effect and of 10% for its quantitative study.

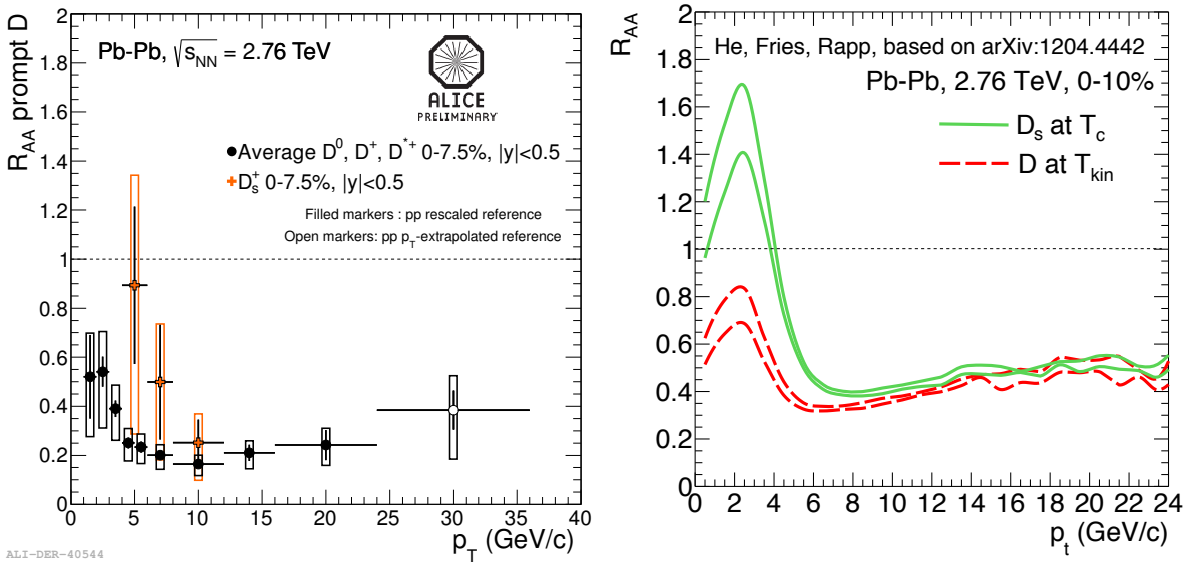

Figure 2.7: Left: R_{AA} of D_s^+ and non-strange D mesons in central Pb–Pb collisions (0–7.5%) at $\sqrt{s_{NN}} = 2.76$ TeV [32]. Right: the same observables from a calculation with charm-quark transport in the QGP and coalescence [33].

Also the comparison of D^0 (or D^+) to D_s^+ v_2 [28, 33] is very interesting. D mesons formed during the medium expansion are expected to couple (through their light-quark content) to the bulk hadronic medium [35] and thus gain additional v_2 from the hadronic phase. Since this effect would be smaller for s than for u and d quarks, a v_2-splitting of D^0 vs. D_s^+ is expected. The effect would be of 20–30% relative difference in v_2 [28, 33, 35], thus requiring, for observation, an experimental accuracy on each v_2 of better than 10%.

A first preliminary measurement of D_s^+ production in $4 < p_t < 12$ GeV/c in central Pb–Pb collisions was carried out with 16×10^6 events from the 2011 Pb run [32]. Figure 2.7 (left) shows the nuclear modification factor $R_{AA}(p_t) = (dN_{AA}/dp_t)/(\langle T_{AA}\rangle d\sigma_{pp}/dp_t)$ for D_s^+ compared to the average R_{AA} of non-strange D mesons (this measurement will be discussed in more detail in the next section, in the context of heavy-flavour energy loss). The D_s^+ nuclear modification factor shows similar suppression as for D^0, D^+ and D^{*+} for $p_t > 8$ GeV/c. For lower transverse momenta, the central values of the measurement show an increase, however the large statistical ($\approx 35\%$) and systematic ($\approx 60\%$) uncertainties do not allow to draw a conclusion on a possible D_s^+/D enhancement. Figure 2.7 (right) shows the results of a calculation [33] that includes heavy-quark transport in the QGP and hadronization via coalescence, obtaining an enhancement of D_s^+/D by about a factor of 2 in the interval $0 < p_t < 4$ GeV/c.

If the initial temperature of the high-density system produced in central collisions is large enough, a thermal production of $c\bar{c}$ pairs may occur, leading to a measurable increase of the total production yields of charm particles [36–39].

Thermal charm production is studied at next-to-leading-order in pQCD in Ref. [38] and it was found that the total yield of charm production may be enhanced by 30 (80)% if initial temperatures of 700 (750) MeV are considered and a charm quark mass value of 1.3 GeV/c^2 is used (see Figure 2.8, left). On the other hand, the enhancement would be marginal if the initial temperature is of the order of 600 MeV or if the charm quark mass is 1.5 GeV/c^2 or higher.

In-medium $c\bar{c}$ production is studied within a partonic transport model in Ref. [39]. As shown in Figure 2.8 (right), the relevance of the effect is found to depend strongly on the initial gluon density assumed for the deconfined system (initial conditions from PYTHIA, Color Glass Condensate or mini-jets) and

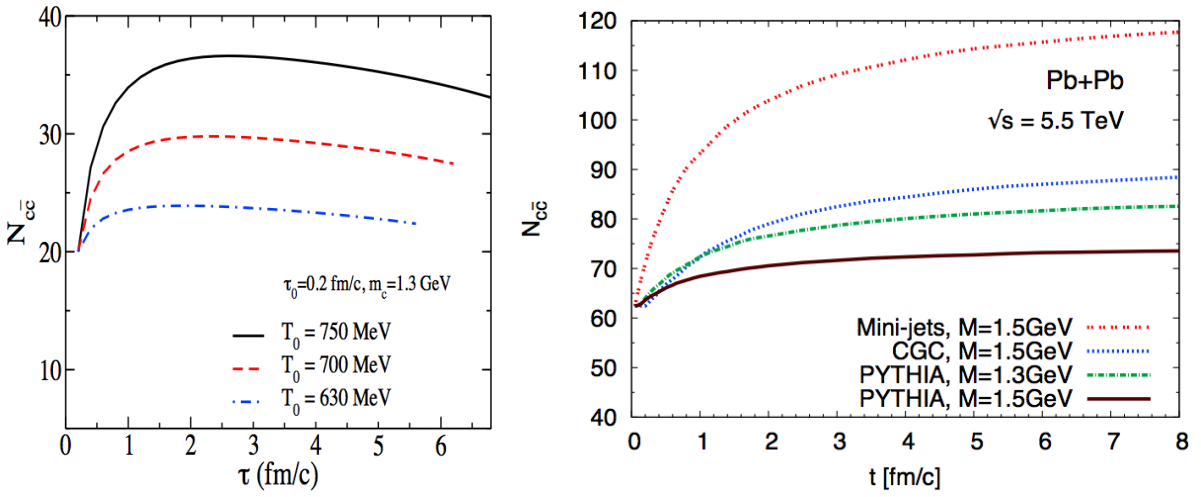

Figure 2.8: Thermal charm production in Pb–Pb collisions at top LHC energy, as a function of the proper time, for two different models. Left: $c\bar{c}$ yields per unit of rapidity at mid-rapidity from [38]; total $c\bar{c}$ yields from [39].

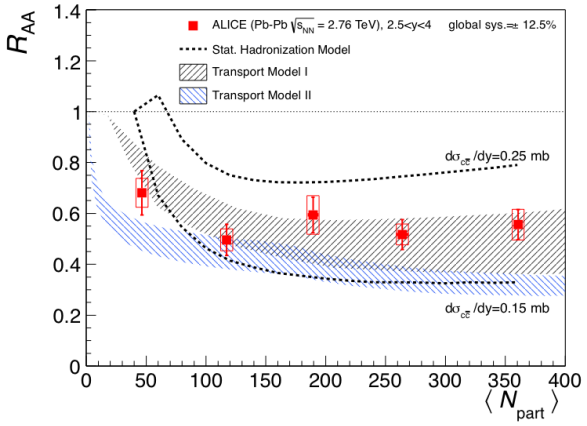

Figure 2.9: Inclusive J/ψ R_{AA} measured in Pb–Pb collisions at $\sqrt{s_{NN}} = 2.76$ TeV compared to the predictions by Statistical Hadronization Model [40], Transport Model I [41] and II [42]. The large uncertainty on the model predictions is due to the lack of knowledge of the total charm production in Pb–Pb collisions.

on the charm quark mass value.

In conclusion, while the yield of possible thermal charm production depends on specific model parameters, it is clear that its observation would provide key information on the initial temperature and density of the deconfined plasma. From the experimental point of view, this effect has to be searched as an enhancement of the total D meson production yields per binary collision in Pb–Pb with respect to pp collisions, or in central with respect to peripheral Pb–Pb collisions. It is, therefore, essential to reconstruct D meson decays down to $p_t = 0$. In the comparison of pp and Pb–Pb, the initial-state modification has to be taken into account. This can be tackled using p–Pb collisions.

The measurement of the total charm production will also provide the natural normalization for the study of medium effects on charmonium production (J/ψ and ψ'). The crucial advantage of this normalization being that the initial-state effects are mostly common between open charm and charmonium and, thus, cancel out in the ratio $R_{AA}^{J/\psi}/R_{AA}^{D}$. In addition, the total charm production yield in Pb–Pb collisions is an ingredient in the model calculations of charmonium regeneration in the QGP [40]. At present, the large uncertainty on the estimate of this yield from perturbative QCD calculations translates into the main limitation in the comparison of statistical models predictions with J/ψ suppression data [43] (see

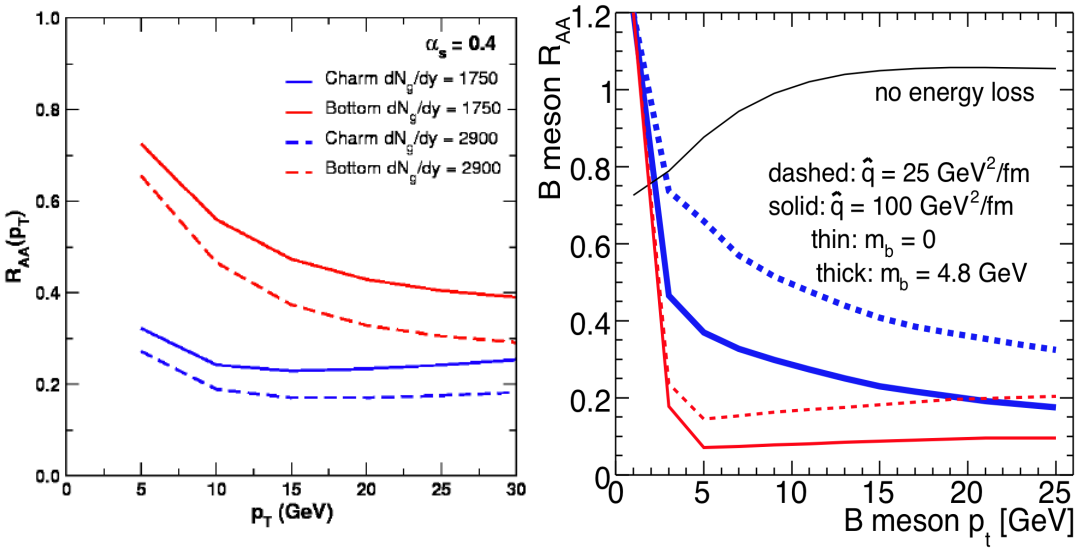

Figure 2.10: Left: prediction for R_{AA} vs p_t for D mesons (blue) and B mesons (red) in Pb–Pb collisions at the LHC, from radiative + collisions energy loss (DGHW) [46]. Right: mass dependence of B meson R_{AA} in Pb–Pb collisions at the LHC from radiative energy loss (ASW) [47].

Figure 2.9). Only a precise measurement of D meson production down to zero transverse momentum can provide a significant improvement in this comparison.

Impact of the ITS upgrade and new measurements

On the basis of the discussion in the previous section, a new improved silicon tracker at mid-rapidity will impact significantly on the following measurements:

- Charm down to zero p_t. See Section 2.3.3.
- D_s down to very low p_t. See Section 2.3.6.1.
- Charmed baryons - Λ_c. See Section 2.3.5.
- Beauty baryons - Λ_b. Once the Λ_c can be experimentally tagged, then also the beauty baryon Λ_b could be measured via the decay $\Lambda_b \rightarrow \Lambda_c + X$.
- Elliptic flow of charmed and beauty mesons and baryons down to low transverse momentum. The baryon sector will be accessible for the first time.

2.2.2 Heavy Quark Energy Loss: Present Status and Further Measurements

One of the distinctive features of the hot and dense medium formed in heavy ion collisions is the strong energy loss induced on the hard partons that are produced in the initial hard scattering processes. Parton energy loss is thought to be dominated by gluon radiation, but also elastic collisions with the medium gluons would play an important role. The investigation of heavy flavour energy loss has a particular interest. Indeed, gluon radiation from heavy quarks is predicted to be suppressed, with respect to the case of light partons, at angles smaller than the quark energy-over-mass (dead cone effect) [44, 45]. Moreover, light flavour hadrons are dominantly produced at LHC energies by hard fragmenting gluons, which lose more energy due to their stronger coupling to the medium. Thus, one has the prediction for the energy loss $\Delta E_g > \Delta E_c > \Delta E_b$. Experimentally, energy loss in heavy ion collisions can be investigated as a function of transverse momentum via the nuclear modification factor R_{AA}.

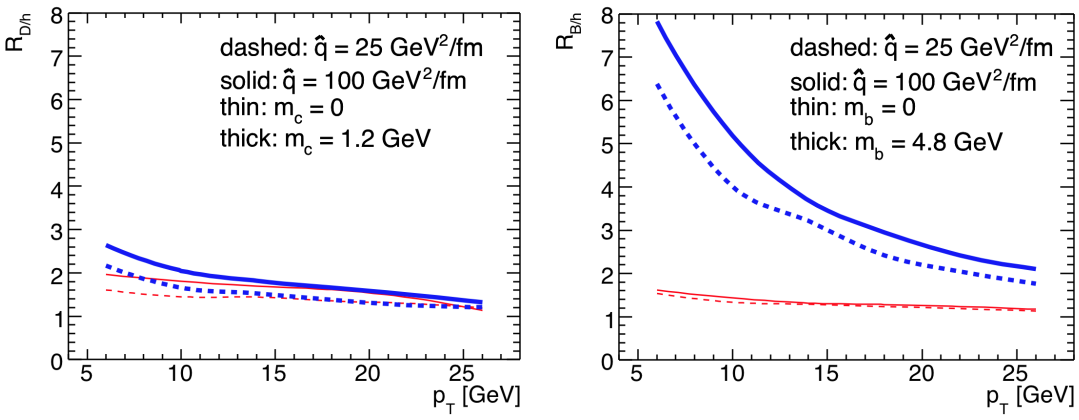

Figure 2.11: Heavy-to-light $R_{\rm AA}$ ratios as predicted by radiative energy loss (ASW) [47]. Left: $R^{\rm D}_{\rm AA}/R^{h}_{\rm AA}$. Right: $R^{\rm B}_{\rm AA}/R^{h}_{\rm AA}$.

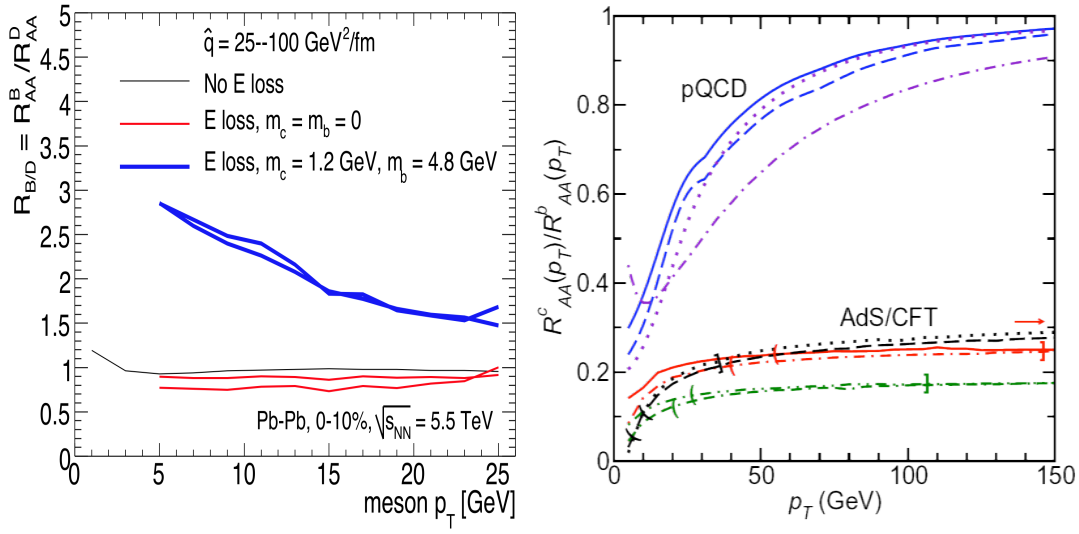

Figure 2.12: Predictions for the comparison of charm and beauty $R_{\rm AA}$ in Pb–Pb collisions at the LHC. Left: $R^{\rm B}_{\rm AA}/R^{\rm D}_{\rm AA}$ vs $p_{\rm t}$ from radiative energy loss (ASW) [47]. Right: $R^{\rm D}_{\rm AA}/R^{\rm B}_{\rm AA}$ vs $p_{\rm t}$ from radiative energy loss (pQCD) and AdS/CFT [48].

Theoretical models based on perturbative QCD with the inclusion of radiative parton energy loss predict for charm mesons a suppression factor of 3–5 and a significantly smaller suppression for B mesons (see left panel of Figure 2.10 [46]). The mass dependence of energy loss is more pronounced for beauty, as seen in the right panel of Figure 2.10 [47]. Mass and colour charge dependence can be investigated experimentally with the ratio $R_{\rm D/h} = R^{\rm D}_{AA}(p_{\rm t})/R^{h}_{AA}(p_{\rm t})$ (see Figure 2.11 [47]). The mass effect is more pronounced at moderately-low transverse momenta. At sufficiently high $p_{\rm t}$ (above ~ 10 GeV/c) the c quark starts to behave essentially as a massless parton. However, the ratio should not tend to one since it becomes sensitive to the colour charge dependence of energy loss.

Even more interesting is the ratio $R_{\rm B/D} = R^{\rm B}_{\rm AA}(p_{\rm t})/R^{\rm D}_{\rm AA}(p_{\rm t})$, which is shown in the left panel of Figure 2.12 [47]. Here, the ratio shows a strong deviation from one in particular at moderately-low $p_{\rm t}$, decreasing only rather slowly for increasing $p_{\rm t}$. String theory models inspired by the AdS/CFT correspondence have been able to describe qualitatively a number of aspects of the heavy ion collisions phenomenology (see e.g. [49]). Predictions for the ratio $R_{\rm D/B} = 1/R_{\rm B/D}$ are shown in the right panel of Figure 2.12 [48]. This ratio has also the advantage of magnifying the differences in the mass and $p_{\rm t}$ dependence of pQCD and AdS/CFT models. While differences are present among pQCD models and

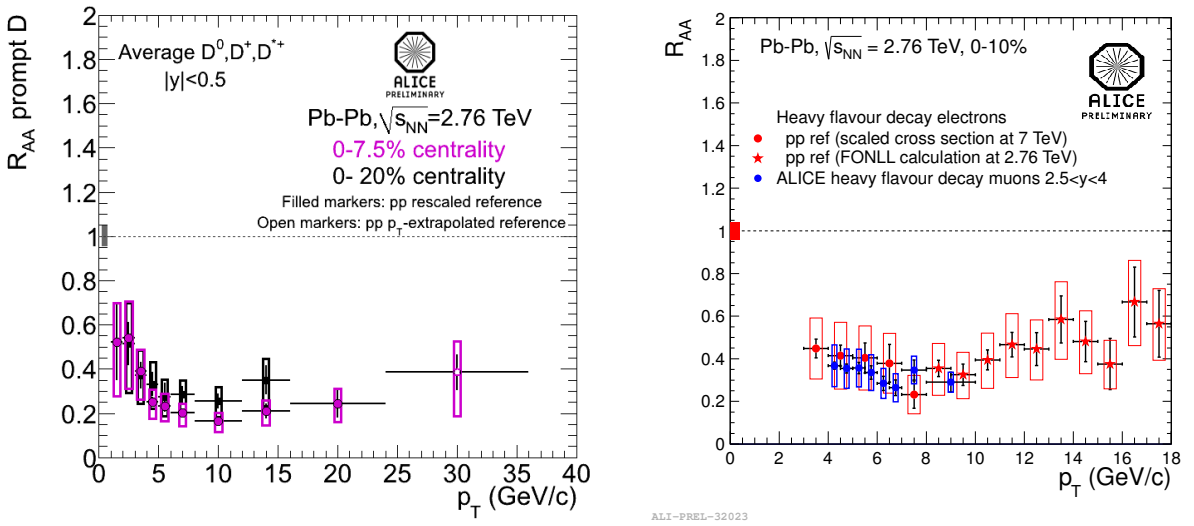

Figure 2.13: Heavy-flavour nuclear modification factors at mid-rapidity in central Pb–Pb collisions at the LHC measured by ALICE. Left: D meson $R_{\rm AA}$ in the centrality classes 0–20% (2010 data) [50] and 0–7.5% (2011 data) [51]. Right: $R_{\rm AA}$ for the heavy-flavour decay electrons [52] and heavy-flavour decay muons [53] in the centrality class 0–10%.

among AdS/CFT models, the two classes of models yield largely different predictions irrespectively of their input parameters.

Using data from 2010 and 2011 runs at the LHC with Pb–Pb collisions at 2.76 TeV, ALICE performed the first measurement of the D meson $R_{\rm AA}$, which is shown in Figure 2.13. With 2010 data the analysis was restricted to $p_{\rm t} > 2$ GeV/c [50]. It was possible to go down to 1 GeV/c using higher-statistics data from the 2011 Pb–Pb run [51], but reaching zero transverse momentum seems to be precluded with the current setup, due to the large background level. In addition, the present accuracy of the $R_{\rm AA}$ measurement is limited to $\approx$ 30–40% by the systematic uncertainties on the B feed-down correction, the signal yield extraction, and the efficiency evaluation. As it will be explained in Sections 2.3.3 and 2.3.4, all these contributions could be substantially reduced with an upgraded vertex detector. The feed-down correction, currently based on pQCD predictions with an hypothesis on the unknown nuclear modification of beauty production, will become more accurate with the direct measurement of the non-prompt fraction of D mesons. The systematic uncertainties on the yield extraction and efficiency correction will be reduced thanks to the higher statistics, that will allow for a better determination of the signal invariant mass shape and for the usage of less stringent selection cuts.

The other key measurement is a precision measurement of beauty energy loss via $R_{\rm AA}$ with coverage down to low $p_{\rm t}$. In ALICE, beauty production is accessed at mid-rapidity via $\mathrm{B} \rightarrow \mathrm{e} + \mathrm{X}$. In the present setup, this will be the only way to measure it. At low $p_{\rm t}$, the component of electrons from charm decays has to be subtracted statistically, implying a significant systematic uncertainty.

The $R_{\rm AA}$ for the heavy-flavour decay electron spectrum at mid-rapidity [52] and for the heavy-flavour decay muon spectrum at forward rapidity [53] are shown in Figure 2.13 (right).

In summary, with the current detector, a beauty production measurement at mid-rapidity may be possible only via displaced single electrons. However, at low $p_{\rm t}$ the subtraction of the background contributions is challenging.

Another interesting possibility is to measure beauty via the J/ψ decay tagging a secondary vertex with two leptons attached. This is a rather clean measurement. A first measurement in Pb–Pb was performed by the CMS Collaboration [54]. The left panel of Figure 2.14 shows the J/ψ pseudo-proper decay length

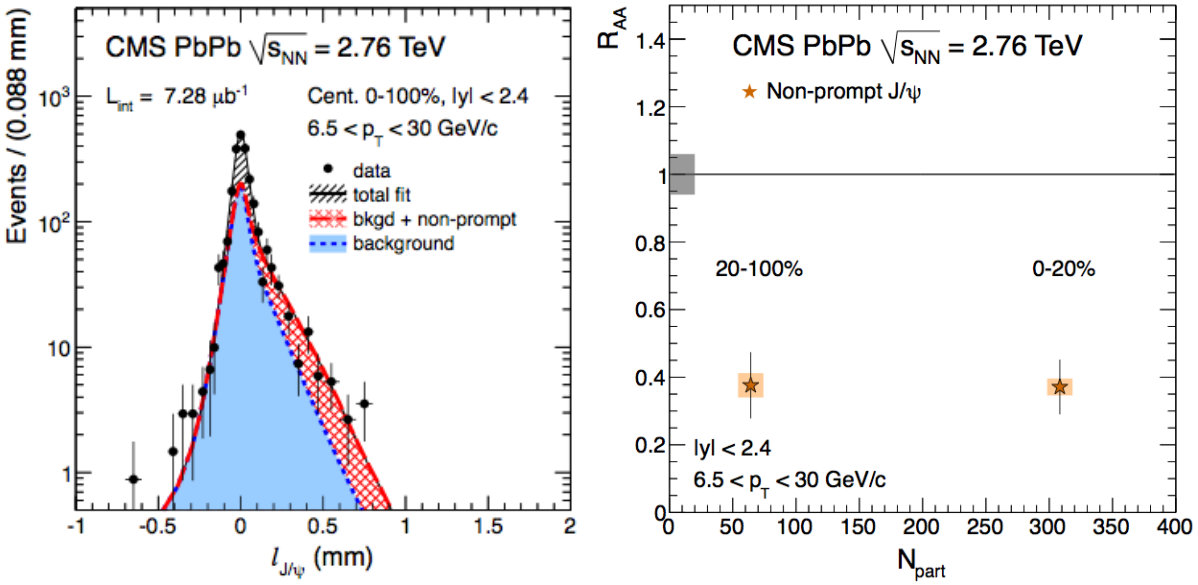

Figure 2.14: Left: J/ψ pseudo-proper decay length measured in Pb–Pb collisions at $\sqrt{s_{NN}}$=2.76 TeV measured by the CMS experiment [54]. Right: R_{AA} of J/ψ from B decays.

($l_{J/\psi} = L_{xy} m_{J/\psi}/p_t$). R_{AA} is shown in the right panel: the suppression is of about a factor 2.5. The CMS measurement is limited to the region J/ψ $p_t > 6.5$ GeV/c, due to the large momentum cut on the decay muons. In the present ALICE setup, at mid-rapidity this measurement is severely limited by the lack of a triggering scheme, which prevents to collect a high-statistics sample, and by the very large combinatorial background for $J/\psi \to e^+e^-$ in Pb–Pb collisions.

Impact of the ITS upgrade and new measurements

On the basis of the discussion in the previous section, a new improved silicon tracker at mid-rapidity would dramatically improve and make accessible for the first time the following measurements in Pb–Pb collisions:

- Beauty measurement via displaced $D^0 \to K\pi$ will be accessible for the first time, with a reach down to D $p_t = 2$ GeV/c. See Section 2.3.4.
- Beauty measurement via displaced $J/\psi \to ee$ and single displaced electrons will be greatly improved. A first assessment of the effect of the upgraded ITS was made in the ITS Upgrade CDR-0 [55]. More detailed studies are in progress.
- Beauty decay vertex reconstruction using any of the previous three channels plus an additional track will be greatly improved.

2.2.3 Low-mass Dileptons: Present Status and Further Measurements

The electromagnetic radiation spectrum emitted in the course of a heavy-ion collision can be expressed by the space-time integral over the differential thermal production rate. The production rate depends on a thermal Bose-Einstein weight and the non-trivial electromagnetic spectral function.

At large masses ($M_{ee} > 1$ GeV/c^2) the spectrum is most sensitive to the initial temperature because the thermal weight leads to a dominance of radiation from the hot early stage. At masses $M_{ee} < 1$ GeV/c^2 the emission spectrum is dominated by radiation from hot and dense hadronic matter at or below T_c, which arises as a consequence of the larger volume at late times contributing to the radiation yield and

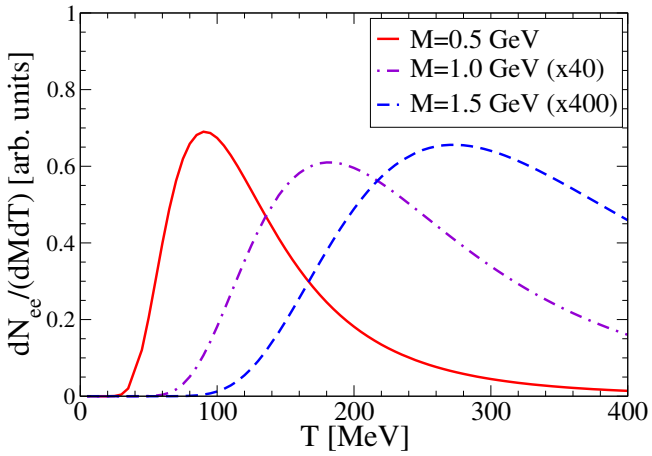

Figure 2.15: Temperature distribution of the thermal dilepton yield in different invariant mass intervals (from [56]).

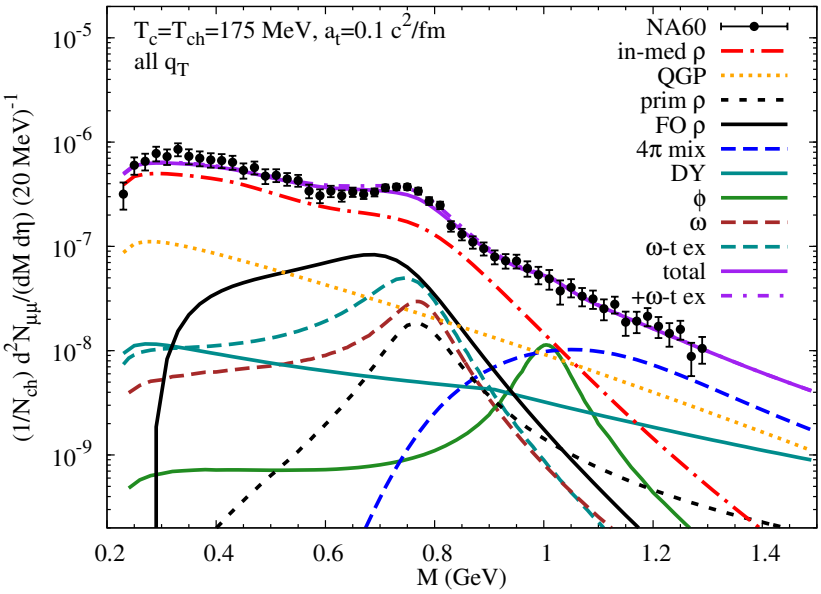

Figure 2.16: Low-mass dimuon excess spectrum in In-In measured by NA60, compared to a calculation assuming strong ρ-meson broadening in a hot and dense hadronic medium (from [56]).

compensating for the smaller thermal weight. This interplay between decreasing thermal weights and increasing space-time volume as the system evolves allows for a detailed investigation of various stages of the collision by proper inspection of different invariant mass windows [56] (see Figure 2.15).

Study of chiral symmetry restoration

The electromagnetic spectral function encodes the relevant microscopic degrees of freedom of the system and their dependence on temperature and density. At low masses ($M_{ee} < 1$ GeV/c^2) the spectral function is saturated by the light vector resonances, in particular the ρ meson. Due to its strong coupling to the hot and dense hadronic medium the ρ spectral function features strong broadening and becomes essentially structureless in the vicinity of the phase transition. This 'melting' behavior of the ρ spectral function, derived from many-body theory [57], has been observed in In-In at the CERN-SPS, where the low-mass dimuon excess spectrum measured by NA60 [58–60] could be well described assuming this scenario [61] (see Figure 2.16).

The unique potential of low-mass dilepton data to assess in-medium properties of hadronic spectral

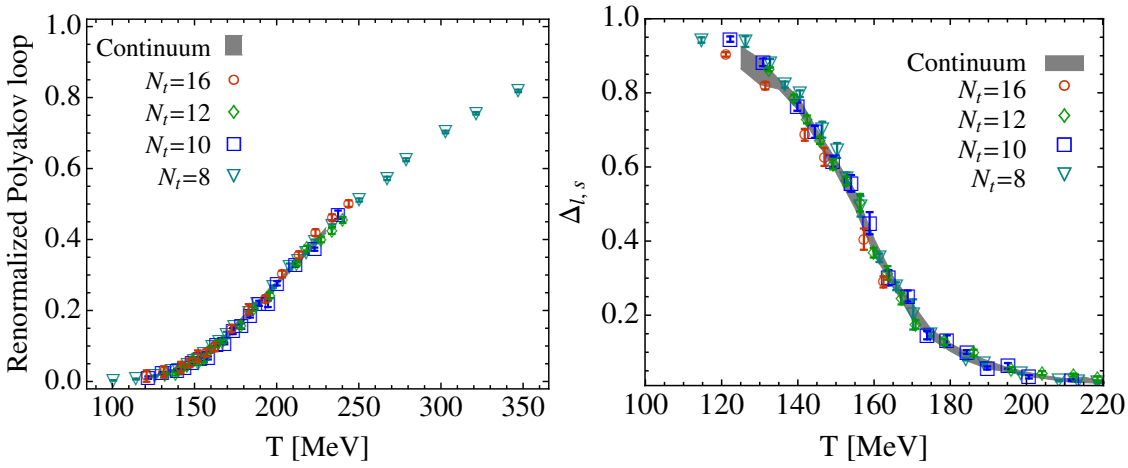

Figure 2.17: Lattice QCD calculations of the order parameters of the deconfinement (left) and the chiral (right) phase transition as a function of temperature [62].

function provides means to study chiral symmetry restoration in heavy-ion collisions. Lattice QCD calculations suggest that the critical temperature of the chiral phase transition is lower than that of deconfinement, giving rise to the expectation that chiral symmetry restoration is manifest in a hot hadronic resonance gas. Recent calculations show that about 60% of the thermal radiation in the low mass region ($0.15 < M_{ee} < 0.6$ GeV/c^2) is emitted in the temperature range $T = 125$–180 MeV [56], which corresponds to the chiral transition region indicated by lattice QCD [62], see Figure 2.17. The outstanding feature of chiral symmetry restoration is the degeneracy of the vector and axial-vector spectral functions. While the axial-vector spectral function is not accessible experimentally, the modification of the vector spectral function is instrumental to provide a connection to chiral symmetry restoration via QCD sum rules [63, 64] and constraints from lattice QCD. A precise measurement of the low mass dilepton spectrum in heavy-ion collisions constitutes the only known means to assess the nature of the chiral phase transition experimentally and is therefore of paramount importance for the understanding of excited QCD matter. Conceptually, a measurement at the LHC is most favourable because a rigorous theoretical evaluation is substantially enhanced by the applicability of lattice QCD at $\mu_B = 0$.

Early temperature

At masses $M_{ee} > 1$ GeV/c^2 the description of the spectral function becomes 'dual' in the sense that hadronic and partonic degrees of freedom lead to the same structureless spectral function. Moreover, the thermal Bose-Einstein weight suppresses contributions from late stages, such that the invariant mass dependence of the thermal dilepton yield is very sensitive to the early temperature of the system (see also Figure 2.15). However, a precise measurement of the thermal yield in this mass window ($M_{ee} >$ 1 GeV/c^2) requires a good understanding of the contribution from correlated semi-leptonic open charm decays (see below).

The spectrum of real direct photons ($M = 0$) has long been considered a most sensitive probe for the source temperature. The measurement of dileptons at very low invariant masses ($0.15 < M_{ee} <$ 0.3 GeV/c^2) and finite transverse momentum ($p_{t,ee} > 1$ GeV/c) provides access to the real direct photon spectrum, by extrapolation of the virtual photon yield to $M = 0$ [15]. This method to infer the direct photon yield is complementary to calorimetry of real photons and conversion measurements. Although the virtual direct photon yield is suppressed by one order in α_{em}, the virtual photon measurement is very powerful because is suffers much less from physical background than the calorimetric measurement. This allows to measure the direct photon yield in the low transverse momentum region ($1 < p_{t,\gamma} < 5$ GeV/c) where a large thermal contribution is expected.

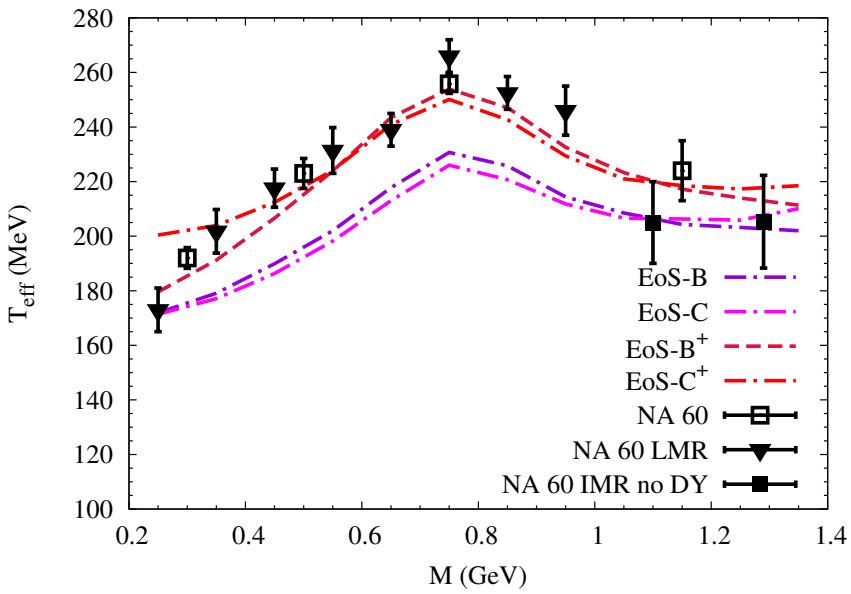

Figure 2.18: Effective slope parameter $T_{\rm eff}$ from exponential fits to the dimuon $p_{\rm t}$ excess spectra measured by NA60 [58, 59]. The data are compared to model calculations assuming different equations of state [61].

Space-time evolution and equation of state

The equation of state, relating the pressure of the system to its temperature, is one of the most fundamental targets to characterize strongly interacting matter. It governs the expansion of the early universe and has obvious phenomenological consequences for the space-time evolution of heavy-ion collisions. The equation of state is a basic ingredient to hydrodynamical models which yield a good description of the observed phenomenon of collective flow. Conceptually, collective flow patterns of final-state hadrons arise from integration over the pressure fields acting at all stages of the collision, and differentiation of partonic and hadronic contributions is typically ambiguous. Electromagnetic probes like dilepton pairs are emitted at all stages of the collision, giving rise to a complex collectivity pattern if studied as a function of invariant mass [65]. Systematic analysis of radial and elliptic flow in different invariant mass windows gives access to the evolution of collectivity at different times during the collision, and may therefore provide stringent constraints on the equation of state [61].

This connection has been demonstrated on the basis of NA60 results from In-In collisions at the SPS [58, 59]. Figure 2.18 shows the "effective temperature" coefficient $T_{\rm eff}$ extracted from the transverse momentum spectra of dimuon pairs. A clear increase is observed below the ρ-meson mass which is consistent with previous observations of radial flow patterns in the $p_{\rm t}$ spectra of light hadrons. The appearance of radial flow is commonly attributed to late collision stages, which govern the emission spectrum at low masses. At higher masses $T_{\rm eff}$ decreases, possibly due to increasing contributions from the partonic stage, where collectivity is less developed. In heavy-ion collisions at the LHC significantly higher initial temperatures are reached, giving rise to even more pronounced contributions from the QGP to dilepton production at high masses. A detailed investigation of radial and elliptic flow as a function of invariant mass will thus provide a unique experimental handle on the equation of state of partonic matter.

2.3 Physics Performance: Heavy Flavour

2.3.1 Possible Measurements and Expected Yields

In this part of the chapter, we present the first performance studies for heavy flavour detection with an upgraded ITS. We consider the following benchmark analyses:

Table 2.1: Heavy quark production at the LHC as expected from pQCD calculations at NLO with nuclear shadowing corrections.

System $\sqrt{s_{\rm NN}}$	Pb–Pb 2.76 TeV	Pb–Pb 5.5 TeV	pp 7 TeV	pp 14 TeV
$\sigma_{\rm NN}^{\rm c\bar{c}}$ [mb]	2.1	3.4	6.9	11.2
$N_{\rm tot}^{\rm c\bar{c}}$ min.bias, 0–10% central	12, 50	19, 80	0.10	0.16
$\sigma_{\rm NN}^{\rm b\bar{b}}$ [mb]	0.08	0.14	0.23	0.50
$N_{\rm tot}^{\rm b\bar{b}}$ min.bias, 0–10% central	0.5, 1.9	0.8, 3.3	0.003	0.007

– Charm meson production via $\rm D^0 \rightarrow K^- \pi^+$;

– Beauty production via $\rm B \rightarrow D^0$ ($\rightarrow \rm K^- \pi^+$);

– Charm baryon production via $\Lambda_{\rm c} \rightarrow \rm pK^- \pi^+$.

The results on the expected impact of the upgrade are reported in the following sections. Other analyses have been started and are in progress:

– $\rm D_s$ production via $\rm D_s^+ \rightarrow K^+K^- \pi^+$, see Section 2.3.6.1;

– Beauty production via $\rm B \rightarrow D^0 \pi^+$, see Section 2.3.6.2;

– Beauty production via $\rm B \rightarrow J/\psi(\rightarrow e^+e^-)$, see Section 2.2.5.2 of the CDR-0 [55];

– Beauty production via $\rm B \rightarrow e^+$, see Section 2.2.5.3 of the CDR-0 [55].

Here, we provide estimates on the possible statistics that could be collected in minimum-bias and central collisions (0–10% centrality class) during a Pb–Pb run at top LHC energy, $\sqrt{s_{\rm NN}} = 5.5$ TeV. For this exercise, we consider the scenario envisaged for the LHC and for the ALICE central barrel conditions after the 2017-18 shutdown, as outlined in [5]. Namely: an interaction rate of 50 kHz for Pb–Pb collisions and the capability to write out all interactions to tape enabled by an enhanced online data compression with the High Level Trigger (HLT). We also assess the opportunity to filter events based on full tracking and vertexing information, available from the HLT, and write to tape only events of interest.

We use the production yields predicted by perturbative QCD and we assume the above Pb–Pb running and data taking scenario. For each analysis, we assume a value for the acceptance times efficiency, which we evaluated based on the ongoing analyses with ALICE data. The estimates for the possible event filtering require also an assumption on the High Level Trigger efficiency, which we set to be equal to the offline selection efficiency for this first exercise, and on the trigger purity, which we assign starting from the signal-to-background ratios that can be expected with the ITS upgrade based on the studies that will be presented in the next sections.

In Table 2.1 we summarize the expected production yields for $\rm c\bar{c}$ and $\rm b\bar{b}$ pairs in central (0–10%) and minimum-bias (0–100%) Pb–Pb collisions at $\sqrt{s_{\rm NN}} = 5.5$ TeV (and for other energies/systems for comparison). The numbers are obtained by applying binary $N_{\rm coll}$ scaling to next-to-leading order perturbative QCD (pQCD) predictions from the HVQMNR calculation [7]. The value of the charm and beauty quark masses and of the pQCD scales are set as: $m_c = 1.2$ GeV$/c^2$, $m_b = 4.75$ GeV$/c^2$, $\mu_R = \mu_F = 2m_c$ for charm and $\mu_R = \mu_F = m_b$ for beauty production. CTEQ6M parton distribution functions are used with the EPS09NLO [16] correction for nuclear shadowing. These predictions are affected by a theoretical uncertainty of a factor 2–3.

Table 2.2: Expected production yields (total and per unit of rapidity at mid-rapidity) for charm and beauty particles (+ anti-particles) in minimum-bias and 0–10% central Pb–Pb collisions at 5.5 TeV, mean proper decay length, branching ratios to the relevant decay channels [67], and typical acceptance. The acceptance factor is defined such that: $N_{\rm Acc} = {\rm d}N/{\rm d}y|_{y=0} \cdot {\rm B.R.} \cdot {\rm Acc.}$

Part.	Yield m.b., 0–10%	$\mathrm{d}N/\mathrm{d}y\|_{y=0}$ m.b., 0–10%	$c\tau$ [μm]	decay channel	B.R.	Acc.
D^0	23, 110	2.3, 11	≈ 120	$\mathrm{K}^-\pi^+$	3.8%	1
D_s^+	4.3, 20	0.4, 2.0	≈ 150	$\phi(\to \mathrm{K}^+\mathrm{K}^-)\pi^+$	$4.4\% \times 49\%$	1
Λ_c	2.9, 14	0.29, 1.4	≈ 60	$\mathrm{pK}^-\pi^+$	5.0%	1
B	1.3, 6.2	0.2, 0.9	≈ 500	$\mathrm{J}/\psi(\to \mathrm{e}^+\mathrm{e}^-)$	$1.2\% \times 6\%$	1
				$\mathrm{D}^0(\to \mathrm{K}^-\pi^+)$	$60\% \times 3.8\%$	1
				e^+	10.9%	1.8
B^+	0.6, 2.7	0.1, 0.4	≈ 500	$\mathrm{J}/\psi(\to \mathrm{ee})\mathrm{K}^+$	$0.1\% \times 6\%$	1
				$\overline{\mathrm{D}}^0(\to \mathrm{K}^+\pi^-)\pi^+$	$0.5\% \times 3.8\%$	1
B_s^0	0.2, 0.9	0.03, 0.13	≈ 500	$\mathrm{J}/\psi(\to \mathrm{ee})\phi(\to \mathrm{KK})$	$0.14\% \times 6\% \times 50\%$	1
Λ_b	0.1, 0.5	0.015, 0.07	≈ 400	$\Lambda_\mathrm{c}(\to \mathrm{pK}^-\pi^+) + \mathrm{e}^-$	$9.9\% \times 5\%$	1
				$\Lambda_\mathrm{c}(\to \mathrm{pK}^-\pi^+) + \mathrm{h}^-$	90%(guess)×5%	1

Table 2.3: Estimated signal statistics and trigger rate for minimum-bias Pb–Pb collisions at a hadronic interaction rate of 50 kHz. The numbers in italics are assumptions, not based on simulation studies.

Particle	Eff	S/ev	S/B	B'/ev	trigger rate (Hz)	S/nb^{-1}
D^0	0.02	$1.6 \cdot 10^{-3}$	0.03	0.21	$11 \cdot 10^3$	$1.3 \cdot 10^7$
D_s^+	0.01	$4.6 \cdot 10^{-4}$	*0.01*	0.18	$9 \cdot 10^3$	$3.7 \cdot 10^6$
Λ_c	0.01	$1.4 \cdot 10^{-4}$	$5 \cdot 10^{-5}$	11	$5 \cdot 10^4$	$1.1 \cdot 10^6$
Λ_c ($p_\mathrm{t} > 2$ GeV/c)	0.01	$0.8 \cdot 10^{-4}$	0.001	0.33	$1.6 \cdot 10^4$	$0.6 \cdot 10^6$
$\mathrm{B} \to \mathrm{D}^0(\to \mathrm{K}^-\pi^+)$	0.02	$0.8 \cdot 10^{-4}$	0.03	$11 \cdot 10^{-3}$	$5 \cdot 10^2$	$0.6 \cdot 10^6$
$\mathrm{B} \to \mathrm{J}/\psi(\to \mathrm{e}^+\mathrm{e}^-)$	0.1	$1.3 \cdot 10^{-5}$	*0.01*	$5 \cdot 10^{-3}$	$3 \cdot 10^2$	$1 \cdot 10^5$
$\mathrm{B}^+ \to \mathrm{J}/\psi\mathrm{K}^+$	*0.01*	$0.5 \cdot 10^{-7}$	*0.01*	$2 \cdot 10^{-5}$	1	$4 \cdot 10^2$
$\mathrm{B}^+ \to \overline{\mathrm{D}}^0\pi^+$	*0.01*	$1.9 \cdot 10^{-7}$	*0.01*	$8 \cdot 10^{-5}$	4	$1.5 \cdot 10^3$
$\mathrm{B}_\mathrm{s}^0 \to \mathrm{J}/\psi\phi$	*0.01*	$1.1 \cdot 10^{-8}$	*0.01*	$4.4 \cdot 10^{-6}$	$2 \cdot 10^{-1}$	$9 \cdot 10^1$
$\Lambda_\mathrm{b}(\to \Lambda_\mathrm{c} + \mathrm{e}^-)$	*0.01*	$0.7 \cdot 10^{-6}$	*0.01*	$2.8 \cdot 10^{-4}$	14	$5 \cdot 10^3$
$\Lambda_\mathrm{b}(\to \Lambda_\mathrm{c} + \mathrm{h}^-)$	*0.01*	$0.7 \cdot 10^{-5}$	*0.01*	$2.8 \cdot 10^{-3}$	$1.4 \cdot 10^2$	$5 \cdot 10^4$

In Table 2.2 we report, for central Pb–Pb at 5.5 TeV, the corresponding yields for the production of D^0, Λ_c, B ($\mathrm{B}^0 + \mathrm{B}^+ + \mathrm{B}_\mathrm{s}^+$), and Λ_b particles (+ their anti-particles), using the branching fractions for c and b quarks as given by the PYTHIA event generator [66]. The mean proper decay lengths ($c\tau$), the relevant final states and their branching ratios are reported as well, along with the typical acceptance (for a tracking acceptance of $|\eta| < 0.9$).

We consider the following running scenario for Pb–Pb:

- instantaneous luminosity: 6×10^{27} cm^{-2}s^{-1}, which (using $\sigma_{\rm PbPb}^{\rm hadronic} = 8$ b) gives a hadronic interaction rate of 50 kHz;
- sustainable rate of readout to tape: up to 50 kHz (see [5]).

We use the information given in Table 2.2, along with the expected reconstruction and selection efficiencies, to estimate the yields of reconstructed decays per event (S/ev), in central Pb–Pb collisions at

$\sqrt{s_{\rm NN}} = 5.5$ TeV. We then compute the estimated statistics per nb^{-1} of integrated luminosity ($S/{\rm nb}^{-1}$). The target Pb–Pb integrated luminosity for the ALICE upgrade program is 10 nb^{-1}.

We assume a trigger efficiency $\varepsilon_{trigger} = 100\%$. The trigger purity is instead related to the signal-to-background ratio S/B because also all the background candidates that pass the selections will fire the trigger; in particular, we have:

$$\text{purity} = S/B' = S/B \times 1/4\,,$$

where B' is the background in the broad invariant mass range (e.g. $\pm 12\,\sigma$) that is necessary to fit the invariant mass distribution. Thus, $S/B' = 1/4 \cdot S/B$, where S/B is the signal-to-background in $\pm 3\,\sigma$ of the invariant mass distribution. The probability that a collision fires the trigger will be

$$\text{triggers/ev} = (S/\text{ev}) \,/\, \text{purity} = (S/\text{ev}) \,/\, (S/B')\,.$$

The trigger rate in minimum-bias collisions is:

$$\text{rate} = (S/\text{ev}) \,/\, \text{purity} \times 50\ \text{kHz} = (S/\text{ev}) \cdot 4 \cdot (B/S) \times 50\ \text{kHz}\,.$$

The signal collected is, per nb^{-1} of integrated luminosity:

$$S/{\rm nb}^{-1}\,\text{with trigger} = (S/\text{ev}) \times \sigma^{\rm hadronic}_{\rm PbPb}[\text{nb}] = (S/\text{ev}) \times 8 \cdot 10^9\,.$$

The results are reported in Table 2.3 for minimum-bias collisions. For the $\rm D^0 \to K^- \pi^+$ channel, the trigger rate would be 11 kHz. For the case of the $\Lambda_{\rm c}$, also considering a minimum $p_{\rm t}$ threshold at 2 GeV/c (the lowest accessible $p_{\rm t}$ according to studies presented in the next section), due to the small S/B ratio, the trigger rate would be very large (16 kHz). The two channels together yield a trigger rate of 27 kHz, with a cut $p_{\rm t} > 2$ GeV/c for $\Lambda_{\rm c}$. This cut at trigger level may prevent a measurement at very low $p_{\rm t}$, which could be possible with further optimization of the selection strategy.

Therefore, we conclude that an online event filtering is not an adequate strategy for low-$p_{\rm t}$ heavy flavour measurements and we opt for writing all interactions to tape at a rate of up to 50 kHz, as allowed by the HLT data compression.

The capability to record all events at 50 kHz in Pb–Pb requires the upgrade of the readout of most of the detectors of the ALICE central barrel, including the TPC, for which the readout chambers have to be replaced completely. If the TPC was not upgraded, the readout capability would be limited to the 0.5 kHz of the current TPC multi-wire proportional chambers. In the following, we compare, for some of the performance studies, the statistical precision that can achieved with or without the high-rate upgrade of all the central barrel detectors. That is, in these two scenarios:

- *high-rate:* read all events at 50 kHz in Pb–Pb, with the target of integrating a luminosity of 10 nb^{-1} after the ITS upgrade;
- *no high-rate:* read events at 0.5 kHz in Pb–Pb, integrating a luminosity of 0.1 nb^{-1} after the ITS upgrade.

We show that a number of key measurements require the *high-rate* upgrade in addition to the ITS upgrade.

2.3.2 Simulation Method

In order to quantify the possible improvement of an upgrade of the ITS, a fast simulation scheme is employed. It is based on existing Monte Carlo productions including the detailed geometry and response of the current ALICE detector setup. The impact of the new ITS is obtained by recomputing reconstructed

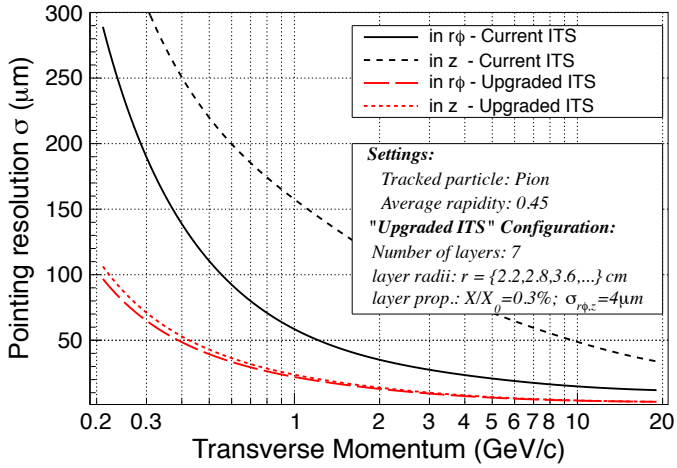

Figure 2.19: Track impact parameter resolution in $r\varphi$ and z (current and upgrade).

track parameters according to the p_{t} and particle species dependent scaling laws as obtained by the Fast Estimation Tool described in Chapter 3. This is done by rescaling the difference to Monte Carlo, keeping any kind of intrinsic correlation of the parameters. The ALICE reference frame has the z axis in the beam direction, the x axis pointing to the centre of the LHC ring, and the y axis pointing upward. In the rotated ALICE reference frame, where the x coordinate is parallel to the track momentum near the origin, the improvement reads as follows:

$$\begin{pmatrix} y \\ z \\ \sin\varphi \\ \tan\theta \\ 1/p_{\mathrm{t}} \end{pmatrix}' = \begin{pmatrix} y_{\mathrm{MC}} + \sigma^{\mathrm{upgrade}}_{d_{0,r\varphi}}(p_{\mathrm{t}})/\sigma^{\mathrm{current}}_{d_{0,r\varphi}}(p_{\mathrm{t}}) \cdot (y - y_{\mathrm{MC}}) \\ z_{\mathrm{MC}} + \sigma^{\mathrm{upgrade}}_{d_{0,z}}(p_{\mathrm{t}})/\sigma^{\mathrm{current}}_{d_{0,z}}(p_{\mathrm{t}}) \cdot (z - z_{\mathrm{MC}}) \\ \sin\varphi \\ \tan\theta \\ (1/p_{\mathrm{t}})_{\mathrm{MC}} + \sigma^{\mathrm{upgrade}}_{1/p_{\mathrm{t}}}(p_{\mathrm{t}})/\sigma^{\mathrm{current}}_{1/p_{\mathrm{t}}}(p_{\mathrm{t}}) \cdot ((1/p_{\mathrm{t}}) - (1/p_{\mathrm{t}})_{\mathrm{MC}}) \end{pmatrix} \tag{2.1}$$

Thus, it is a simple scaling of the residuals of the impact parameters in $r\varphi$ and z, $d_{0,r\varphi}$ and $d_{0,z}$, as well as of the transverse momentum p_{t}, with respect to their true values (MC), known from the generated particle kinematics. The scaling factors are the ratios of the upgrade/current resolutions on these variables. The track polar angle θ remains unchanged and the inclination φ is zero by the choice of the coordinate frame. This approach is called *Hybrid*, because it applies the detector performance of the upgraded ITS to full simulations of the current ITS. The corresponding analysis flow is shown in Figure 2.20.

A drawback of this approach is that it does not allow to study the effect of an extended pseudo-rapidity acceptance, a possibility that is actually being considered for the design of the upgraded ITS, to reach for example a coverage $|\eta| < 1.5$ or even larger, using end-caps. The impact of this extension on the physics performance is not assessed here, but it will be addressed in the near future with dedicated simulation studies.

For our performance studies we have considered as a baseline the configuration for the upgraded ITS that

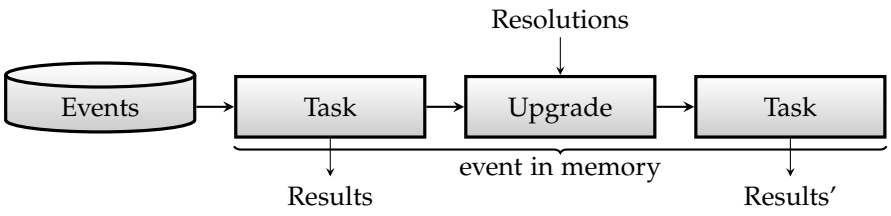

Figure 2.20: Scheme of the *Hybrid* simulation approach for the ITS upgrade studies.

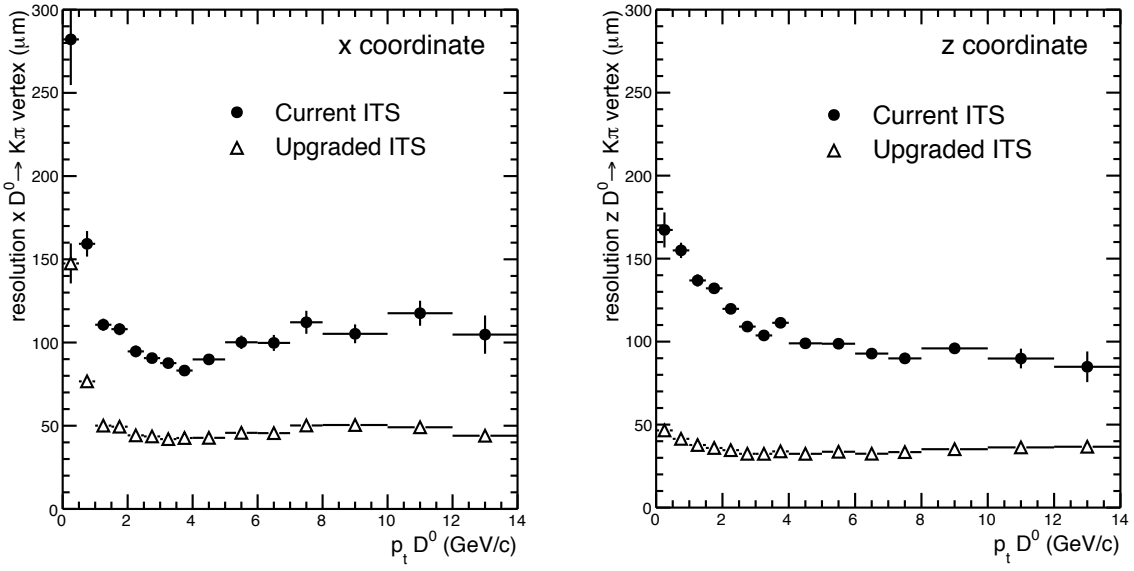

Figure 2.21: $D^0 \to K^-\pi^+$ secondary vertex position resolutions for current and upgrade scenarios: x (left) and z (right) coordinates.

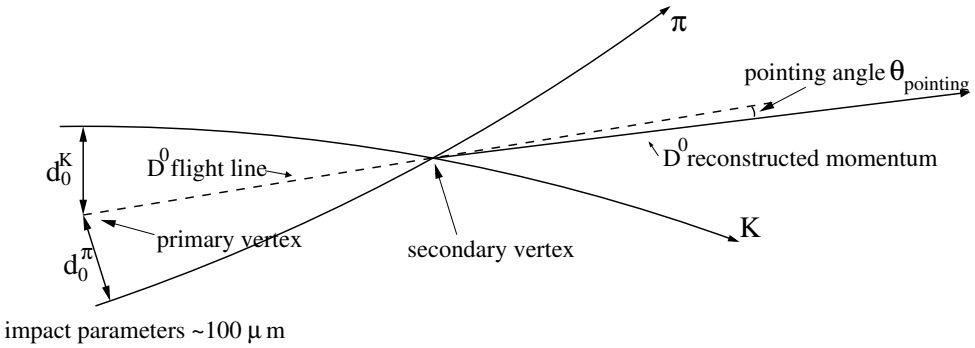

Figure 2.22: Schematic view of the D^0 decay in the $D^0 \to K^-\pi^+$ channel.

is described in Chapter 3: 7 layers with radii of (2.2, 2.8, 3.6, 20.0, 22.0, 41.0, 43.0) cm, instrumented by pixel detectors with intrinsic resolution $(\sigma_{r\varphi}, \sigma_z) = (4,4)$ μm, and with a thickness of 0.3% of the radiation length, X_0, per layer. Figure 2.19 shows the corresponding charged pions impact parameter resolutions as a function of transverse momentum for the upgraded ITS compared to those of the current ITS. The scaling factors of the *Hybrid* approach are the ratios of these two resolutions. As an example, the resolutions on the reconstructed position of the $D^0 \to K^-\pi^+$ decay vertex are shown in Figure 2.21. Performance studies based on this approach will follow in the next sections.

2.3.3 D^0 Meson Reconstruction as a Benchmark for Detector Performance

As described in the first part of this chapter, the D meson R_{AA} was measured in Pb–Pb collisions at $\sqrt{s_{NN}} = 2.76$ TeV via the reconstruction of the $D^0 \to K^-\pi^+$ (BR=3.89%, $c\tau \approx 123$ μm), $D^{*+} \to K^-\pi^+\pi^+$ (via $D^{*+} \to D^0\pi^+$, strong decay, BR=67.7%), and $D^+ \to K^-\pi^+\pi^+$ (BR=9.4%, $c\tau \approx 312$ μm) decay channels (see [67] for the decay properties quoted). All analyses are based on the reconstruction and selection of secondary vertex topologies with a few hundreds of microns separation from the primary vertex. Displaced tracks are selected and good alignment between the D meson momentum and the flight-line connecting the primary and decay vertex is required (i.e. small pointing angle, see the

sketch of the D^0 decay in Figure 2.22). As shown in Figure 2.22, due to the relativistic boost, the pion and kaon tracks have an intrinsic impact parameter in the transverse plane typically of the order of the D^0 $c\tau$ for sufficiently high D^0 transverse momentum, thus they can be identified as displaced tracks if the track resolution in the vicinity of the vertex is of the order of tens of microns. With 2010 data, the $D^0 \to K^-\pi^+$ decay channel was reconstructed in Pb–Pb collisions in the transverse momentum range $2 < p_t < 16$ GeV/c and yielded the most precise R_{AA} measurement, with a statistical error of the order of 25% in the centrality class 0–20% [50]. A preliminary measurement in the range $1 < p_t < 24$ GeV/c was also carried out, using Pb–Pb collisions in the centrality class 0-7.5% from the 2011 run. The possibility to have a direct reference of the performance on real data allows for a more realistic study of the benefits that would come from an upgrade of the ITS. Therefore, the D^0 case can be considered as a benchmark for all the D meson analyses.

2.3.3.1 Statistical Precision in Pb–Pb Collisions with the ITS Upgrade

Here we present a comparison of the performance achievable in Pb–Pb collisions with the current and upgraded ITS configurations, considering the centrality class 0–20%, which is the same that was used for the first published R_{AA} measurement [50]. The *Hybrid* approach described in the previous section was applied to a Monte Carlo simulation sample produced with the HIJING 1.36 event generator [68] and with additional heavy flavour particles added to each event using the PYTHIA 6.4.21 generator [66]. The HIJING generator yields a charged particle multiplicity in central collisions similar to the one measured at the LHC. The response of the full ALICE detector was included via the GEANT3 transport package and a detailed description of the geometry of the apparatus. The precision on the measurement of D^0 production performed with 2010 Pb–Pb data was taken as a reference: in the 0–20% centrality class the statistical significance was of the order of 8–10 in the $2 < p_t < 12$ GeV/c interval and the statistical uncertainty (which approximately corresponds to the inverse of the statistical significance) was at the level of 10–15%. The simulation study was performed using the same cut values for the two ITS configurations, in order to single out the effect of the improved tracking resolutions. The cuts were fixed to values close to those used for the 2010 Pb–Pb data analysis[1]. The selected signal (raw) yield was obtained by multiplying the corrected D^0 p_t spectrum, dN/dp_t measured with the 2010 data, by the efficiency calculated from the simulation for the current or upgraded ITS configuration. The selected background yield in the D^0 mass region was scaled in the simulation so as to match, for the current ITS case, the value measured in the data. The same background scaling factor was then used also for the upgraded ITS case.

The main cut variables used to extract the D^0 signal are the product of decay track impact parameters, the cosine of the pointing angle, and the decay length. For the background, composed mainly of pairs of primary tracks, the distribution of the product of decay track impact parameters ($d_0^K \times d_0^\pi$) is symmetric and peaks at 0, the width being determined by the detector impact parameter resolution. For the D meson signal, the distribution is asymmetric because the displacement of the secondary vertex induces a large tail at negative values of the product. The cosine of the pointing angle is peaked towards 1 for signal candidates, while it has a flatter distribution for the background. The decay length distribution of reconstructed D^0 meson is the convolution of the true decay length distribution and a resolution term, which characterizes the background distribution. The narrower the background distribution is, the better the signal and background shapes can be distinguished.

An improved detector resolution would provide a better separation between signal and background, thus the possibility to reject more background and use less stringent cuts in order to keep more signal, increasing the selection efficiency. Generally, this also allows for reducing the systematic uncertainties arising from a not fully precise description of the detector properties (including alignment) and performance (e.g. vertex and track reconstruction precision). A comparison of the $d_0^K \times d_0^\pi$ distributions for back-

[1] Further improvement, in the upgrade case, can arise from a dedicated optimization of the cut values or from the introduction of additional cuts. This point is briefly discussed at the end of the section.

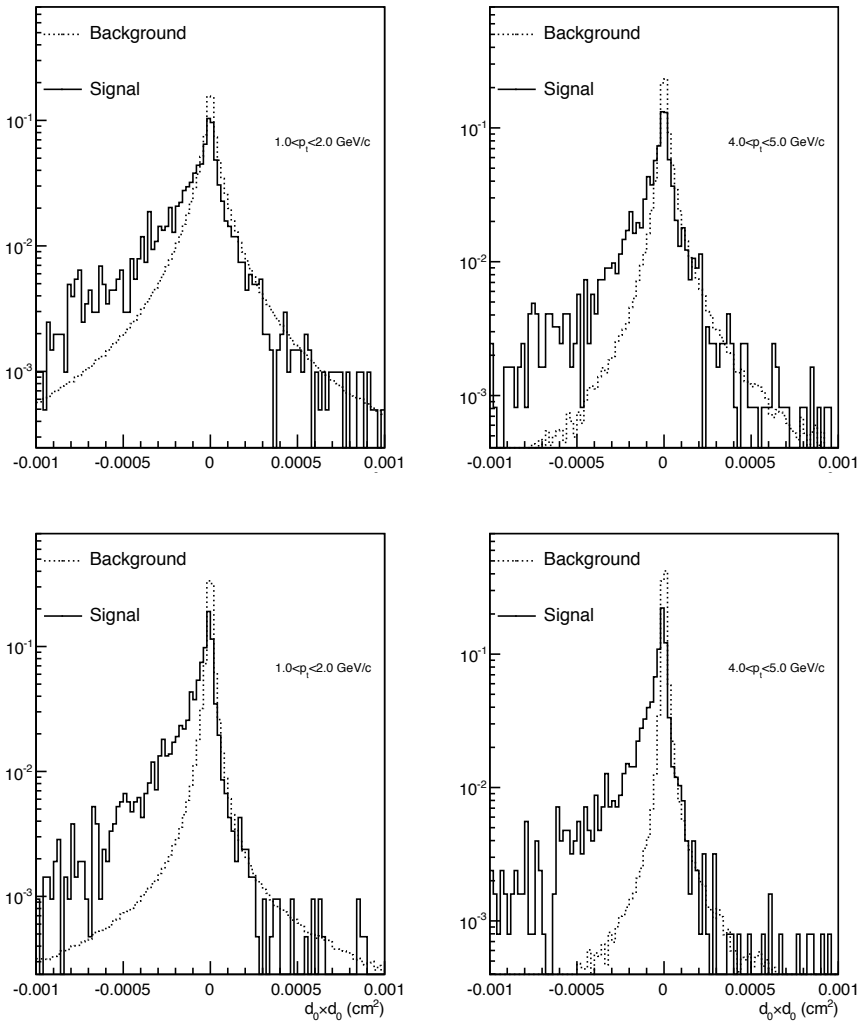

Figure 2.23: $D^0 \to K^-\pi^+$: products of the decay tracks impact parameters for background and signal candidates for the current ITS configuration, in two different p_t ranges. Upper panels: current ITS. Lower panels: Upgraded ITS.

ground and signal is shown for $1 < p_t < 2$ GeV/c and $4 < p_t < 5$ GeV/c in Figure 2.23 for the current and upgraded ITS configurations, in the upper and lower panels, respectively. The signal–background separation clearly improves in the ITS upgrade case.

The comparison of the cut efficiencies in the current and upgrade scenarios, reported[2] in Figure 2.24, shows that almost the same signal is selected in the two cases for $p_t > 2$ GeV$/c$. Conversely, the background rejection improves by a factor of 6 for $p_t > 2$ GeV$/c$. As shown in Figure 2.25, this determines a large increase of the signal-to-background ratio (factor of 6) and of the statistical significance (factor of 2–3), here scaled by the square root of the sample size.

As an example, Figure 2.26 (top) shows the comparison of the invariant mass distributions obtained in the current and upgraded ITS scenarios for $2 < p_t < 4$ GeV/c from the heavy-flavour enriched MC simulation described above. Important to note that in the range $0 < p_t < 2$ GeV/c (bottom panel of the same figure) the background rejection improves by a factor of 25 allowing the extraction of a clear

[2]The figure shows also the efficiency for secondary D^0 from B decays, which is relevant for the discussion in Section 2.3.4.

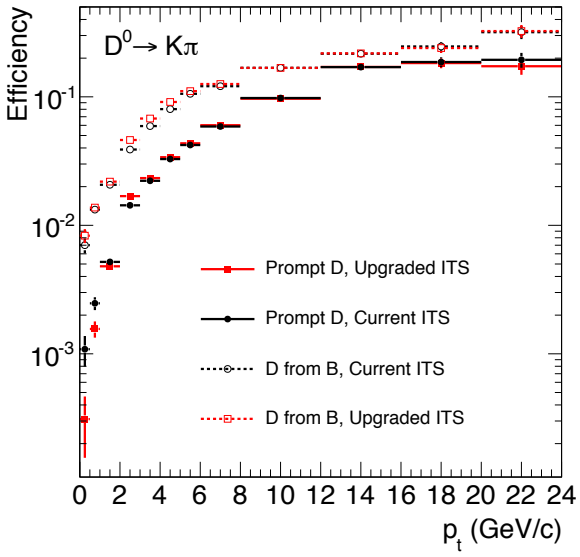

Figure 2.24: $D^0 \to K^-\pi^+$: reconstruction and selection efficiency for prompt D^0 and D^0 coming from B decays, in the current ITS and upgrade ITS cases. The same selection cuts are used for the two scenarios.

D^0 signal (with significance of about 9) that is not observed with the current ITS configuration. The production of D mesons in central Pb–Pb collisions has never been measured in this p_t range. Thus, some hypotheses on the expected signal and background levels were made[3]. The spread obtained for the signal-to-background ratio and for the significance are displayed by the boxes in Figure 2.25 (the markers represent the values obtained with $R_{AA}^{D^0} = 0.5$ and a global background scaling factor of 8.5 and $k = 0.7$, see footnote).

In order to quantify the expected significance for a new measurement with the upgraded ITS, we consider an integrated luminosity of 10 nb^{-1}, which would lead to 1.7×10^{10} central events (0–20%). In these conditions, the D^0 significance is larger than one hundred at any p_t. For comparison, the significance in the 2011 run, corresponding to 16×10^6 central events, is about 6 for $1 < p_t < 2$ GeV/c. At very low p_t (0–2), even considering the uncertainties in the nuclear modification factor and background which enter in the estimation of the significance, the measurement will be quite precise (significance larger than 50 for 10 nb^{-1}).

[3] In order to get a more realistic estimate of the achievable performance, the signal was estimated via a binary scaling of the FONLL prediction of D^0 meson production in pp collisions at 2.76 TeV [69] and using a range of hypotheses on its nuclear modification in Pb–Pb due to initial state and medium effects:

$$S = R_{AA}^{D^0} \times 2 \times \frac{d\sigma}{dp_t}^{\text{FONLL}} \times \Delta p_t \times \varepsilon \times \langle T_{AA} \rangle \times N_{ev}. \quad (2.2)$$

In this formula $\langle T_{AA} \rangle$ is the average nuclear overlap function calculated via the Glauber model for the centrality range $0-20\%$. The nuclear modification factor, $R_{AA}^{D^0}$, was varied between 0.3 and 1 to account for both possible energy loss and nuclear shadowing effects. The factor 2 accounts for the fact that both particles and anti-particles are reconstructed, while the theoretical prediction refers to the particle only. The values shown in Figure 2.24 for prompt D^0 mesons were used for the acceptance times efficiency factor, ε. The signal S was evaluated separately in the p_t ranges (of width Δp_t) $0 < p_t < 0.5$, $0.5 < p_t < 1$, $1 < p_t < 2$ GeV/c, and then summed. The background obtained from the heavy-flavour enriched MC simulation with the *Hybrid* method was scaled up by a factor 7–10. This was estimated by extrapolating to the range $0 < p_t < 2$ GeV/c the ratio of the background in data to that in the MC calculated for $p_t > 2$ GeV/c with the current ITS. Due to the extrapolation uncertainty this factor was varied between 7 and 10. Background pairs are composed mainly of primary pions. Therefore the background amount is sensitive to the pion nuclear modification factor, roughly as $B \propto (R_{AA}^{\pi})^2$. To account for the unknown p_t dependence of the pion R_{AA} for $p_t < 2$ GeV/c and for a possible discrepancy between the pion suppression in data and MC the scaled background was further varied by a factor $k = 0.5$–1.7.

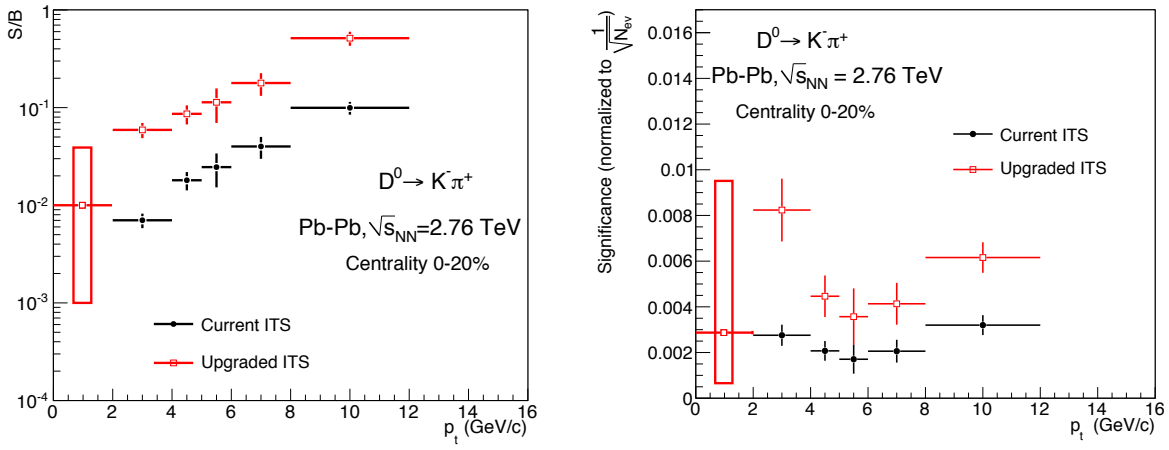

Figure 2.25: $D^0 \to K^-\pi^+$: comparison of the signal-to-background ratio (left) and significance per event (right) obtained for the current and upgraded ITS. A different procedure was used to estimate the expected signal and background for $p_t < 2$ GeV/c and for $p_t > 2$ GeV/c (see text for details).

As discussed in the first part of this chapter, the measurement of charm production down to zero transverse momentum in heavy-ion collisions is of crucial importance for testing the QCD-predicted colour-charge and mass dependencies of parton energy loss (R_{AA} measurement), for assessing the degree of thermalization of charm quarks in the medium (flow measurement), and for disentangling the role of initial state effects (p–Pb studies).

For the comparison presented above, the same selection was applied in the simulation for both the current and upgrade scenarios. However, the better separation between signal and background in the upgrade case allows one to vary the values of the cuts in order to further increase: a) the statistical significance, thus reducing the statistical uncertainty; b) the signal-to-background ratio, enhancing the signal purity and the capability of "tagging" D^0 mesons, e.g. for correlation studies; c) the signal amount, thus the efficiency, providing a better control of the systematic uncertainties. Furthermore, the large improvement in the z resolution will allow for the exploitation of new variables to effectively reject the background. These studies will be carried out in detail in the near future.

2.3.3.2 Systematic Uncertainty on D^0 Reconstruction and Prompt Charm R_{AA}

We estimated the systematic uncertainties that we expect on the measurement of prompt D^0 production in the $D^0 \to K^-\pi^+$ channel after the upgrade of the ITS on the basis of those evaluated for the measurement performed by ALICE with 3×10^6 Pb–Pb events in the centrality class 0–20% [50]. Typical values are reported in Table 2.4 for the lowest and highest p_t intervals reachable in the current and upgraded ITS scenarios and, for the latter, also for the p_t range covered by the current measurement [50]. A reduction of the systematic uncertainties can derive from the following features:

- Improved spatial and momentum resolutions. These will allow for a reduction of the background yield, for the capability of performing a more p_t-differential measurement, and for an increase of the selection efficiency avoiding the selection of D mesons in the tails of the cut variables, where a precise description of the real shape in MC simulations is generally harder.

- Higher statistics. In [50], the evaluation of systematic uncertainties was affected by the interplay of pure systematic effects and statistical fluctuations due to the limited statistics available: the higher statistics will allow for a detailed study of systematic effects, unaffected by statistical fluctuations.

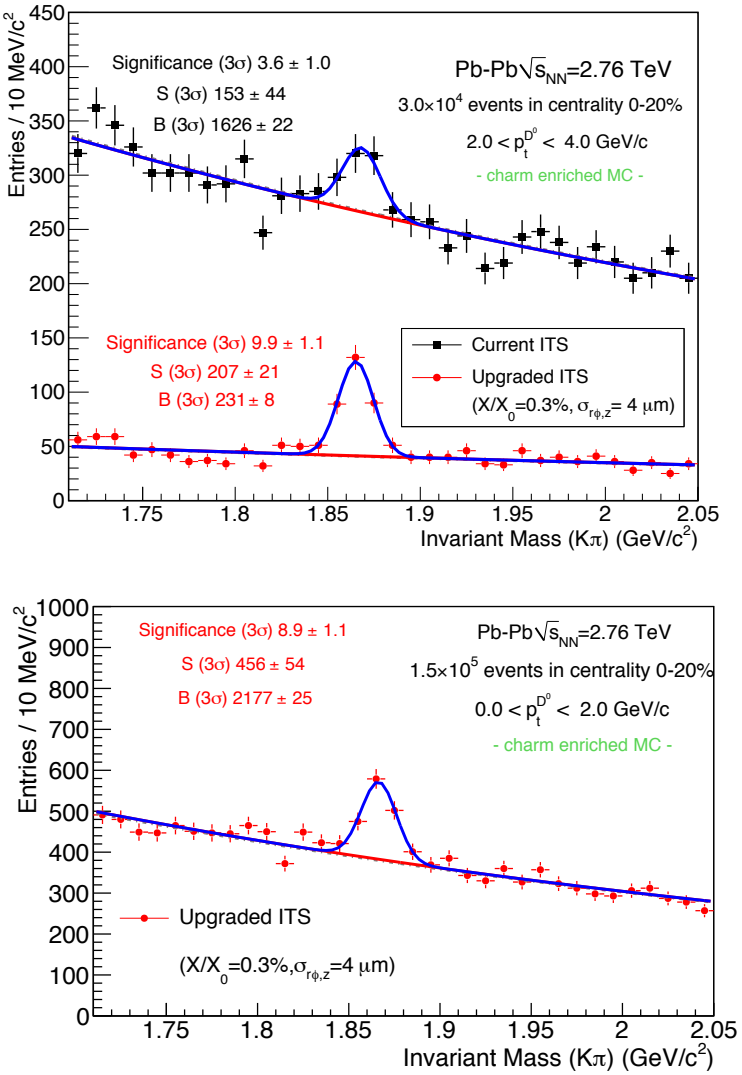

Figure 2.26: $D^0 \to K^-\pi^+$. Top: comparison between the invariant mass distributions of D^0 candidates with $2 < p_t < 4$ GeV/c obtained from the analysis of $\sim 3 \times 10^4$ central (0–20%) Pb–Pb events at $\sqrt{s_{NN}} = 2.76$ TeV (HIJING events enriched with charm signals) with the current and upgrade scenarios. Bottom: invariant mass distribution in $0 < p_t < 2$ GeV/c obtained from the analysis of $\sim 1.5 \times 10^5$ central (0–20%) Pb–Pb events at $\sqrt{s_{NN}} = 2.76$ TeV (same as above) with the upgrade scenario.

In this respect, the D^0 could be used as a benchmark also for other heavy-flavour analysis (e.g. D_s, Λ_c reconstruction).

These features relate to the various sources of systematic uncertainty as follows.

– Feed-down correction: in [50] the fraction of secondary D^0 from B decays, $f_{\text{feed-down}}$, was estimated relying on the FONLL [69] prediction of beauty production and by assuming the nuclear modification factor of B mesons R_{AA}^{B} according to $1/3 < R_{AA}^{\text{D from B}} / R_{AA}^{\text{prompt D}} < 3$. Both the improved resolution and the higher statistics will allow to estimate $f_{\text{feed-down}}$ using data-driven methods. In particular, for $p_t > 2$ GeV/c, the method based on the fit of the impact parameter distribution of the candidate, described in the next section, will be used. As described in the next paragraph, the statistical and total systematic uncertainties on the fraction of prompt D^0 are expected to be $< 1\%$ and $< 5\%$, respectively. At low momentum, the short decay length of B mesons limits the per-

Table 2.4: Comparison of the relative systematic uncertainties on the prompt D^0 meson production yields in Pb–Pb collisions evaluated with 2011 Pb–Pb data with the values expected after the upgrade of the ITS, for lowest and highest accessible p_t bins. For the ITS upgrade case, also the values expected in the p_t range accessible with 2010 Pb–Pb data are shown.

	Current ITS (from [50])		ITS & ALICE upgrade		
p_t interval (GeV/c)	2–3	12–16	0–2	2–16	24–32
Yield extraction	8%	10%	4%	1%	2%
Tracking efficiency	10%	10%	8%	8%	8%
Cut efficiency	13%	10%	8%	8%	8%
PID efficiency	$^{+15}_{-5}$%	5%	5%	5%	-
MC p_t shape	4%	3%	2%	1%	1%
FONLL feed-down corr.	$^{+2}_{-14}$%	$^{+6}_{-8}$%	$^{+5}_{-45}$%	-	-
$R_{AA}^{feed-down}/R_{AA}^{prompt}$	$^{+4}_{-10}$%	$^{+14}_{-27}$%	$^{+7}_{-16}$%	-	-
Impact par. fit feed-down corr.	-	-	-	3%	4%
BR	1.3%		1.3%		

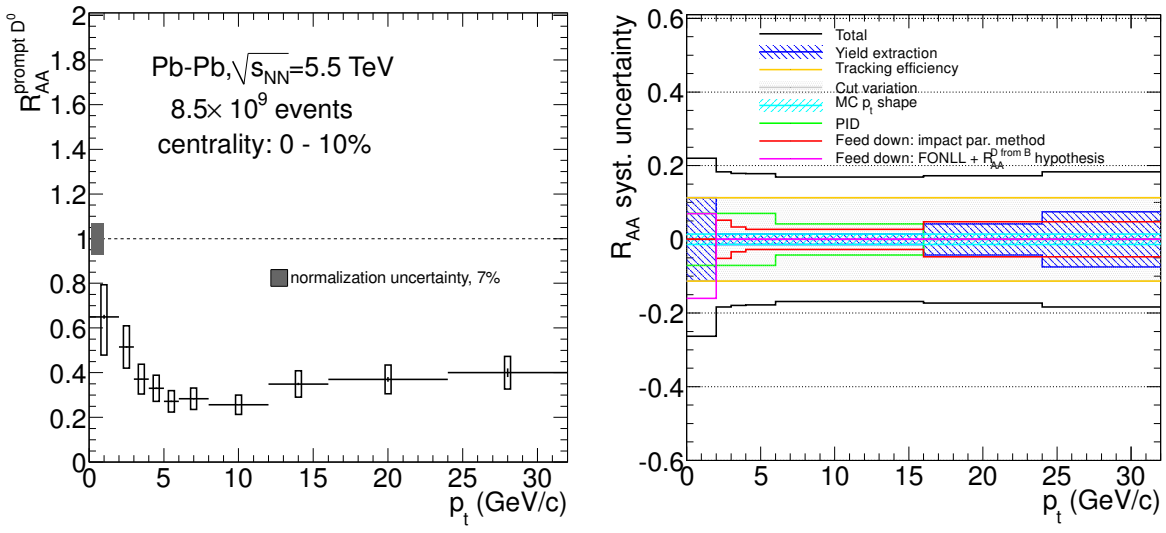

Figure 2.27: Systematic uncertainties on prompt D^0. Left: Nuclear modification factor of prompt D^0 mesons in central Pb–Pb for $L_{int} = 10$ nb^{-1} with statistical and systematic uncertainties. Right: contributions to the relative systematic uncertainty.

formance of this method: the extension of its applicability down to $p_t = 1$ GeV/c is under study. For $p_t < 2$ GeV/c we considered that we will have to rely on FONLL. Given that the contribution of secondary D below 1 GeV/c is modest ($\approx 6\%$ before topological cuts), in Table 2.4 we reported the uncertainty on FONLL prediction evaluated for the measurement of D^0 production for pp collisions at $\sqrt{s} = 7$ TeV [70] in the $1 < p_t < 2$ GeV/c range, as the systematic uncertainty in $0 < p_t < 2$ GeV/c. Note that the large $^{+5}_{-45}$% uncertainty quoted will not affect the measurement of $R_{AA}^{prompt\,D}$ since this contribution cancels in the ratio of Pb–Pb and pp spectra.

– Yield extraction: the higher signal-to-background ratio and the larger statistics will provide a

strong reduction of the uncertainty on the signal extraction from the invariant mass fit down to 1% in the $p_{\rm t}$ range considered in [50].

– $p_{\rm t}$ shape of D mesons in the simulation: the correction of the raw yield for the cut selection efficiency can be biased by a difference in the shape of the $p_{\rm t}$ spectra in data and Monte Carlo, due to the variation of the efficiency within the $p_{\rm t}$ interval in which the signal is extracted. Due to the larger statistics and the improved significance, a more $p_{\rm t}$-differential measurement will be performed, reducing the effect of this systematic uncertainty.

– PID efficiency: the uncertainty on the correction for the PID selection was estimated in [50] by comparing the signals obtained with and without PID selection. However, in the latter case, the statistical uncertainty is much larger and the larger background reduces the stability of the mass fit. The larger statistics and the higher signal-to-background ratio, even without PID selection, will allow for a precise estimate of this uncertainty. We believe that the 5% value estimated on the proton-proton analysis at $\sqrt{s} = 7$ TeV [70] can be considered as a realistic value.

– Cut efficiency: this contribution is estimated from the stability of the corrected yield against the variation of the selection cuts. The larger statistics and the possibility to release the cut selection will probably allow to slightly reduce this uncertainty.

– Tracking efficiency: the same considerations done for the previous source apply.

Figure 2.27 (left) shows the nuclear modification factor of prompt $\rm D^0$ with the systematic and the statistical uncertainties expected for 8.5×10^9 central (0–10%) Pb–Pb events, corresponding to $L_{\rm int} = 10$ nb^{-1}. The right panel shows the $p_{\rm t}$ dependence of the various contributions to the relative systematic uncertainty.

2.3.4 B Meson Production via Displaced $\rm D^0$

Most of the B meson decay channels include a $\rm D^0(\overline{D}^0)$[4]. According to the FONLL perturbative QCD calculations [69], in pp collisions at $\sqrt{s} = 7$ TeV, the ratio of $\rm D^0$ from B decay and prompt $\rm D^0$ increases with transverse momentum, from $\approx 5\%$ at $p_{\rm t} \approx 1$ GeV/c to $\approx 20\%$ at $p_{\rm t} \approx 20$ GeV/c. As illustrated in Figure 2.28, the kaon and pion tracks coming from secondary $\rm D^0$ decays are, on average, more displaced from the primary vertex than those coming from the decay of a prompt $\rm D^0$, due to the relatively long lifetime of B mesons ($c\tau \approx 460$–490 μm [67]). Therefore, the selection applied on reconstructed $\rm D^0$ candidates, optimized to prefer secondary vertices displaced from the primary vertex, further enhances the secondary-to-prompt ratio of reconstructed $\rm D^0$ up to typical values around 10% even for $p_{\rm t} < 5$ GeV/c.

The ALICE measurement of prompt D meson production used FONLL prediction of beauty production to subtract the contribution of secondary D [50]. The uncertainty of this contribution, evaluated by considering the spread of the predictions obtained by varying the parameters entering the theoretical calculation, ranges between 10% and 30% depending on $p_{\rm t}$. In the measurement of the D meson nuclear modification factors, the above uncertainty partially cancels in the ratio of Pb–Pb and pp spectra. However, the unknown B meson $R_{\rm AA}$ yields a further and relevant uncertainty (up to 25%) on the D meson $R_{\rm AA}$ [71].

A direct measurement of the fraction of prompt D mesons would:

– avoid the usage of theoretical predictions and assumptions on beauty production and nuclear modification factor in the charm production measurements in pp and Pb–Pb;

[4] $\rm BR(b_{hadr.} \to D^0 + X) = 61.0 \pm 3.1\%$, for $\rm B^{\pm}/B^0/B_s^0/b-baryon$ admixture [67].

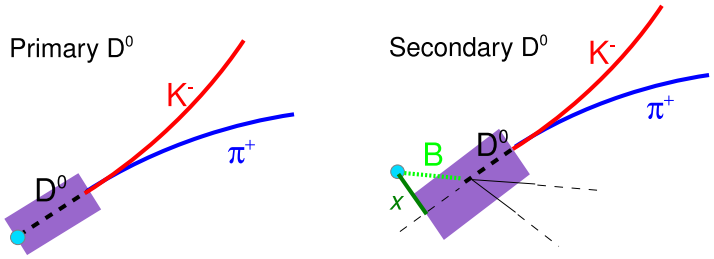

Figure 2.28: Schematic representation of a $D^0 \to K^-\pi^+$ decay for prompt (left) and secondary (right) D^0 mesons. The blue dot represents the primary vertex. The rectangle represents the contribution of the detector charm impact parameter resolution function to the observed D^0 impact parameter (see text). The thin dashed line is the B meson flight line while x, the continuous line, is the true impact parameter of the secondary D^0.

– open the possibility to perform an inclusive measurement of the B meson production and nuclear modification factor, via the p_t spectra of D mesons from B decays.

2.3.4.1 Method and Statistical Precision

The fraction of prompt D^0 mesons can be measured by exploiting the different shapes of the impact parameter distributions of primary and secondary mesons. This approach has been used already in pp (or $p\bar{p}$) collisions by the CDF Collaboration [72] to measure the production of prompt D mesons at $\sqrt{s} = 1.96$ TeV ($p\bar{p}$) and by the LHCb Collaboration [73] to measure the production of B mesons at $\sqrt{s} = 7$ TeV at forward rapidity. The limited statistics available for the ALICE measurements of D meson production only allowed this approach to be used as a cross-check of the theory driven methods mentioned above. In this section the different factors that determine the performance of this method are discussed, in relation to the improvements achievable with the ITS upgrade.

The main factors determining the performance achievable with this method are the available statistics, the uncertainty deriving from the subtraction of the background impact parameter distribution, and the resolution of the *D* meson impact parameter, which is directly related to the resolution of the track position in the vicinity of the primary vertex.

The *Hybrid* simulation approach was used to study the effect of the improved track position and p_t resolutions for the ITS upgrade configuration. Figure 2.29 (left panel) shows the impact parameter distribution for prompt and secondary D^0 in $2 < p_t < 3$ GeV/c as obtained from a heavy-flavour enriched MC simulation of pp collisions at $\sqrt{s} = 7$ TeV produced with the PYTHIA generator. For example, the probability to assign a 100 μm impact parameter to a prompt D^0 decreases by a factor of more than 3 in the upgraded ITS case, with respect to the current ITS case. The detector resolution function can be modeled with a Gaussian term plus exponential tails. In Figure 2.29, right panel, the σ_D parameter (Gaussian width), obtained by fitting the prompt D^0 impact parameter distribution with this functional form, is reported as a function of transverse momentum for the current and upgraded ITS scenarios. An improvement by a factor of around 2 is obtained in the latter case.

The side bands of the invariant mass distribution are used to model the impact parameter distribution of the background that is subtracted from the impact parameter distribution of D^0 candidates in the mass peak region. The uncertainties in the background shape, due to statistical fluctuations in the distribu-

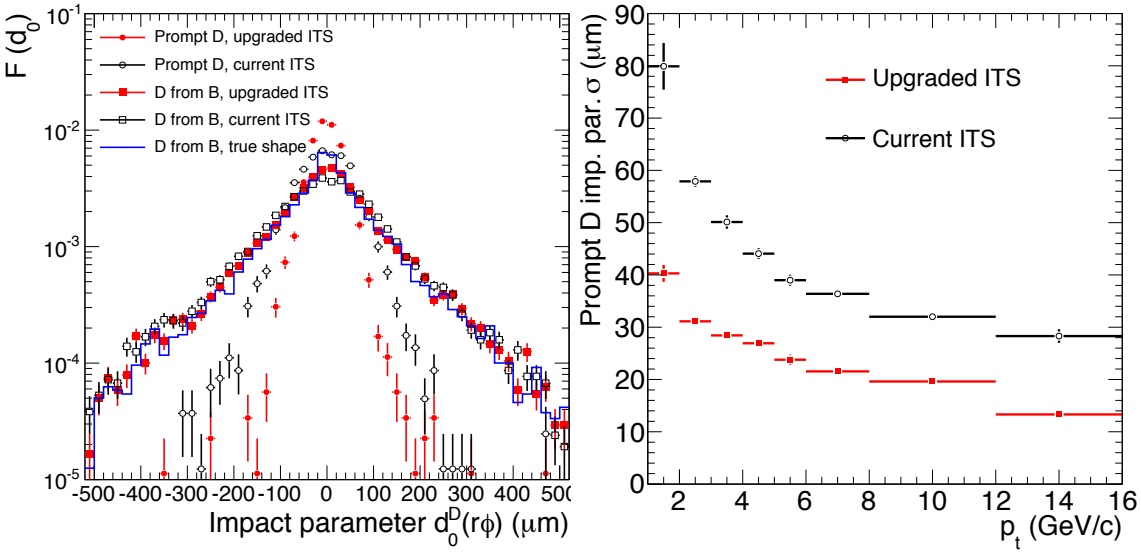

Figure 2.29: D^0 from B decays. Left: comparison of the impact parameter distributions for prompt and secondary D^0 obtained with the current and upgrade ITS configurations in the transverse momentum range $2 < p_t < 3$ GeV/c. Right: sigma of the Gaussian term of the detector resolution function, representing the D^0 impact parameter resolution, for current and upgrade ITS scenarios.

tion, and on the amount of background, estimated from the fit to the invariant mass distribution, affect the performance of the fit. The large reduction of the background expected in the ITS upgrade scenario (Section 2.3.3) should strongly reduce the impact of background subtraction uncertainties on the achievable performance.

An estimation of the performance for the measurement of beauty production in central Pb–Pb collisions using the fraction of non-prompt D^0 mesons was carried out, starting from the simulation results on the impact parameter resolution, the D^0 S/B ratio, and the expected D^0 signal statistics. For the latter, we have considered a sample of 10^8, 10^9, or 1.7×10^{10} events in the centrality class 0–20% (the last value corresponds to an integrated luminosity of 10 nb^{-1}). An additional input parameter of the study is the value of the fraction of non-prompt D mesons, for which we have considered two cases, 0.10 and 0.20, for illustration, and then used the p_t dependence observed in proton–proton data.

We used the following procedure to study the performance and the systematic uncertainties affecting the extraction of the fraction of prompt ($f_{\rm prompt}$) and secondary ($f_{\rm feed-down}$) D^0 mesons via the fit of D^0 candidate impact parameter distribution.

For each p_t interval, using the values of signal and background expected for a given statistics, and a realistic value of the fraction of prompt D^0, we combined several times (100) template histograms of the reconstructed impact parameter of prompt, secondary, and background D^0 candidates, in order to produce a set of template histograms of the inclusive impact parameter distribution. Each time, a Poissonian smearing is applied to the input histograms, obtained from MC simulations accounting for the improved spatial and momentum resolutions expected from the upgrade of the ITS. The background input histogram is fitted with a Gaussian function with exponential tails before smearing, and the background template is generated from the fit result. The same template is used for generating the histograms of the impact parameter distribution of D^0 background candidates in the signal and side-band regions of the invariant mass distribution. However, each time, an independent Poissonian smearing is applied, accounting also for the ~ 10 times larger statistics in the side-band region. Using the unsmeared impact

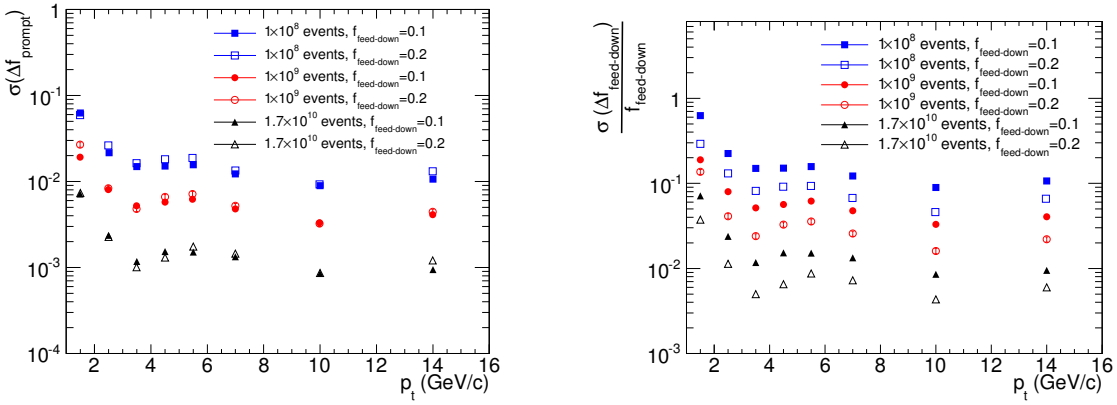

Figure 2.30: Left: comparison of the statistical uncertainties on the fraction $f_{\rm prompt}$ of $\rm D^0$ mesons from B decays in central Pb–Pb collisions (three cases of integrated luminosity, with 1.7×10^{10} events corresponding to 10 $\rm nb^{-1}$) with the upgrade of the ITS and for two cases of the input fraction of non-prompt $\rm D^0$ mesons (0.1 and 0.2). Right: the corresponding relative statistical uncertainty on the non-prompt fraction $f_{\rm feed-down}$.

parameter distribution of prompt $\rm D^0$, the distribution of the true impact parameter of secondary $\rm D^0$, the side-band background histogram, and the background yield as inputs, each data-like template is fitted, following the procedure described in the previous section.

The distribution of the (100) residuals between the fraction of prompt (or, equivalently, secondary) $\rm D^0$ recovered by the fit and the input one (recalculated after the Poissonian smearing of the prompt and secondary templates) is fitted with a Gaussian. In the absence of any bias, the distribution of the residuals should be well described by a Gaussian centered in zero and with the sigma representing the statistical uncertainty on the $f_{\rm prompt}$ ($f_{\rm feed-down}$) parameter. By varying the input signal yield, signal over background, $f_{\rm prompt}$, and by using input distributions obtained from Monte Carlo simulations with different impact parameter resolutions, the performance of the method has been studied for different rate scenarios (number of events) and for the spatial resolutions of current and upgraded ITS.

Figure 2.30 shows the statistical uncertainty on $f_{\rm prompt}$ (left) and $f_{\rm feed-down} = 1 - f_{\rm prompt}$ (right) as a function of $p_{\rm t}$ estimated with the above procedure, for 10^8, 10^9 and 1.7×10^{10} Pb–Pb events, for two different input $f_{\rm feed-down}$ values, 0.1 and 0.2. The larger relative uncertainty on $f_{\rm feed-down}$ with respect to $f_{\rm prompt}$ is due to the values of $f_{\rm prompt}$ considered. The actual values depend on both the ratio of prompt to secondary D mesons produced and on the cut selection, which enhances the fraction of secondaries. Typically, $f_{\rm feed-down}$ ranges from 0.1 at low $p_{\rm t}$ up to 0.15–0.25 for $p_{\rm t} > 8$ GeV/c [70]. This $p_{\rm t}$-dependence was taken into account to estimate the relative statistical uncertainty on $f_{\rm feed-down}$ expected in the *high-rate* scenario for the centrality range 0–20% with the current and upgraded ITS spatial resolution, reported in the top panel of Figure 2.31. The large improvement in the performance derives from the better background rejection rather than from the capability of better resolving prompt and secondary $\rm D^0$, as indicated by the comparison of the statistical uncertainty for the current ITS case (black triangle) with that obtained with the current ITS spatial resolution but with the signal-to-background ratios expected from the upgrade of the ITS (empty triangles). The statistical uncertainty in the *no high-rate* scenario, reported in the bottom panel, does not allow to extract $f_{\rm feed-down}$ with the current ITS and limits its feasibility to $p_{\rm t} > 3$ GeV/c, with a 10% uncertainty, also in the upgrade case. Conversely, in the *high-rate* scenario the statistical precision allows to perform this measurement down to $p_{\rm t} = 1$ GeV/c. However, the applicability of this method below 2 GeV/c is still under study and might be limited by the short decay length of low-$p_{\rm t}$ B mesons in the laboratory (small Lorentz boost) .

Since the statistical uncertainty on the measurement of the total $\rm D^0$ yields is expected to be of the order

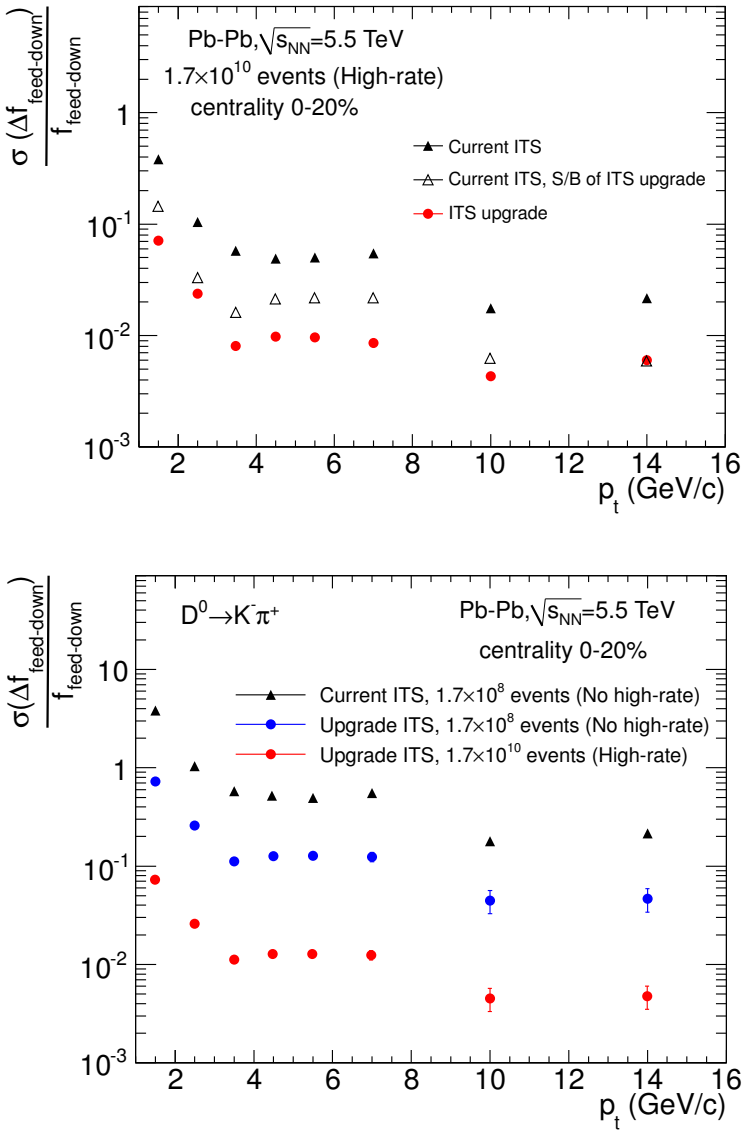

Figure 2.31: Top: relative statistical uncertainty on $f_{\mathrm{feed-down}}$ expected in the *high-rate* scenario for the centrality range 0-20% with the upgraded and current ITS spatial resolution. The empty markers highlight the effect deriving from the background reduction. A realistic p_{t} dependence was considered for $f_{\mathrm{feed-down}}$. Bottom: performance in terms of statistical uncertainties expected with the current ITS in the low rate scenario, and with the upgraded ITS in both the low and high rate scenarios.

of 1%, the values shown in the figure coincide in practice with the relative statistical uncertainty on the measurement of beauty production. The results are very promising, with a statistical uncertainty smaller than 10% down to D^0 p_{t} of 1 GeV/c, for 10 nb^{-1}. Since the mass difference of B and D mesons is larger than 3 GeV/c^2, the decay of a B meson with transverse momentum below 1 GeV/c can yield a D meson with $p_{\mathrm{t}} > 2$ GeV/c. Therefore, the measurement will give access to B mesons with p_{t} down to almost 0.

2.3.4.2 Systematic Uncertainty on the Measurement of the Prompt and Secondary Fractions

Systematic uncertainties were studied by biasing the input ingredients/parameters of the fit procedure, and evaluated by comparing the mean and the sigma of the residual distributions with and without a given

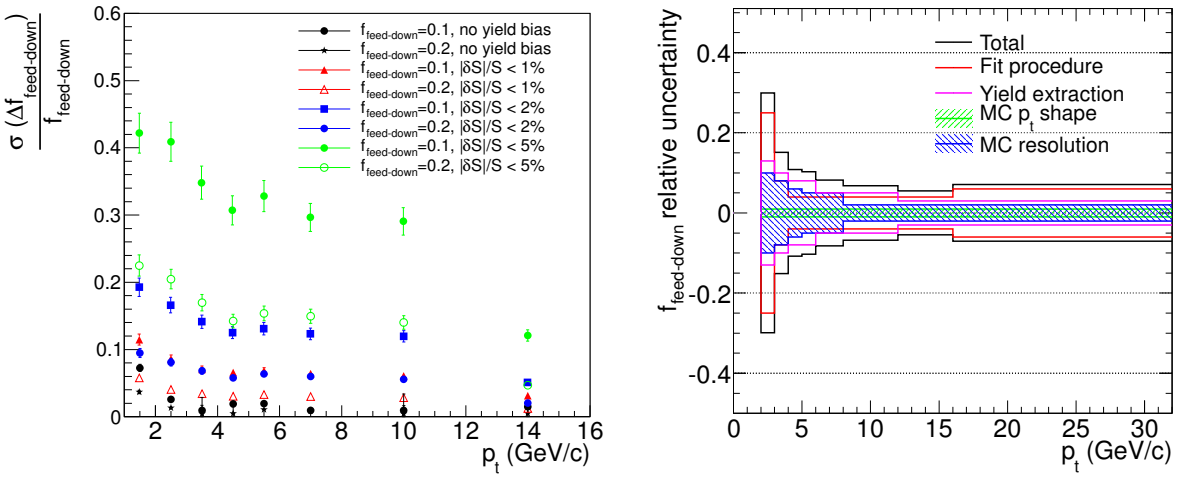

Figure 2.32: Left: study of the systematic uncertainty on $f_{\mathrm{feed-down}}$ extraction deriving from the systematic uncertainty on the yield extraction (see text for details). Right: p_{t} dependence of the different sources of systematic uncertainty on $f_{\mathrm{feed-down}}$.

bias. The following sources were considered:

- Fit procedure: the mean of the Gaussian of the residuals shows a systematic difference with respect to zero even in the absence of any bias. The effect, contained within 3% on f_{prompt}, has a $\sim 22\%$ size on $f_{\mathrm{feed-down}}$ in $2 < p_{\mathrm{t}} < 3$ GeV/c. This discrepancy is still under study.

- Yield extraction: the subtraction of the impact parameter distribution of the background in the D^0 mass signal region is done using the impact parameter distribution in the side bands, normalized to the exact amount of background in the signal region. While the statistical uncertainties on the signal and background yields recovered from the mass fit will be negligible for $p_{\mathrm{t}} > 2$ GeV/c, the $\delta S/S \sim 1$–2% systematic uncertainty on the signal (see Table 2.4) can influence the impact parameter fit. This effect was studied by varying the amount of background subtracted, considering that $\delta B/B = \delta S/S \times S/B$, utilizing the values of the signal over background ratio expected after the upgrade of the ITS and sampling $\delta S/S$ according to a uniform distribution within $\pm 1, 2$ and 5%. Figure 2.32 (left) shows the sigma of the $f_{\mathrm{feed-down}}$ residual distribution obtained as a function of p_{t} for two $f_{\mathrm{feed-down}}$ cases. As expected, the effect decreases with p_{t} due to the larger signal-to-background ratio.

- Monte Carlo resolution and Monte Carlo p_{t} shape: in the fit procedure, the template distributions of the reconstructed impact parameter of prompt D^0 and of the true impact parameter of secondary D^0 are fitted and the fit functions are used as ingredients in the convolution performed in the final fit, which is therefore sensitive to their shape. A discrepancy between the actual distributions and the Monte Carlo ones can derive from a not precise description of the spatial resolutions, due for instance to misalignment, and from a difference of the B and D meson p_{t} spectra in Monte Carlo and data. The latter can be relevant because the spatial resolution is p_{t} dependent and because the exponential shape of the distribution of the true impact parameter of secondary D^0 is sensitive to the decay length of the parent B meson. In order to study the effect of a different track spatial resolution in data and Monte Carlo, we used template histograms obtained from a simulation in which the track impact parameter resolution was deteriorated by 10% at low p_{t} and by $\sim 30\%$ at high p_{t} to simulate the data impact parameter distributions and we used the standard distributions as input for the fit. The resulting systematic uncertainty on $f_{\mathrm{feed-down}}$ is of the order of 10% at low

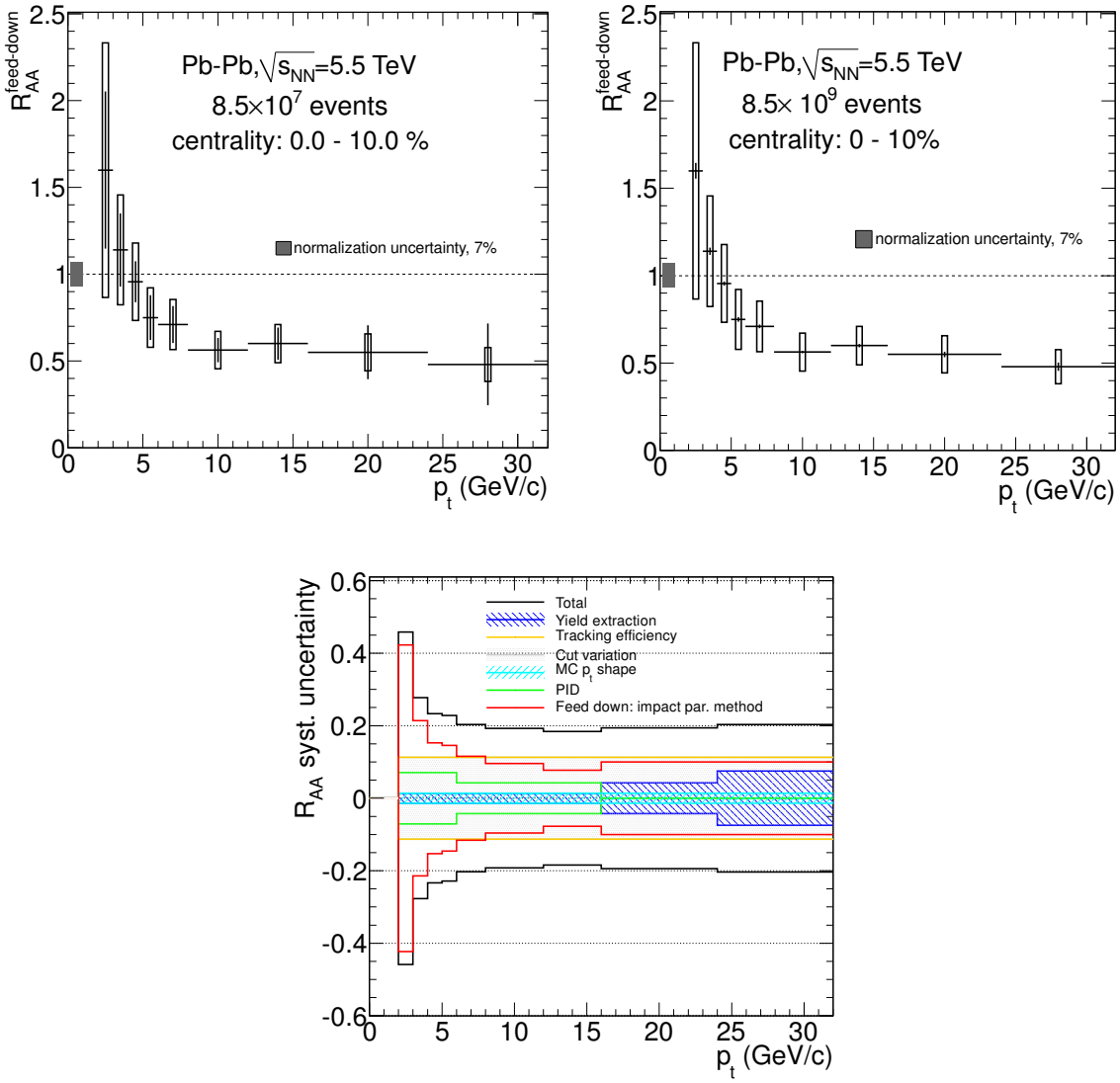

Figure 2.33: Nuclear modification factor of D^0 from b-hadron decay for (top-left) 8.5×10^7 (*no high-rate* scenario) and (top-right) 8.5×10^9 (*high-rate* scenario) Pb–Pb events in the centrality range 0–10%. Bottom panel: p_t dependence of the contributions of the relative systematic uncertainty.

p_t and decreases with p_t. The effect of a different meson p_t shape in data and Monte Carlo was studied by considering, in each p_t interval, the p_t shape predicted by FONLL [69] for prompt and secondary D or a flat distribution. The estimated systematic uncertainty on $f_{\text{feed-down}}$ is smaller than 2%.

The p_t dependence of each uncertainty considered is reported in the right-hand panel of Figure 2.32 for $p_t > 2$ GeV/c. The total 35% uncertainty in $2 < p_t < 3$ GeV/c is by far dominated by the fit procedure contribution: it is likely that further studies could bring to a better understanding and a reduction of this uncertainty.

2.3.4.3 Performance for the measurement of the beauty-to-charm relative nuclear suppression

The expected performance on the nuclear modification factor of D^0 from B decays is shown in Figure 2.33 for the *no high-rate* (left) and *high-rate* (right) scenarios. In the *high-rate* scenario, the mea-

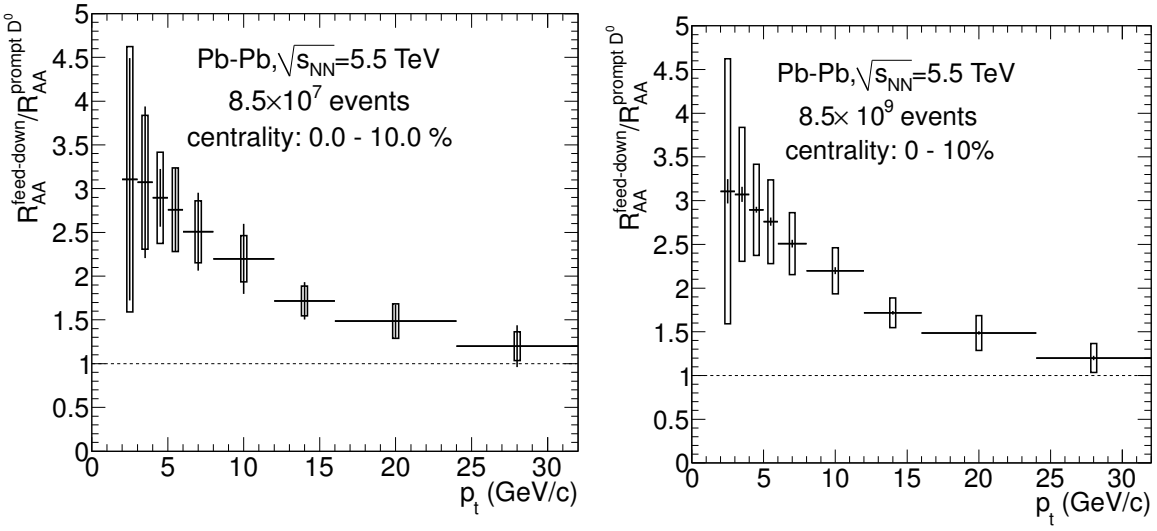

Figure 2.34: Ratio of the nuclear modification factors of prompt D mesons and D mesons from B decay in the *no high-rate* (left) and *high-rate* (right) scenarios for Pb–Pb collisions in the centrality range 0–10%.

surement uncertainty is completely dominated by systematic uncertainties in the whole p_{t} range. In the *no high-rate* scenario, systematic uncertainties are larger than the statistical ones at low p_{t}, while for $p_{\mathrm{t}} > 5$ GeV$/c$ they have a comparable or smaller size.

The ratio of the nuclear modification factors of D^0 from B and prompt D^0 is shown in Figure 2.34 for the *no high-rate* (left) and *high-rate* (right) scenarios. In the former, the statistical uncertainties are very similar to the systematic uncertainties in essentially all p_{t} intervals. This indicates that this measurement would benefit substantially from the *high-rate* capabilities, because an integrated luminosity of at least 1 nb^{-1} (8.5×10^8 events in the class 0–10%) would make the statistical uncertainties subdominant.

It should be stressed that, to avoid as much as possible arbitrary choices, our evaluation of the systematic uncertainties was driven by the estimates performed with the current ITS and with a data sample much smaller in size with respect to that expected after the upgrade of the ITS in both the *high-rate* and *no high-rate* scenario. We believe that the quoted values are hence rather conservative: the large statistics in the *high-rate* scenario and the higher signal purity expected after the detector upgrade should allow for a detail investigation of each source of systematic uncertainty that could easily bring to a better understanding of the detector response and of the analysis issues. Conversely, in the *no high-rate* scenario, statistical fluctuations of comparable size than systematic uncertainties could limit the understanding of the systematic uncertainties themselves, hence the physics performance.

2.3.4.4 Charm and Beauty Azimuthal Anisotropy v_2

We have estimated the expected precision on the measurement of v_2 for prompt and secondary D mesons with the upgraded ITS and with an integrated luminosity of 10 nb^{-1}. We have scaled the statistical uncertainties obtained from the simulation studies, considering that the significance/event is the same for central (0–20%) and semi-central events (e.g. 30–50%). This feature is observed in the D^0 analysis from 2010 data [50].

The v_2 extraction can be performed using the raw signal yields in two large intervals of azimuthal angle φ with respect to the Event Plane (EP) direction Ψ_{EP}, determined for each collision [74]: $[-\pi/4 < \Delta\varphi < \pi/4] \cup [3\pi/4 < \Delta\varphi < 5\pi/4]$ (in-plane) and $[\pi/4 < \Delta\varphi < 3\pi/4] \cup [5\pi/4 < \Delta\varphi < 7\pi/4]$ (out-of-plane). Given the in-plane and out-of-plane yields, N_{in} and N_{out}, v_2 can be obtained as $v_2 = (\pi/4) \cdot$

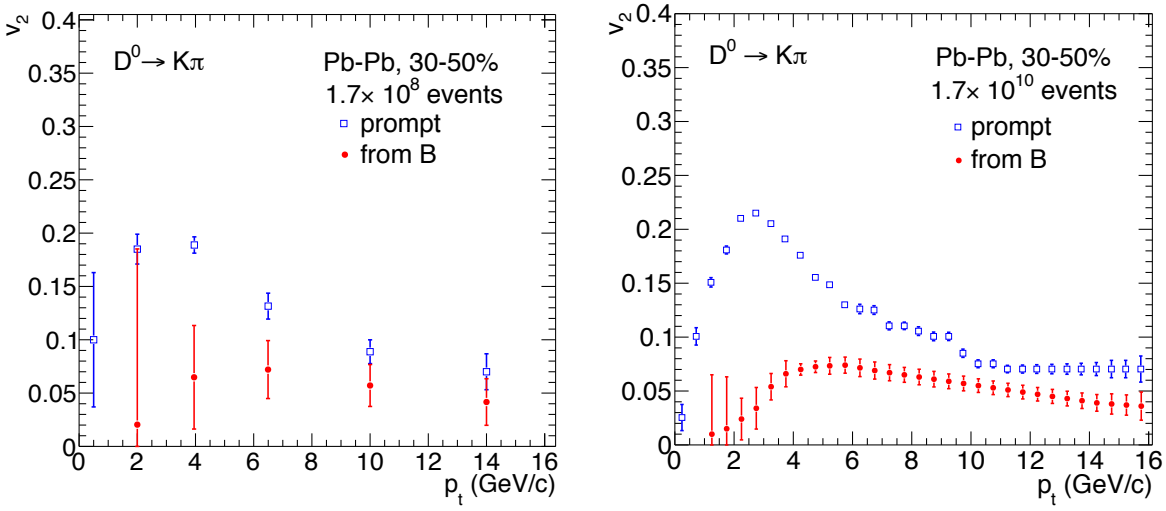

Figure 2.35: Estimated statistical uncertainties on v_2 of prompt and secondary D^0 mesons in the *no high-rate* (left) and *high-rate* (right) scenarios for Pb–Pb collisions in the centrality range 30–50%.

$(N_{\rm in} - N_{\rm out})/(N_{\rm in} + N_{\rm out})$, neglecting the higher harmonics. In order to measure separately v_2 for prompt (charm) and secondary (beauty) D mesons, the prompt fraction will be determined for the in-plane and out-of-plane signals using the D^0 impact parameter fit, as described in the first part of this section.

We have estimated the statistical uncertainties on v_2 considering that the relative statistical uncertainties on $N_{\rm in}$ and $N_{\rm out}$ are $\sqrt{2/(1 \pm v_2)}$ times larger, respectively, than those on the total raw yield and assuming $v_2(p_{\rm t})$ for prompt and secondary D mesons as in the predictions of the BAMPS model [19], shown in the top-right panel of Figure 2.2 (the v_2 for non-prompt J/ψ is used for D^0 from B decays). The resulting statistical uncertainties are reported in Figure 2.35 for $1.7 \cdot 10^{10}$ events in the 30–50% centrality class, which correspond to 10 $\rm nb^{-1}$, and for $1.7 \cdot 10^8$ events, which correspond to 0.1 $\rm nb^{-1}$ (*no high-rate* scenario). The systematic uncertainties are expected to be rather small, since most of them are common for the $N_{\rm in}$ and $N_{\rm out}$ raw yields and cancel in the v_2 ratio. A detailed estimation is being carried out.

2.3.5 Charm Baryons: $\Lambda_c \to pK^-\pi^+$ as a Benchmark Case

The physics motivation for the measurement of charm baryon production was discussed in the first part of this chapter. The most promising measurement is the decay of the Λ_c^+ in three charged prongs (p, K^-, and π^+) with a B.R. of about 5.0% [67]. In order to identify the decay vertex, a very high resolution is needed, owing to the short mean proper decay length of the Λ_c, $c\tau \approx 60$ μm [67]. Therefore, an improvement of the resolution would allow a much cleaner separation of its decay point (the secondary vertex) from the interaction point (primary vertex) with respect to the current ITS.

The decay channel of $\Lambda_c \to pK^-\pi^+$ is studied by analyzing the invariant mass of fully-reconstructed three-prong decays, selected by applying topological cuts and particle identification criteria, namely the proton and kaon identification using the TPC and TOF information. As for the D^0 case, our simulation study used the *Hybrid* approach and the upgraded configuration of the ITS. To discriminate the Λ_c signal against the background, which is made mostly of primary particles, a study of the cuts on kinematical and topological variables was carried out. The analysis cuts optimized to extract the signal in pp collision data at $\sqrt{s} = 7$ TeV were used as a starting point. However, these are not fully adequate for taking advantage of the ITS upgrade potential, because the increased impact parameter resolution provided by the new detector allows a better discrimination of the signal against the background, hence less stringent cuts allow for rejecting effectively the background but minimize the loss of the signal.

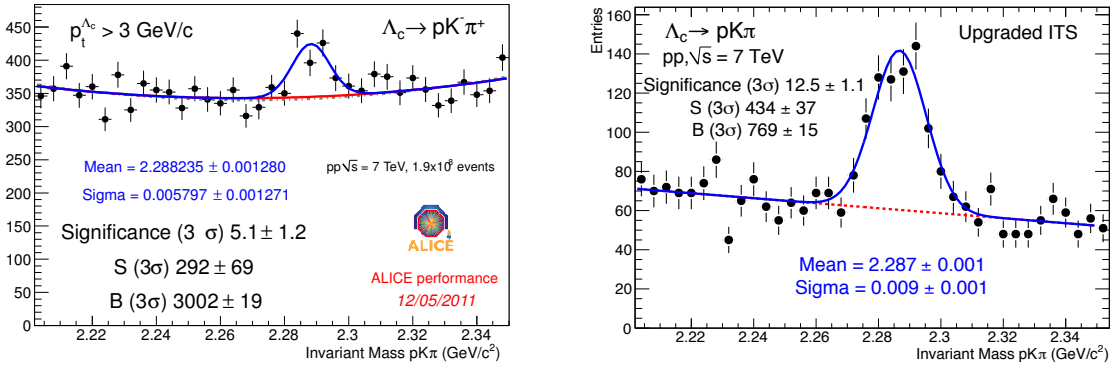

Figure 2.36: $\Lambda_c \rightarrow pK^-\pi^+$ candidates invariant mass distribution for $p_t > 3$ GeV/c in pp collisions at 7 TeV (1.9×10^8 events). Left: pp collision data. Right: *Hybrid* simulation with the ITS upgrade configuration. The sample statistics in the simulation is the same as in the data, while the selection cuts were optimized specifically for the upgrade scenario.

The optimization of the cuts with the ITS Upgrade layout has been performed by studying the distribution of the kinematical variables used to reject the background against the signal. A comparison has been done between the amount of signal and background rejected with the current analysis cuts and with the new ones: the new cuts represent a compromise between the maximization of the significance and the minimization of the signal loss.

The most effective cut variables are:

- The cosine of the pointing angle (θ_p): the angle formed by the vector connecting the primary to the secondary vertex and the momentum of the Λ_c, obtained as the sum of the momenta of its three decay tracks at the secondary vertex. The cut $\cos\theta_p > 0.75$ allows one to reduce significantly the background while only rejecting a very small amount of signal. In the current analysis with the present detector this cut is $\cos\theta_p > 0$.
- The Λ_c decay length (L): the distance between the primary and the secondary vertex. The current analysis uses $L > 70$ μm; a further background rejection with the upgraded ITS is achievable by imposing $L > 80$ μm in pp and a tighter p_t-dependent cut in Pb–Pb (e.g. $L > 200$ μm at $p_t = 4$ GeV/c).
- The minimum p_t of the three decay tracks. This selection enables a very strong reduction of the combinatorial background in the low-p_t region. Also in this case, the cut value depends on Λ_c transverse momentum.

2.3.5.1 Results for pp Collisions

In Figure 2.36 (left) we show the invariant mass distribution of $\Lambda_c \rightarrow pK^-\pi^+$ candidates with $p_t > 3$ GeV/c, obtained from a data sample of 1.9×10^8 proton–proton events, collected with the ALICE minimum bias trigger, at $\sqrt{s} = 7$ TeV. The Λ_c is visible, however the significance is low, due to the limited efficiency for background rejection. In the right-hand panel of the same figure, we show the distribution as it is expected for the ITS upgrade case for the same event statistics obtained with the *Hybrid* approach on a sample of pp events produced with the PYTHIA generator (with the Perugia-0 tune). Signal and background yields are rescaled in order to match the features observed in data, as explained in the following. For the background, the scaling factor is simply the ratio of the sample sizes for the data and the simulation $N_{\rm data}/N_{\rm MC}$ ($1.9 \times 10^8/1.3 \times 10^8$). For the signal, in addition to this factor, a 10% correction was included in order to equalize the total $c\bar{c}$ cross section yielded by

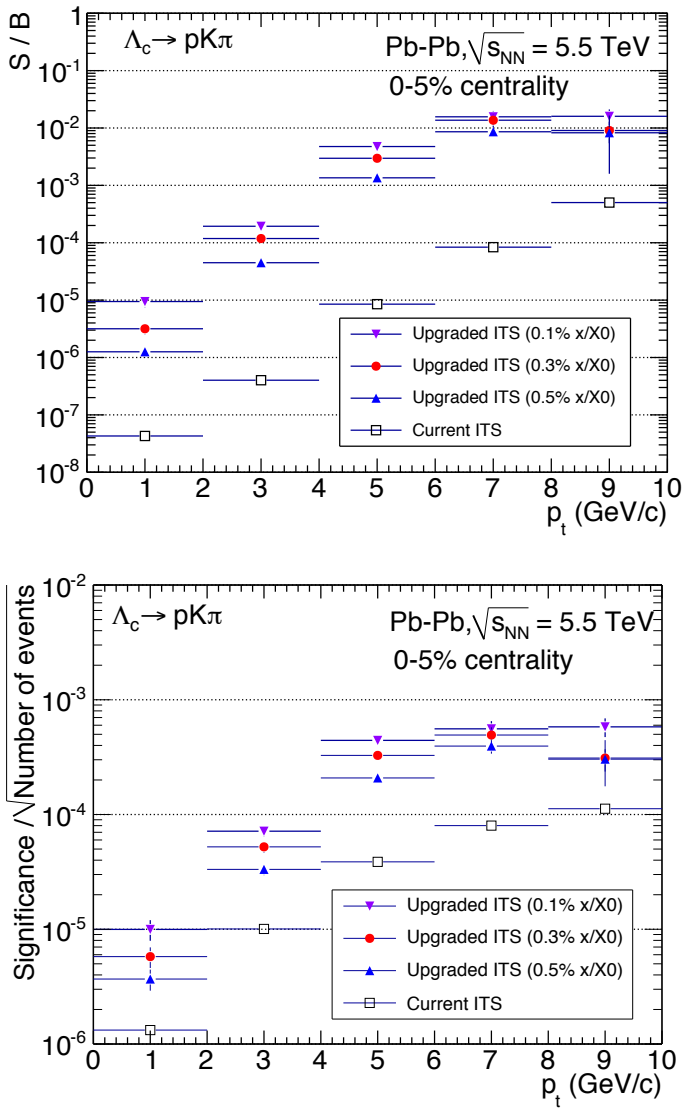

Figure 2.37: $\Lambda_c \rightarrow pK^-\pi^+$ in central Pb–Pb collisions at $\sqrt{s_{NN}} = 5.5$ TeV: signal-to-background ratio (upper panel) and significance per event (lower panel) for current and upgraded ITS. For the upgrade, three different scenarios are considered: the baseline configuration is labelled "0.3%"; the cases labelled "0.1%" and "0.5%" represent variations of the layer thickness only (with respect to the baseline configuration), for the innermost two layers to 0.1% of radiation length and for all layers to 0.5% of radiation length, respectively.

PYTHIA Perugia-0 to the one measured in ALICE (preliminary value, which is consistent with the final published one [75]), $\sigma_{pp}^{c\bar{c}} = 7.73 \pm 0.54(stat.)^{+0.74}_{-1.38}(syst.) \pm 0.44(lumi.)^{+1.90}_{-0.87}(extr.)$ mb. For the ITS upgrade scenario we obtain a significance of about 12 for Λ_c with $p_t > 3$ GeV/c, to be compared to the current value from data of about 5. The increase of the signal statistics is about 50% (less stringent cuts are used for the upgrade case) and the increase of the signal-to-background ratio is more than a factor of 5.

2.3.5.2 Results for Pb–Pb Collisions

The Λ_c signal could not be observed with the 2010 Pb–Pb data sample, because of the very large combinatorial background. Therefore, we do not have a baseline selection, nor a direct comparison with data. We have studied the selection strategy using a dedicated simulation sample of about 10^4 central

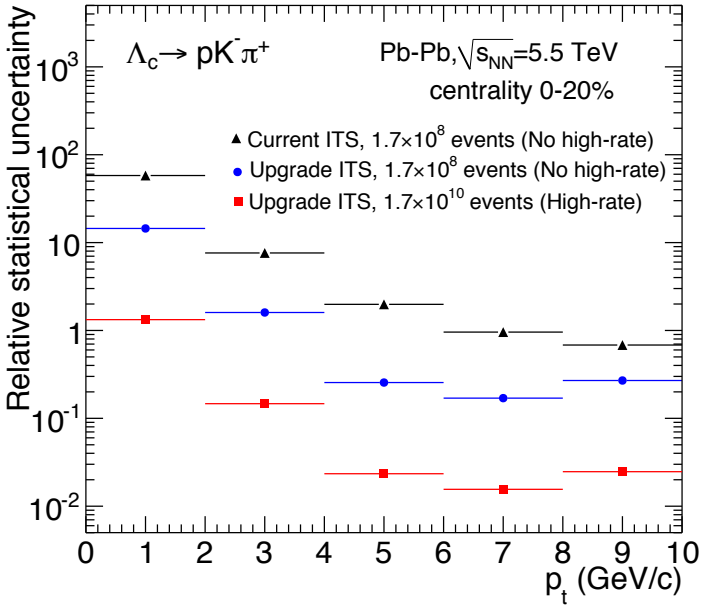

Figure 2.38: Comparison of statistical precision for different cases of ITS performance and integrated luminosity: current and upgraded ITS; *high-rate* scenario, i.e. 50 kHz readout rate that provides 10 nb^{-1}; *no high-rate* scenario, i.e. 500 Hz readout rate that provides 0.1 nb^{-1}.

(0–10%) Pb–Pb events at $\sqrt{s_{\rm NN}} = 5.5$ TeV produced with the HIJING event generator. In each event, 20 $\Lambda_c \rightarrow pK^-\pi^+$ decays were added, in order to obtain a high-statistics signal sample allowing for the study of the selection cuts. The signal per event was then rescaled to the pQCD expectation $dN/dy = 1.4$ (see Table 2.2) and also the branching ratio (5%) normalization was accounted for. A p_t-dependent weight was applied to each signal particle such that the shape of the p_t distribution of the simulated Λ_c matches the prediction of the FONLL pQCD calculation for D mesons at $\sqrt{s} = 5.5$ TeV [69]. In this Monte Carlo sample the current ITS detector layout was simulated without any inactive module, at variance with the simulations used for example for the D^0 study, and the effect of the ITS upgrade on the tracking precision was included a posteriori using the *Hybrid* approach. Three different upgrade configurations were tested: the baseline configuration of 0.3% of the radiation length per layer (as for the D^0 studies), and two other cases that represent variations of the layer thickness only (with respect to the baseline), for the innermost two layers to 0.1% of the radiation length and for all layers to 0.5% of radiation length, respectively. A cut optimization study was carried out with the aim of maximizing the signal significance. It was found that the two most effective cuts for the ITS upgrade scenario are the Λ_c decay length and the minimum p_t of the decay tracks. The results, in terms of S/B ratio and significance per event, are reported in Figure 2.37 as a function of p_t. The signal-to-background ratio improves by a factor 400 (in $2 < p_t < 4$ GeV/c) from current to upgraded ITS, while the significance improves by a factor 5–10 in all p_t intervals above 2 GeV/c. Considering an integrated luminosity of 10 nb^{-1} (1.7×10^{10} central events in the centrality class 0–20%) the significance is 1.3×10^5 times the values reported in the figure, that is: 7 in 2–4 GeV/c, 40 in 4–6 GeV/c, 53 in 6–8 GeV/c. Figure 2.38 shows the comparison of statistical precisions for the current and upgraded ITS in two scenarios of integrated luminosity: 10 nb^{-1} (*high-rate* capability) and 0.1 nb^{-1} (*no high-rate* capability). Since the integrated luminosity differs by a factor 100 in the two scenarios, the precision differs by a factor 10. With the upgraded ITS in the *no high-rate* scenario, the precision is marginal in the whole p_t range. While in the *high-rate* scenario, Λ_c production should be measurable down to a transverse momentum of 2 GeV/c in central collisions.

The signal-to-background ratio is expected to be very small at low p_t ($\sim 10^{-4}$ in 2–4 GeV/c). There-

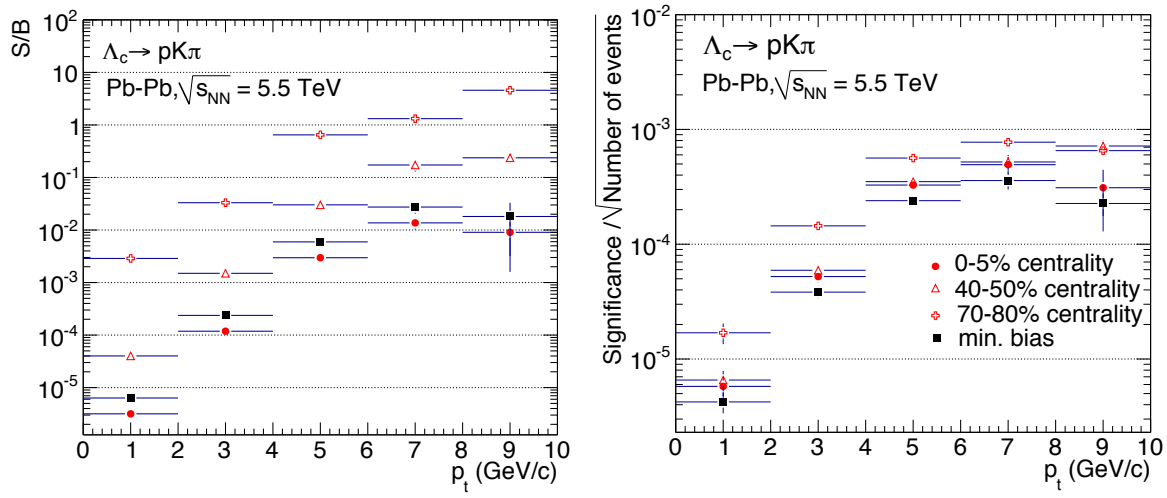

Figure 2.39: $\Lambda_c \rightarrow pK^-\pi^+$ in Pb–Pb collisions at $\sqrt{s_{NN}} = 5.5$ TeV: signal-to-background ratio (left panel) and significance per event (right panel) for the upgraded ITS with the baseline configuration with 0.3% x/X_0 layer thickness. The results from the simulation for 0–5% central collisions are scaled to minimum bias, semi-peripheral (40–50%) and peripheral (70–80%) collisions.

fore, the signal yield extraction from the invariant mass distributions will require a dedicated strategy to minimize the systematic effects from background fluctuations and correlated backgrounds. This aspect is discussed in detailed in Section 2.3.5.3.

The performance in non-central collisions was estimated by scaling the signal and background yields with centrality. and evaluating the signal-to-background ratio and the significance. The Λ_c signal S was scaled according to the number of binary nucleon–nucleon collisions N_{coll}, using a constant scaling factor for all transverse momentum intervals $S_P = S_C \cdot (N^P_{coll}/N^C_{coll})$, where C and P stand for central and peripheral collisions, respectively, S_C being the signal resulting from the simulation study. The three-track combinatorial background was scaled according to $B_P = B_C \cdot (N^P_{coll}/N^C_{coll})^3/(R^{charged}_{CP})^3$, where $R^{charged}_{CP}$ is the central-to-peripheral nuclear modification factor of charged hadrons. In principle, we should consider, for each background candidate, the p_t-dependent nuclear modification factors of the three decay particles, and use their product as a weight for that candidate. We use, instead, the aforementioned scaling with an R_{CP} value constant with p_t and conservatively chosen as the minimum value of the measured $R_{CP}(p_t)$ for charged hadrons. This minimum is close to the value of R_{CP} for $p_t \rightarrow 0$. Therefore, this scaling is de facto equivalent to scaling the background with the third power of the charged multiplicity $B_P = B_C \cdot (dN^P_{ch}/d\eta \,/\, dN^C_{ch}/d\eta)^3$, because $R_{CP}(p_t \rightarrow 0) \approx (N^P_{coll}/N^C_{coll})/(dN^C_{ch}/d\eta \,/\, dN^P_{ch}/d\eta)$.

Figure 2.39 shows the significance and the signal-to-background ratio in three centrality classes (0–5%, 40–50%, 70–80%) and in minimum-bias collisions —in this case the background was scaled using $\langle (dN_{ch}/d\eta)^3 \rangle$ instead of $\langle dN_{ch}/d\eta \rangle^3$. The performance in peripheral collisions is better, in terms of significance, by about a factor of 2 with respect to central collisions, with a significance of 20 in $2 < p_t < 4$ GeV/c for 1.7×10^{10} events (in a centrality class like 70–90% or 60–80%, for an integrated luminosity of 10 nb^{-1}). This would allow for the measurement of the central-to-peripheral nuclear modification factor for $p_t > 2$ GeV/c. In addition, the signal-to-background ratio becomes quite large in peripheral collisions. This will allow for an accurate determination of the width of the Λ_c invariant mass signal, which can then be used as a constraint for the signal extraction in central collisions, where the signal-to-background ratio is very low. In semi-central Pb–Pb collisions (40–50% in Figure 2.39), the significance is the same as in central collisions. With an integrated luminosity of 10 nb^{-1}, a measurement of the Λ_c elliptic flow can be performed for $p_t > 4$ GeV/c in semi-central collisions (e.g. 30–50%) and for $p_t > 2$ GeV/c in peripheral collisions collisions (e.g. 60–80%).

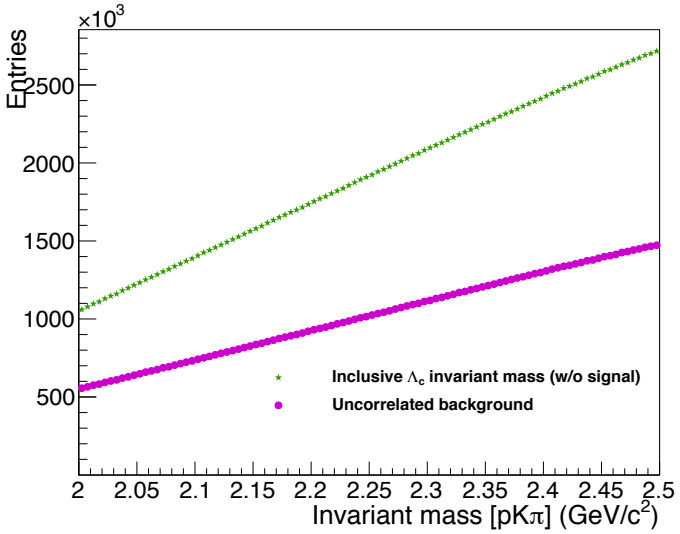

Figure 2.40: $\Lambda_c \rightarrow pK\pi$ invariant mass distribution from central Pb–Pb events (HIJING) for $4 < p_t < 6$ GeV/c. The total background is shown by the star symbols, while the contribution from uncorrelated background by circle symbols.

2.3.5.3 Background Study in Pb–Pb Collisions

Since the Λ_c signal-to-background ratio in Pb–Pb central collisions is expected to be very small (e.g. 10^{-4} in $2 < p_t < 4$ GeV/c), a study of the background sources was carried out to estimate their possible impact on the signal extraction.

Two main sources of background have been considered: the combinations of three uncorrelated tracks and the combinations of two or three tracks coming from a common particle decay (correlated background). Figure 2.40 shows the total and the uncorrelated background invariant mass distribution for Λ_c candidates with $4 < p_t < 6$ GeV/c that pass the selection cuts, in central Pb–Pb events produced with the HIJING event generator.

The uncorrelated background accounts for a large fraction of the total background. This contribution can be estimated precisely using the event mixing technique, and subtracted from the invariant mass distribution prior to the fit that is used to extract the signal yield. A first investigation in the simpler case of the $K^0_S \rightarrow \pi^+\pi^-$ decay and in a low-statistics sample for the $\Lambda_c \rightarrow pK\pi$ decay in pp collisions showed that the shape of the background is well reproduced by the mixed events.

The correlated background can feature structures in the invariant mass distribution that can affect the signal extraction if they are comparable with the position and width of the Λ_c signal. In this first study, the following cases were considered:

- 2 tracks from a common D meson decay (in particular D^+, D^{*+}, D_s^+ and D^0 were considered separately) and 1 uncorrelated track;
- 3 tracks from a common D meson decay;
- 2 tracks from a common Λ_c decay and 1 uncorrelated track;
- 2 tracks from a common resonance decay (K^{0*}, Δ^{++}, $\Lambda(1520)$, ρ, η, η', ω, ϕ were considered) and 1 uncorrelated track.

The simulated sample used for this study contains about 5×10^4 central Pb–Pb HIJING events at $\sqrt{s_{NN}} =$ 5.5 TeV. In these events the charm hadrons (D and Λ_c) were forced to decay in decay channels with only

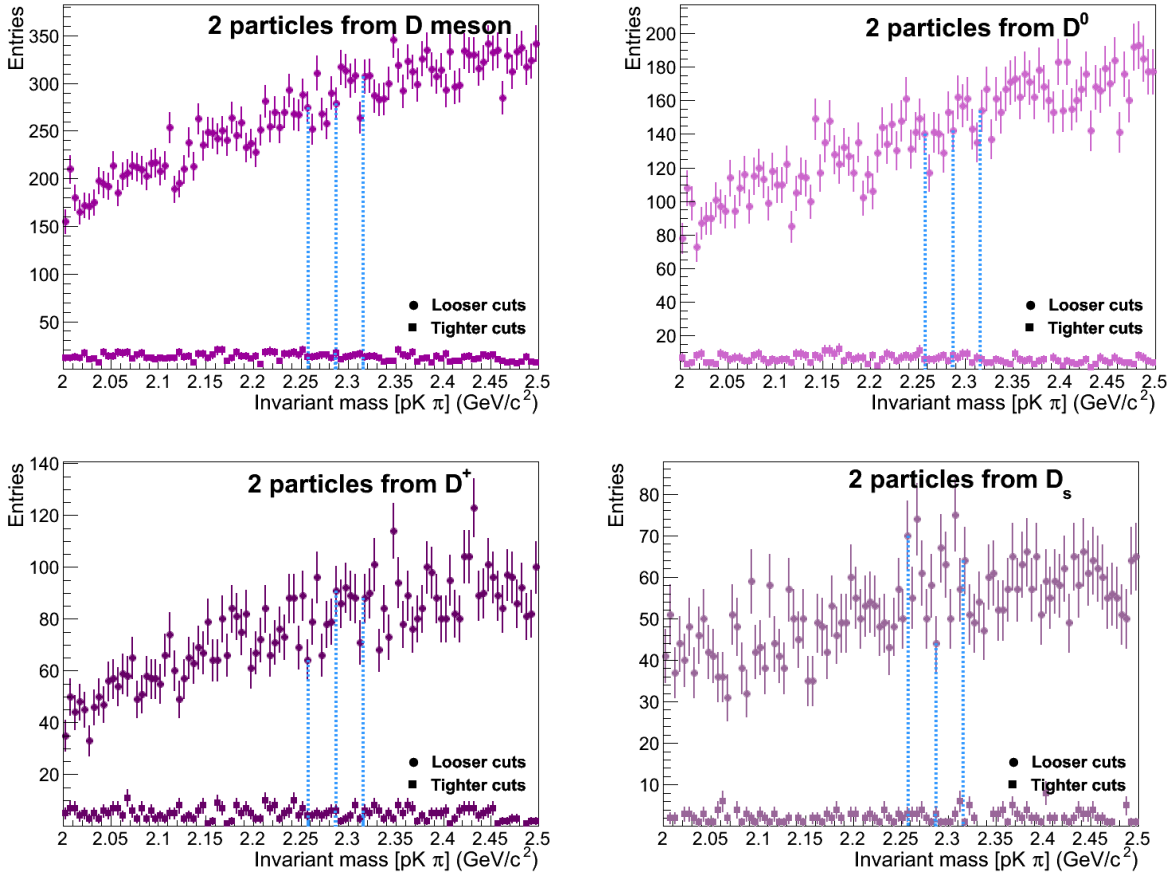

Figure 2.41: [pKπ] invariant mass distributions of the correlated background candidates (4–6 GeV/c) with 2 tracks from a common D meson decay. From top left to bottom right: all D mesons, D^0, D^+, and D_s^+. The dashed lines show the position of the Λ_c mass and a $\pm 3\sigma$ range.

charged hadrons in the final state, because these are more likely to yield a large invariant mass, close to the Λ_c mass of 2.286 GeV/c^2, when the [pKπ] mass hypotheses are used for the three tracks. These decay channels have typical branching ratios of the order of 5–10%. Two sets of topological selections were considered, both looser with respect to those used to optimize the significance (previous section), so as to preserve enough background statistics for the study.

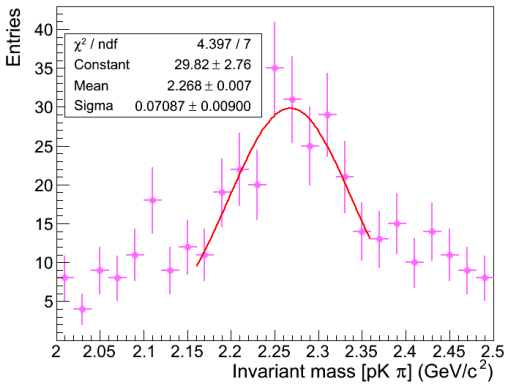

Figure 2.42: [pKπ] invariant mass distribution of correlated background candidates (4–6 GeV/c) with 3 tracks from a common D meson decay. The distribution is fitted with a Gaussian function.

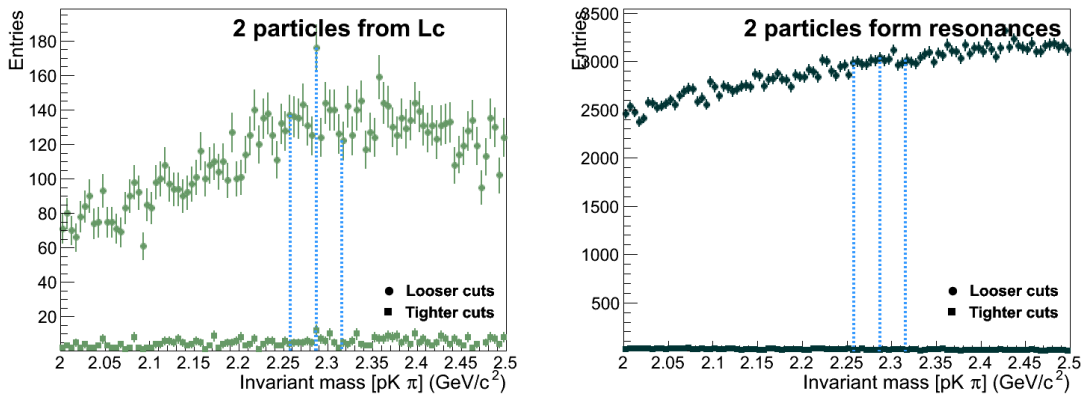

Figure 2.43: [pKπ] invariant mass distribution of correlated background candidates (4–6 GeV/c) with two of the tracks originating from a Λ_c (left) or from a resonance decay (right).

Table 2.5: Ratio of the considered background sources to the Λ_c signal in the range $M_{\Lambda_c} \pm 3\sigma$. Signal and background were evaluated with the same selection cuts in the range $4 < p_t < 6$ GeV/c.

Background source	Ratio to Λ_c signal (M_{Λ_c})$\pm 3\sigma$)
2 tracks from same D	4
3 tracks from same D	0.1
2 tracks from same Λ_c	1
2 tracks from same resonance	50

Table 2.6: Breakdown of the systematic uncertainty of the various Λ_c measurements (the symbol $\oplus$ indicates quadratic sum).

Contribution	Systematic uncertainty (%)					
	$N^{\text{Pb–Pb}}_{\Lambda_c}$	$N^{\text{pp}}_{\Lambda_c}$	R_{AA}	$(\Lambda_c/\text{D}^0)_{\text{Pb–Pb}}$	$(\Lambda_c/\text{D}^0)_{\text{pp}}$	$\frac{(\Lambda_c/\text{D}^0)_{\text{Pb–Pb}}}{(\Lambda_c/\text{D}^0)_{\text{pp}}}$
Tracking efficiency	12	12	12$\oplus$12	4	4	4$\oplus$4
PID	7	7	7$\oplus$7	5	5	5$\oplus$5
Yield extraction	5	5	5$\oplus$5	5$\oplus$1	5$\oplus$1	5$\oplus$1$\oplus$5$\oplus$1
MC correction	8	8	8$\oplus$8	8$\oplus$8	8$\oplus$8	8$\oplus$8$\oplus$8$\oplus$8
MC p_t shape	2	2	2$\oplus$2	2$\oplus$2	2$\oplus$2	2$\oplus$2$\oplus$2$\oplus$2
Feed-down	20	10	17	20$\oplus$3	10$\oplus$3	17$\oplus$3$\oplus$3
B.R.	26	26	0	26$\oplus$1	26$\oplus$1	0
Total (excl. B.R.)	26	26	30	25	18	27
Total (incl. B.R.)	37	37	30	36	32	27

In Figure 2.41 the invariant mass distributions of the background candidates in the interval $4 < p_t < 6$ GeV/c with 2 tracks coming from the same D meson are shown. Within the statistical uncertainties, the distributions have a smooth shape without structures in the Λ_c mass region, shown as a 2.286 GeV/$c^2 \pm 3\sigma$ band (where $\sigma = 8$ MeV/c^2 is the expected mass resolution for this p_t interval). Figure 2.42 shows the background candidates with all the three tracks are coming from a common D meson decay. In this case, a structure roughly centered at the Λ_c mass is present. However, a Gaussian fit indicates that the structure is about 10 times broader than the Λ_c signal distribution (≈ 70 MeV/c^2 vs. 8 MeV/c^2). In Figure 2.43 the background contributions given by two tracks coming from Λ_c (left panel) or resonances (right panel) decays are reported. Both distributions are smooth within statistical fluctuations.

In Table 2.5 the contribution of each of the considered sources is quantified in terms of its ratio to the Λ_c signal in the range $M_{\Lambda_c} \pm 3\sigma$. Signal and background were evaluated with the same selection cuts in the

range $4 < p_t < 6$ GeV/c and the yields were corrected for the branching ratios of the decays that were forced in the simulation. The only background source that features a clear structure at the Λ_c mass (3 tracks from the decay of the same D meson) has a total yield 10 times smaller than that of the Λ_c signal, in addition to being much broader in invariant mass. This large suppression factor is most likely induced by the PID selection: one of the three tracks is required to be compatible with a proton; since D mesons do not decay to protons, at low and intermediate p_t this selection is very efficient in the rejection of this kind of background.

2.3.5.4 Considerations on Systematic Uncertainties

Since Λ_c production was not measured in Pb–Pb so far, the estimation of the systematic uncertainty is made on the basis of the "experience" with D meson measurements and of the uncertainties expected for the D^0 case (Section 2.3.3.2). In the following, the different contributions are discussed, first for the Λ_c cross section, and then for the R_{AA} and the Λ_c/D^0 ratio. A summary is given in Table 2.6.

Yield extraction After the subtraction of the uncorrelated background with event-mixing, the correlated contributions are left. In the previous section it was shown that these are not expected to affect significantly the signal extraction via an invariant mass fit. Therefore, we assume that the yield extraction has the same systematic uncertainty as for the D^0 analysis.

Tacking efficiency Due to the presence of three prongs we assumed three times the single track uncertainty (4%).

PID efficiency For this analysis tight PID cuts are applied for two tracks, the kaon and the proton. We, therefore, assume twice the systematic uncertainty expected for the D^0 analysis, where tight cuts are applied on one track (kaon).

Selection efficiency This correction has turned out to be of the same order for D^0, D^+ and D^{*+} analyses; we assume that it will be similar for the Λ_c.

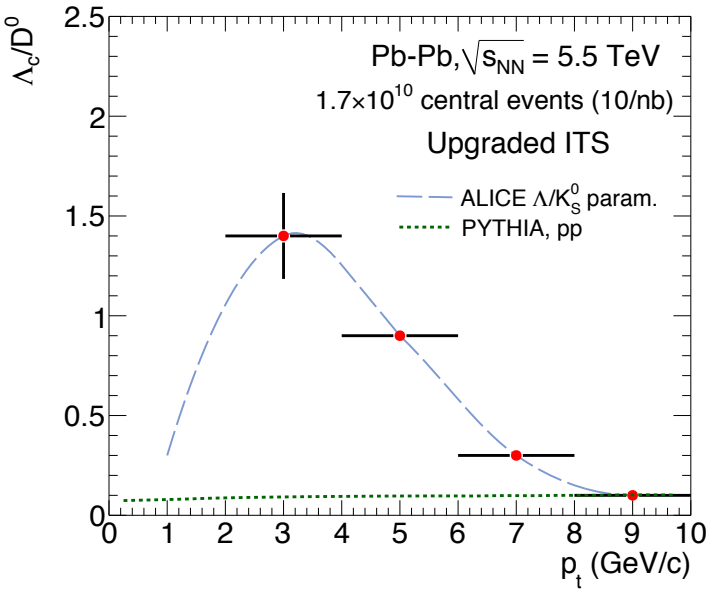

Figure 2.44: Estimated statistical uncertainties on the measurement of the Λ_c/D^0 ratio using 1.7×10^{10} central Pb–Pb collisions (0–20%), corresponding to an integrated luminosity of 10 nb^{-1}. The points are drawn on a line that captures the trend and magnitude of the Λ/K^0_S ratio (see Figure 2.4). The expectation from the PYTHIA 6.4.21 generator [66] for Λ_c/D^0 in pp collisions (7 TeV) is also shown.

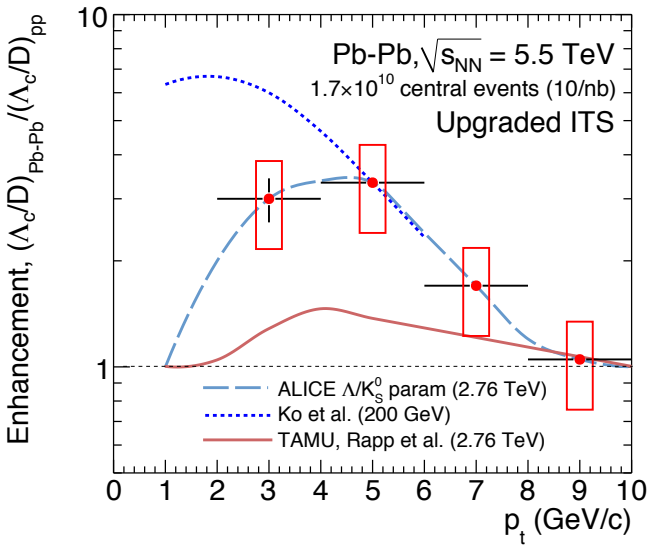

Figure 2.45: Enhancement of the Λ_c/D ratio in central Pb–Pb (0–20% for $L_{int} = 10$ nb^{-1}) with respect to pp collisions. Two model calculations [29, 33] are also shown.

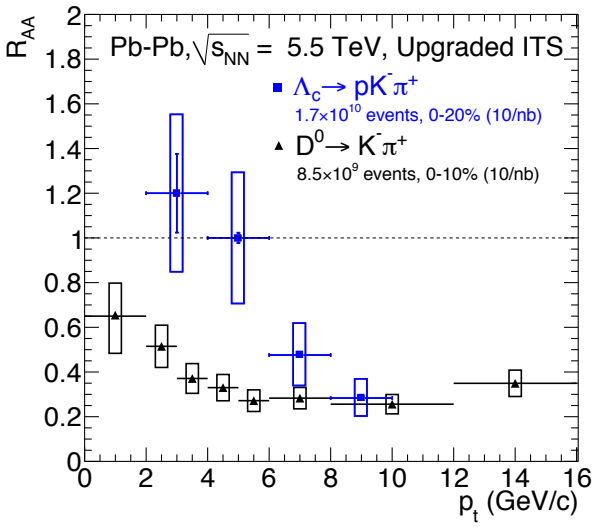

Figure 2.46: Λ_c and D^0 R_{AA} in central Pb–Pb collisions (0–20% for Λ_c, 0–10% for D^0) for $L_{int} = 10$ nb^{-1}.

Feed-down from Λ_b decays We assume a systematic uncertainty similar that on *D* mesons with the current data [50]. Due to the low signal-to-background ratio, it is unlikely that, even in the high-rate scenario, the feed-down contribution can be estimated using the impact parameter fit technique as planned for D mesons (see Section 2.3.4). Therefore, we plan to proceed as it is done on the current data for the D analyses, that is, to rely on an hypothesis on the Λ_b production. For the Pb–Pb case, this implies an assumption on the Λ_b R_{AA}. If there will not be any Λ_b measurement available in Pb–Pb, we will base our hypothesis on the measurement of the B R_{AA}, varying the Λ_b/B ratio in a reasonable range, e. g. $1 < R_{AA}(\Lambda_b)/R_{AA}(B) < 2$ (similar to that of the Λ/K^0 R_{AA} ratio). If the fraction of secondary Λ_c is kept at the level of 10–15%, similar to the current values of D analyses, it is likely that the overall uncertainty is contained within about 20%.

Branching ratio (B.R.) This is the uncertainty from [67].

In the case of ratios (Λ_c R_{AA} and Λ_c/D^0), some contributions to the systematic uncertainty cancel. In particular, does the tracking efficiency in case of the Λ_c/D^0 ratio for two of the three tracks. This is not assumed in the case of R_{AA} because of the different collision environments. In the R_{AA} and the double ratio $\frac{(\Lambda_c/D^0)_{Pb-Pb}}{(\Lambda_c/D^0)_{pp}}$, the branching ratio uncertainties cancel.

2.3.5.5 *Performance for the Measurement of Baryon/Meson Ratio and* R_{AA}

Figure 2.44 shows the expected statistical uncertainties for the measurement of the Λ_c/D^0 ratio using 1.7×10^{10} central Pb–Pb collisions (0–20%), corresponding to an integrated luminosity of 10 nb^{-1}. The points are drawn on a line that captures the trend and magnitude of the Λ/K^0_S ratio (see Figure 2.4). The systematic uncertainty is not shown, because it is affected by the 26% uncertainty on the branching ratio of $\Lambda_c \to pK\pi$. The expectation from the PYTHIA 6.4.21 generator [66] for Λ_c/D^0 in pp collisions (7 TeV) is also shown.

Figure 2.45 shows the enhancement of the Λ_c/D ratio in central Pb–Pb (0–20% for $L_{int} = 10$ nb^{-1}) with respect to pp collisions. Statistical and systematic uncertainties (from Table 2.6) are shown. It is assumed that the statistical uncertainties for the D^0 measurements (see Figure 2.27-left) and for the Λ_c measurement in pp (see discussion in Section 2.5) are negligible with respect to those for the Λ_c measurement in Pb–Pb. The points are drawn on a line that captures the trend and magnitude of the Λ/K^0_S double-ratio. The two model calculations presented in Figures 2.5 [33] and 2.6 [29] are shown to illustrate the expected sensitivity of the measurement.

Figure 2.46 shows the Λ_c R_{AA} as a function of p_t in central Pb–Pb collisions (0–20%) for $L_{int} = 10$ nb^{-1}. Also in this case, it is assumed that the statistical uncertainties for the Λ_c measurement in pp are negligible with respect to those in Pb–Pb. The values of R_{AA} at which the points are drawn are obtained combining Figures 2.27-left and 2.45. The prompt D^0 R_{AA} (from Figure 2.27) is also shown, for comparison.

2.3.6 Outlook: Ongoing Studies

2.3.6.1 *Reconstruction of* D_s^+ *Mesons*

As discussed in detail in Section 2.2.1, the study of the D_s^+ production in heavy-ion collisions allows one to measure the effects of the strangeness enhancement on charmed-strange mesons, which is predicted to play a role in the intermediate transverse momentum region (up to a factor 2 enhancement of D_s^+/D) [28, 33, 34]. D_s^+ mesons and their antiparticles ($c\tau \approx 150$ μm) are reconstructed in ALICE in the decay chain $D_s^+ \to \phi\pi^+$ (and its charge conjugate) followed by $\phi \to K^-K^+$. The branching ratio of the chain $D_s^+ \to \phi\pi^+ \to K^-K^+\pi^+$ is $2.28 \pm 0.12\%$ [67].

In order to reduce the large combinatorial background, D_s^+ candidates are selected according to topological cuts, e.g. decay length, invariant mass of the reconstructed ϕ meson and the cosine of the pointing angle, which is the angle between the reconstructed D_s^+ meson momentum and the line connecting the primary and secondary vertex. A crucial role in the background rejection is played by the particle identification, which is based on measurement of the specific energy loss, dE/dx, from the TPC and the time-of-flight from the TOF detector. Compatibility cuts are applied on the difference between the measured signals and those expected for a pion or a kaon. The PID selection provides a background rejection of a factor 20–30 at low p_t, as shown in Figure 2.47 for the p_t intervals 3–4 and 4–6 GeV/c.

The D_s^+ p_t-differential cross section was measured in pp collisions at $\sqrt{s} = 7$ TeV in the p_t range from 2 to 12 GeV/c with a statistical significance of 4–5 depending on the transverse momentum [76]. Preliminary results for Pb–Pb collisions at 2.76 TeV in the centrality range 0–7.5% show a significance of 3–4 in the interval 4–12 GeV/c [32].

In order to address the performance for D_s^+ measurements with *high-rate* capabilities and the upgraded ITS, we have carried out two first studies, described in the following:

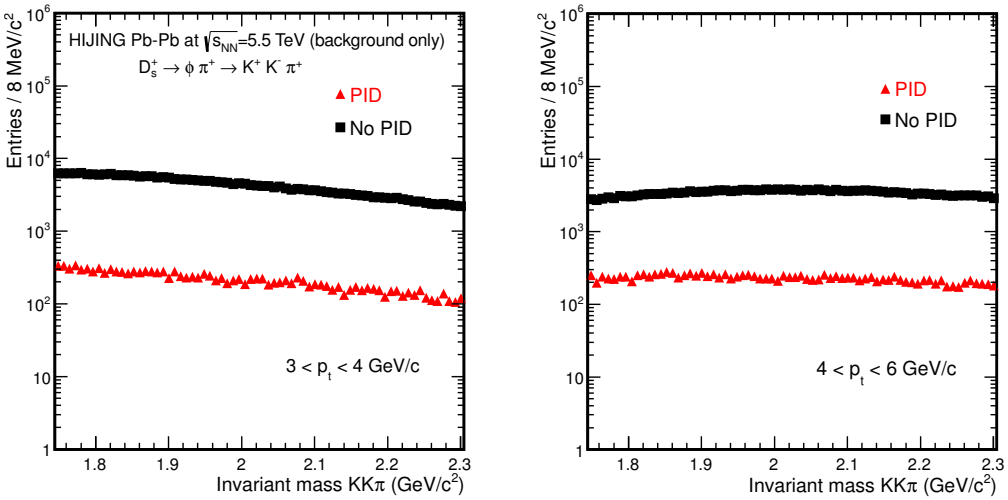

Figure 2.47: Background distributions of D_s^+ candidates in two p_t intervals, 3–4 and 4–6 GeV/c with and without PID selection applied.

Table 2.7: Statistical significances expected for the D_s^+ measurement for central Pb–Pb events (0–7.5%), for the 2011 sample and scaled to two scenarios of integrated luminosity.

Integrated luminosity	Significance		
	p_t interval (GeV/c)		
	4–6	6–8	8–12
28 μb^{-1} (Pb–Pb 2011) [32]	4.0 ± 1.0	3.3 ± 0.9	4.2 ± 0.9
0.1 nb^{-1} (in 1 GeV/c bins)	7	5	5
10 nb^{-1} (in 1 GeV/c bins)	70	50	50

– Effect of *high-rate* capabilities: extrapolation of the performance on the 2011 Pb–Pb data sample to the target integrated luminosity after LS2.

– Effect of upgraded ITS: preliminary study based on simulation with the *Hybrid* approach.

Effect of high-rate capabilities

We present here an estimate of the expected statistical significance for the two scenarios of integrated luminosity: 0.1 nb^{-1} (*no high-rate*) and 10 nb^{-1} (*high-rate*). The values have been obtained by scaling with the square root of the number of the events the significances of the 2011 Pb–Pb data.

In Table 2.7 the statistical significance in the centrality range 0–7.5% is presented for different p_t intervals. The calculation assumes the signal extraction performed in bins of 1 GeV/c. The scaled significances are 5–7 and 50–70, for the two cases of integrated luminosity, equivalent to a statistical uncertainty associated to the measurement of about 20% in the *no-high rate* scenario and of about 2% in the *high-rate* scenario.

Recent theoretical calculations [28] indicate that the measurement of D_s^+ elliptic flow can provide interesting information concerning the effects of diffusion in the hadronic phase. In these calculations, the v_2 of D_s^+ mesons is predicted to be reduced by 30–40% in the intermediate p_t region with respect to that of non-strange D mesons. Also in this case, in order to appreciate this difference, a very precise measurement is required. We provide here an estimation of the statistical significances expected for the

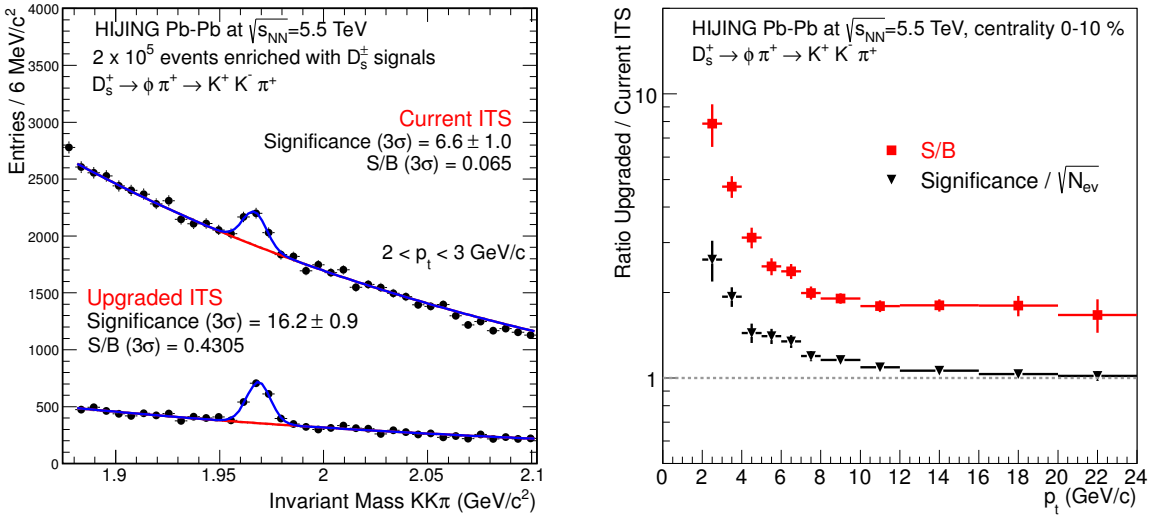

Figure 2.48: Left: example of [KKπ] invariant mass distribution in a charm-enriched MC sample analyzed with the *Hybrid* approach. Right: D_s^+ statistical significance and signal-to-background ratio with upgraded ITS divided by the values obtained with the current ITS, as a function of p_t.

v_2 measurements starting from the first preliminary results of signal extraction in the centrality range 20–40% obtained on the 2011 Pb–Pb data sample. In the two scenarios of integrated luminosity (0.1 and 10 nb^{-1}), the significances expected in the p_t range 3–5 GeV/c are about 7–8 and 70–80, respectively, for p_t bins of 1 GeV/c. The values for the *no high-rate case* are not sufficient to perform a φ-differential analysis and obtain a precise measurement of v_2.

We conclude that both the analyses, R_{AA} and v_2, would largely benefit from the high statistics provided by the *high-rate* upgrade of the ALICE central barrel.

Effect of upgraded ITS with improved resolution

The performance in terms of significance and S/B ratio has been studied with the current and upgraded ITS configurations, applied via the *Hybrid* approach. HIJING simulations for Pb–Pb collisions in the centrality range 0–10% were used, with additional D_s^+ signals embedded to increase the statistics. An example of [KKπ] invariant mass distribution in the range $2 < p_t < 3$ GeV/c is shown in Figure 2.48 (left). In right-hand panel of the same figure, the significance and the signal-to-background ratio with upgraded ITS divided by the values obtained with the current ITS are presented in the p_t range 2–24 GeV/c. A large increase of both significance and S/B is observed in the low-intermediate momentum region with the upgraded detector. This result is particularly promising, since in this p_t range a very precise measurement is required to distinguish between different theoretical models. The study will be soon extended down to zero p_t.

2.3.6.2 *Full Reconstruction of* B *Mesons in the Channel* $B^+ \to \overline{D}^0\pi^+$

With the ITS upgrade the full kinematic reconstruction of beauty hadrons may become accessible for the first time in high-energy nucleus–nucleus collisions. A first feasibility study on the reconstruction of charged B mesons via their decay topology in 0–10% most central Pb–Pb collisions is in progress. The analysis strategy is described in the following. First results should be available in the near future.

We consider the reconstruction of B^+ mesons (and charge conjugates) via the decay chain $B^+ \to \overline{D}^0\pi^+$ (B.R.=0.481%, $c\tau \approx 492\ \mu$m) and subsequently $\overline{D}^0 \to K^+\pi^-$ (B.R.=3.88%, $c\tau \approx 123\ \mu$m) [67]. This

Table 2.8: B meson selection variables.

Selection Variable	Value	Threshold
$d_0^{\mathrm{D}^0} \times d_0^{\pi}$ (cm^2)	-5×10^{-5} to 5×10^{-5}	upper
p_{t}^{π} (GeV/c)	1.0 to 1.5	lower
$p_{\mathrm{t}}^{\mathrm{D}^0}$ (GeV/c)	2.0 to 6.0	lower
L^{xyz} (cm)	0.00 to 0.03	lower
L^{xyz}/σ^{xyz}	0.0 to 3.0	lower
$\cos\left(\theta_{\mathrm{pointing}}\right)$	0.80 to 0.92	lower
$\cos(\theta^{xy}_{\mathrm{pointing}})$	0.91 to 0.98	lower

requires, due to the moderate production yields and the small branching ratios, an efficient selection to enhance the signal-to-background ratio. Due to the large mass of the B meson (5.28 GeV/c^2), the transverse momentum of the decay pion is of the order of 1 GeV/c and thus much higher than the average momentum of inclusive (mostly primary) pions. This allows for a large reduction of the combinatorial background by selecting high p_{t} pions. Further reduction of the background is achieved by reconstructing the secondary vertices of the B^+ and of the D^0 decays, which are separated from the primary vertex by several hundreds of μm.

A first estimate of the expected signal as a function of transverse momentum was derived by scaling the FONLL [69] prediction of B meson production in pp collisions at $\sqrt{s} = 5.5$ TeV by the number of binary collisions:

$$S = R_{\mathrm{AA}}^{\mathrm{B}^+} \times 2 \times \int_{p_{\mathrm{t}}^{min}}^{p_{\mathrm{t}}^{max}} \left(\frac{d\sigma}{dp_{\mathrm{t}}}\right)_{\mathrm{B}^+}^{FONLL} dp_{\mathrm{t}} \times f_{\mathrm{b}\to\mathrm{B}^+} \times \mathrm{B.R.} \times \langle T_{\mathrm{AA}}\rangle^{0-10\%} \tag{2.3}$$

Here, $\langle T_{\mathrm{AA}}\rangle^{0-10\%}$ is the average nuclear overlap function calculated via the Glauber model for the 10% most central collisions. The FONLL prediction of the cross section was scaled with the fragmentation fraction $f_{\mathrm{b}\to\mathrm{B}^+}$ [67] and the branching ratios. The factor 2 accounts for the fact that only particles are considered in the theoretical prediction, whereas particles and antiparticles are reconstructed in the analysis. Further, a range of hypotheses on the nuclear modification in Pb–Pb due to initial state and medium effects was defined. The R_{AA}^{B} has only been measured at high p_{t} in the $\mathrm{B}\to\mathrm{J}/\psi$ channel [54]. For simplicity a constant value of 0.4 was applied in all bins of p_{t}, and an uncertainty of $\pm$50% was taken into account. From this estimate we expect about 6×10^5 B mesons in the considered decay channels with all decay daughters within the acceptance of the ALICE central barrel in 8.5×10^9 Pb–Pb events in the 0-10% centrality class, corresponding to an integrated luminosity of 10 nb^{-1}. This number represents the total number of $\mathrm{B}^{\pm}$ mesons that can be potentially reconstructed. Reconstruction and selection efficiency will decrease this number.

The acceptance-times-efficiency factor, Acc $\times\,\varepsilon$, was computed with the *Hybrid* approach from a dedicated Monte Carlo sample of Pb–Pb collisions, generated with the HIJING 1.36 event generator [68] in the centrality class 0–10% and enhanced heavy-flavour signals from the PYTHIA 6.4.21 generator [66]. With this simulation, a set of the most promising topological and kinematical selection variables was identified. These are: the product of the impact parameters of the B meson daughter particles, which are displaced from the primary vertex, $d_0^{\mathrm{D}^0} \times d_0^{\pi}$, the two and three dimensional $\cos\left(\theta_{\mathrm{pointing}}\right)$ of the B meson, the (normalized) decay length L^{xyz} (L^{xyz}/σ^{xyz}), and the transverse momentum of the daughter particles, $p_{\mathrm{t}}^{\mathrm{D}^0}$ and p_{t}^{π}.

All cuts on the B meson topology and kinematics were kept relatively loose, in order to keep as much signal as possible. Further, a loose set of cuts on the $\mathrm{D}^0\to\mathrm{K}^-\pi^+$ (and c.c.) selection was applied. Thus, the acceptance-times-efficiency factor Acc $\times\,\varepsilon$ is of the order of 10% for p_{t} around 10 GeV/c. Table 2.8 shows the selection variables and the typical cut valus. A detailed optimization of all selection criteria to maximize the significance as a function of p_{t} is currently ongoing. This set of selection variables was

then used to estimate the background $B_{\text{ITS Upgrade}}$:

$$B_{\text{ITS Upgrade}} = \frac{B_{\text{current ITS}}(data)}{B_{\text{current ITS}}(MC)} \times B^{Hybrid}_{\text{ITS Upgrade}}(MC) \tag{2.4}$$

Here, the background determined from data with the current ITS setup was scaled by the background estimated from MC simulations with the *Hybrid* approach, to account for the improved resolution.

On the basis of equations 2.3 and 2.4, the significance of the B measurement can be calculated and scaled to the equivalent of 10 nb^{-1}. Although the study is not yet at a level that allows us to give precise numbers here, we have encouraging indications that the signal could be extracted starting from a p_{t} of 5–10 GeV/c. Especially in the low-p_{t} region, a large improvement can still be achieved by tighter tuning of the selection criteria. In addition, other topological selection variables have not yet been studied and can yield an improved reduction of the background. Detailed studies to further maximize the signal significance are ongoing.

2.4 Physics Performance: Low-mass Dileptons

The measurement of low-mass e^+e^- pairs in Pb–Pb collisions at LHC energies poses major experimental challenges. A powerful assessment of the electromagnetic radiation spectrum requires acceptance for dilepton pairs at invariant masses and transverse momenta as low as $M_{\text{ee}} \approx p_{\text{t,ee}} \approx T$. This implies electron detection down to $p_{\text{t}} = 0.1$–0.2 GeV/c. Since the production rates of thermal dileptons are low (suppressed by $\propto \alpha^2$) a very good electron identification is mandatory to suppress combinatorial background from hadronic contamination. Moreover, electrons from π^0 Dalitz decays and photon conversions (mainly from $\pi^0 \to \gamma\gamma$) form a substantial combinatorial background. This demands for a low material budget before the first active detector layer and offline strategies to detect e^+e^- pairs from photon conversions and Dalitz pairs for further rejection. The large combinatorial background prevents also a straight-forward online trigger scheme. Consequently, high data rates need to be handled by the detectors and the readout systems.

These experimental requirements will be fulfilled after the luminosity increase of the LHC, providing Pb–Pb collisions at 50 kHz, and a substantial upgrade of the ALICE detector and readout systems. Moreover, the enhanced low-p_{t} tracking capability of the ITS will allow to track electrons down to $p_{\text{t}} \geq 0.05$ GeV/c (see Chapter 3). This will substantially improve the reconstruction efficiency of photon conversions and Dalitz pairs for combinatorial background suppression.

The improved impact parameter resolution of the upgraded ITS will also enable efficient tagging of electrons from semi-leptonic charm decays, thus allowing to separate the displaced charm contribution from prompt dileptons. This is of particular importance since a measurement of the thermal dilepton yield requires a precise knowledge of the hadronic contributions. These include dileptons from correlated charm decays, which form a substantial physical background and dominate the mass spectrum at $M_{\text{ee}} > 1.1$ GeV/c^2. Suppression of electrons from charm via their impact parameter distribution to the primary vertex will be significantly improved with the upgraded ITS. As a consequence, the systematic uncertainties on the thermal excess yield related to the subtraction of the charm contribution from the inclusive dilepton yield will be reduced.

The main tracking and PID detector for electrons is the TPC, providing particle identification via the measurement of the specific energy loss by ionization, dE/dx. Additional PID information is obtained from the TOF system to suppress hadrons at $p < 3$ GeV/c. Operation at the nominal magnetic solenoid field of $B = 0.5$ T implies that soft particles do not reach the TOF, leading to a drastic efficiency loss for $p_{\text{t}} < 0.4$ GeV/c. Therefore a dedicated running period with a reduced magnetic field of $B = 0.2$ T is foreseen for the measurement of low-mass dileptons. This will improve the acceptance for low-p_{t} electrons in TOF.

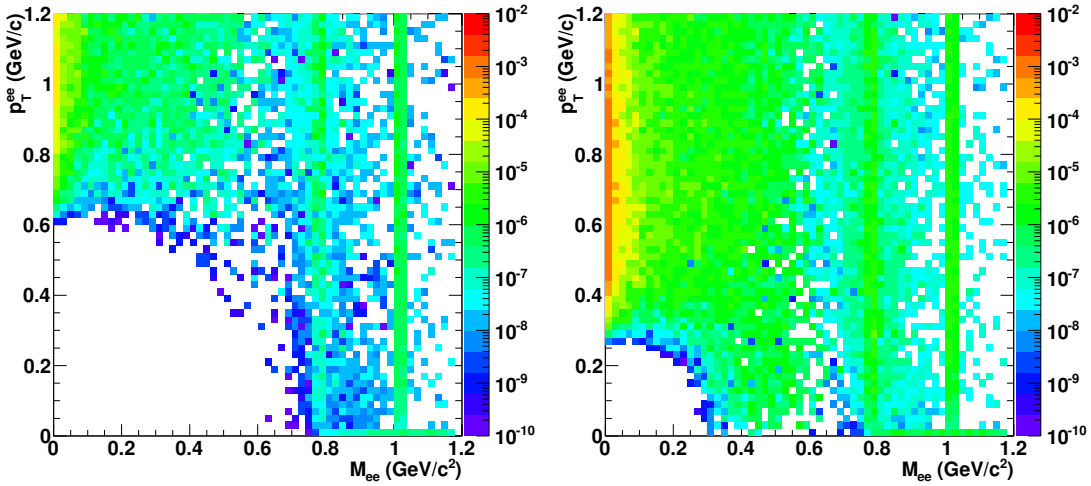

Figure 2.49: Acceptance for e^+e^- pairs from PYTHIA at $B = 0.5$ T (left) and $B = 0.2$ T (right).

The improvement of low-p_t electron reconstruction allows to explore the most interesting kinematic range at low M_{ee} and $p_{t,ee}$. This is illustrated in Figure 2.49, where the dilepton acceptance as a function of M_{ee} and $p_{t,ee}$ is shown for a tracking and PID scheme using ITS, TPC and TOF at $B = 0.5$ T (left) and $B = 0.2$ T (right). While the low-p_t cut-off at $B = 0.5$ T causes a large loss of acceptance at low M_{ee} and $p_{t,ee}$, the acceptance is dramatically improved at $B = 0.2$ T. We therefore foresee a dedicated low-field Pb–Pb run of one month at $B = 0.2$ T for the measurement of low-mass dileptons.

To assess the anticipated significance of a low-mass dilepton measurement with the upgraded ALICE detector in Pb–Pb collisions at $\sqrt{s_{NN}} = 5.5$ TeV, a detailed simulation has been performed. In the following, we consider an experimental setup including the upgraded ITS with 7 pixel layers and an upgraded TPC with continuous readout, operated at $B = 0.2$ T. The upgrade of the TPC increases the readout rate by about a factor 100, allowing to collect all of the 50 kHz delivered by the LHC after the luminosity upgrade. In this case an integrated luminosity $L_{int} \approx 3$ nb^{-1} can be collected in one month. The expected number of events is $2.5 \cdot 10^9$ in the centrality class 0–10%, and $5 \cdot 10^9$ in the class 40–60%. The performances are compared to the current ALICE setup, operated at a magnetic field of $B = 0.2$ T. In this scenario, we expect in a typical one-month heavy-ion run an integrated luminosity $L_{int} \approx 0.03$ nb^{-1}, corresponding to $2.5 \cdot 10^7$ and $5 \cdot 10^7$ Pb–Pb collisions in the centrality classes 0–10% and 40–60%, respectively.

The tracking efficiency for single electrons in $|\eta| < 0.84$ at $B = 0.2$ T is calculated using a detailed simulation, based on the GEANT3 transport code, of the current ALICE apparatus. Electron reconstruction includes charged particle tracking in the ITS and the TPC. Additionally, a TOF signal within $\pm 3\sigma$ of the TOF resolution around the nominal electron position is required. PID information is also included from the TPC, where a $\pm 3\sigma$ band of the dE/dx resolution around the nominal electron peak position is applied. Electron candidates are required to have an associated hit in the innermost layer of the ITS in order to reject electrons from conversions in the detector material. The resulting reconstruction efficiency for single electrons is parametrized as a function of p_t and used for further fast simulations employing different event generators, see left panel of Figure 2.50. Also shown for comparison is the electron efficiency with the current ITS at $B = 0.5$ T.

The improved tracking efficiency of the upgraded ITS has been accounted for by scaling the electron reconstruction efficiency from full simulation for the current apparatus by the p_t-dependent ratio of the ITS efficiency for the upgraded ITS over that for the current ITS, obtained from the Fast Estimation Tool (see Chapter 3). The standalone efficiencies of the current and the upgraded ITS are shown in the right

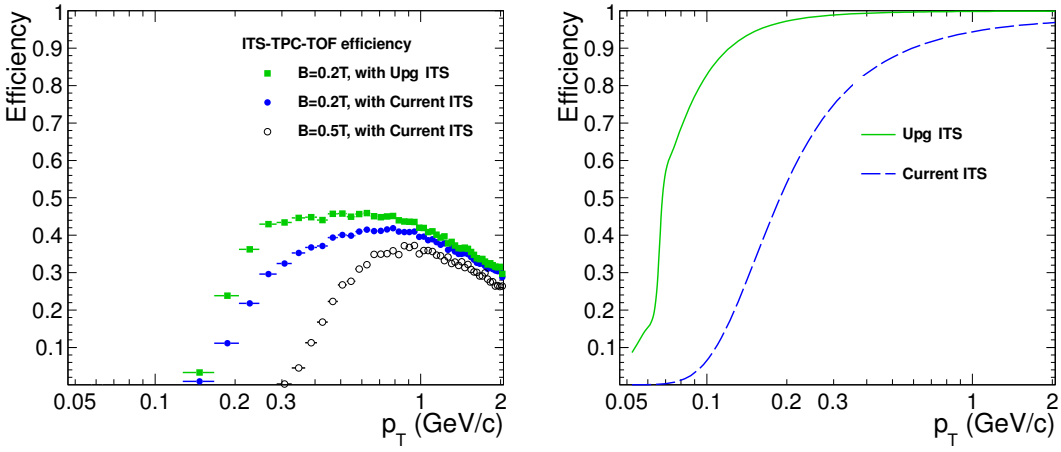

Figure 2.50: Left: Combined ITS-TPC-TOF efficiencies for electrons in $|\eta| < 0.84$ at $B = 0.2$ T for the current ITS (blue circles) and the upgraded ITS (green rectangles) as a function of $p_{\rm t}$. Also shown for comparison is the efficiency with current ITS at $B = 0.5$ T (open circles). Right: Standalone tracking efficiency of the current and the upgraded ITS system.

panel of Figure 2.50 (see Chapter 3 for details). It is furthermore assumed that the performance of the upgraded TPC in terms of tracking efficiency and dE/dx resolution is the same as for the current TPC. The resulting efficiency for electron tracks with upgraded ITS and $B = 0.2$ T is shown in Figure 2.50 (left panel), compared to that for the current ITS and $B = 0.2$ or 0.5 T.

An important feature of the upgraded ITS is the improved capability to separate prompt from displaced electrons. Prompt electrons originate from all thermal sources and decays of the mesons (ρ, ω, ϕ, and the Dalitz decays of π^0, η, η', ω). Displaced electrons include those from semi-leptonic decays of charmed hadrons and conversions in the detector material. The separation is based on the impact parameter (d_0) to the primary vertex in the transverse plane, which can be measured with significantly improved resolution with the upgraded ITS. Figure 2.51 shows the efficiency of displaced electrons from conversions and charm decays for the current and the upgraded ITS system, as a function of the prompt efficiency. While the separation of displaced electrons from charm is significantly improved with the upgraded ITS, there is only a small improvement for conversions. The reason is that the upgraded ITS requires also a new beam pipe with smaller radius, which is the main converter before the first detector layer. The smaller lever arm to the main vertex compensates the improved intrinsic resolution of the upgraded ITS. On the other hand, a tight cut on the d_0 suppresses electrons from charm over prompt electrons by more than a factor 2, implying a suppression of pairs from correlated charm decays by about a factor five over prompt pairs. This improved capability of the upgraded ITS is one of the key features of the ALICE upgrade to enable a measurement of thermal radiation at the LHC despite the large physical background from charm, as will be demonstrated below.

2.4.1 Hadronic Cocktail and Background

A realistic physics input into the simulation of the expected dilepton signal is mandatory in order to achieve a solid estimate of the physics performance. To this end, we compute the dilepton signal composed of the contributions listed below.

The hadronic cocktail includes contributions from the decays of light pseudoscalar and vector mesons. The yield is adjusted to the charged-particle densities: $\langle {\rm d}N_{\rm ch}/{\rm d}\eta \rangle = 1750$ and $\langle {\rm d}N_{\rm ch}/{\rm d}\eta \rangle = 248$ in the centrality classes 0–10% and 40–60%, respectively, for Pb–Pb collisions at $\sqrt{s_{\rm NN}} = 5.5$ TeV. The particle ratios and the spectral shapes are extrapolated from existing heavy-ion data at lower energies.

The contribution from correlated semi-leptonic charm decays is based on calculations from the PYTHIA

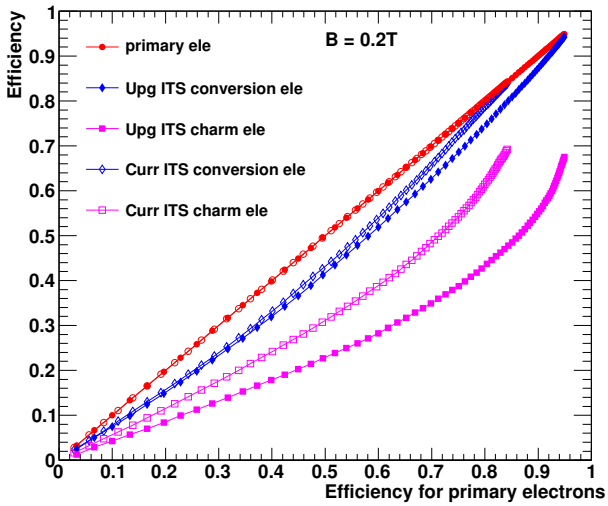

Figure 2.51: Efficiency for electrons from charm (magenta) and conversions (blue) as a function of the efficiency for prompt (primary) electrons, for current ITS (open symbols) and upgraded ITS (full symbols).

event generator. A total charm cross section of $\sigma_{c\bar{c}} = 7.55$ mb in pp at $\sqrt{s}$= 5.5 TeV has been used. This value is derived by interpolation of existing measurements [70, 75, 77, 78]. Around mid-rapidity, a differential cross section $d\sigma_{c\bar{c}}/dy = 1.34$ mb is used, also taken from interpolation. The charm yields are scaled by $\langle N_{\rm coll}\rangle = 1625\,(125)$ for Pb–Pb collisions in the centrality class 0–10% (40–60%).

The calculation of thermal dilepton radiation from the hadronic phase and the QGP is based on a hadronic many-body approach [57] and on perturbative emission rates. Medium-modified spectral functions and a realistic space-time evolution are included [61]. This approach has proven to provide a quantitative description of dilepton data over a wide range of collision energies [56].

With the exception of the π^0, ω and ϕ mass regions, the yield is dominated by the contribution from correlated charm decays. Thermal radiation from the hadronic phase, sensitive to chiral symmetry restoration, dominates over that from QGP in the low-mass window. In turn, QGP radiation outshines the hadronic contribution at $M_{\rm ee} > 1$ GeV/c^2, where information on the early temperature can be extracted. However, in all mass regions an extraction of thermal radiation requires careful subtraction of the contribution from hadronic decays and, in particular, from charm.

The measured raw dilepton yield is dominated by combinatorial pairs of electrons and positrons, which arise from random combinations of tracks from uncorrelated decays, mainly π^0-Dalitz, and from conversions. This combinatorial background contribution can be estimated by means of like-sign pair combinations or event-mixing techniques, and subtracted from the unlike-sign distribution. However, a small signal-to-background ratio (S/B) limits the statistical significance of the signal and a systematic uncertainty can arise from the background subtraction method. To minimize the contribution of combinatorial pairs, leptons from conversions and Dalitz decays must be identified and removed from the sample. To this end, all electrons and positrons from an event are combined in pairs and rejected if they form a "close pair" with small invariant mass ($M_{\rm ee} < 0.05$ GeV/c^2) and small opening angle ($\theta_{\rm ee} < 0.1$). Since leptons from conversions or π^0-Dalitz decays typically have small momentum, the capability of Dalitz and conversion rejection is much enhanced by the improved ITS efficiency for standalone tracking at low $p_{\rm t}$.

In order to estimate the combinatorial background, S/B, and the corresponding significance $1/\sqrt{N_{\rm ev}} \cdot S/\sqrt{S+B}$, we used a sample of simulated pp events with a realistic modeling of conversions via the GEANT3 transport code and a detailed description of the ALICE apparatus. Parametrized efficiencies (see Figure 2.50) for electron and positron tracks are applied. Tracks are rejected if they form a close

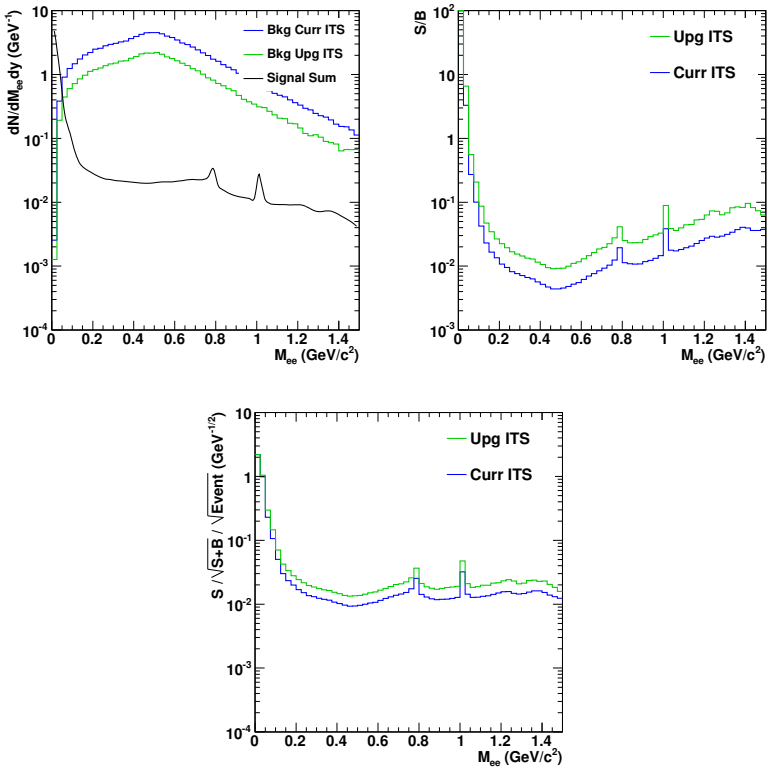

Figure 2.52: Signal and background distributions (left), S/B (middle) and significance per event (right) in 0–10% Pb–Pb collisions at $\sqrt{s_{\rm NN}}$= 5.5 TeV.

pair with any of the other reconstructed lepton tracks, including standalone tracks which are only found in the ITS. In order to mimic the combinatorial background in Pb–Pb, a number of pp events are overlaid to match the corresponding $\langle {\rm d}N_{\rm ch}/{\rm d}\eta \rangle$ in semi-central or central Pb–Pb collisions.

Examples for the expected combinatorial background in central Pb–Pb collisions for the current and upgraded ITS are shown in Figure 2.52. The upgraded ITS improves S/B by a factor 2 with respect to the current ITS.

2.4.2 Systematic Uncertainties

The dominant sources of systematic uncertainties on the dilepton measurement arise from the large combinatorial and physical backgrounds.

The relative systematic uncertainty on the combinatorial background $\Delta B/B$ propagates into the extracted inclusive dilepton signal error as $\Delta S/S = \Delta B/B \cdot B/S$. For the studies below we assume conservatively $\Delta B/B = 0.0025$ which corresponds to the number quoted by the PHENIX collaboration in a similar analysis [79]. The systematic uncertainty on S is calculated bin-by-bin based on the corresponding S/B, as shown in Figure 2.52.

A measurement of the thermal excess yield requires a precise subtraction of the hadronic cocktail and the contribution from charm from the inclusive dilepton yield. For the hadronic cocktail we assume a relative uncertainty of 10%. We note that ALICE has the unique capability to measure π^0 and η down to low $p_{\rm t}$ via conversions [80] and can therefore constrain the uncertainty on the hadronic cocktail.

For the subtraction of the charm contribution a relative systematic uncertainty of 20% is assumed. Also here we note that the yield of correlated dilepton pairs from charm decays can be well constrained by inversion of the d_0 cuts, which enhances the charm contribution, and by the exclusive measurement of

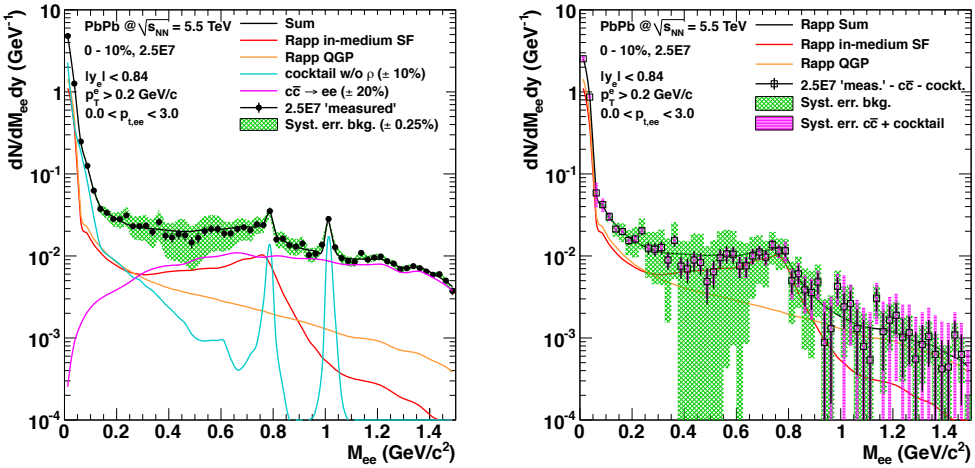

Figure 2.53: Inclusive e^+e^- invariant mass spectrum (left) and excess spectrum (right) for 0–10% most central Pb–Pb collisions at $\sqrt{s_{\rm NN}}$= 5.5 TeV with the current ITS, $2.5 \cdot 10^7$ events (*no high-rate* scenario). No tight d_0 cut is applied. The green boxes show the systematic uncertainties from the combinatorial background subtraction, the magenta boxes indicate systematic uncertainties related to the subtraction of the cocktail and charm contribution.

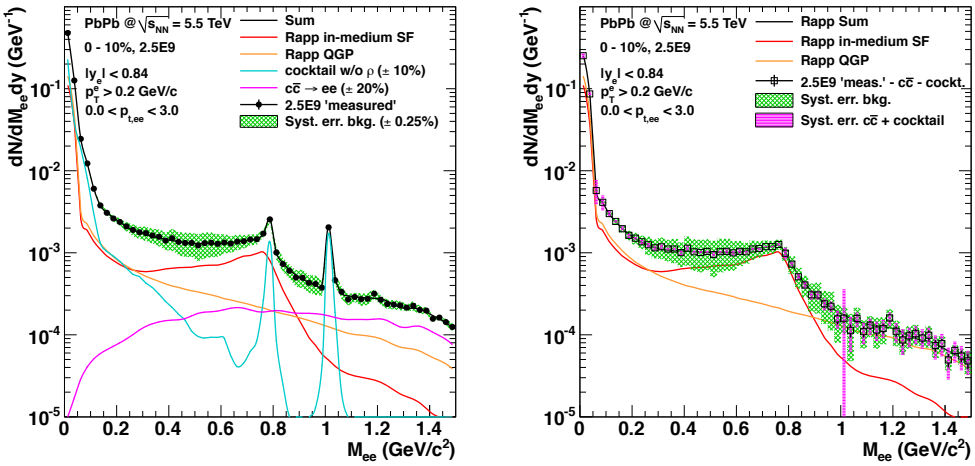

Figure 2.54: Inclusive e^+e^- invariant mass spectrum (left) and excess spectrum (right) for 0–10% most central Pb–Pb collisions at $\sqrt{s_{\rm NN}}$= 5.5 TeV with the upgraded ITS, $2.5 \cdot 10^9$ events (*high-rate* scenario). Tight d_0 cut is applied. The green boxes show the systematic uncertainties from the combinatorial background subtraction, the magenta boxes indicate systematic uncertainties related to the subtraction of the cocktail and charm contribution.

charmed hadrons at low $p_{\rm t}$ with complementary methods in ALICE.

2.4.3 Results on Physics Performance

In the following, the results of the physics performance study described before are discussed. The invariant mass and transverse momentum distributions are not corrected for reconstruction and selection efficiency. They are compared to the physical signals (like thermal radiation) convoluted with the parametrized efficiencies, to give an impression of the sensitivity. It is assumed that the above-mentioned corrections, which have to applied in the data analysis, do not add a significant contribution to the total systematic uncertainty.

Figure 2.53 (left) shows the inclusive e^+e^- invariant mass spectrum in the 0–10% most central Pb–Pb

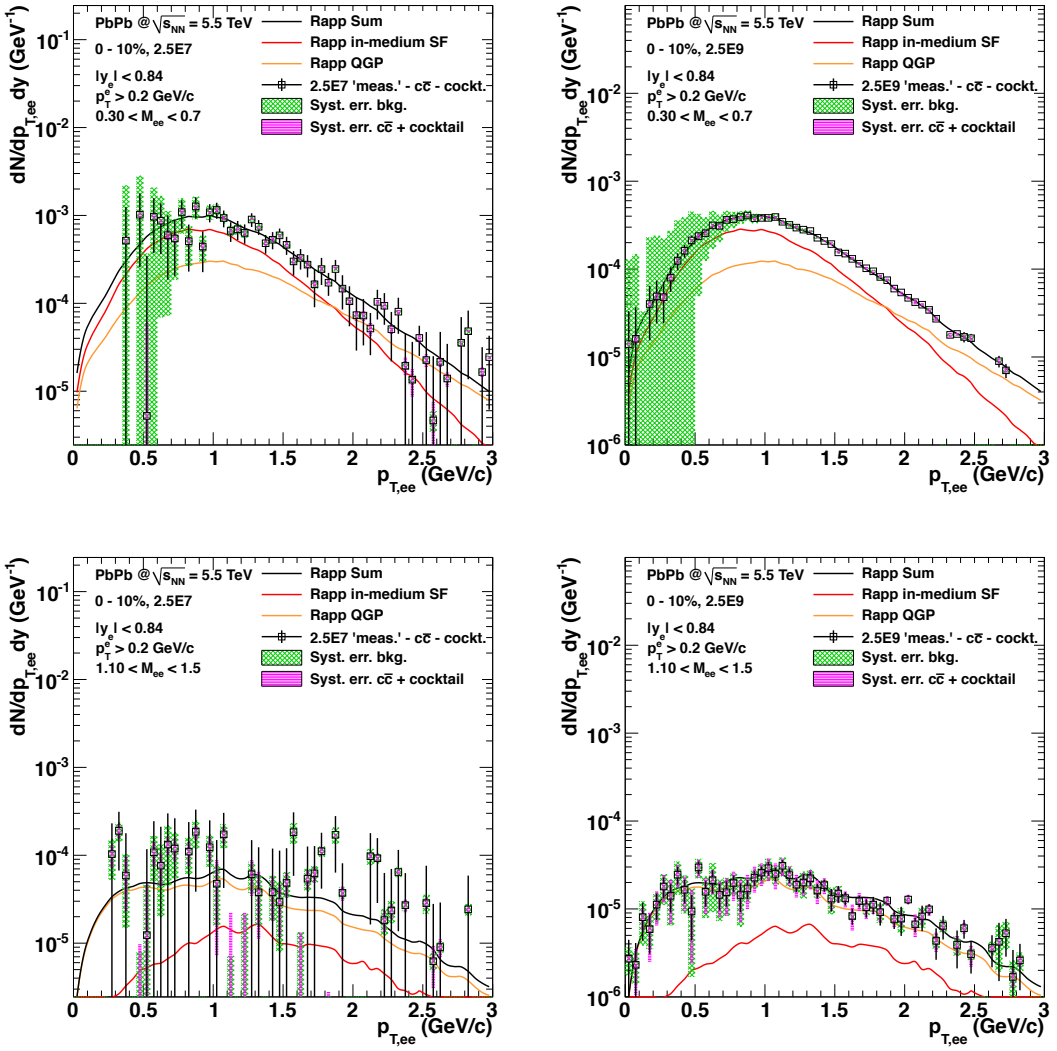

Figure 2.55: Transverse momentum e^+e^- excess spectra in 0–10% most central Pb–Pb collisions at $\sqrt{s_{\rm NN}}$= 5.5 TeV in intervals of invariant mass for current ITS, $2.5 \cdot 10^7$ events, left and upgraded ITS, $2.5 \cdot 10^9$ events, right. Tight d_0 cut is applied. The green boxes show the systematic uncertainties from the combinatorial background subtraction, the magenta boxes indicate systematic uncertainties related to the subtraction of the cocktail and charm contribution.

collisions at $\sqrt{s_{\rm NN}}$= 5.5 TeV with the current ITS and $2.5 \cdot 10^7$ events. No d_0 cut is applied to reject displaced electrons. The same spectrum after subtraction of the hadronic cocktail and the charm contribution (the "excess spectrum") is shown in the right panel of Figure 2.53. The low-mass region $M_{\rm ee} < 1$ GeV/c^2 is dominated by the systematic uncertainties related to the subtraction of the combinatorial background. In the mass region $M_{\rm ee} > 1$ GeV/c^2, the systematic uncertainties from the charm subtraction do not allow for a quantitative estimation of the thermal radiation spectrum.

With the upgraded ITS, a tight d_0 cut is quite effective to reject displaced electrons. In addition, the high-rate capability is a key element for this analysis. The expected inclusive e^+e^- invariant mass spectrum and the excess spectrum in this scenario are shown in Figure 2.54. The statistical precision achievable in the *high-rate* scenario would allow for a detailed and differential investigation of dilepton production.

Transverse momentum spectra provide valuable information on the degree of collectivity of the dilepton sources. Moreover, their mass dependence is related to collectivity in different stages of the collision and

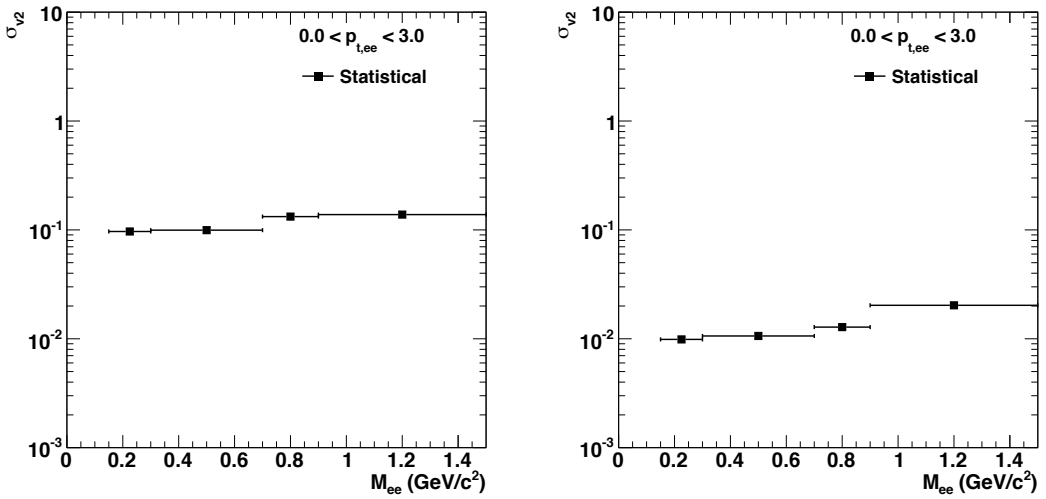

Figure 2.56: Expected absolute statistical uncertainty of the elliptic flow coefficient v_2 of the e^+e^- excess spectrum as a function of M_{ee}. Results are shown for Pb–Pb collisions at 40–60% centrality for current ITS and $5 \cdot 10^7$ events (*no high-rate*) in the left panel and for upgraded ITS and $5 \cdot 10^9$ events (*high-rate*) in the right panel. Tight d_0 cuts are applied.

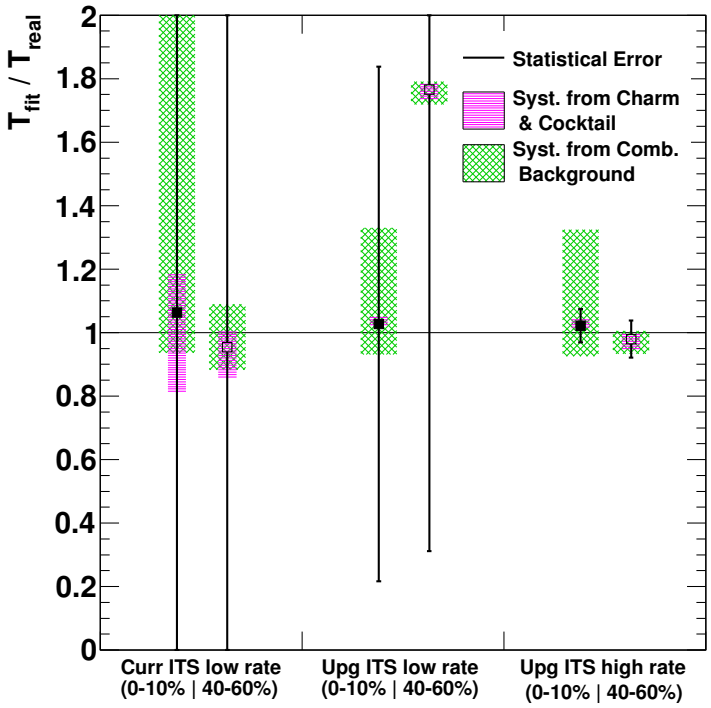

Figure 2.57: Expected relative uncertainty on the extraction of the T parameter from a fit to the invariant mass excess spectrum in $1.1 < M_{\mathrm{ee}} < 1.5$ GeV/c^2 (see text). The results are shown for different scenarios, with tight d_0 cuts, and for 0–10% and 40–60% event centrality. Error bars show the statistical uncertainties. The green boxes show the systematic uncertainties from the combinatorial background subtraction, the magenta boxes indicate systematic uncertainties related to the subtraction of the cocktail and charm contribution.

may give access to partonic flow, if measured at sufficiently high masses. The combination of thermal and collective motion is encoded in the effective temperature parameter $T_{\rm eff}$, which can be extracted from an exponential fit to the excess $p_{\rm t,ee}$ spectra in intervals of invariant mass. Examples of mass-dependent transverse momentum spectra are shown in Figure 2.55.

With the upgraded ITS in the *high-rate* scenario (right panels in Figure 2.55) a detailed measurement of the $p_{\rm t,ee}$ spectra is possible, allowing an extraction of $T_{\rm eff}$, with a statistical precision of the level of $\sigma(T_{\rm eff})/T_{\rm eff} \approx 1\%$.

A more detailed investigation of dilepton collectivity and a possible access to the partonic equation of state is expected from a measurement of the elliptic flow coefficient v_2 as a function of $M_{\rm ee}$. To this end, the physics performance study is extended to semi-central collisions, where elliptic flow is most pronounced. The relative systematic uncertainties in semi-central collisions are smaller than in central collisions, due to larger S/B and smaller relative contribution from charm, due to $\langle N_{\rm coll}\rangle$ scaling. The absolute statistical uncertainties on v_2 as a function of $M_{\rm ee}$ are shown in Figure 2.56 for the current and upgraded ITS scenarios. With the *high-rate* and upgraded ITS scenario, an invariant-mass dependent v_2 measurement with absolute statistical uncertainty of the order of $\sigma(v_2) \approx 0.01$–0.02 can be achieved.

Information on the early temperature of the system can be derived from the invariant-mass dependence of the dilepton yield at masses $M_{\rm ee} > 1$ GeV/c^2. To quantify the sensitivity of the anticipated measurement we employ an exponential fit, $\mathrm{d}N_{\rm ee}/\mathrm{d}M_{\rm ee} \propto \exp(-M_{\rm ee}/T_{\rm fit})$, to the simulated spectra in the invariant mass region $1 < M_{\rm ee} < 1.5$ GeV/c^2. The fit parameter $T_{\rm fit}$ is compared to $T_{\rm real}$ which is derived from the same fit to the thermal input spectrum. The ratio $T_{\rm fit}/T_{\rm real}$ for Pb–Pb collisions in the 0–10% and 40–60% centrality classes is shown in Figure 2.57. Only the *high-rate* scenario with upgraded ITS allows for a precise measurement of the slope parameter in the relevant $M_{\rm ee}$ range, with statistical and systematic uncertainties of about 10%.

2.5 pp Running for Heavy-Flavour Reference Data

We have studied the requirements for the proton–proton reference data to be used to investigate QGP-effects in heavy-flavour production. In particular:

- the beauty-to-charm suppression ratio $R_{\rm AA}^{\rm feed-down}/R_{\rm AA}^{\rm prompt\,D}$ requires the measurement of the production cross section of prompt and secondary D mesons;
- the search for the enhancement of the baryon-to-meson ratio for charm requires, in addition, the measurement of the $\Lambda_{\rm c}$ production cross section.

The requirements in terms of both integrated luminosity and centre-of-mass energy are assessed.

2.5.1 pp Integrated Luminosity

We start from the consideration that the statistical uncertainty on the pp reference has to be negligible with respect to that of the Pb–Pb measurement, e.g. $\sqrt{2}$ times smaller (so that the combined relative statistical uncertainty is about 20% larger than the Pb–Pb uncertainty). Since the relative statistical uncertainty is the inverse of the statistical significance $1/\mathscr{S} = \sqrt{S+B}/S$, the requirement is:

$$\mathscr{S}_{\rm pp} = \sqrt{2}\cdot\mathscr{S}_{\rm Pb-Pb}\,. \tag{2.5}$$

This condition leads to different requirements in terms of statistics, depending on the S/B ratio, thus on the background level. The two extreme cases are the following.

– *High-background measurements* (this is the case for charm production measurement, particularly at low transverse momentum): $S \ll B$, thus $\mathscr{S} = S/\sqrt{B}$, and the condition becomes

$$S_{\rm pp}/\sqrt{B_{\rm pp}} = \sqrt{2}\cdot S_{\rm Pb-Pb}/\sqrt{B_{\rm Pb-Pb}}$$

thus

$$N_{\rm pp} = 2\cdot N_{\rm Pb-Pb}\cdot[(\mathscr{S}/\sqrt{N})_{\rm Pb-Pb}/(\mathscr{S}/\sqrt{N})_{\rm pp}]^2$$

with N the number of events in pp and Pb–Pb (in a given centrality class, e.g. 0–20%).

– *Background-free measurements* (this is the case e.g. for jets): $S \gg B$, thus $\mathscr{S} = \sqrt{S}/S = 1/\sqrt{S}$, and the condition becomes

$$S_{\rm pp} = 2\cdot S_{\rm Pb-Pb}$$

thus

$$N_{\rm pp} = 2\cdot N_{\rm Pb-Pb}\cdot[(S/ev)_{\rm Pb-Pb}/(S/ev)_{\rm pp}] \approx 2\cdot N_{\rm Pb-Pb}\cdot\langle N_{\rm coll}\rangle$$

assuming approximate scaling of the signal per event with the number of binary nucleon–nucleon collisions; for central Pb–Pb events ($\langle N_{\rm coll}\rangle \simeq 1500$):

$$N_{\rm pp} \simeq 3\cdot 10^3\cdot N_{\rm Pb-Pb,0-10\%}\,.$$

For the D meson production measurements performed with pp and Pb–Pb data collected in 2010 [50,70], the ratio of $(\mathscr{S}/\sqrt{N})_{\rm Pb-Pb}/(\mathscr{S}/\sqrt{N})_{\rm pp}$ was about 5–7 depending on $p_{\rm t}$ (considering Pb–Pb collisions in the centrality class 0–20%). Therefore, the condition above would give $N_{\rm pp} = 25$–$50\,N_{\rm Pb-Pb}$. The analysis was carried out with 300 million pp events and 3 million central Pb–Pb events, thus a ratio of 100. Indeed, the statistical uncertainty on the pp reference was much smaller (by a factor 2 typically) than that on Pb–Pb.

In the following, we estimate the required reference statistics for low-$p_{\rm t}$ charm measurements (*High-background case*)[5].

For the case of $\rm D^0 \to K^-\pi^+$ reconstruction, we have estimated the value of $\mathscr{S}/\sqrt{N}$ (significance per event) for pp collisions with the upgraded ITS using the following procedure.

– We started from the value of $\mathscr{S}/\sqrt{N}$ obtained on pp data at $\sqrt{s} = 7$ TeV from the 2010 run [70].

– We assumed that the signal/event is the same with the upgraded ITS. This is justified by the observation that the efficiency is the same with current and upgraded ITS, for the same cut values (see Figure 2.24).

– We assumed that the background/event is reduced, with the upgraded ITS, in pp by the same factor as in Pb–Pb, i.e. a factor about 5 (see Figure 2.25-left).

The left-panel of Figure 2.58 shows $\mathscr{S}/\sqrt{N}$ for pp collisions for current ITS (from [70]) and upgraded ITS. The right-panel of the same Figure shows $\mathscr{S}/\sqrt{N}$ for upgraded ITS in central Pb–Pb collisions (from Figure 2.25-right) and in pp collisions. The ratio $(\mathscr{S}/\sqrt{N})_{\rm Pb-Pb}/(\mathscr{S}/\sqrt{N})_{\rm pp}$ is about 5. Therefore, the required number of pp events is about 50 times the number of central Pb–Pb events that will be used for the $\rm D^0$ analysis.

[5] For completeness, we work out the numbers also for the *Background-free case*: the condition $N_{\rm pp} \simeq 3\cdot 10^3\cdot N_{\rm Pb-Pb,0-10\%}$ is equivalent to $L_{\rm int,pp}\sigma^{\rm inel}_{\rm pp} \simeq 3\cdot 10^3\cdot L_{\rm int,Pb-Pb}\cdot 10\%\cdot\sigma^{\rm hadronic}_{\rm Pb-Pb}$. Thus, using $\sigma^{\rm inel}_{\rm pp} = 70$ mb and $\sigma^{\rm hadronic}_{\rm Pb-Pb} = 7$ b, $L_{\rm int,pp} = 3\cdot 10^4\,L_{\rm int,Pb-Pb}$. Hence, $L_{\rm int,pp} = 300$ pb^{-1} for $L_{\rm int,Pb-Pb} = 10$ nb^{-1}. For example, this luminosity can be integrated in 10^7 s at a rate of 2 MHz.

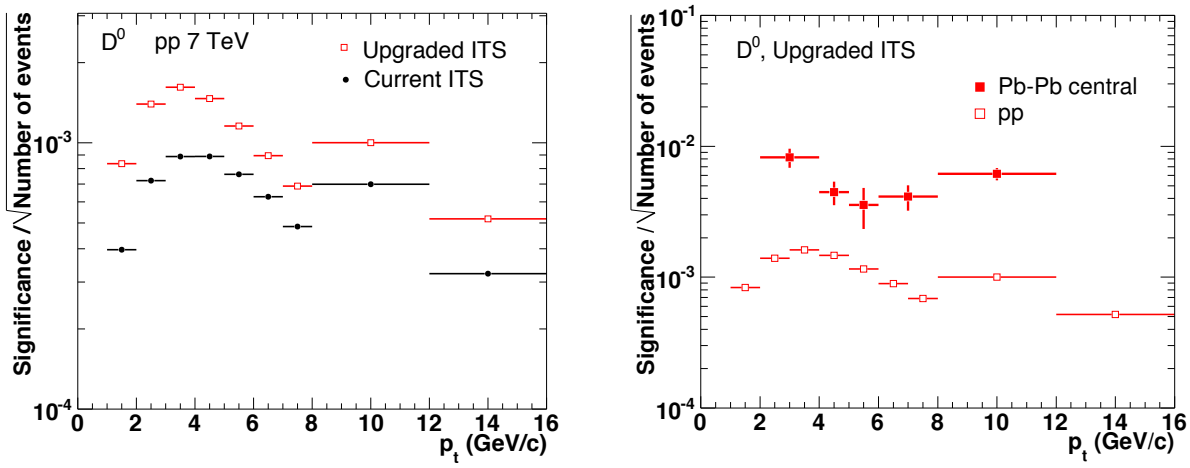

Figure 2.58: Significance/event for D^0 reconstruction in pp collisions. Left: $\mathscr{S}/\sqrt{N}$ for pp collisions for current ITS (from [70]) and upgraded ITS. Right: $\mathscr{S}/\sqrt{N}$ for upgraded ITS in central Pb–Pb collisions (from Figure 2.25-right) and in pp collisions.

Table 2.9: Summary of required proton–proton integrated luminosity.

Measurement	Pb–Pb $L_{\rm int}$	pp $L_{\rm int}$
D^0	10 nb^{-1}	6 pb^{-1}
D^0	2 nb^{-1}	1.2 pb^{-1}
Λ_c	10 nb^{-1}	0.6 pb^{-1}

If the Pb–Pb analysis will be carried out with 10 nb^{-1} (about $8\cdot10^9$ events in the centrality class 0–10%), the required reference pp sample is about $4\cdot10^{11}$ events, corresponding to $L_{\rm int,pp}\approx 6$ pb^{-1}. This sample can be collected in 10^6 s at 400 kHz, for example. If the D^0 analysis in Pb–Pb will be carried out with 2 nb^{-1} (about $1.5\cdot10^9$ events in the centrality class 0–10%), the required reference pp sample is about $8\cdot10^{10}$ events, corresponding to $L_{\rm int,pp}\approx 1.2$ pb^{-1}. This sample can be collected in 10^6 s at 80 kHz, for example.

For the case of $\Lambda_c\to {\rm pK}^-\pi^+$ reconstruction, since the measurement was not yet carried with pp data, we base our considerations on different arguments. The possible enhancement of the ratio $\Lambda_c/{\rm D}$ will have to be studied in Pb–Pb collisions as a function of centrality, in comparison with the pp reference. Since the significance/event for Λ_c reconstruction is expected to be larger for more peripheral collisions (see Figure 2.39), the case of the most peripheral centrality class (e.g. 60–80%) dictates the required precision of the pp reference. We assume, conservatively, that the significance/event in pp will be the same as in peripheral Pb–Pb collisions, $(\mathscr{S}/\sqrt{N})_{\rm Pb-Pb,periph.}/(\mathscr{S}/\sqrt{N})_{\rm pp}=1$. Thus, the required pp statistics is $N_{\rm pp}=2\cdot N_{\rm Pb-Pb}$. With $L_{\rm int,Pb-Pb}=10$ nb^{-1}, the number of events in a centrality class covering 20% of the hadronic cross section is $1.7\cdot10^{10}$. Therefore, $N_{\rm pp}\approx 4\cdot10^{10}$, corresponding to $L_{\rm int,pp}\approx 0.6$ pb^{-1}. This sample can be collected in 10^6 s at 40 kHz, for example.

The integrated luminosity requirements are summarized in Table 2.9.

2.5.2 pp Centre-of-Mass Energy

After the second long shut-down (LS2), the LHC is foreseen to accelerate the hadron beams at the nominal energy of $Z/A\cdot 7$ TeV, and the collision centre-of-mass energy will be $\sqrt{s}=14$ TeV for pp and $\sqrt{s_{\rm NN}}=5.5$ TeV for Pb–Pb. If the pp reference data are collected at 14 TeV, the charm and beauty production cross sections have to be scaled to the Pb–Pb energy, in order to define the nuclear modification factors $R_{\rm AA}(p_{\rm t})$. The scaling factors can be obtained using perturbative QCD calculations, like

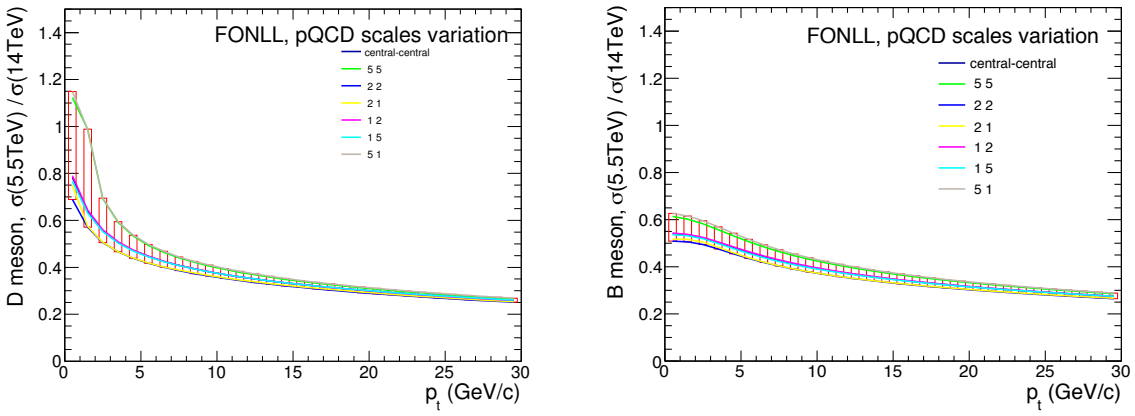

Figure 2.59: Scaling factors for D (left) and B (right) mesons from $\sqrt{s} = 14$ to 5.5 TeV using FONLL.

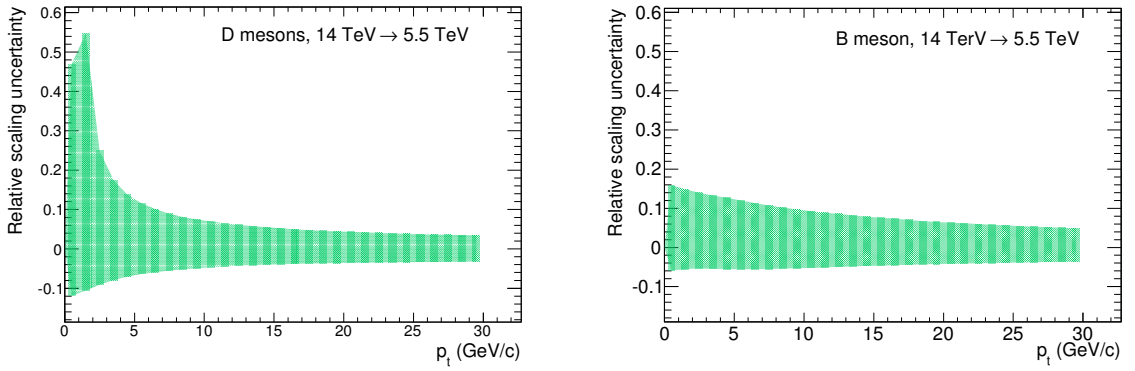

Figure 2.60: Relative scaling uncertainty for D (left) and B (right) mesons.

FONLL [69], as it was already done for the first measurement of the D meson R_{AA} [50]. The definition of the scaling factor and of its theoretical uncertainty are described in detail in [81] for the case of $\sqrt{s} = 7$ TeV and 2.76 TeV. The uncertainty is constructed from the envelope of the scaling factors obtained by varying the values of the perturbative scales (for factorization μ_F and renormalization μ_R) independently within the ranges $0.5\,m_{\mathrm{t}} < \mu_{F,R} < 2\,m_{\mathrm{t}}$ (m_{t} is the transverse mass of the heavy quark), with the constraint $0.5 < \mu_F/\mu_R < 2$. Figure 2.59 shows these envelopes for D mesons (left) and B mesons (right). The corresponding relative uncertainties are shown in Figure 2.60. For the case of D mesons at low p_{t}, the uncertainty is larger than 50% ($p_{\mathrm{t}} < 2$ GeV/c). This would be the dominant uncertainty in the measurement of the D meson nuclear modification factor and of the beauty-to-charm double-ratio $R_{\mathrm{AA}}^{\mathrm{feed-down}}/R_{\mathrm{AA}}^{\mathrm{prompt\,D}}$ (see Figure 2.34) at low p_{t}. Therefore, the reference pp data should be collected at the same centre-of-mass energy as the Pb–Pb data.

Chapter 3

Detector Functional Requirements

3.1 Introduction

In this chapter we will discuss the functional requirements of the new ITS in order to achieve the physics performance which has been assessed in the previous chapter. The ITS upgrade aims to improve (*i*) the resolution of the track impact parameter by a factor 3 or better (at p_t =1 GeV/c) with respect to the present ITS, (*ii*) the stand-alone tracking capability with a momentum resolution of a few percents up to 20 GeV/c, and (*iii*) the readout rate capabilities.

The tracking performance has been studied using an analytical method, referred to as the "Fast Estimation Tool" (FET) which has been further developed into a Fast Monte Carlo Tool (FMCT). The FET provides accurate determination of the tracking resolution (both for the spatial and the momentum components) as a function of the detector configuration. It can also provide an estimate of the tracking efficiency. The outcome of this study is the definition of a baseline new configuration, referred to as "upgraded ITS" in this document. The particle identification performance has been studied with an independent approach.

The robustness of the new layout will be discussed by studying how the key performance of the detector would be degraded in the event of a dramatic reduction of the detector efficiency (one dead layer). There will also be a discussion of the performance of a few different configurations, which are obtained from the baseline configuration by changing the material budget and/or the intrinsic resolution and position of the layers.

3.2 Performance of the present ITS detector

The present ITS detector consists of six cylindrical layers of silicon detectors based on three different technologies. Moving outwards from the interaction region, there are two layers of Silicon Pixel Detector (SPD), two layers of Silicon Drift Detector (SDD) and two layers of double sided Silicon Strip Detector (SSD). The main parameters of the layers (radial position, length along beam axis, number of modules, spatial resolution) and material budget are summarized in Table 3.1. The material budget reported in the table takes into account the ϕ-averaged material (including sensors, electronics, cabling, support structures and cooling) associated with radial paths through each layer. Another 1.30 % of X_0 comes from the thermal shields and supports installed between SPD and SDD barrels and between SDD and SSD barrels, thus making the total material budget for perpendicular tracks equal to 7.66 % of X_0.

Figure 3.1 shows the impact parameter resolution as a function of the transverse momentum in central Pb–Pb collisions for ITS-TPC combined tracking and requiring 6 ITS clusters per track. The resolutions in the bending plane ($r\phi$) and in the longitudinal direction (z) are shown in the left and right panels, respectively.

Table 3.1: Characteristics of the six ITS layers, the beam-pipe and the thermal shields

Layer / Type	r [cm]	$\pm z$ [cm]	Number of modules	Active area per module $r\phi \times z$ [mm^2]	Intrinsic resolution [μm] $r\phi$	z	Material budget X/X_0 [%]
Beam pipe	2.94	-	-	-	-		0.22
1 / pixel	3.9	14.1	80	12.8×70.7	12	100	1.14
2 / pixel	7.6	14.1	160	12.8×70.7	12	100	1.14
Th. shield	11.5	-	-	-	-		0.65
3 / drift	15.0	22.2	84	70.2×75.3	35	25	1.13
4 / drift	23.9	29.7	176	70.2×75.3	35	25	1.26
Th. shield	31.0	-	-	-	-		0.65
5 / strip	38.0	43.1	748	73×40	20	830	0.83
6 / strip	43.0	48.9	950	73×40	20	830	0.83

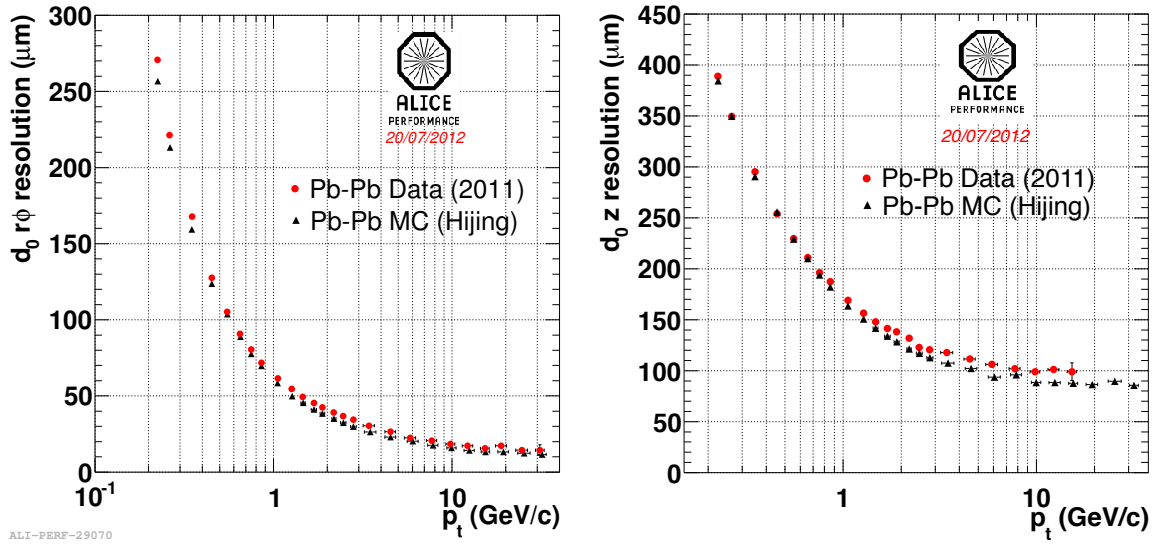

Figure 3.1: Impact parameter resolution of the present ITS versus p_t, for the $r\phi$ (left panel) and z (right panel) components. Reconstructed tracks have been selected requiring successful refit in ITS and 6 ITS clusters per track.

In Figure 3.2 the relative p_t resolution is shown as a function of p_t for ITS stand-alone and ITS-TPC combined tracks, which have been selected requiring 6 ITS clusters per track. The p_t resolution provided by the ITS stand-alone is about 6 % for tracks with $p_t < 2$ GeV/c. Due to the smaller lever arm and the limited number of points, this is worse by about an order of magnitude with respect to the ITS-TPC combined tracks. In the ITS stand-alone mode the p_t resolution reaches the value 10 % at $p_t = 10$ GeV/c.

In Figure 3.3 the ITS stand-alone tracking efficiency is shown as a function of p_t for Monte Carlo Pb–Pb central collisions. The efficiency is defined as the number of "good" refitted tracks (i.e. tracks with ≥ 3 associated clusters and without any fake associated cluster from another track) divided by the number of "trackable" particles. A "trackable" particle has been defined as a particle with at least three reconstructed clusters on three different ITS layers and at least one of the reconstructed points on one of the three innermost layers. The definition of trackable particles using reconstructed clusters instead of *potential* hits, for example GEANT energy deposit, has been preferred in order to separate the algorithmic tracking efficiency from other inefficiency sources. In the plot of Figure 3.3 the ideal case of the ITS detector with all modules 100 % efficient has been considered.

The four layers equipped with drift and strip detectors provide a measurement of the specific energy

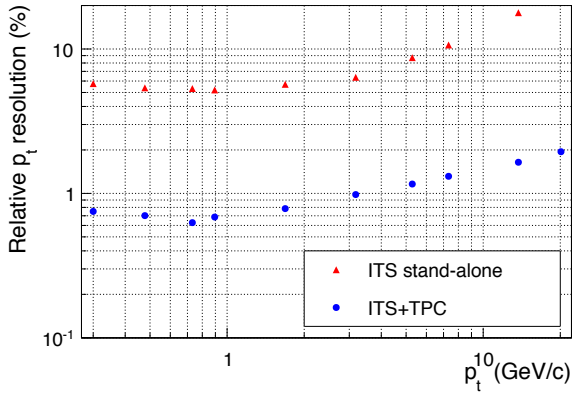

Figure 3.2: ITS stand-alone relative p_t resolution compared to ITS-TPC combined resolution in the p_t range $[0.3, 30]$ GeV/c [82].

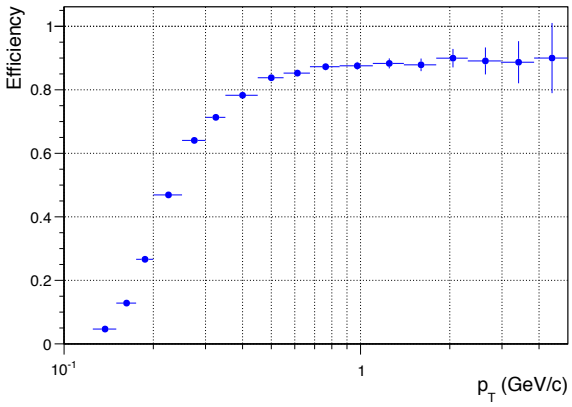

Figure 3.3: ITS stand-alone tracking efficiency as a function of p_t obtained in a Monte Carlo simulation of central PbPb collisions without any ITS dead module.

loss, dE/dx, which can be used for particle identification. The energy loss measurement in each layer is corrected for the track length in the sensitive volume using the tracking information. In the case of SDD clusters, a linear correction is applied to account for the dependence of the reconstructed raw charge on the drift length due to the combined effect of charge diffusion and zero suppression. For each track, the dE/dx is calculated using a truncated mean: the average of the lowest two points, in case four points are measured, or a weighted sum of the lowest (weight 1) and the second lowest point (weight 1/2), in case only three points are measured. Figure 3.4 shows the truncated mean dE/dx for a sample of ITS stand-alone tracks along with a parametrization of the most probable value [83] based on the Bethe-Bloch formula.

We conclude this section by reporting the performance of the ITS detectors in terms of readout rate capabilities. Table 3.2 lists the readout time and maximum event readout rate under the assumption of no back pressure from the DAQ network. It should be noted that the readout time of the three ITS detectors depends only marginally on the detector occupancy and, therefore, is very similar for p-p and Pb-Pb events.

3.3 Experimental conditions assumed in the simulation

Beam pipe: The present beam pipe is 4.82 m long with a central part made of a straight beryllium tube of length 3.95 m, wall thickness 0.8 mm and outer radius 29.8 mm [84]. For the ALICE upgrade, the

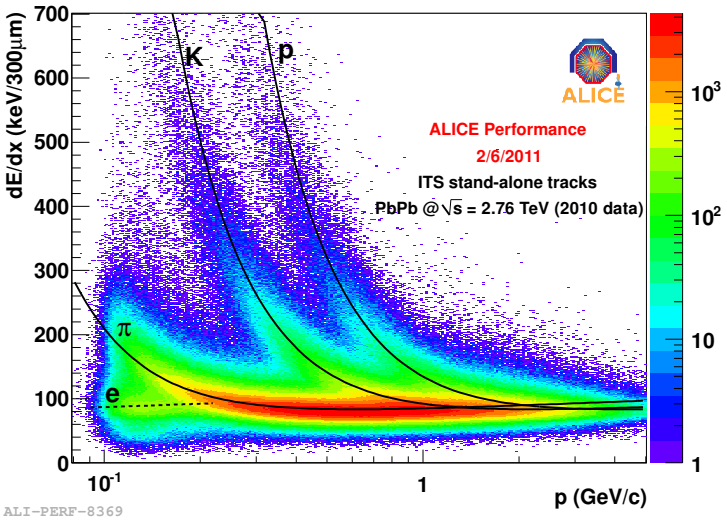

Figure 3.4: Specific energy loss $\mathrm{d}E/\mathrm{d}x$ as a function of the momentum measured with the ITS stand-alone in Pb–Pb collisions. The lines are a parametrization of the detector response based on the Bethe-Bloch formula.

Table 3.2: Readout time and maximum rate, assuming 100% dead time, of the ITS sub-detectors.

detector	R/O time (μs)	Max. rate (Hz)
SPD	296	3300
SDD	1023	985
SSD	310	3265

baseline scenario includes the installation of a new beam pipe with a wall thickness of 0.8 mm and an outer radius of 19.8 mm. See Section 5.4 for a detailed discussion.

Particle load: The charged particle density in central Pb–Pb collisions at the top LHC energy determines the maximum density of particles in the different detector layers and consequently the occupancy per layer and in the individual channels. A relevant contribution to the hit density in a given layer comes from secondary particles, which are mostly produced in the interaction of other particles with the material of the beam pipe and of the inner layers.
By extrapolating the measured charged particles in central Pb–Pb collisions at $\sqrt{s_{NN}} = 2.76$ TeV using the $s_{NN}^{0.15}$ scaling [85] one obtains $\mathrm{d}N_{\mathrm{ch}}/\mathrm{d}\eta \simeq 1970$ for central Pb–Pb collisions at $\sqrt{s_{NN}} = 5.5$ TeV. Based on a Monte Carlo simulation for central Pb–Pb collisions, which uses the HIJING generator tuned to such a charged particle multiplicity, the hit density of both primary and secondary charged particles has been estimated. The number of secondary particles depends on the actual material budget distribution. For the study of the "particle load", the material budget has been assumed conservatively to be the same as the present ITS. In Figure 3.5 the total hit density due to the charged particles produced in a central Pb–Pb collision at the top LHC energy is shown as a function of z for three radial positions.

An additional contribution to the overall particle load comes from the electromagnetic interactions of the crossing ions, among which the dominant process in terms of cross section is the $\mathrm{e}^+\mathrm{e}^-$ pair production [86, 87]. These will be referred to as QED electrons. The cross section of single pair production (about 220 Kb) is about 98 % of the total cross section. The flux of these electrons through the detectors which are close to the beam pipe can be rather high [88]. The flux of QED electrons was estimated by means of a Monte Carlo generator implemented in the AliRoot framework [89]. The results are illustrated in Figure 3.6.

Table 3.3 summarizes the expected maximum hit densities for primaries, secondaries and QED electrons.

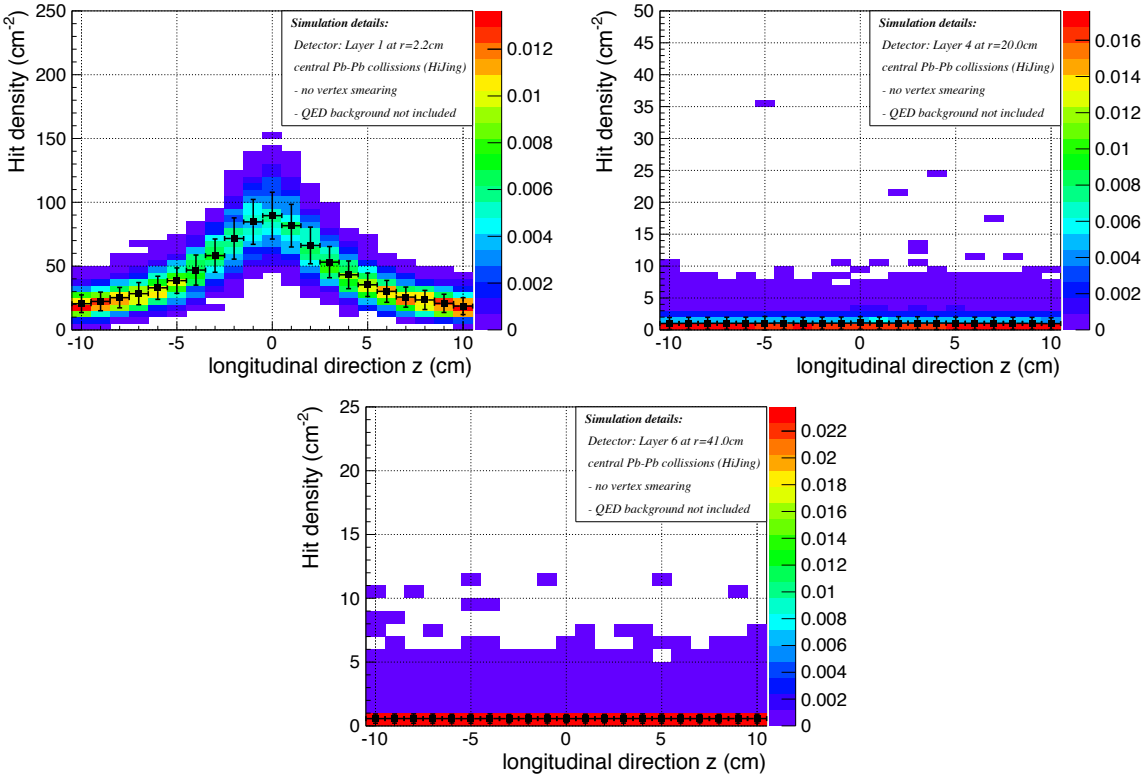

Figure 3.5: Local hit density in Pb–Pb collisions at top LHC energy as a function of the the longitudinal coordinate z for cylindrical layers at radial distance of 2.2 cm (top-left panel), 20 cm (top-right panel) and 41 cm (bottom panel). The points and error bars show respectively the average hit density and the corresponding RMS due to statistical fluctuations. The palette (color) scale shows the frequency profile of the distribution of the hit density at a given z. A magnetic field of 0.5 T and the material budget distribution of the present beam pipe and ITS have been assumed.

Table 3.3: Expected hit densities in central Pb–Pb collisions (including secondaries produced in the materials) and QED electrons for different integration times. Interaction rates of 50 (and 8) kHz and a 0.5 T magnetic field have been assumed.

Radius (cm)	Primary and secondary particles per event (cm^{-2})	QED electrons for τ=100 ns (cm^{-2})		QED electrons for τ=1 μs (cm^{-2})		QED electrons for τ=50 μs (cm^{-2})	
		8 kHz	50 kHz	8 kHz	50 kHz	8 kHz	50 kHz
2.2	74.05	0.022	0.137	0.220	1.374	10.99	68.71
2.8	45.71	0.014	0.085	0.136	0.848	6.79	42.42
3.6	27.65	0.008	0.051	0.082	0.513	4.11	25.66
20.0	0.90	0.000	0.002	0.003	0.017	0.13	0.83
22.0	0.74	0.000	0.001	0.002	0.014	0.11	0.69
41.0	0.21	0.000	0.000	0.001	0.004	0.03	0.20
43.0	0.19	0.000	0.000	0.001	0.004	0.03	0.18

The latter contribution depends on the detector integration time. The values reported in the table refer to the radial position of the layers for the ITS upgrade scenario under study (see Section 3.5.2).

Detector acceptance: This study focuses on the central rapidity region and therefore the detector has been assumed to have a barrel geometry. The ITS acceptance has been determined based on its matching with the current external barrel detectors. For physics studies which require an extended coverage at

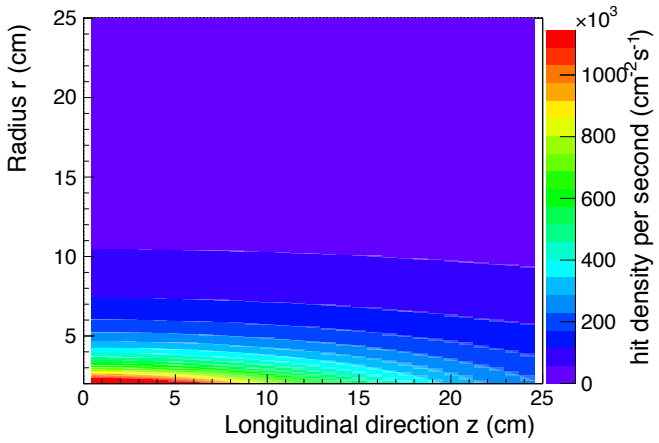

Figure 3.6: Flux density of QED electrons (the number of QED electrons per cm^2 and per second) in Pb–Pb running at top LHC energy at an interaction rate of inelastic collisions of 50 kHz (for the designed interaction rate of 8 KHz, a linear scaling factor can be applied). The local flux density is shown as a function of the radial distance r and the longitudinal coordinate z assuming the ALICE magnetic field of 0.5 T. The material budget distribution of the present beam pipe and ITS has been assumed.

forward rapidities, additional layers with an end-cap like geometry are more suited, in particular at large radii.

In Figure 3.7 a cut view of the ALICE TPC, TOF, TRD and EMCAL detectors is shown; the polar angles of the lines from the nominal Interaction Point (IP) to the most external corners of these detectors are also indicated. The acceptance of the TPC, for tracks traversing its full radial extension, corresponds to $|\eta| < 0.92$. The TRD and TOF have the same acceptance as the TPC, while the EMCAL acceptance is smaller. The line for tracks traversing half of the TPC radial extension is drawn, because the TPC can efficiently reconstruct also these tracks. In the latter case the acceptance of the TPC extends to $|\eta| < 1.22$. So far we have considered the acceptance for tracks emitted from the nominal IP. However, in the Pb–Pb interactions at $\sqrt{s_{NN}} = 5.5$ TeV the luminous region would spread around the nominal IP with a longitudinal Gaussian distribution with $\sigma_z^{\rm lumi} = 5.61$ cm [90]. The requirement of accepting all tracks within a given η range from this luminous region determines the longitudinal length of each ITS layer. In Figure 3.8 we plot the half-length of the barrel as a function of the distance from the beam, assuming $|\eta| < 0.92$ or $|\eta| < 1.22$ for tracks originating from the nominal IP ($z_{vtx} = 0$) and from vertices within $|z_{vtx}| < \sigma_z^{\rm lumi}$ and $|z_{vtx}| < 1.39\sigma_z^{\rm lumi}$ (90% of the total). In the following sections, we assume for the acceptance of the upgraded ITS the condition corresponding to 90% of the luminous region and a pseudo-rapidity coverage of $|\eta| < 1.22$.

Number and radius of layers: The optimization of the detector parameters has been studied by considering primarily the stand-alone performance and monitoring that the efficiency of the track matching from the TPC to the ITS stays at an excellent level in the ITS-TPC combined tracking mode.

The performance have been studied considering a 7-layer layout, made of a combination of pixel (hybrid and/or monolithic) and/or strip layers.

Material budget: Based on the most recent developments in pixel detector technologies, which will be discussed in detail in the next chapter, a substantial reduction of the material budget can be achieved by reducing the thickness of the silicon detector components, i.e. sensor and front-end electronics in case of hybrid pixel, and the material budget of the services (mechanical support, cooling system, read-out system). We will show in Section 3.5.1 the effect of the material budget of the first layer (varying X/X_0 between 0.3 % and 0.9 %) on the track impact parameter resolution. For the remaining layers the same material budget as in the current ITS (see Table 3.1) will be assumed for this particular study.

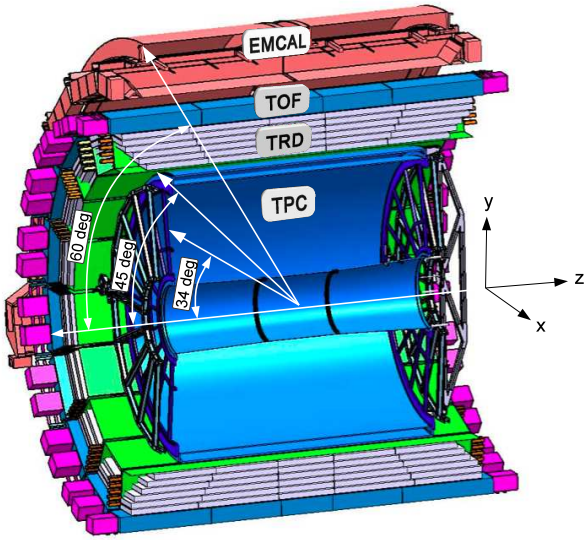

Figure 3.7: ALICE cut view along the yz-direction. The lines drawn from the nominal Interaction Point (IP) indicate the acceptance of the TPC for tracks traversing the whole (45^o) or half (34^o) of its radial extension. The EMCAL acceptance is also indicated.

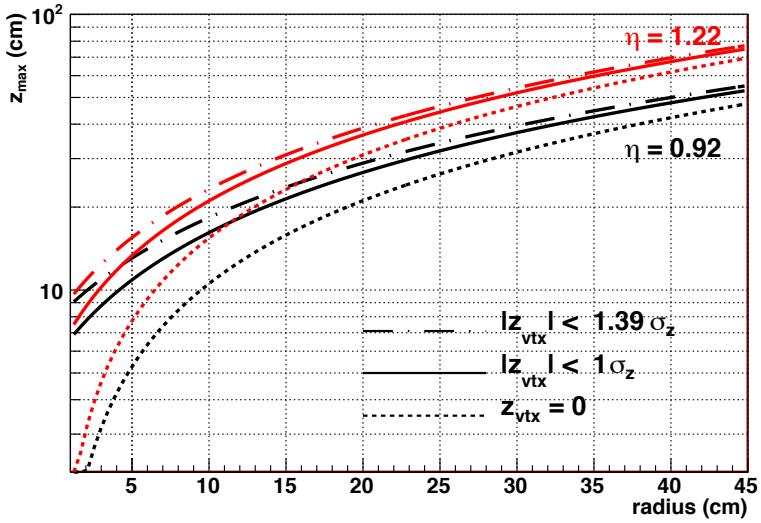

Figure 3.8: Half-length of the barrel (z_{max}) versus the radial distance from the beam to provide acceptance in η within 0.92 (in black) and 1.22 (in red) for tracks originating from the nominal IP (dotted lines), and for all events with vertices within $\pm\sigma_z^{\rm lumi}$ (68.5% of the events, full lines) and $\pm 1.39\sigma_z^{\rm lumi}$ (90% of the events, dash-dotted lines).

Detector segmentation: The segmentation of the detector determines the intrinsic spatial resolution of the reconstructed track points. As an example, in the case of an ideal digital detector, the resolution is given by $d/\sqrt{12}$, where d is the size of the elementary cell in that direction. A small segmentation of the detector is also important to keep the occupancy at a low value. An excellent resolution of the first layer is fundamental for the resolution of the impact parameter at high $p_{\rm t}$ where the effect of the multiple scattering becomes negligible. For the outer layers, a good resolution is also important to improve the $p_{\rm t}$ resolution and the tracking efficiency in the ITS stand-alone mode. In our studies we have assumed an

intrinsic spatial resolution of 4 μm in both $r\phi$ and z. For the outermost layers, the option of 20 (830) μm spatial resolution in $r\phi$ (z) is also considered, corresponding to the expected performance in case they are equipped with strip detectors.

3.4 Simulation Tools

Two simulation methods were developed: a semi-analytical Fast-Estimation-Tool (FET) and an extension of this method, called the Fast Monte Carlo Tool (FMCT). These tools were validated against the performance of the current ITS design as well as against each other for an ITS upgrade scenario. A detailed Monte Carlo (MC) method, based on transport codes and fully integrated within the AliRoot code [91], is also beeing developed. It provides results compatible with those of the FET and FMCT, the residual small differences being due to not yet fully optimized tracking in the MC method, which requires an appropriate local reconstruction. The results presented in the following are thus based on the FET and FMCT. A more detailed description of all tools can be found in [92].

The FET is based on a "Toy-Model" tool originally developed by the STAR HFT collaboration [6]. It allows a simplified description of the detector layout and adopts a tracking method as described in in [93]. The simplest model of a central barrel detector is a combination of cylindrical layers with the properties of radius r, radiation length X/X_0, and the intrinsic detector resolution in the $r\phi$ and z components ($\sigma_{r\phi}$, σ_z). The intrinsic (or cluster) resolution of a layer largely depends on the cell-size of the detection layer that corresponds to the segmentation of the cylinder. It is taken into account in the method by determining the magnitude of the covariance matrix elements at the various stages of the tracking. Furthermore, the traversed material and the cluster resolution depend on the inclination angle of the charged particle with respect to the layer normal. The original "Toy-Model" was extended and adapted in various ways in order to answer the key questions of the ITS upgrade proposal, which include the ITS upgrade stand-alone tracking capabilities. For example, the tracking code itself was replaced with the Kalman technique [94], which is implemented in the standard ALICE software framework [91]. A detailed description of the method and its extensions can be found in [92].

A further evolution of this method, called the Fast Monte Carlo Tool (FMCT), allows the estimation of the tracking performance from the reconstruction of a probing particle embedded in the background as expected from collisions. In contrast with the FET, the FMCT is able to disentangle the performance of a detector layout from the efficiency of specific track-finding algorithms. This is done by accounting for the competition between the track candidates of different length and quality, and represents an approach much closer to that of the full MC based simulation and reconstruction.

Both methods have been validated against the pp and Pb–Pb data sample collected by ALICE. As an example, Figure 3.9 shows the official ITS performance plots with superimposed results from the FET calculations using the current ITS layout (see Table 3.1).

In Figure 3.10 a comparison between the the FET and FMCT is shown for the current and an "upgraded ITS" layout (the latter as described in Section 3.5.2).

3.5 Upgrade scenario

3.5.1 Impact parameter resolution

The performance of a vertex detector, in particular its capability to separate secondary vertices of heavy flavour decays from the main interaction vertex, is determined by the impact parameter resolution (σ_{d_0}). This is the convolution of the primary vertex resolution and the track pointing resolution. For Pb–Pb collisions the uncertainty on the primary vertex position, whose determination is based on a large number of reconstructed tracks, is negligible with respect to that of the track spatial position, and therefore the

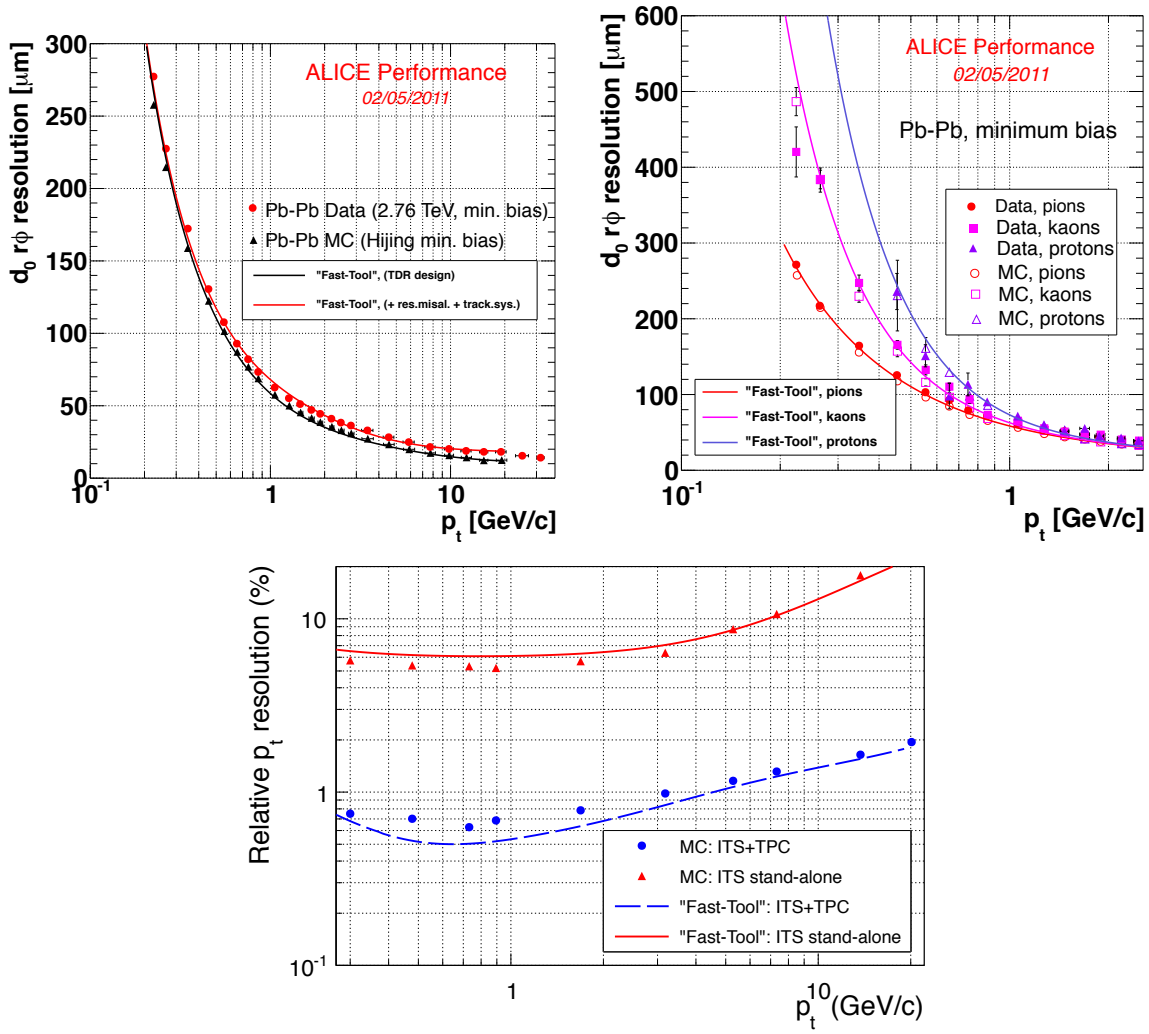

Figure 3.9: Validation of the Fast-Estimation-Tool: comparison with the performance of the present ITS. Transverse ($r\phi$) impact parameter resolution for unidentified charged particles (top-left panel) and for different particle species (top-right panel), and p_{t} resolution (bottom panel) as function of p_{t} .

d_0 resolution coincides with the track pointing resolution. The impact parameter resolution is mainly determined by the properties of the first layer. In order to study how the impact parameter resolution depends on the properties of the innermost layer, a dedicated study has been performed using the current ITS layout with an additional innermost layer (L0). The d0 resolution as function of radial distance, material budget and intrinsic spatial resolution of L0 is discussed herein.

Radial distance: Figure 3.11 shows the pointing resolution as a function of the transverse momentum for three values of the radial position of layer L0, the material budget and the spatial resolution being those of the current pixel detector. The results for the current ITS without L0 are also reported for comparison.

Material budget: The pointing resolution as a function of the transverse momentum is shown in Figure 3.12 in the case of layer L0 placed at 2.2 cm and three values of its thickness in units of radiation length, X/X_0, assuming the spatial resolution of the current pixel detector. The results for the current ITS without L0 are also reported for comparison.

Intrinsic spatial resolution: The pointing resolution as a function of the transverse momentum is shown in Figure 3.13 in the case of layer L0 placed at 2.2 cm and $X/X_0 = 0.3$ % and three values of the

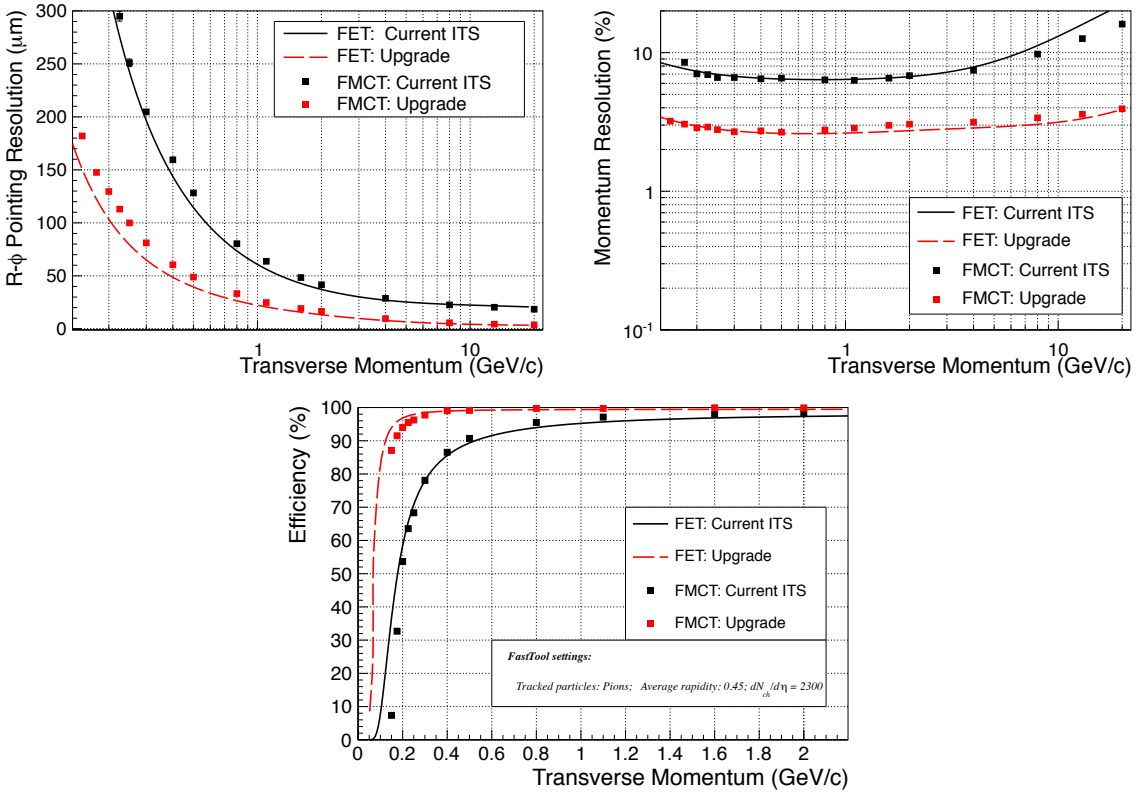

Figure 3.10: Comparison of the two simulation methods used in this study for the current ITS and the upgraded ITS.

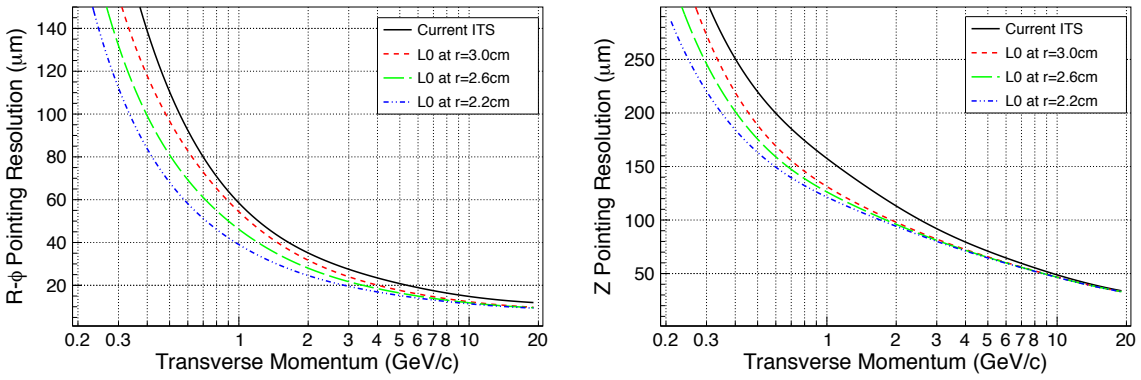

Figure 3.11: $r\phi$ (left) and z (right) pointing resolutions of charged pions at the primary vertex versus transverse momentum p_{t} for different radii of the layer L0 in ITS-TPC combined tracking mode.

intrinsic spatial resolution. The results for the current ITS without L0 are also reported for comparison.

In summary, the studies described in this section show that, by adding an innermost layer (L0) to the present ITS detector, the impact parameter resolution can be improved by a factor 3 at 400 MeV/c, assuming for L0 a radial distance of 22 mm from the beamline, a radiation length of 0.3 % of X_0 and a spatial resolution of 4 μm.

3.5.2 Definition and performance of the baseline upgrade scenario

In this section the baseline upgrade option, referred to as “upgraded ITS”, is described. The number and radial positions of the new layers have been optimized with the Fast-Estimation-Tool described in

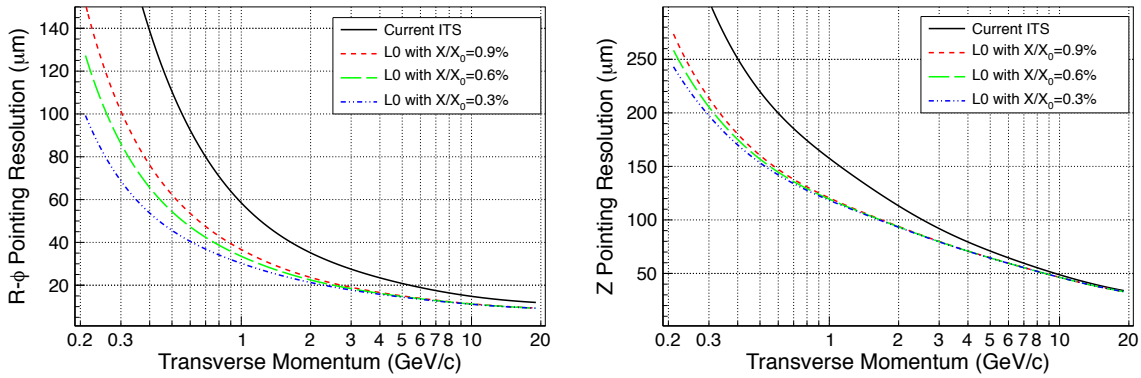

Figure 3.12: $r\phi$ (left) and z (right) pointing resolution of charged pions at the primary vertex versus transverse momentum p_t for different material budget of the layer L0 in ITS-TPC combined tracking mode.

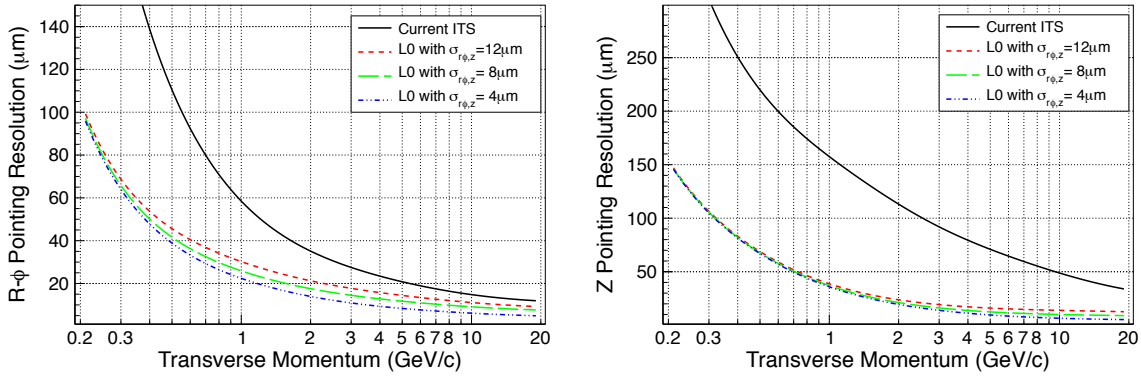

Figure 3.13: $r\phi$ (left) and z (right) pointing resolution of charged pions at the primary vertex versus transverse momentum p_t for different values of the intrinsic spatial resolution of the layer L0 in ITS-TPC combined tracking mode.

Section 3.4. The longitudinal extensions of the new layers are determined by the condition described in Section 3.3, corresponding to a pseudo-rapidity coverage of $|\eta| < 1.22$ over 90% of the luminous region. This study assumes an intrinsic resolution of 4 μm, both in $r\phi$ and z, and a material budget of 0.3 % of X_0, which can be achieved by detectors based on monolithic pixels as discussed in the following chapters.

The baseline scenario assumes a completely new ITS detector made of 7 layers of pixel and, in case, strip detectors, based on the ongoing developments discussed in Chapters 4 and 5. This detector configuration is summarized in Table 3.4. In the table the resolution and the material budget for the case where the outermost layers are equipped with microstrip detectors are indicated in brackets. The number of layers and their radial positions have been determined taking into account the available space between the new beam pipe and the outermost radius of the current ITS. The outcome of the simulations indicates that an improved tracking efficiency and p_t resolution in stand-alone mode is obtained by grouping the layers in an innermost triplet, an intermediate pair and an outermost pair.

The performance of the upgraded ITS and the current ITS are compared in Figures 3.14, 3.15, 3.16 and 3.17 for both ITS stand-alone and ITS-TPC combined tracking mode. Figure 3.14 shows the pointing resolution to the vertex for charged pions. Left and right panels show the ITS stand-alone and ITS-TPC combined tracking modes, respectively. Both the $r\phi$ and z components are shown in the same plots for the only pixel and the combined pixel/strip configurations (see Table 3.4). As an example, at a p_t of about 400 MeV/c, an improvement of a factor 3 and 5 is achieved for the $r\phi$ and z components, respectively.

Table 3.4: Characteristics of the upgrade scenario. The numbers in brackets refer to the case of microstrip detectors.

Layer / Type	r [cm]	$\pm z$ [cm]	Intrinsic resolution [μm] $r\phi$	z	Material budget X/X_0 [%]
Beam pipe	2.0	-	-		0.22
1 / new pixel	2.2	11.2	4	4	0.30
2 / new pixel	2.8	12.1	4	4	0.30
3 / new pixel	3.6	13.4	4	4	0.30
4 / new pixel (strip)	20.0	39.0	4 (20)	4 (830)	0.30 (0.83)
5 / new pixel (strip)	22.0	41.8	4 (20)	4 (830)	0.30 (0.83)
6 / new pixel (strip)	41.0	71.2	4 (20)	4 (830)	0.30 (0.83)
7 / new pixel (strip)	43.0	74.3	4 (20)	4 (830)	0.30 (0.83)

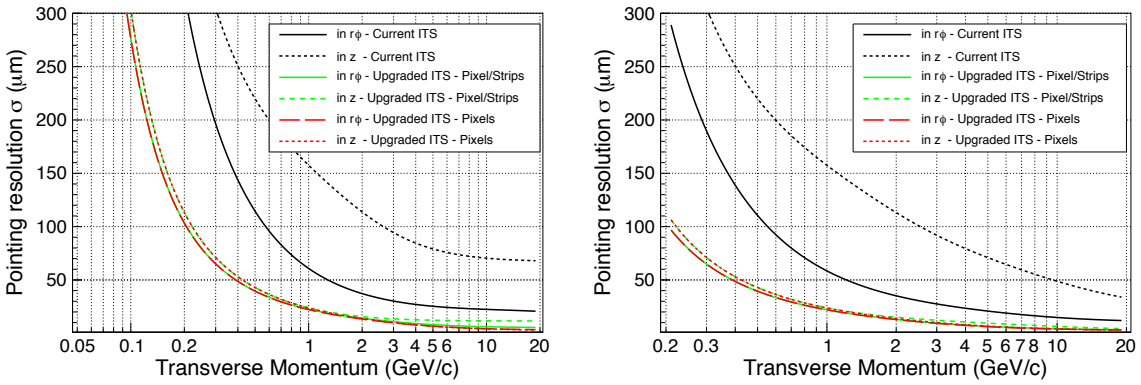

Figure 3.14: Pointing resolution to the vertex of charged pions as a function of the transverse momentum for the current ITS and the upgraded ITS. Left panel: ITS stand-alone tracking; right panel: ITS-TPC combined tracking.

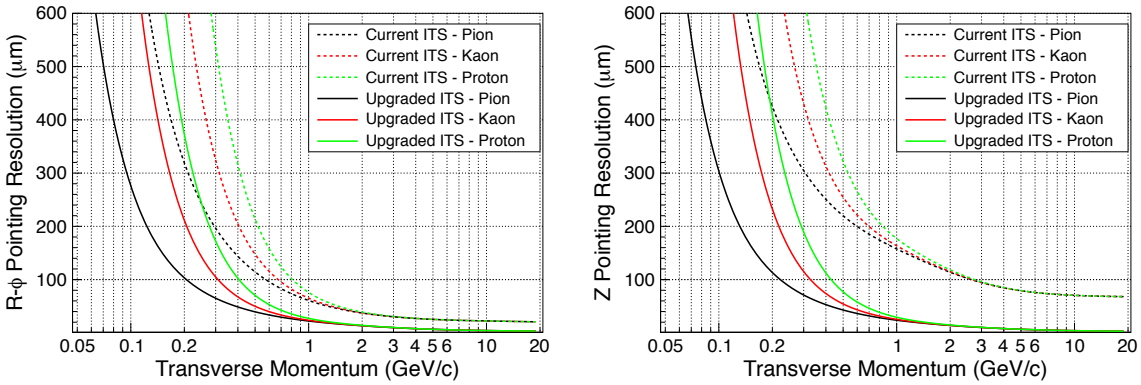

Figure 3.15: Pointing resolution to the vertex versus transverse momentum p_t for different particle species in the ITS stand-alone tracking mode for the current ITS (dotted lines) and the upgraded ITS (full lines). The $r\phi$ and z components are shown in the left and right panel, respectively.

It should be noticed that for the present ALICE set-up the ITS-TPC combined tracking provides at high p_t a sizeable improvement with respect to the ITS stand-alone tracking. Conversely, in the case of the upgraded ITS, adding the information from the TPC does not yield any further improvement. Similar results are obtained for the other particle species, as shown in Figure 3.15.

Figure 3.16 illustrates the improvements in terms of the transverse momentum resolution. For the ITS

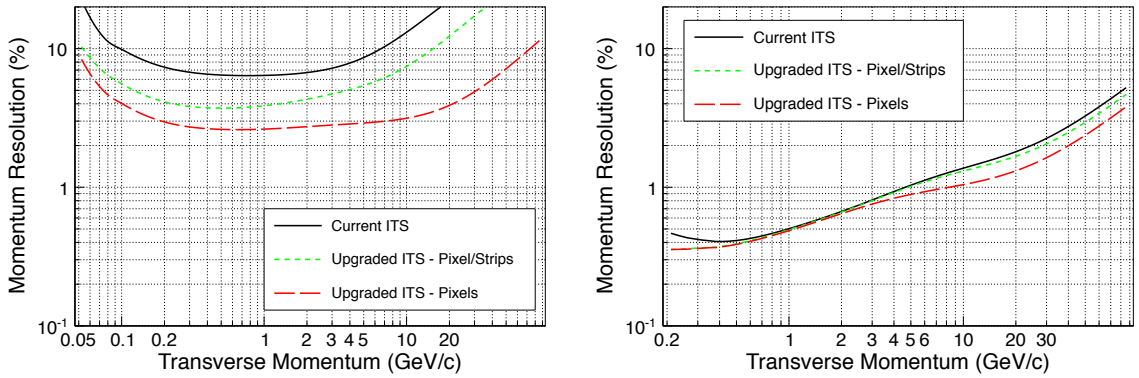

Figure 3.16: Transverse momentum resolution as a function of p_t for charged pions for the current ITS and the upgraded ITS. The results for the ITS stand-alone and ITS-TPC combined tracking mode are shown in the left and right panel, respectively.

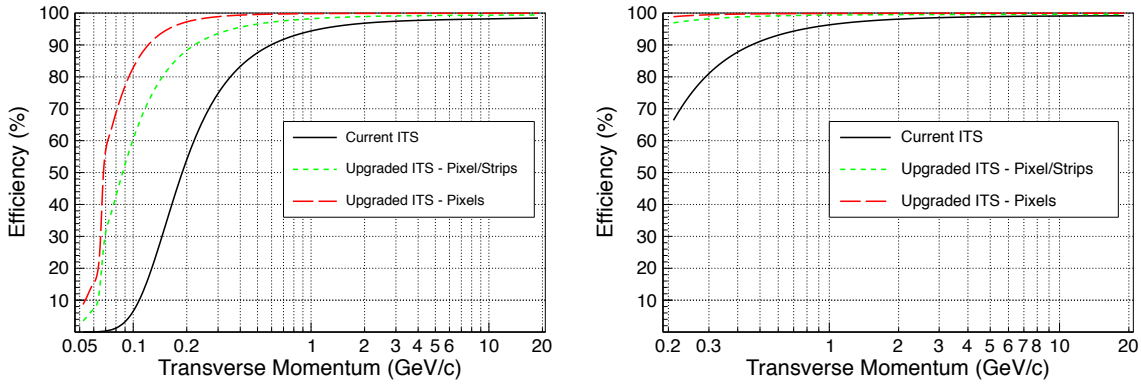

Figure 3.17: Tracking efficiency of charged pions for the current and upgraded ITS in the ITS stand-alone (left panel) and ITS-TPC combined (right panel) tracking modes.

stand-alone tracking mode, the upgraded ITS yields a dramatic improvement. It should be noticed that the p_t resolution in the stand-alone mode benefits significantly from the intrinsic resolution of the outer layers, and in particular at high p_t . In the ITS-TPC combined tracking mode (right panel of Figure 3.16) at low p_t (below 400 MeV/c) both upgraded ITS configurations would improve the resolution due to the reduction of the material budget of the innermost layers. At high p_t the full pixel configuration provides a better resolution.

Finally, Figure 3.17 shows the tracking efficiency in case of the ITS stand-alone tracking (left panel) and the ITS-TPC combined tracking (right panel). An impressive improvement with respect to the current ITS is obtained with the upgraded ITS configuration for $p_t < 1$ GeV/c; in stand-alone mode the improvement obtained if all layers are equipped with pixels is enhanced.

3.5.3 Tracking performance with reduced magnetic field

Data taking with a reduced magnetic field with respect to the standard 0.5 T can extend the minimum p_t reach of reconstructed charged particles, which may be relevant, for instance, for the study of dilepton pairs (see Section 2.4). In Figure 3.18 the ITS stand-alone tracking efficiency and the transverse momentum resolution with a magnetic field $B = 0.2$ T are shown as a function of p_t for the upgrade scenarios discussed in Section 3.5.2. The performance with the standard magnetic field of 0.5 T is also shown superimposed for comparison. An improvement of the tracking efficiency can be appreciated only for $p_t < 80$ MeV/c, for both configurations under study. Conversely, the p_t resolution is instead worsened

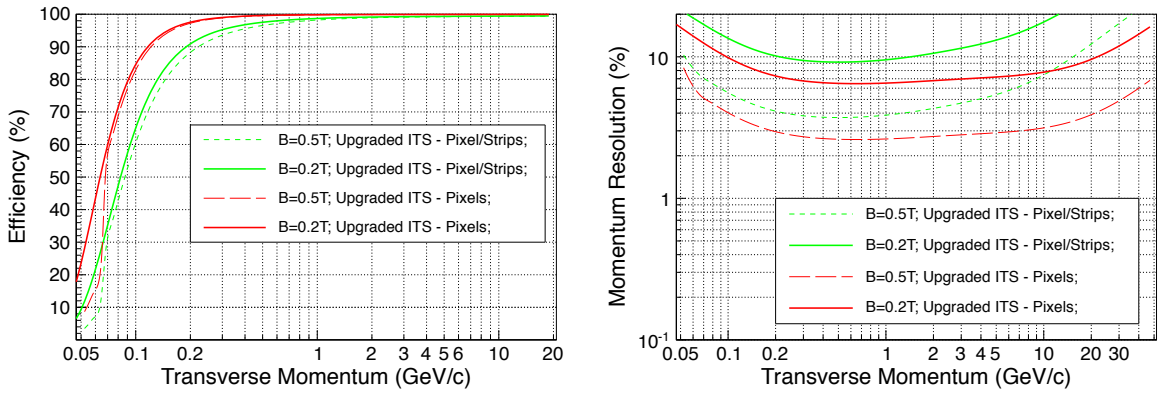

Figure 3.18: ITS stand-alone tracking efficiency (left) and transverse momentum resolution (right) for the 7-layer upgrade scenarios defined in Table 3.4 using a reduced magnetic field $B = 0.2$ T as compared to the standard $B = 0.5$ T.

by more than a factor 2 at $p_{\mathrm{t}} = 1$ GeV/c.

3.6 Particle Identification

In this section we discuss the possibility to perform proton, kaon and pion identification by the specific energy loss (dE/dx) measurement in the $1/\beta^2$ region with the upgraded ITS.

3.6.1 Simulation tools

Two simulation approaches have been considered to study the PID capabilities of the new ITS detectors: the "Truncated-Mean" and the "Bayesian". These two methods were developed for the current ITS detector [95] and they have been adapted to the detector configurations under study. For this study, a 7-layer layout has been assumed. In order to correctly reproduce the energy loss in the thin detectors assumed for the upgrade scenarios, a dedicated Monte Carlo simulation has been developed to study the energy deposition per unit length in 15 and 100 μm thick detectors. These two values are plausible for an implementation of the detector with monolithic and hybrid pixels, respectively. In Figure 3.19 the distributions of the specific energy-loss in 15 and 100 μm thick detectors are compared to that of the current 300 μm for pions of 500 MeV/c. The most probable energy-loss values are obtained by fitting the dE/dx distributions with a Landau function. Diffusion, charge collection inefficiency, noise and

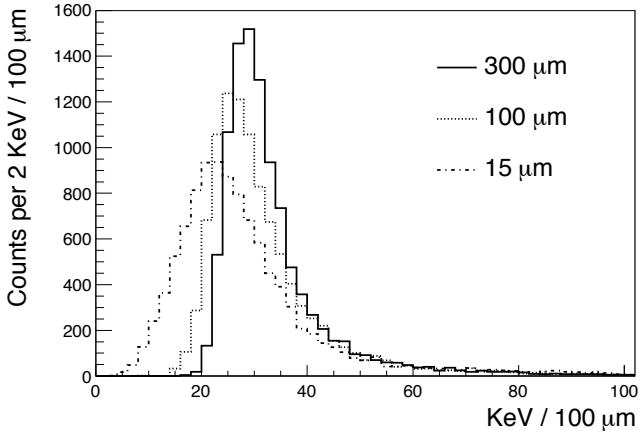

Figure 3.19: Simulation of dE/dx distributions of Minimum Ionizing Particles in silicon detectors with different thicknesses.

digitization of the detector response have been introduced in the simulation.

Truncated Mean method. This approach consists in computing a truncated mean of the charge values produced by a crossing track in the various layers. A single value of the $\mathrm{d}E/\mathrm{d}x$, obtained after normalizing to the length of the track segment in the silicon volume, is assigned to each track. Then, the arithmetic mean of the n lowest $\mathrm{d}E/\mathrm{d}x$ values among the ones of the clusters attached to the track is computed. The number n of $\mathrm{d}E/\mathrm{d}x$ values is set to a fixed fraction f of the total number of clusters attached to the track. By default the value $f = 1/2$ is used. In case n is an odd number, the mean is computed using the $(n-1)/2$ lowest $\mathrm{d}E/\mathrm{d}x$ values, the $(n-1)/2$ highest $\mathrm{d}E/\mathrm{d}x$ values are not used, and the remaining cluster with intermediate $\mathrm{d}E/\mathrm{d}x$ enters in the mean with a weight of $1/2$ [1].

The calibration of the PID algorithm is based on building the distribution of the $\mathrm{d}E/\mathrm{d}x$ for the tracks of each hadron species in a given momentum interval. These distributions are fitted with Gaussian functions. The distribution of the mean values of the Gaussian fits as a function of their momentum is then fitted to a parametrized formula (used in the PHOBOS experiment [83]):

$$\mathrm{d}E/\mathrm{d}x = \frac{E_0}{\beta^2}\left(b + 2\cdot\ln\gamma - \beta^2\right) \tag{3.2}$$

where E_0 and b are the free parameters. An example of this fit is shown in Figure 3.20. The fitted mean value, for a given particle type i, will be indicated with $M_G[i]$. The sigma of the Gaussian fits $\sigma_G[i]$, corresponding to the resolution, is found to be independent of the track momentum. With this method, the particle identity of a reconstructed track is assigned to the species i for which the quantity $|\mathrm{d}E/\mathrm{d}x - M_G[i]|/\sigma_G[i]$ is lowest. The $M_G[i]$ and $\sigma_G[i]$ parameters are used to calculate the average separation in units of σ_G between the particle types as a function of the momentum, according to the following:

$$x(\pi) = \frac{M_G[\pi] - M_G[K]}{\sigma_G[K]} \tag{3.3}$$

$$x(P) = \frac{M_G[P] - M_G[K]}{\sigma_G[K]} \tag{3.4}$$

Landau+Gauss method. This method is based on computing for each layer the probability that the measured signal is produced by an electron, pion, kaon or proton. The $\mathrm{d}E/\mathrm{d}x$ distributions for tracks of each species in a given momentum interval are built for each layer. These distributions are then fitted with a convolution of a Landau and a Gaussian functions yielding 3 parameters, namely Most Probable Value (MPV), Landau sigma (σ_L) and Gaussian sigma (σ_G). The Landau function describes the particle energy loss and the Gaussian represents the smearing of the signal due to the detector response. Examples of such fits are reported in Figure 3.21.

The dependence of these 3 parameters on the track momentum is fitted with ad hoc functions for each layer and for each particle species, which are used in the particle identification algorithm. An example of the MPV as a function of momentum for pions, kaons and protons is shown in Figure 3.22. Using these functions it is possible to compute for each track the probability of the track being an electron, kaon, pion or proton starting from the measured track momentum and the energy deposition in each layer. The

[1] Alternatively, an approach based on a weighted mean has also been considered. In this case, the values of the energy deposit of all clusters attached to the track are used; a single $\mathrm{d}E/\mathrm{d}x$ value is assigned to the track according to the following formula:

$$\mathrm{d}E/\mathrm{d}x = \left[\sqrt{\frac{1}{N_{layers}}\sum_{i=1}^{N_{layers}}\left(\frac{1}{\mathrm{d}E/\mathrm{d}x_i}\right)^2}\right]^{-1} \tag{3.1}$$

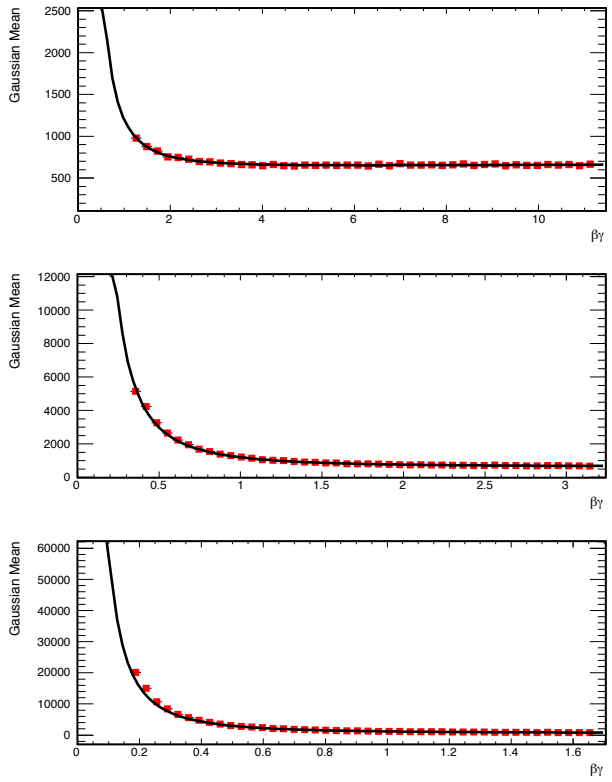

Figure 3.20: The Gaussian mean parameter as a function of $\beta \cdot \gamma$ for pions (top), kaons (middle) and protons (bottom) with superimposed the results of the fit with equation 3.2.

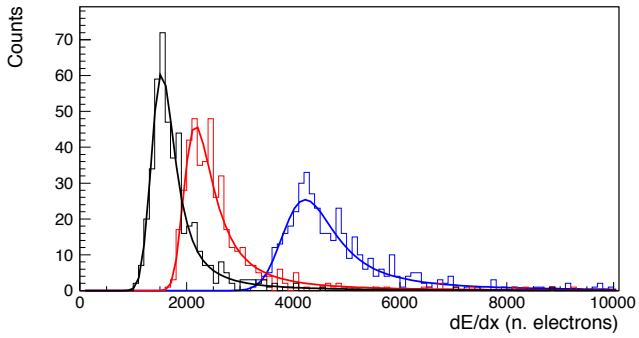

Figure 3.21: Distributions of the energy loss, with the convoluted Gaussian-Landau fits superimposed, for pions (black), kaons (red) and protons (blue) with momentum $0.608 < p < 0.640$ GeV/c.

probabilities extracted from each layer are then multiplied, resulting in an array of 4 (electron, pion, kaon and proton) probabilities. The identity is assigned to the track using the hypothesis with the largest probability.

3.6.2 Results

The two methods described above provide similar results. Therefore, in the following only those obtained with the Truncated-Mean method are discussed. Three detector configurations with different numbers and thicknesses of the layers providing PID information have been studied:

a) **4 layers 300 μm thick each.** This configuration corresponds to the current ITS. The performance in pp collisions was used to extract the specific energy loss information. A noise of 700 electrons

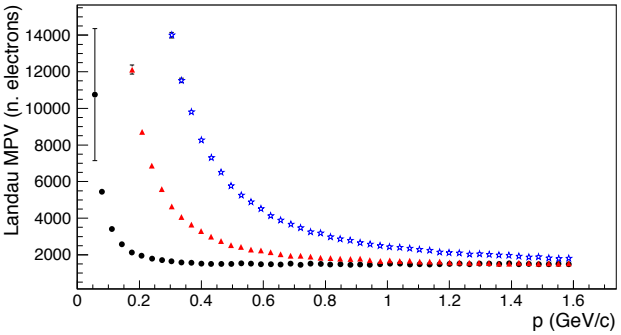

Figure 3.22: Behavior of the Most Probable Value parameter as a function of momentum for pions (circles), kaons (triangles) and protons (stars).

and a charge collection efficiency of 95 % were assumed in the simulation as well as an 11-bit ADC with a dynamic range of 20 MIP.

b) **7 layers 15 μm thick each.** The dimension of the pixel is assumed to be 20×20 μm^2 and an analogue readout based on an 8-bit ADC has been considered.

c) **3 layers 100 μm thick each + 4 layers 300 μm thick each.** A Time-Over-Threshold (TOT) readout has been considered for the 3 layers of 100 μm thickness. It has been assumed a signal over noise ratio of 46, as reported in [96], and an 8-bit clock counter with a dynamic range of about 20 MIP, which implies a MIP signal of 325 ns for a 40 MHz clock. For the 4 layers of 300 μm thickness, the same readout as in case a) has been taken into account. For all layers the charge collection efficiency has been fixed at 95%.

$\mathrm{d}E/\mathrm{d}x$ **resolution.** The $\mathrm{d}E/\mathrm{d}x$ resolution as a function of the integrated thickness of the silicon layers is shown in Figure 3.23. The resolution was evaluated as the ratio $\sigma_G[\pi]/M_G[\pi]$ for pions with a momentum $1.024\,\mathrm{GeV}/c \leq p \leq 1.056\,\mathrm{GeV}/c$. The $\mathrm{d}E/\mathrm{d}x$ resolution goes from 20 % for 105 μm integrated thickness, corresponding to the configuration b), to about 9 % for 1.2 mm integrated thickness corresponding to the configuration a), and therefore to the present ITS.

Particle species separation The comparison of the three configurations for the particle species separation is reported in Figure 3.24.

For the configuration with 4 layers of 300 μm it is possible to have a 3 sigma separation of kaons from protons with momentum lower than 1.2 GeV/c and pions with momentum lower than 0.7 GeV/c. This performance is very similar to the one obtained with configuration c). A worsening in the separation capabilities is found, as expected, using 7 layers of 15 μm silicon detector. The particle species separation for the b) configuration (monolithic) has also been studied assuming the detector performance of the MIMOSA detector [97], which will be described in the following chapter. In this simulation the charge sharing and the collection efficiency have been introduced. A threshold equal to 120 electrons and a Gaussian noise of 20 electrons have also been taken into account. It was found that the separation between the particle species is practically the same using a 6-bit or 8-bit ADC and it deteriorates significantly in the low momentum region using a 4-bit ADC. In the following, for the 7 layers of 15 μm silicon detector configuration, a readout based on an 8-bit ADC has been assumed.

Efficiency and contamination. In this study two data samples of different electron, pion, kaon and proton relative abundances have been generated: the relative abundances as extracted i) from 900 GeV pp data [98] and ii) from preliminary 2.76 TeV Pb–Pb data. The efficiency $\varepsilon(i;\mathrm{p})$ and the contamination $\mathrm{K}(i;\mathrm{p})$ for the particle type i (pions, kaons and protons) in each momentum bin [p, p+Δp] are defined as

follows:

$$\varepsilon(i;p) = \frac{N_{Good}(i;p)}{N_{True}(i;p)}$$
$$K(i;p) = \frac{N_{Fake}(i;p)}{N_{ID}(i;p)}$$

where $N_{Good}(i;p)$ is the number of particles of type i correctly tagged as i, $N_{True}(i;p)$ is the number of generated particles of type i in the momentum range [p, p+Δp], $N_{Fake}(i;p)$ is the number of particles tagged as i without being of type i and $N_{ID}(i;p)$ is the total number of tracks identified as i ($N_{ID}(i;p)$=$N_{Good}(i;p)$+$N_{Fake}(i;p)$).

The efficiency and the contamination in all detector configurations are shown in Figure 3.25 and 3.26 for the two Monte Carlo samples with different π^+, K^+ and p relative abundances. The results indicate that the PID performance achievable with the hybrid configuration c) is similar to that of the present ITS with 4 layers 300 μm thick featuring analog readout. With a 7 layer 15 μm thick detector configuration, the particle separation is still possible, although in a reduced momentum range.

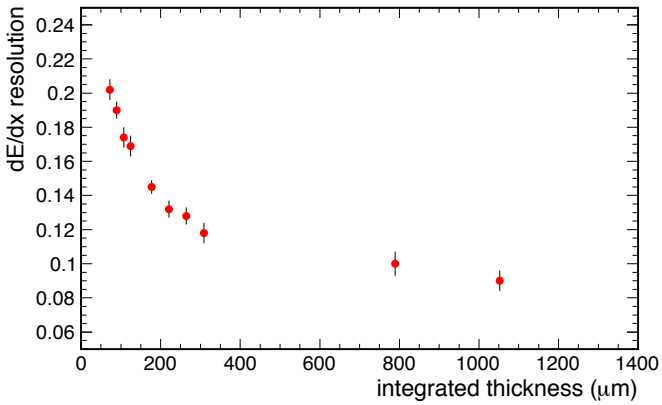

Figure 3.23: The dE/dx resolution as a function of the integrated thickness of the silicon layers used for the PID.

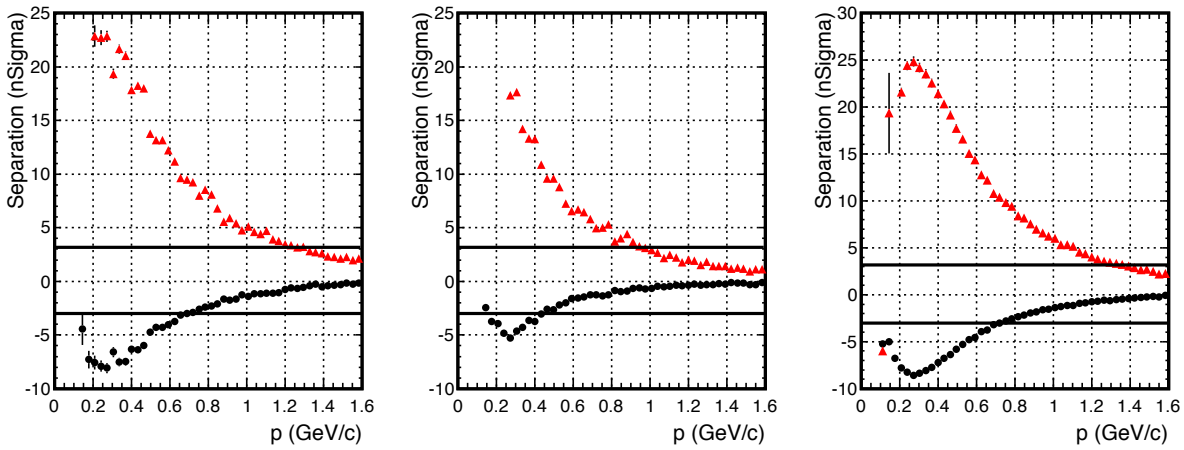

Figure 3.24: Pion to kaon separation (black circles) and proton to kaon separation (red triangles) in unit of sigma in the case of 4 layers of 300 μm (left panel), 7 layers of 15 μm (central panel) and 3 layers of 100 μm + 4 layers of 300 μm (right panel) silicon detectors. The horizontal lines correspond to a 3 sigma separation.

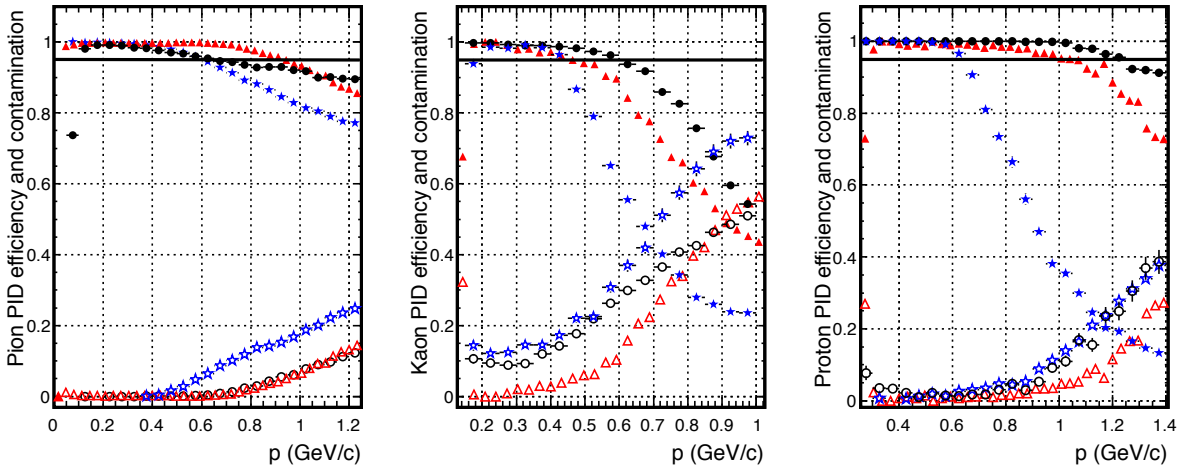

Figure 3.25: Efficiency (closed symbols) and contamination (open symbols) as a function of the particle momentum assuming the relative abundances of π^+, K^+ and p as extracted from pp data at $\sqrt{s} = 900$ GeV [98] for different configurations: 4 layers 300 μm thick (black circles), 3 layers 100 μm thick + 4 layers 300 μm thick each (red triangles) and 7 layers 15 μm thick silicon detectors (blue stars). Pions, kaons, and protons are shown in the left, middle and right panels, respectively. In all plots a line corresponding to a PID efficiency of 95 % is drawn as a reference.

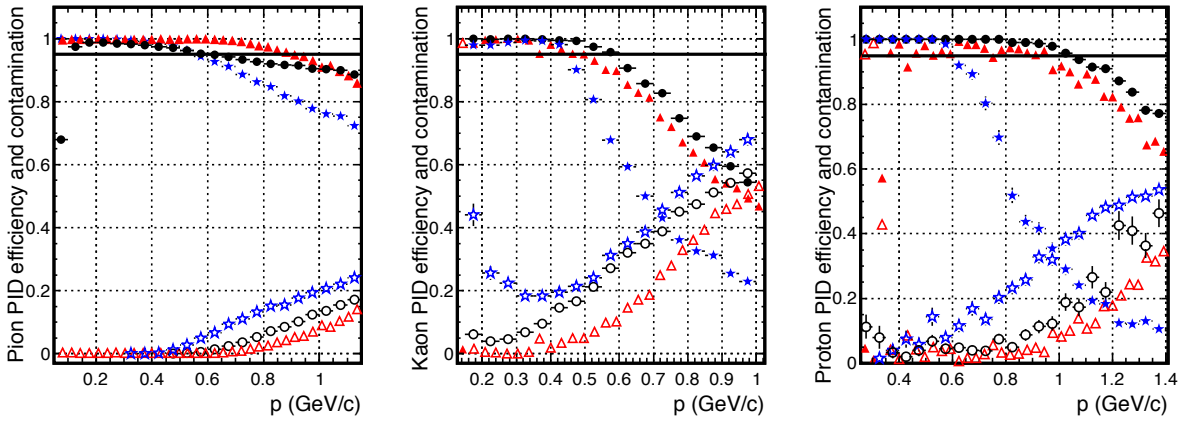

Figure 3.26: Efficiency (closed symbols) and contamination (open symbols) as a function of the particle momentum assuming the relative abundances of π^+, K^+ and p as obtained from preliminary Pb–Pb data at $\sqrt{s_{NN}} = 2.76$ GeV for different configurations: 4 layers 300 μm thick (black circles), 3 layers 100 μm thick + 4 layers 300 μm thick each (red triangles) and 7 layers 15 μm thick silicon detectors (blue stars). Pions, kaons, and protons are shown in the left, middle and right panels, respectively. In all plots a line corresponding to a PID efficiency of 95 % is drawn as a reference.

3.7 Timing requirements

The interaction rates assumed for the study described in this section are 200 KHz for pp and 50 KHz for Pb–Pb. These values may imply a significant pile-up rate in the detector, depending on the integration time, which has an impact on event reconstruction and analysis.

If the total occupancy from triggered and pile-up interactions significantly exceeds the occupancy of a central Pb-Pb collision, the reconstruction efficiency drops due to the ambiguity of the cluster to track association at inner layers. With 50 kHz interaction rate and 20 (50) μs integration time window, on average about one (two) extra Pb-Pb collision will be read-out on top of the triggered event, and only

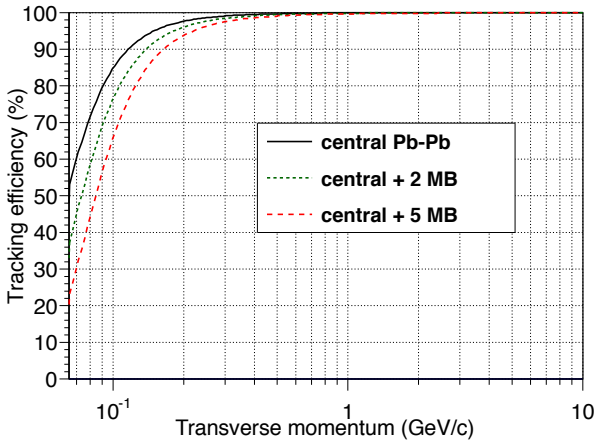

Figure 3.27: Reconstruction efficiency of the upgraded ITS setup for triggered central Pb-Pb collision with or without the pile up of extra events, whose multiplicity is the average one for minimum bias Pb–Pb collisions. In all cases 5% detection inefficiency per plane is assumed.

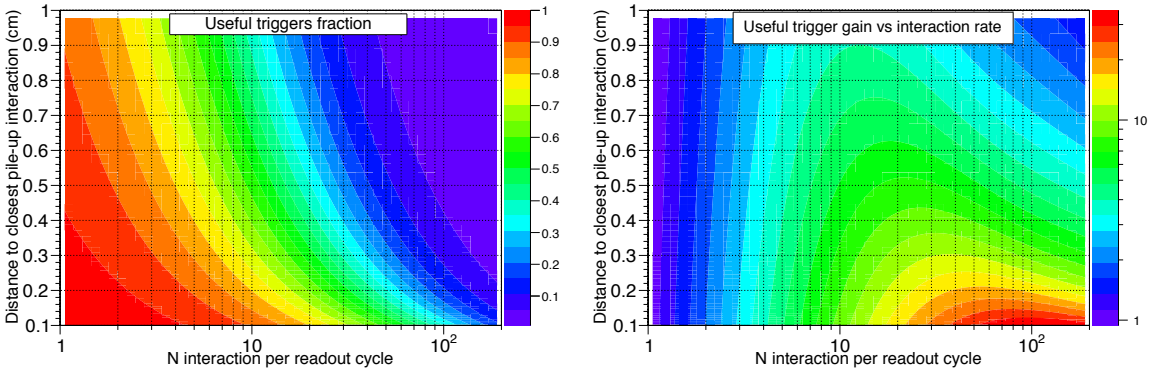

Figure 3.28: Left panel: Fraction of triggered vertices isolated from nearest pile-up vertex as a function of isolation distance and the number of integrated collisions per readout cycle in pp collisions. Right panel: overall gain in terms of triggered events that can be analyzed as a function of the isolation distance and the number of integrated collisions per readout cycle in pp collisions. Gaussian profile with σ = 5 cm is assumed for the luminous region along the beam.

in about 10% of the triggers five or more extra collisions will be piled-up assuming an integration time window of 50 μs. Figure 3.27 shows the degradation of reconstruction efficiency for triggered central Pb-Pb collisions piled up with two or five extra events, whose charged particle multiplicity is the average of the multiplicities in minimum bias Pb–Pb collisions.

To prevent the reconstruction efficiency loss to be significant, particularly at low $p_{\rm t}$, the time resolution in the highest occupancy layers should not exceed $\approx$ 20 μs. Actually, a similar time resolution is desirable also for the outer layers in order to facilitate the cluster matching throughout the whole detector.

In pp collisions, where a large pile-up is expected, the issue is the correct assignment of each track to its own interaction vertex. For primary tracks, assuming the vertexing and tracking capabilities of the upgraded ITS, the pile-up vertices should be separated from the triggered one by at least 1 mm in order to correctly assign the tracks to the triggered vertex. For the heavy flavour decay tracks, the $\sim$1 mm isolation should be enough for the short lived Λ_c, while for the B-mesons an isolation of $\sim$1 cm is required.

The left panel of Figure 3.28 shows the fraction of isolated triggered pp vertices as a function of isolation distance to closest pile-up vertex and the number of integrated collisions per readout cycle. A Gaussian profile with σ = 5 cm is assumed for the luminous region along the beam direction.

Assuming a 200 KHz interaction rate and a 20 μs integration time (corresponding to an average of 4 piled-up collisions), 5 % of the triggered vertices will not be separated by 1 mm or more from those of the piled-up collisions, while for an analysis requiring $\sim$ 1 cm vertex separation, approximately half of the triggered vertices can be used. The right panel shows the overall gain in terms of triggered events that can be analyzed as a function of the isolation distance and the number of integrated collisions per readout cycle.

The pile up ambiguities would be further reduced if at least one point for each track carries a precise time-stamp.

3.8 Radiation environment

Detailed studies were done in the past for the expected dose in the ALICE detector according to the standard running scenario [99]. The dose values have been recently re-evaluated, as reported in [100]. In these studies, the radiation is dominated by pp and high-luminosity Ar–Ar runs, the Pb–Pb collisions representing only about $1/6$ of the time integrated radiation load [100]. The factor $1/6$ is an overestimate because the computations were done taking into account the initial expected higher multiplicity environment of ion collisions, corresponding to $\mathrm{d}N_{\mathrm{ch}}/\mathrm{d}\eta = 8000$ for central Pb–Pb collisions.

The expected doses and hadron fluences for the upgraded ITS detector are computed here based on these studies [2], by scaling down the formerly overestimated Pb–Pb multiplicity, and assuming the following target statistics for physics studies:

- 4×10^{11} pp inelastic interactions;
- 8.5×10^{10} Pb–Pb inelastic collisions.

A conservative safety factor of 4 and 2 is further applied for the pp and Pb-Pb interactions, respectively, to take into account inefficiency from data taking and data quality requirements to target the above mentioned statistics.

In Figure 3.29, the expected doses and hadron fluences as a function of the radial distance to the beams are shown, corresponding to this running scenario. The expected radiation levels are also summarized in Table 3.5 for the radial positions corresponding to the upgraded ITS.

Table 3.5: Expected radiation levels for the upgraded ITS (see text for details)

	Radius [mm]	1 MeV n [cm^{-2}]	TID [krad]
Layer 1	22	263.9×10^{10}	178.0
Layer 2	28	164.6×10^{10}	110.0
Layer 3	36	101.3×10^{10}	66.6
Layer 4	200	7.5×10^{10}	2.3
Layer 5	220	6.9×10^{10}	2.0
Layer 6	410	5.1×10^{10}	0.7
Layer 7	430	5.0×10^{10}	0.6

[2] The hadron flux values, which are given in 1 MeV neutron equivalent, are taken from [99] and have been renormalized by a factor 0.94. The latter is the ratio between the dose values quoted in [100] and in [99].

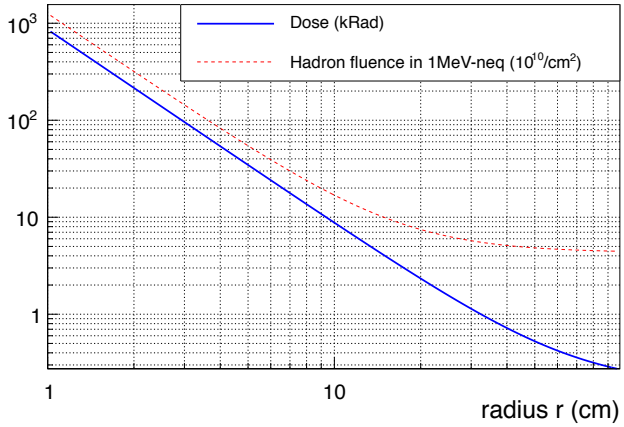

Figure 3.29: Integrated dose and hadron fluences (in 1 MeV neutron equivalent) as a function of the radial distance to the beams for the running scenario as explained in the text.

3.9 Further studies

3.9.1 Tracking performance with reduced intrinsic resolution of the outermost layers

The tracking performance of some alternative configurations, mainly with a reduced intrinsic resolution of the four outermost layers, are discussed in this section. The reduced intrinsic resolution of the outer layers that is assumed in this study can be, for instance, the consequence of either increasing the pixel size or grouping (e.g. electronically) more pixels together. The alternative configurations are compared with the baseline upgrade option of 7 layers based on monolithic pixels featuring an intrinsic resolution of (4 μm, 4 μm) and a total material budget per layer of 0.3 % X_0 (black lines in Figure 3.30). The alternative configurations taken into account for this study are:

– the three innermost layers with intrinsic resolution of $(6\,\mu\text{m},\ 6\,\mu\text{m})$ and a total material budget per layer of $0.5\%X_0$, the four outermost layers with intrinsic resolution of $(20\,\mu\text{m},\ 800\,\mu\text{m})$ and a total material budget per layer of $0.8\%X_0$ (green lines). This configuration would correspond to the adoption of hybrid pixel and strip detectors for the innermost and the outermost layers, respectively. As expected, the performance of this configuration turns out to be very similar to that of the other baseline upgrade option, which is not considered in this section.

For the following three options the properties of the three innermost layers have been assumed to remain the same as for the baseline configuration, while for the four outermost layers the material budget is still 0.3 % X0 per layer and the intrinsic resolution is:

– $(40\,\mu\text{m},\ 40\,\mu\text{m})$ (red lines), which would correspond to grouping 10×10 (monolithic) pixels;

– $(80\,\mu\text{m},\ 80\,\mu\text{m})$ (blue lines), corresponding to a group of 20×20 pixels;

– $(8\,\mu\text{m},\ 160\,\mu\text{m})$ (purple lines), corresponding to a group of 2×40 pixels.

The results for the pointing resolution, tracking efficiency and momentum resolution as a function of p_{t} are shown in Figure 3.30.

The main differences are observed for the momentum resolution, the pointing resolution and the tracking efficiency remaining almost unchanged. The configuration corresponding to a grouping of 2×40 pixels (purple lines) would preserve tracking efficiency closest to that obtained assuming an intrinsic resolution of $(4\,\mu\text{m},\ 4\,\mu\text{m})$ for all seven layers.

3.9.2 Dependence of ITS-standalone tracking efficiency on the layer detection efficiency

In this section we study the effect on the global tracking efficiency under the assumption of a reduced overall detection efficiency of the layers. The reduced detection efficiency might be due to either limited acceptance and dead areas, or intrinsic inefficiency of the detector. The case of having all the seven layers (at the same time) with an efficiency of 95 %, 85 %, 75 % and 65 % have been simulated. The tracking efficiency has been defined as the ratio of the number of reconstructed tracks with at least four correct clusters associated to the tracks and no wrongly associated cluster (from other particles) to the number of "trackable" tracks (i.e. tracks passing through at least four layers). The detection efficiency of the individual layers has been assumed to be 100%, because typically silicon detectors present very high detection efficiency. The results are shown in Figure 3.31. It is worth to stress that typical values of detection efficiency for non dead zones of silicon detectors are around 99 %.

3.9.3 Redundancy

This section deals with the detector performance in the event of a dramatic reduction of the detector efficiency. In particular we compare the performances of the 7-layer upgrade scenario discussed in Section 3.5.2, whose characteristics are summarized in Table 3.4, with that of another configuration with 2 more layers (9-layer configuration) with the same intrinsic resolution as the others. The positions of the two extra layers in this new configuration have been optimized to provide the best tracking efficiency in the event of one layer being completely dead. The results of the study suggest to have one extra layer between the most external doublet and the intermediate one and the other close to the innermost triplet.

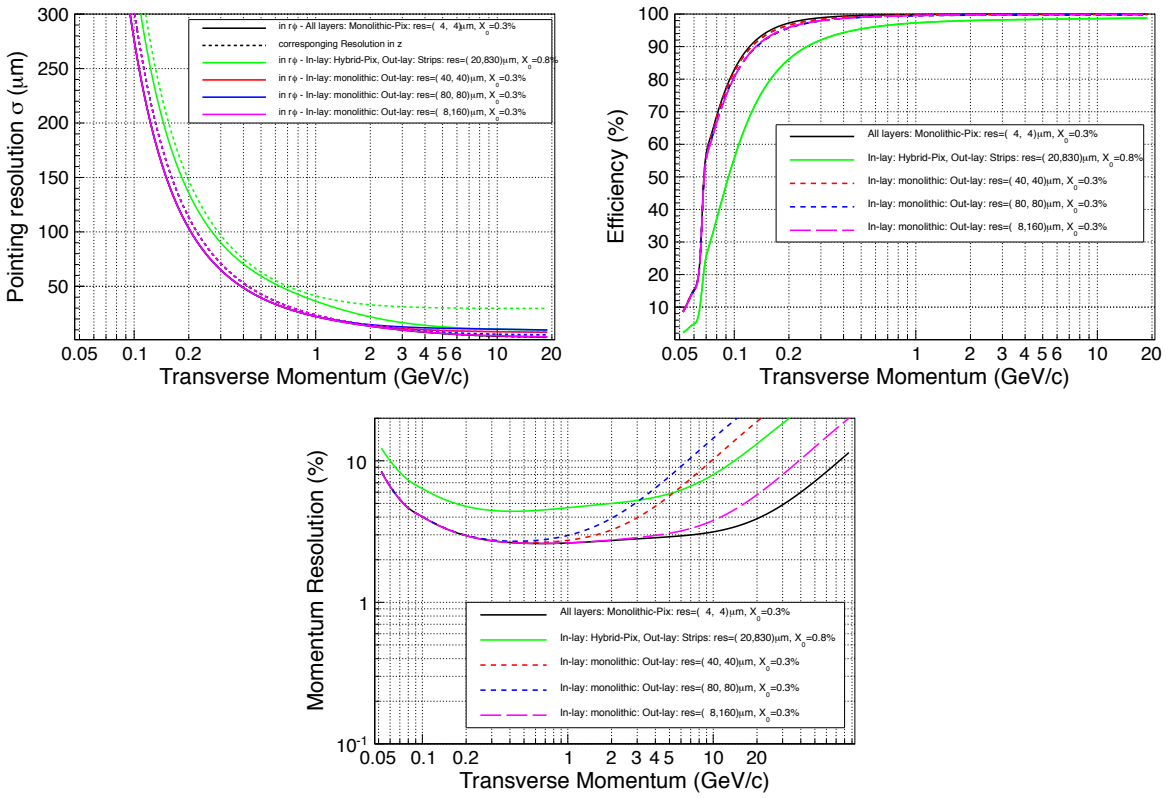

Figure 3.30: Tracking performance obtained by assuming relaxed intrinsic resolutions for the four outer most layers, ascompared to baseline upgrade configurations, corresponding to the adoption of monolithic pixels for all layers (black lines) or a combination of hybrid pixels and strips. In particular, the pointing resolution (top-left panel), t he tracking efficiency (top-right panel) and the pt resolution (bottom pannel) are shown as a function of p_{t} .

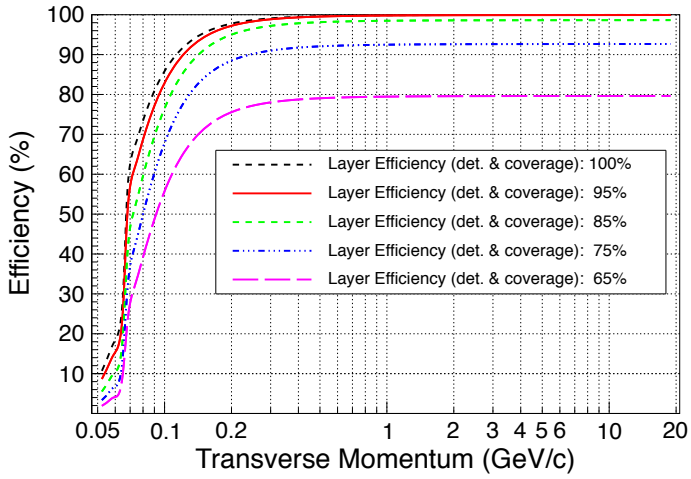

Figure 3.31: Tracking efficiency as a function of p_t for the upgraded ITS detector, assuming different reduced detection efficiency for all seven layers of the layout.

The radial positions of this optimized configuration are thus $\{2.2, 2.8, 3.6, 4.2, 20.0, 22.0, 33.0, 41.0, 43.0\}$ cm. In Figure 3.32 and 3.33 the efficiency and the momentum resolution as a function of p_t are shown for the two configurations with 7 and 9 layers, respectively, in the case of one dead layer. The standard case of all layers properly working is also shown as reference. The pointing resolution, which depends mainly on the first two layers, does not change. The result of this study proves that the configuration with 9 layers would prevent the drop of the tracking efficiency for those tracks where a hit in an intermediate layer has not been produced.

3.9.4 Performance of modified upgrade scenarios

In this section we show how the performance of the upgraded detector would improve or worsen, by considering different values for the intrinsic precision and the material budget with respect to the baseline, i.e. 7 layers of 0.3 % of X_0 and 4 μm intrinsic resolution. The effect of having the innermost layer at an even smaller radius will be also discussed, which requires a beam pipe at a reduced radius. In particular, the following configurations have been considered:

- all layers presenting a larger material budget $X/X_0 = 0.5\%$ and an intrinsic resolution of 6 μm;
- the baseline configuration but the innermost layer (L0) having a smaller material budget of $X/X_0 = 0.1\%$ and unchanged intrinsic resolution of 4 μm;
- the previous configuration but the first layer at a radius of 2.0 cm instead of the baseline 2.2 cm, and a beam pipe of 1.8 cm radius.

In the top panels of Figure 3.34 the $r\phi$ pointing resolution to the vertex as a function of p_t for these modified configurations is compared to that of the present detector and the upgrade baseline (upgraded ITS) configurations. The z pointing resolution is shown only for the present ITS detector, because for all upgrade scenarios it is very similar to the $r\phi$ distribution of the corresponding configuration. The transverse momentum resolution as a function of p_t is shown in the bottom panels of Figure 3.34 for the same configurations. At $p_t \approx 0.4$ GeV/c about an additional factor 2 of improvement would be obtained for the pointing resolution, with respect to the baseline configuration, by considering the configuration with the innermost layer at a radius 2.0 cm.

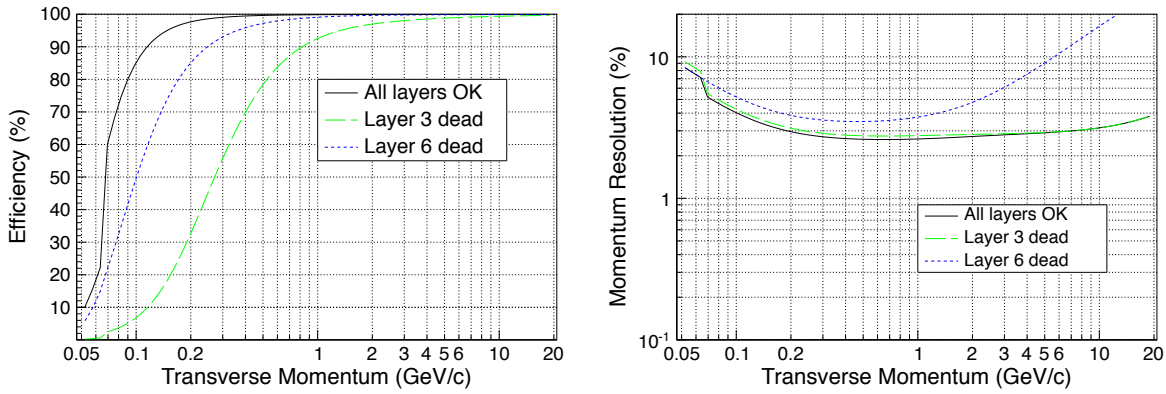

Figure 3.32: Tracking efficiency (left) and momentum resolution (right) for the 7-layer upgrade scenario defined in Table 3.4. The radial distances of the layers are {2.2, 2.8, 3.6, 20.0, 22.0, 41.0, 43.0} cm. The scenario where layer 3 at 3.6 cm (cyan) or layer 6 at 41.0 cm (green) is dead is compared to the case of all layers properly working.

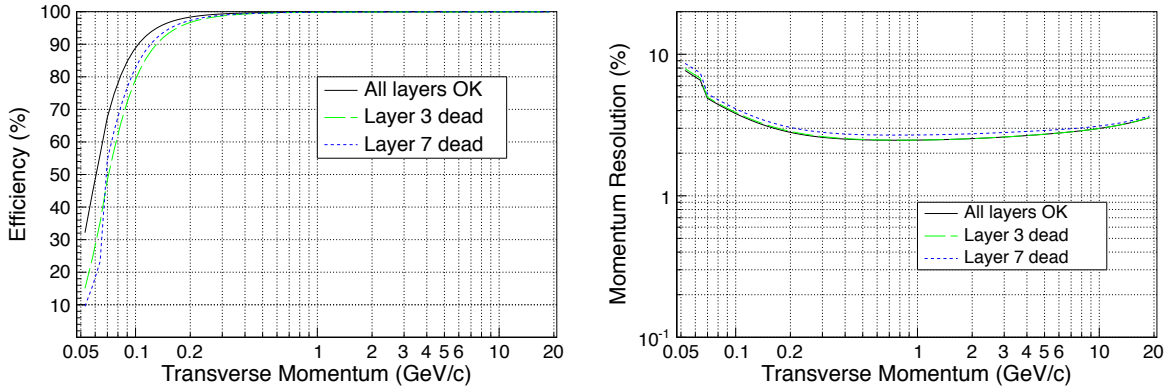

Figure 3.33: Tracking efficiency (left) and momentum resolution (right) for the new configuration with two extra layers, see the text for details. The radial distances of the layers are {2.2, 2.8, 3.6, 20.0, 22.0, 41.0, 43.0} cm. The scenario where layer 3 at 3.6 cm (cyan) or layer 7 at 33.0 cm (green) is dead is compared to the case of all layers properly working.

3.9.5 Layer geometry

Mechanically, the layers can be assembled to form a barrel based on planar staves of finite width and, optionally, by introducing overlaps between adjacent layers to have good hermeticity. In particular for the innermost layer the specific assembly adopted can have an influence on the impact parameter resolution.

The overlaps in the azimuthal direction can be realized using either a “turbo-like” geometry or a “two-radii” geometry. Both options would introduce an azimuthal ϕ dependence of the impact parameter resolution due to the larger material budget in the directions of the overlaps. Apart from the overlaps, a modulation of the impact parameter resolution as a function of ϕ is also due to the non constant radial distance $r(\phi)$ of the points of each stave. On the one hand, this latter effect is less relevant for a stave of small width; on the other hand, the number of overlaps (equal to the number of staves) would be larger and therefore the average material budget and impact parameter resolution would increase.

In Figure 3.35 the pointing resolution as a function of ϕ is shown for the turbo-like and two-radii geometry for the case of two stave widths, a “small” (about 1.45 cm) and a “large” (about 1.9 cm) one, assuming an overlap between adjacent staves of 0.2 cm. In this simulation, the upper part of each stave, corresponding to the region of the overlap, is assumed to be dead; therefore for tracks crossing the overlaps only one space point is produced, as for the regions without the overlaps. Given this hypothesis, for

the turbo-like geometry it has been assumed that the insensitive region would be that of the border with larger r. In Figure 3.35 the case of an ideal cylindrical layer is also shown for comparison.

The dependence of the mean pointing resolution as a function of the stave width, in the two geometries, is shown in Figure 3.36 for different values of the overlaps between adjacent staves, assuming the minimum radius of this innermost layer equals 2.2 cm. A minimum is observed at a width which depends on the size of the overlaps.

For the first layer two different cases have been considered in terms of azimuthal segmentation in staves, 12 and 14, for both layouts (turbo and two-radii). A dead area of 0.2 cm is assumed to be placed only on one side of each stave. The outcome of this study is presented in Figure 3.37, which suggests that the turbo-like geometry is slightly better than the two-radii one, the mean pointing resolution being smaller by a few percent. The reason is that in the turbo-like geometry the dead part of all staves can be placed at the larger radius; therefore the tracks crossing an overlap would have the hit on the stave closer to the vertex and thus a better pointing resolution to the main vertex. No significant difference is observed between the 12 and 14 stave geometries.

In Chapter 5 the various possible solutions for the mechanical assembly of the upgraded detector are discussed. The radii that can be obtained from the mechanical point of view with given assumptions in terms of clearance, dead area, chip dimension, etc. are slightly different from those of the simplified geometry used to define the baseline configuration of the upgraded ITS. However, the effect of these variations on the tracking performance is minor, as can be seen in Figure 3.38.

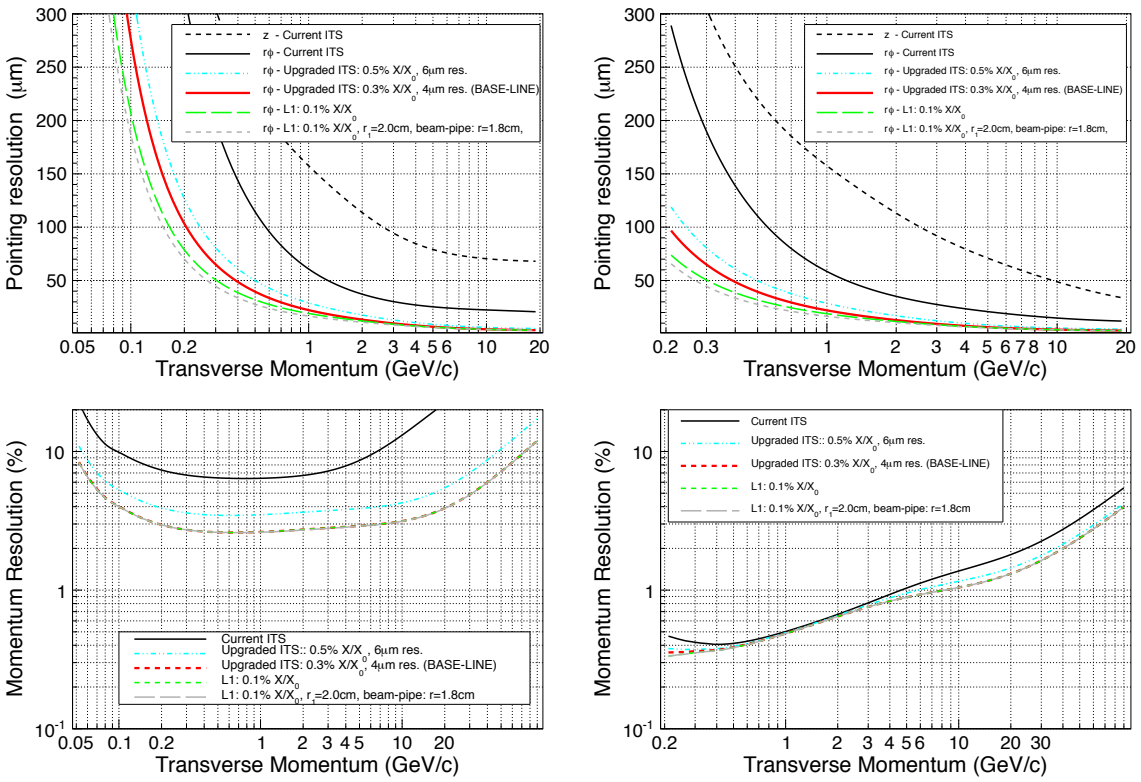

Figure 3.34: Top panels: pointing resolution to the vertex of charged pions as a function of the transverse momentum for the current ITS and different options of the upgraded detector, see text for details. Bottom panels: transverse momentum resolution for charged pions as a function of p_t for the current ITS and different options of the upgraded detector. Left and right panels show the ITS stand-alone and the ITS-TPC combined tracking, respectively.

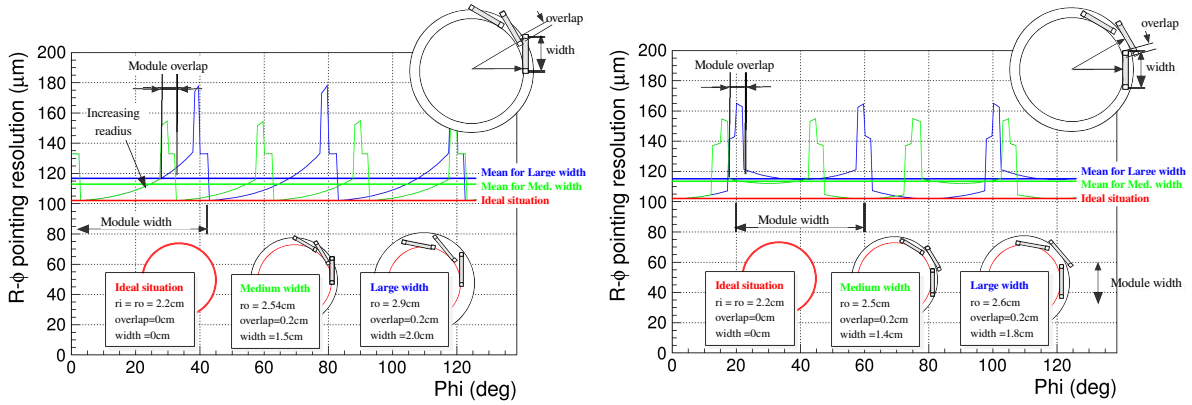

Figure 3.35: Pointing resolution to the vertex versus ϕ for charged pions with transverse momentum p_{t} of 0.2 GeV/c. Two different layer geometries are considered: a "turbo-like" geometry (left panel) and a "two-radii" geometry (right panel). In all cases the minimum radius of the innermost layer is assumed to be $r_0 = 2.2$ cm and an overlap region of 0.2 cm is considered. The green curves show the case 1.5 cm and 1.4 cm wide for the turbo-like and two-radii geometry, respectively. The blue curves show the case of a larger stave width, in particular 2.0 cm and 1.8 cm for the turbo-like and two-radii geometry, respectively. The average values of the pointing resolution is indicated with the thick lines with the same colors. As a reference, also the ideal case of a perfect cylindrical geometry is shown in red.

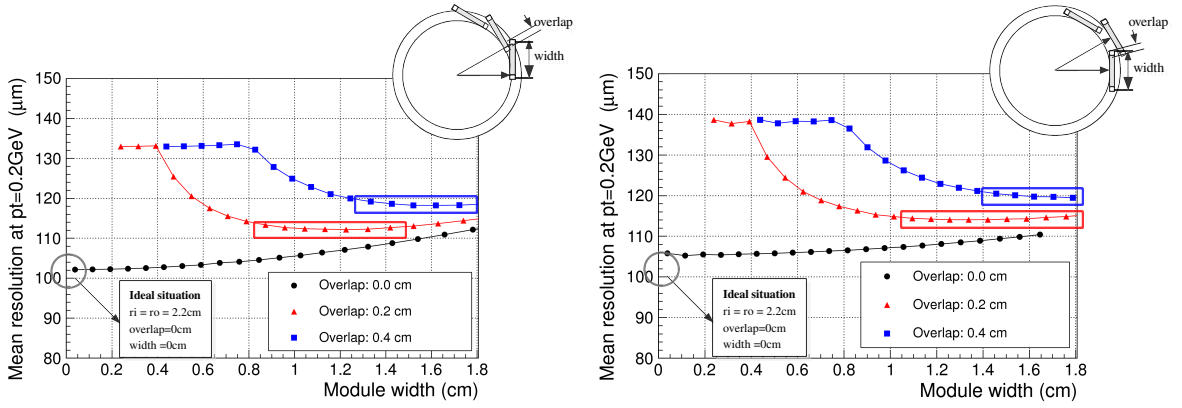

Figure 3.36: Mean pointing resolutions to the vertex versus the width of the stave for charged pions with p_{t} of 0.2 GeV/c, for different sizes of overlaps. The left panel shows the case of a turbo-like geometry, the right panel that of a two-radii geometry.

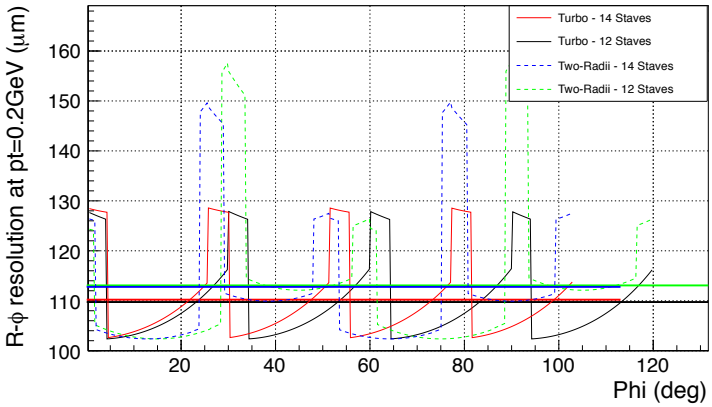

Figure 3.37: Pointing resolution to the vertex versus ϕ for pions with transverse momentum p_t of 0.2 GeV/c. The turbo-like and two-radii geometries are compared in configurations with either 12 or 14 staves, see text for details.

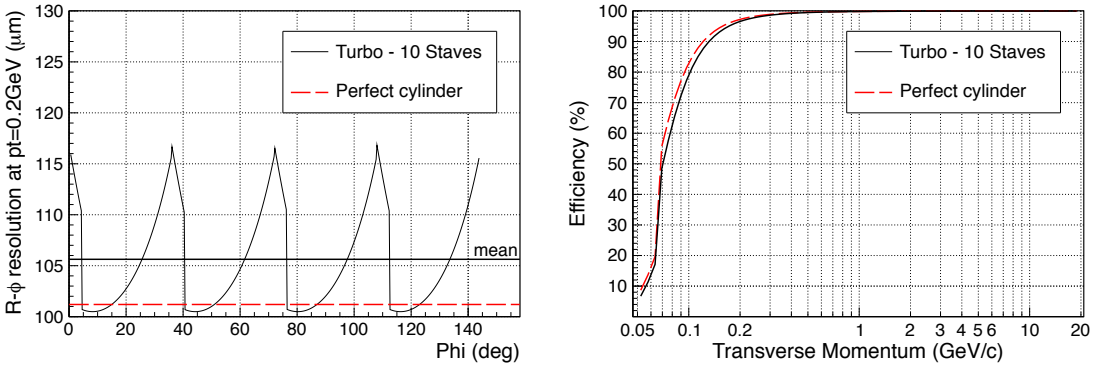

Figure 3.38: Pointing resolution as a function of the azimuthal angle for charged pions with p_t of 0.2 GeV (left panel) and efficiency versus p_t (right panel) for the ideal geometry used to define the baseline upgraded ITS configuration (in red) and for a realistic turbo-like assembly with 10 staves for the innermost layer (in black). The horizontal black line in the left panel shows the average over ϕ of the realistic assembly.

Chapter 4

Detector Technical Implementation

4.1 Introduction

This chapter summarizes the technical requirements and operating conditions for the upgrade of the ALICE ITS and presents the different technology options and possible implementations.

The new ITS will consist of seven layers of silicon tracking detectors as described in Chapter 3. The two options currently under study are:

- **Layout 1:** All seven layers are built using monolithic silicon pixel detectors.
- **Layout 2:** The innermost three layers are equipped with silicon pixel detectors followed by four layers of silicon strip detectors.

In case of Layout 1 all layers will provide the same pointing resolution of about 4 μm (compared to presently 12 μm in the two innermost layers) which improves the tracking efficiency in the low momentum region (see Chapter 3) and enhances the momentum resolution. Layout 2 provides a spatial precision in r-ϕ in the outer layers which is comparable with the performance of silicon strip detectors similar to the present system and will also provide particle identification based on the information from the strip layers. The fake hit rate due to hit ambiguities in the strip layers is expected to be less than 5%. For both layouts the material budget especially of the innermost layers will be optimized to achieve a total material budget per layer of 0.3% X_0.

4.2 Requirements and Operating Conditions

The different layers of the ALICE ITS are divided into two groups: layer 1, layer 2 and layer 3 are referred to as the inner layers, while layers 4 through 7 are referred to as outer layers. In the case of Layout 2 this splitting distinguishes also the silicon pixel detector layers from the silicon strip detector layers. Tables 4.1 and 4.2 summarize the technical specifications for the inner and outer layers:

- The **material budget** has to meet stringent requirements especially for the innermost layers in order to improve the impact parameter resolution. The design target of 0.3% X_0 per layer is within reach using monolithic pixel detectors as is shown in Chapter 5. While for larger radii a maximum material budget of 0.8% X_0 is acceptable.
- The **chip size** for the innermost layers is tentatively set to be 15 mm $\times$ 30 mm. This size complies with the optimum mechanical arrangement of the inner layers around the beam to achieve a high

Table 4.1: Technical specifications for the inner layers (layers 1-3) of the new ITS.

Parameter	Design Value	Comment
Material Budget per Layer	0.3% X_0	Max.: 0.5% X_0
Chip Size	15 mm $\times$ 30 mm	Target Size
Pixel Size (r-ϕ)	20 μm	Max.: 30 μm
Pixel Size (z)	20 μm	Max.: 50 μm
Readout Time	$\leq$30 μs	Max.: 50 μs
Power Density	0.3 W/cm^2	Max.: 0.5 W/cm^2
Hit Density	150 hits/cm^2	Peak Value
Radiation Levels (Layer 1, r=22 mm)	700 krad (TID) 1×10^{13} n_{eq}/cm^2 (NIEL)	Safety-factor: 4

Table 4.2: Technical specifications for the outer layers (layers 4-7) of the new ITS.

Parameter	Design Value	Comment
Material Budget per Layer	0.3% X_0	Max.: 0.8% X_0
Cell Size (r-ϕ)	$\leq$70 μm	
Cell Size (z)	$\leq$2 cm	
Readout Time	$\leq$30 μs	Max.: 50 μs
Power Density	0.3 W/cm^2	Max.: 0.5 W/cm^2
Hit Density	$\approx$1 hit/cm^2	Layer 4
Radiation Levels (Layer 4, r=200 mm)	10 krad (TID) 3×10^{11} n_{eq}/cm^2 (NIEL)	Safety-factor: 4

pointing resolution as discussed in Section 3.9.5. It is also compatible with the maximum reticle size in the 0.18 μm CMOS process offered by TowerJazz of 2.5 cm $\times$ 3.2 cm.

– The reduced **pixel size** with respect to the present system allows to improve the pointing resolution and tracking efficiency in r-ϕ and improve the background reduction capability in z. A pixel length of approximately 20 μm leads to a pointing resolution of about 4 μm, while at larger radii 20 μm resolution are acceptable. Strip detectors with a pitch of 95 μm as proposed in Layout 2 are thus complying with this requirement. However, Layout 1, which proposes the use of pixel layers with a cell size in the order of 20 μm also at larger radii, shows an improvement in the pointing resolution at high p_T and in the tracking efficiency over the full momentum range (see Figures 3.14, 3.16).

– A **readout time** of 20 μs results in average in one additional pile up event for 50 kHz Pb-Pb collisions. On the other hand it is crucial to reduce the readout time as much as possible within the given power budget to separate primary and secondary vertices from different interactions.

– A target **power density** of 0.3 W/cm^2 puts stringent constraints on the design of the readout chips and the power distribution. This requires using deep sub-micron technology for the design of the readout chips and optimizing the chip readout architecture for shaping times of the order of μs.

– The **radiation levels** for the innermost layers are in the order of 700 krad and 10^{13} n_{eq}/cm^2 for a collected data set corresponding to 10 nb^{-1} Pb-Pb and 6 nb^{-1} p-p collisions. These radiation levels include a safety factor of 4. It is crucial to ensure full functionality in terms of radiation hardness especially for the innermost layer. At larger radii the radiation levels are significantly lower and do not present a limitation for the technology.

4.3 Pixel Detector Technologies

4.3.1 Pixel Concepts and Technologies

Two pixel detector technologies are under consideration for the ALICE ITS [55, p.76]: hybrid and monolithic silicon pixel detectors. The following section describes both underlying concepts and the 0.18 μm CMOS technology which has been selected for a dedicated R&D for the new ITS.

4.3.1.1 Monolithic Sensors

Monolithic sensors embed sensing diode and front-end electronics on the same silicon chip. They are produced using commercial CMOS technologies that are optimized for large volumes and are therefore very cost-effective. The sensor can be thinned down to 50 μm, offering a significant reduction in material budget. Pixel sizes of 20 μm $\times$ 20 μm or less are standard with these technologies. Among the different options presented in the previous version of this document, the quadruple-well CMOS Imaging Sensor (CIS) process provided by TowerJazz[1] has been identified as the most promising candidate and has thus been selected for a dedicated R&D within ALICE.

One key question to be addressed within such R&D is the radiation hardness of CMOS sensors in view of the expected radiation levels foreseen in ALICE. Additional issues are the design of an optimized pixel cell and of a low power readout architecture. To study these aspects several prototypes have been designed and submitted for production. Some of them have already been fabricated and are under test. Additional test chips optimized to study different readout concepts are in preparation.

The 0.18 μm CMOS Technology by TowerJazz offers several interesting features:

- Due to the feature size of 0.18 μm and gate oxide thickness below 4 nm it is expected that the process is substantially more robust to total ionizing dose than other technologies (such as 0.35 μm) employed up to now as baseline for the production of CMOS sensors in particle physics applications.
- The feature size and the number of metals available (up to six) are already adequate to implement high density and low power digital circuits. This is essential since the digital circuitry will be located at the periphery of the pixel matrix and its area must be minimized to reduce the dead material as much as possible.
- It is possible to produce the chips on wafers with an epitaxial layer of up to 18 μm thickness and with a resistivity between 1 and 5 kΩ·cm. With such a resistivity, a substantial part of the epitaxial layer will be depleted at the reverse bias voltage (1-2 V) normally applied to the collection diodes in CMOS sensors. This increases the signal-to-noise ratio and may improve the resistance to non ionizing irradiation effects.
- The access to a stitching technology, which allows producing sensors with dimensions exceeding those of a reticule enables manufacturing die sizes up to a single die per 200 mm diameter wafer. As a result, insensitive gaps in between neighbouring chips disappear, the alignment of sensors on a stave is facilitated and the chip power extraction gets more efficient.
- The availability of a quadruple-well option allows the production of pixel structures with significantly enhanced functionality [101].

The last point is a unique feature of this process and can be key to enable low power readout architectures. It is discussed in more detail in the following. Figure 4.1 shows a standard monolithic pixel cell (on

[1] TowerJazz, http://www.jazzsemi.com/

the left) compared with one implemented using the quadruple-well feature (on the right). In standard implementations, the sensing diode is an nwell normally used as the substrate of PMOS transistors.

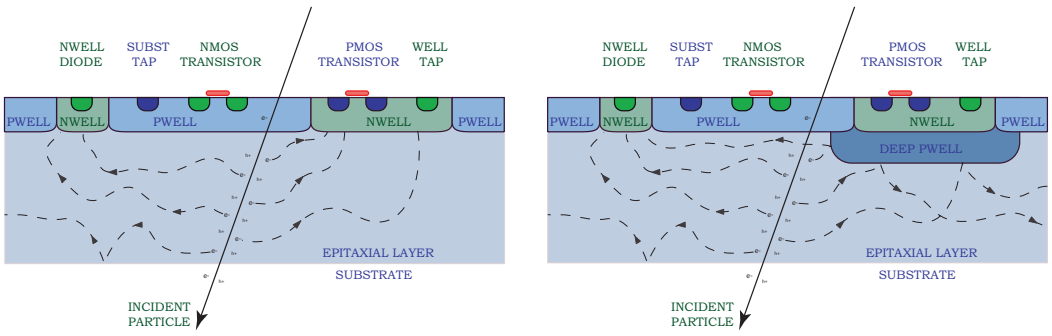

Figure 4.1: Comparison between standard and quadruple-well pixel concept.

As a consequence, only NMOS transistors can be used in the pixel area. In fact, any PMOS transistor requires an additional nwell that competes with the sensing diode in collecting the signal charge and affects the signal-to-noise ratio. The front-end electronics located in the pixel must fully rely on NMOS devices, so only simple, low-gain amplifiers or source followers can be implemented. Hit discrimination, which requires more sophisticated signal processing, can not be performed at the pixel level and the full matrix must be scanned during the readout phase. A few alternatives have been proposed to allow the use of PMOS in the pixel, like the use of deep-nwell [102] and of High Voltage CMOS technologies [103]. However, both options lead to a significant increase of the capacitance of the sensing electrode. Therefore, the power consumption in the front-end must be increased accordingly to preserve an adequate signal-to-noise ratio. The use of a quadruple-well circumvents this problem. A deep pwell is implanted in the region where the front-end electronics is foreseen. The nwells that accommodate the PMOS transistors are fabricated on top of the pwell. The signal electrons are reflected by the pwell and can be collected only by the sensing diode. Its size can then be tailored to optimize the charge collection efficiency and the signal-to-noise ratio, while full CMOS front-end electronics can be put in the pixel.

The effectiveness of the quadruple-well approach has already been demonstrated. Circuits with complex front-ends similar to those used for hybrid sensors readout have already been produced [104]. The focus of the ALICE R&D is on assessing the radiation hardness and on studying the quadruple-well approach in order to design circuits that minimize the power consumption and, consequently, affect the overall material budget.

4.3.1.2 Hybrid Pixels

Hybrid pixels are a mature technology presently employed in all four major LHC experiments. In a hybrid detector, the sensor and the front-end electronics are fabricated on two separate chips and then mated with the bump bonding technique. This offers the advantage of optimizing the sensor and its front-end electronics separately at the expense of extra thickness and cost. The radiation load foreseen in the ALICE ITS does not present a concern for this type of sensors. State-of-the-art hybrid pixels have a cell size of 50 μm $\times$ 50 μm, but the evolution of the interconnection technology is expected to put cell sizes of 30 μm $\times$ 30 μm soon within reach. In the recent months the focus on the hybrid pixel detectors was on the production of assemblies with the final thicknesses and the completion of the production of the first edgeless epitaxial silicon sensors. First results are presented in Section 4.3.4.5.

4.3.2 System Aspects

Table 4.3 shows the nominal z-coverage of the individual layers. The values of layers 1-2-3, 4-5 and 6-7 are very similar suggesting to use modules of equal length for each of the three groups. As mentioned in

Section 4.2 a tentative chip size of 1.5 cm $\times$ 3 cm is assumed. The modules for the inner layers will thus be formed by aligning 9 chips to provide 27 cm coverage in z, while 50 chips are required to provide the coverage of the outermost layer 7.

Table 4.3: Nominal z-coverage of the ITS layers and z length of the modules.

Layer Radius (mm)	Nominal z-Coverage (mm)	Module Length in z (mm)	Number of Modules
22	$\pm$ 112	270	12
28	$\pm$ 121	270	16
36	$\pm$ 134	270	20
200	$\pm$ 390	843	48
220	$\pm$ 418	843	52
410	$\pm$ 712	1475	96
430	$\pm$ 743	1475	102

The overall system must be optimized to minimize the material in the sensitive area while providing easy operation and maintenance along with adequate reliability. The configuration of the detector is chosen such that all services are connected from one side along z only (see Chapter 5). It is also foreseen to make at least the innermost layers easily removable to ensure a yearly access of at least the inner part of the new detector. The module layout, the signal and power distribution and the interconnection technology are the key issues discussed in this section.

4.3.2.1 Module Layout

The module design assumes a sensor size of 15 mm $\times$ 30 mm, with the shorter length referring to the r-ϕ direction. These dimensions approximately correspond to the maximum chip size available in the TowerJazz process without the use of stitching, so they represent a conservative hypothesis. It is also assumed that the sensitive area in r-ϕ is 13 mm, while 2 mm are left to accommodate the on-chip readout electronics.

The inner layers will be instrumented with the same type of module, built by aligning 9 dies and connecting them to a single bus cable (see also Chapter 5). The length of z = 27 cm is chosen to guarantee that the third layer has an η-coverage of 1.22. A conceptual design of the inner modules is shown in Figure 4.2.

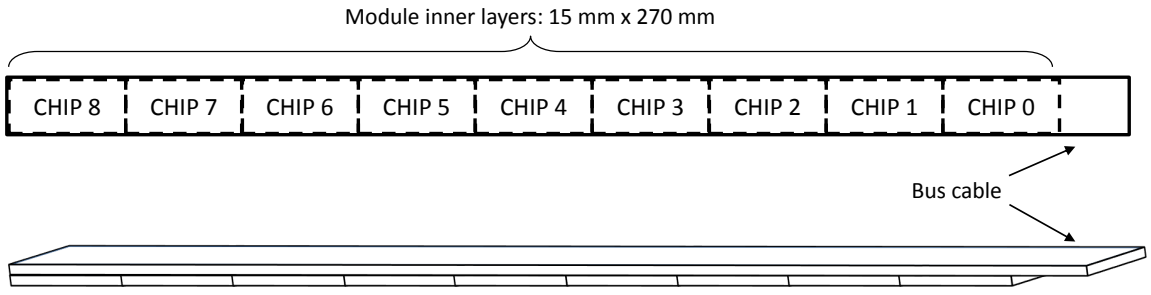

Figure 4.2: Module layout for the inner layers.

If Layout 1 will be adopted for the ITS, monolithic pixels will equip also the outer layers. In this case, the baseline option foresees two sensors connected face-to-face, so that the insensitive area due to the chip periphery is put at the border of the module. The use of two chips in a row is necessary to avoid excessively narrow structures that can pose severe challenges to the robustness of the mechanical support. The concept of the outer modules is shown in Figure 4.3.

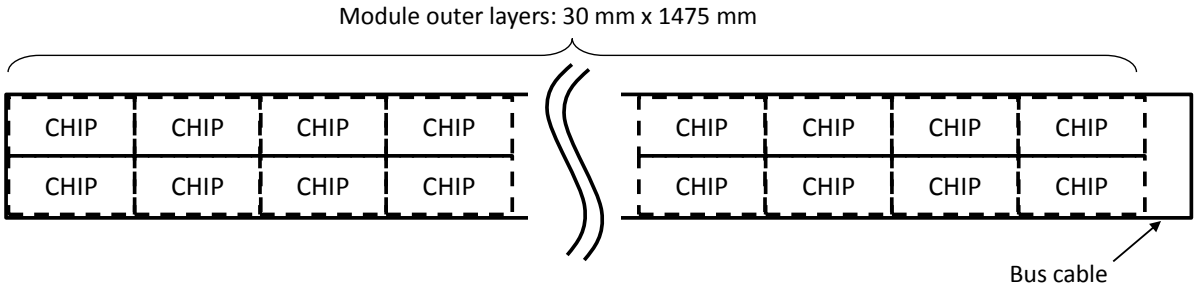

Figure 4.3: Module layout for the outer silicon pixel layers.

The two intermediate layers could be served by a single module with a length of 840 mm equipped with 28 sensors, while the two outermost layers could employ a module with 50 chips.

4.3.2.2 Chip Input and Output

In order to minimize the traces on the bus, the number of I/Os will be kept to a minimum. The sensor chip will be connected to the periphery using only digital signals with a differential transmission scheme. This is mandatory to minimize switching noise and to have a proper control of ground loops as well as to reach high speed transmission. The LVDS standard is hence a suitable option. With LVDS, the information is transmitted by steering a current either in one or the other direction between the two output lines, depending on the logic value to be transmitted. The current range is between 2.5 and 4.5 mA, and the line is terminated with a 100 Ω resistor (differential).

The sensor chip needs the following I/O:

- CLK: master clock to control the operation of the on-chip synchronous digital logic.
- CHIP_CTRL: write/read chip configuration, trigger and global chip reset.
- DATA_OUT: output port to send data out.

Figure 4.4 shows a schematic view of the connections scheme for one pixel chip. All connections are LVDS differential pairs. The CLK and DATA_OUT connections are uni-directional, while the CHIP_CTRL is bi-directional. A schematic view on how the connections are shared and arranged on an inner layer module is shown in Section 4.3.2.5.

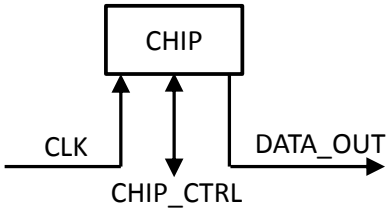

Figure 4.4: Schematic view of the input and output of a single chip.

The power consumption of an LVDS driver building block is between 5 and 10 mW, depending on the details of the implementation. However, the receiver of the CHIP_CTRL port does not need to be high speed. In this case slower receivers operating with less power can also be considered. This strategy is presently employed in the SDD layers of the ALICE ITS, where custom differential receivers with a power consumption of 0.5 mW per I/O are employed up to a transmission frequency of 40 MHz [105].

4.3.2.3 Data Transmission

The data bandwidth requirements are more severe for the inner layer, where a track density of 150 particles/cm^2 per event is expected. Assuming that each cluster is encoded with a 32-bit word and that the readout rate is 50 kHz, the required data bandwidth per cm^2 is 240 Mbit/s, while the total bandwidth per sensor is 936 Mbit/s, which can be accommodated in a single serial link with a speed of 1 Gbit/s. This demands an on chip high-speed serializer with a PLL (Phase-Locked Loop) to multiply the master clock frequency. In the inner layers each sensor needs a dedicated line for data transmission, so the I/O bus needs 22 lines with controlled impedance.

Moving to the fourth layer, the hit density drops to approximately 0.9 tracks/cm^2, reaching a value of only about 0.2 tracks/cm^2 in the outermost layer. On the other hand, the number of sensors per module increases. Since the maximum number of lines on the module cable is fixed, the outputs must be multiplexed. For example, in the fourth layer, a group of 8 sensors needs a bandwidth of 100 Mbit/s. At this low speed, one can send the data directly to the patch panels, where the electro-optical conversion takes place using commercial transceivers. The situation is different for the inner layers. In principle, LVDS allows the transmission of data at a theoretical rate up to 2 Gbit/s or more over lengths of several meters, but to reach such a speed the cable quality is essential. High performance cables are however bulkier, and their use might be prevented by mechanics and space constraints. In this case, the conversion from the electrical to the optical domain will take place on a service board located at the end of the modules.

As IPs (Intellectual Properties) the TowerJazz process offers some of the blocks which are needed in a data transmission system, such as LVDS drivers and PLL. These parts will be evaluated from the point of view of performance and radiation hardness and if the results will not be satisfactory, custom components will be developed.

4.3.2.4 Power Distribution

The front-end chip will have on board Low Drop Out regulators (LDO). Capless regulators, which employ only on chip capacitors for decoupling, are an attractive possibility and are becoming more and power popular for system-on-chip applications. A number of different designs are documented in the literature and they are also available as IP blocks. The use of DC-DC converters to power the modules is also considered. A dedicated R&D is being pursued by the CERN microelectronics group [106] on DC-DC converters optimized for particle physics applications. Particular emphasis is put on magnetic field compatibility and low noise performance. The converter fits in a board of 28 mm $\times$ 13 mm that could be located at the end of the staves.

One key issue with power distribution lines is the ringing introduced by the cable inductance when switching transients occur on the chip. From the point of view of the average power consumption, it is an advantage to have circuits that are powered-down if they are not in use. However, this puts more stringent requirements on the design of the bus and of the local decoupling network for the ASIC, possibly affecting also the material budget.

The design of the power planes becomes more challenging as the modules become longer. In case CMOS sensors are adopted for the outer layers, it is important to reduce as much as possible their power consumption to allow efficient cooling and uniform power supply distribution over long distances. This may lead to two different sensor optimization for the inner and outer layers. In the outer layers, in fact, a pixel size of 100 μm $\times$ 100 μm is still adequate from the point of view of the pointing resolution. Monolithic pixels as large as 70 μm $\times$ 70 μm have already been reported. The use of larger pixels however helps to reduce the power consumption only if the bias current in the front-end is not increased. This can nevertheless lead to worse signal to noise ratio and charge collection efficiency. Studies to optimize the design and aspect ratio of bigger cells suitable for the outer layer are in progress and first

results are reported in Section 4.3.4.4.4.

Providing power connection at both end of the modules is of course an advantage. A study is being carried out to see if a system of self-locking connectors [107] as used for the ALICE TPC would allow having a power connection of the barrels on both ends without the need to do manual cabling. This solution, schematically shown in Figure 4.5, would preserve the possibility of a fast insertion/extraction of the barrels during shutdowns; the signal connections will still be routed to one side of the barrel to maintain the fast access scenario.

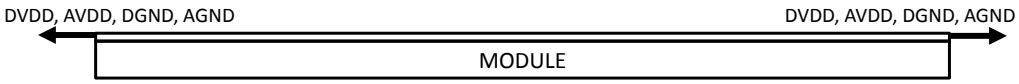

Figure 4.5: Schematic view of the power connection concept to both ends of the barrels. The signals are connected only on one side to maintain the fast access possibility.

4.3.2.5 Bus Cable

The bus cable will provide the chip I/O and power connections for each of the pixel chips in a module and will connect them via lines and power planes to the periphery. Detailed studies are being carried out to develop an electrical model of a bus cable and to study the different options of the layout. Figure 4.6 shows a schematic view of a bus cable layout for an inner layer module. The power planes are separated into AVDD-AGND and DVDD-DGND for analog and digital supplies, respectively. The signal lines are arranged on one side of the bus above the DGND plane which is used as reference to control the impedance of the signal lines.

Table 4.4 shows a list of the signal lines needed to connect the 9 chips in one inner layer module. The clock (CLK) is common to the 9 chips using an M-LVDS (multi-point-multi-drop LVDS) line. Similarly, the CHIP_CTRL connection is also a common M-LVDS line per module. The DATA_OUT connection is individual for each chip. A schematic view of the connection scheme for one inner layer module is shown in Figure 4.7.

Table 4.4: List of lines for an inner layer module indicating the number of differential pairs.

	Number of lines
CLK	1×2
CHIP_CTRL	1×2
DATA_OUT	9×2
Total/module	22

The width of the bus is limited by the dimension of the chips in r-ϕ which is tentatively 15 mm. As shown in Figure 4.6 the study is considering a double sided bus cable. In order to minimize the contribution of the bus cable to the material budget, it is foreseen to use a polyimide insulator with Aluminum as conductors. Results from first prototypes are presented in Section 4.3.4.7.

4.3.2.6 Interconnection

Aluminum wedge wire bonding is a standard technique to connect ASICs with PCBs (Printed Circuit Board) or bus cables which is also used in the present ALICE silicon pixel detector. This approach is fully compatible with the material budget requirements for the ALICE ITS. However, this requires wire bonding pads which are located at the periphery of the chip which will contribute to the insensitive region of the module. Studies are being carried out to assess the suitability of novel interconnection techniques such as Chip-On-Flex (COF) structures. In this case the contact pads of the chip are re-routed to a part or

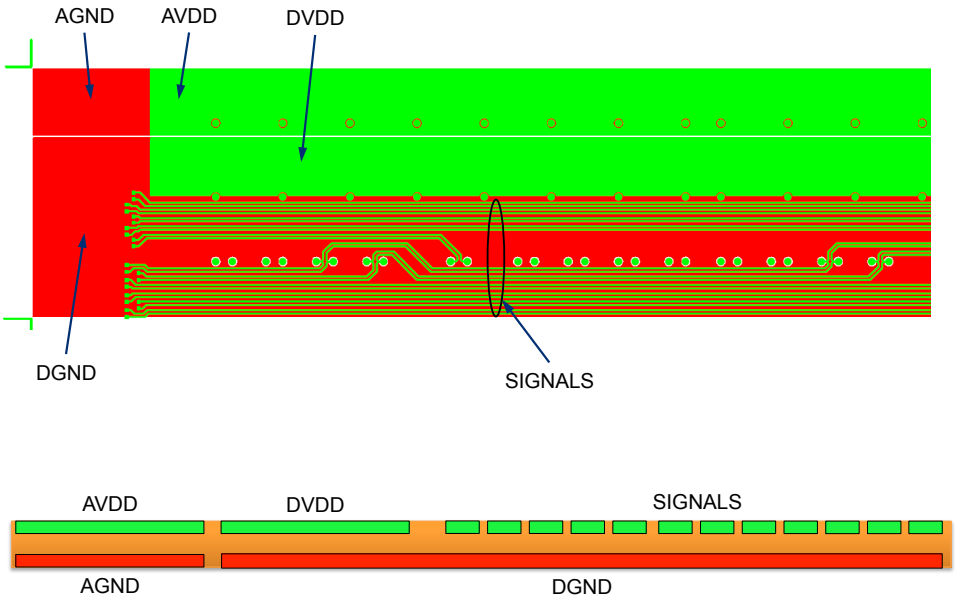

Figure 4.6: Layout study of a bus cable for a module of the inner layers. The top image shows the top view of the cable indicating the power planes and signal lines, while the bottom image shows the cross section through the cable.

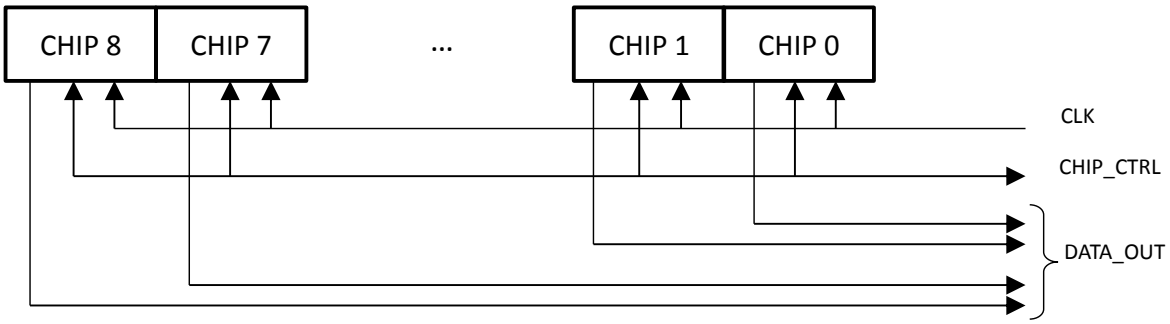

Figure 4.7: Signal connection scheme of an inner layer module. The CLK and CHIP_CTRL lines are common to all chips, while the DATA_OUT lines are individual for each chip.

the full surface of the chip where the connection to the bus cable is done by low impedance connections. Electrically this presents an advantage in comparison to wire bonding contacts which usually have a higher impedance than BGA (Ball Grid Array) type contacts.

The different types of interconnections that are under investigation for the ALICE ITS are:

- BGA ball connections using a pick and place machine and reflowing the balls inside a furnace.
- Solder ball connections using laser soldering.
- Au-stud bonding connections using a small layer of conductive adhesive to connect the stud.
- Ultra-Thin Chip Packaging (UTCP) [108].

The different thermal expansion coefficients of the bus cable and the silicon die will limit the use of standard furnaces. Studies are in preparation to find polyimides which are thermally matched to the

silicon. Figure 4.8 shows the cross section of a double layer bus assuming solder ball connections for laser soldering. The different metallurgical layers and their thicknesses are shown. First prototype results are reported in Section 4.3.4.7. Further studies to investigate the different interconnection options are currently ongoing.

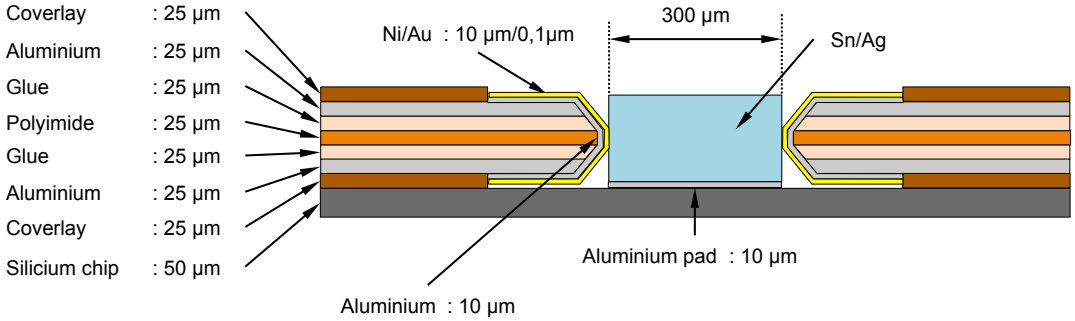

Figure 4.8: Schematic view of the bus cable cross section for solder ball connection using laser soldering. The different conducting and insulating layers and their respective thicknesses are shown.

4.3.3 Chip Architectures

The studies on readout architecture are focused on monolithic CMOS sensors, but techniques developed in this context can be easily adapted to readout hybrid pixels as well. Therefore, a readout scheme for hybrids pixels is not discussed separately and prototyping on silicon of dedicated front-end ASICs is not pursued at the moment.

Two readout architectures are under study for the ALICE pixels. The first architecture is based on the rolling shutter technique. The second topology employs a sparsified readout of the pixel matrix, so that only zero-suppressed data are transferred to the periphery. A design and prototyping effort is underway to identify the most suitable readout approach. The choice between the two schemes will depend on the results on readout speed, power consumption and noise obtained on these prototypes.

4.3.3.1 Monolithic CMOS Sensors with Rolling Shutter Read-Out

Rolling shutter is the standard approach for the readout of monolithic CMOS sensors. With this method the pixel matrix is continuously scanned row by row. This architecture results in a low power consumption, since only one row is being read out and powered at a time. In the present MIMOSA sensors [109, 110] the power consumption corresponds to 150-250 mW/cm^2 depending on the number of columns per surface unit and on their length.

In order to guarantee the small pixel size, the electronics inside each pixel is kept to a minimum, as shown in Figure 4.9. A pixel cell contains only the sensing element, a preamplifier, a clamping node ensuring in-pixel CDS (Correlated Double Sampling) and a row selector.

The first element after the collecting diode is the preamplifier. Its feed-back loop also provides the bias voltage of the pixel, with the advantage of a continuous leakage current compensation. A row selector activates one row at a time, and connects the pixels to the discriminators located at the end of column, where the signal is digitized after a second CDS that compensates the pixel-to-pixel offset. A sparsification algorithm is implemented on the digitized data, that identifies and encodes patterns of hits on one row of pixels, retaining only the information of the column address of the first pixel hit and the number of contiguous hits. With the processing of the matrix row by row, the sparsification and zero suppression algorithm will generate output states at a Poisson-distributed rate, going from zero states to a maximum number that depends on the chip occupancy. To equalize the output data rate

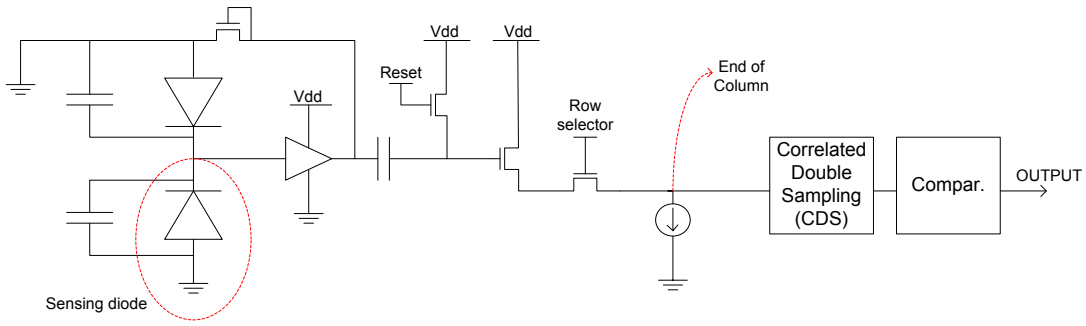

Figure 4.9: Simplified schematic of a pixel cell.

and limit the data bandwidth, a buffer will be implemented, in the form of memory blocks. For the existing sensors MIMOSA26 [97] and MIMOSA28 (alias ULTIMATE, being assembled on the STAR-PXL detector [111]), two memories are implemented and they are alternatively selected: when one memory is being written, the other is read, and viceversa.

The time between two consecutive readouts of the same row defines the integration time, which is of the order of 100 μs for state of the art CMOS sensors. This time must be significantly reduced to comply with the 50 kHz interaction rate. A sensor with an extension of the rolling shutter, low power architecture of ULTIMATE is under development for the ITS upgrade. This new sensor, called MISTRAL (standing for "**MI**MOSA **S**ensor for the **TR**acker of **AL**ICE"), is intended to increase the readout speed by a factor of at least four and to improve the radiation tolerance by one order of magnitude.

The baseline option of the MISTRAL sensor employs analogue readout, thus relying on the long-standing experience accumulated with the MIMOSA sensors. Each pixel column is connected to an end-of-column discriminator, which takes about 200 ns to process the signal. Assuming a pixel size of 20 μm $\times$ 20 μm (nearly the pitch of the ULTIMATE chip) one has 512 pixels for a column length of 1 cm. This would result in an integration time of 100 μs if standard rolling shutter is employed. This time can be cut by a factor of two by reading out two rows simultaneously. This approach imposes implementing two discriminators per column instead of one. For the sake of noise considerations, the column width needs some enlarging, e.g. to 22 μm. From the point of view of space resolution, elongated pixels of 20 μm $\times$ 40 μm (or 22 μm $\times$ 33 μm) are still well suited to the ALICE specifications. By halving the number of pixels in a column, one reduces the integration time correspondingly, without any further increase in power consumption. A readout time of 25 μs (or 30 μs) can hence be achieved, with an estimated power density of $\lesssim$ 400 mW/cm^2.

Alternatively, the potential of the quadruple-well option of the CMOS process may be exploited, by moving the discriminator from the column periphery into the pixel cell. With this approach, a discriminator is attached to one single pixel and the power consumption associated to the analog readout disappears. Moreover, since only (digital) signals above threshold are transferred, the row readout time shrinks to 100 ns or less. A readout time of 12-15 μs may thus be achieved by reading out two rows simultaneously. The expected power density amounts to $\lesssim$ 300 mW/cm^2. In addition, as the bulky fast discriminators are removed from the end of column, more digital logic can be accommodated and more rows can be read out in parallel. For instance, reading out simultaneously four rows would lead to 6-8 μs readout time, with a power density remaining below 500 mW/cm^2. This in-pixel discriminator architecture being less mature than the end-of-column one, it still requires a dedicated R&D effort before it can be validated for the ITS.

Finally, one should mention that the MIMOSA family has a triggerless architecture, meaning that once the readout of the pixel matrix is started, the frames are sent out continuously at a fixed frequency, independently from the collision rate. Studies are ongoing on a micro-circuit that will be implemented

inside the MISTRAL sensor to select only those frames that correspond to a collision that has activated the ALICE L0 trigger. This will reduce the chip power consumption and the output bandwidth, since not all the frames will be sent out.

4.3.3.2 Monolithic CMOS Sensors with Data Driven Read-Out

The use of in-pixel discriminators also offers the opportunity of a data driven readout, in which only the pixels above a given threshold transfer their data to the chip periphery. In this scheme, the detecting diode is biased by a diode which is linked to a reference voltage and provides the leakage current drawn by the detecting diode. The node connecting, detecting and biasing diode is linked to the amplifier input. The open loop amplifier amplifies the signal and also includes filtering to shape the signal and optimize the signal-to-noise performance. The amplifier output is connected to a comparator of which the threshold can be adjusted. A hit detected by the comparator is stored into a latch or onto a capacitor which retains the hit information even after the comparator output returns to zero, and interfaces with the priority encoder for the readout. A schematic of the circuit is shown in Figure 4.10.

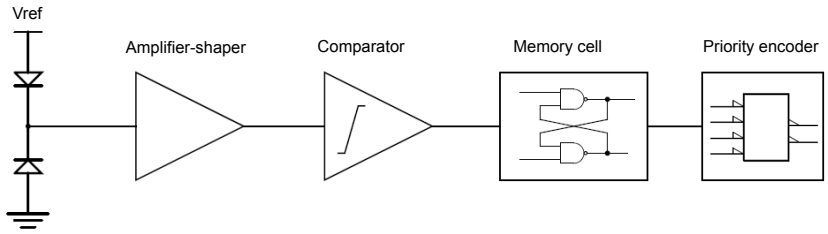

Figure 4.10: Scheme of a front-end for data driven readout.

Each pixel is organized into an analog section (containing the sensing diode, the front-end amplifier and the discriminator) and a digital section, which hosts the readout logic. The pixels are then arranged in double columns with a mirrored layout. This strategy is often employed also in front-end chips for hybrid pixel sensors and avoids close proximity between the digital part of a pixel and the analog section of the neighboring one. The concept is visualized in Figure 4.10.

Priority encoding is one method to allow the implementation of a data driven readout and is being extensively explored in the framework of the ALICE R&D. The advantage of this technique is that it does not require hard-wire encoding of the address of each pixel. Furthermore, it can be implemented without distributing a readout clock to the pixel matrix, favoring low power consumption and low noise. To explain the method, a simple case with eight pixels is illustrated in Figure 4.11.

Note that the readout chain is obtained by repeating the same basic logic block. The basic unit has a forward and a feed-back signal path (represented respectively with blue and red lines in Figure 4.11). The readout is organized in more hierarchical layers. In each layer, a portion of the desired address is generated. The first layer receives inputs directly from the pixel matrix. If at least one of the pixels is active, a valid signal is propagated down the chain and a feed-back signal is issued. Suppose, for instance that the two pixels connected to the topmost block have both valid outputs and that the pixel with lower number has higher priority. A valid signal is generated by the topmost block (valid[0]=1) and propagated down the chain, so that also valid[6] in the last block is driven high. This triggers the generation of a feed-back signal, which is applied to fdbk[6] and propagated backwards. The rising edge of the feed-back signal allows one block to take control of the address line, which in the internal layers is shared among all the units in the same column (or double column). Since valid[4] is high, the line fdbk[4] is activated and a ”0” is put on addr[2]. Since valid[0] is high, a ”0” is also encoded on addr[1] and the feed-back signal is propagated on fdbk[0]. Both data[0] and data[1] are high, but the pixel with higher priority (data[0]) is our example) is selected and a ”0” is generated on addr[0]. Hence, the address ”000”

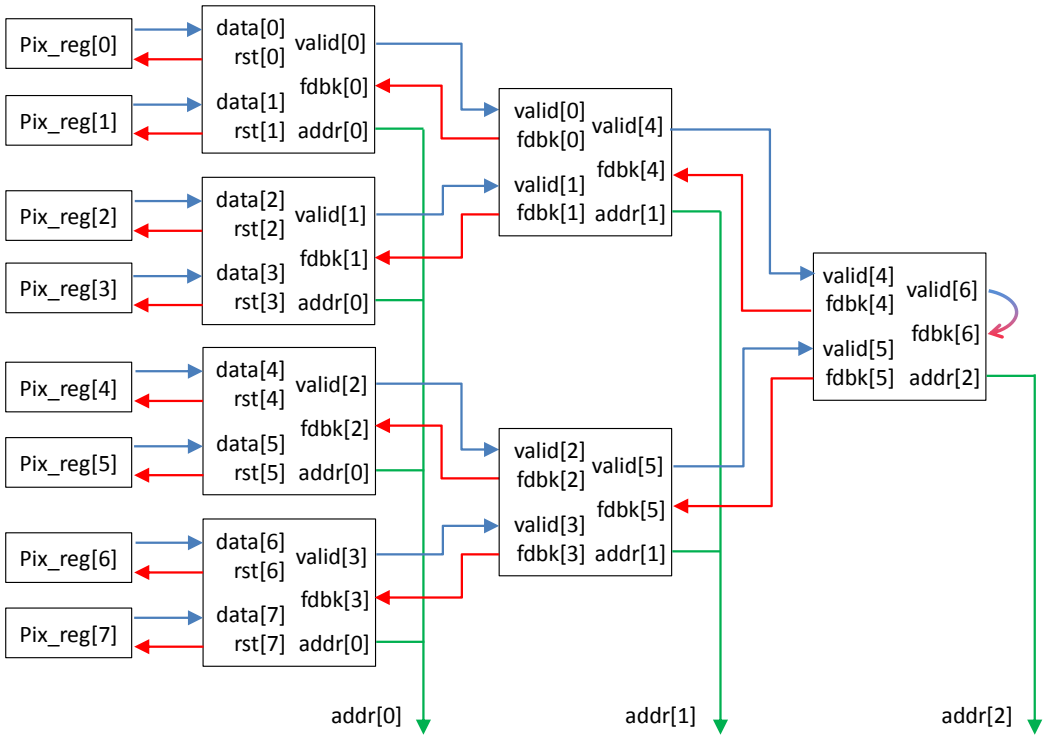

Figure 4.11: Block diagram of readout with priority encoding and decoding for reset.

is encoded on the bus. The feed-back signal also selects the interested pixel for reset, which occurs on the negative edge of the feed-back itself. Then, data[0] is driven low and a new read out cycle can start. The readout will proceed in the same way, but this time, since data[0] is low and data[1] is high, the address ”001” is produced.

The number of layers in a priority encoding scheme depends on the number of inputs that a basic block can handle. For instance, in our example one could have a unit block with four inputs. In this case, the output address line will be a two-bit bus and only two levels of hierarchy will be needed. In general, it can be proven that if N is the total number of pixels to be readout and b is the number of inputs of the basic block, the number of layers and the total number of blocks are respectively given by:

$$N_{layer} = log_b(N) \tag{4.1}$$

$$N_{block} = \frac{N-1}{b-1} \tag{4.2}$$

For example, if 256 pixels have to be readout one needs an 8 bit output bus. If the basic block has four inputs, applying the above formulas results in four layers with a total number of 85 blocks. Increasing the number of bits per block reduces the number of layers and hence the propagation delay, but increases the complexity of the design of the unit cell. Different segmentation are being explored to find the right balance between readout speed and layout complexity.

The interval between two consecutive readout cycles depends on the propagation delay of the logic, but a time of 100 ns can be considered a conservative assumption. Therefore, addresses are produced on the output bus at a 10 MHz rate. To make an estimation of the overall readout speed let’s suppose to have a pixel size of 20 μm $\times$ 40 μm, which results in a matrix with 256 $\times$ 512 pixels per cm^2 and in 512 pixels per each double column. Assuming a density of 100 tracks per cm^2 per event and a cluster multiplicity

of eight, at each interaction three hit pixels are expected in a double column. In this case, the readout requires 300 ns. Even considering some inhomogeneity in the hit distribution, the transfer of only zero suppressed data from the matrix to the periphery allows a full scan in a time scale of the order of one microsecond. It has been estimated that the power consumption of the priority encoding scheme is less than 30 mW/cm^2.

Although this looks very promising, one must take into account that in a data driven scheme the very front-end of all the pixel cells are active simultaneously, whereas in the rolling shutter approach only a few rows at a time are switched on. Therefore, particular care must be taken in the design of the in-pixel signal processing chain. Here two solutions are under investigation: one based on continuous time signal processing and another in which the front-end is activated on the L0 trigger signal. Assuming in fact that the front-end (amplifier+discriminator) is switched on for 0.5 μs at every trigger, the average duty cycle at 50 kHz is only 2.5%. A total bias current of 4 μA during the on phase and a power supply of 1.8 V will result in an average power of 90 mW/cm^2. The impact of power supply noise arising from the simultaneous activation of many cells must however be studied carefully.

Finally, it must be mentioned that the quadruple well technology makes possible also alternative sensor design employing more traditional front-ends. In fact, the desired speed and power consumption could be obtained with a different arrangement of the matrix. The idea is to organise the sensor in sub-arrays, see Figure 4.12. Each pixel would have an analogue front-end and would it be controlled in much the same way as a conventional pixel. Columns and then subarrays would be built up from this pixel . The size of the subarray could be tailored to match the required specifications, like speed and power consumption. In order to avoid any dead space, circuitry (labelled column-circuitry) which is normally integrated at the end of the column, can be incorporated directly in the column. This scheme has been already pioneered in the Cherwell prototype [104]. Such a design avoids dead regions in the periphery and can be particularly interesting to cover large surfaces, as more sensors can be tiled minimizing the insensitive area between them.

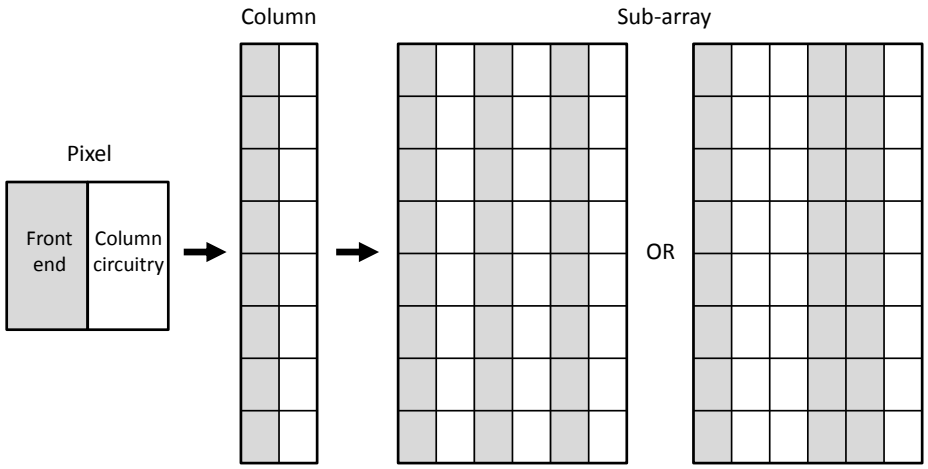

Figure 4.12: Concept of CMOS sensor avoiding dead area at the periphery.

4.3.4 Prototype Development and Test

A dedicated R&D for the ALICE ITS has been started to address the following technical key topics:

- Study on the radiation hardness of the TowerJazz 0.18 μm CMOS process.
- Study of charge collection, noise performance and tracking efficiency of prototype circuits implemented in TowerJazz 0.18 μm CMOS process before and after irradiation.

– Study of readout architectures and optimization of the power dissipation.

– Study of construction and assembly of thin modules.

– Layout of the modules and signal and power connection schemes.

– Investigation of novel compact interconnection schemes and development of a light weight bus cable.

In the following sub-sections test plans and first results of these studies are reported.

4.3.4.1 Irradiation Tests

The radiation levels expected for the HL (High Luminosity) phase impose stringent requirements on the radiation hardness of the innermost layers of the ALICE ITS. As described in more detail in Chapter 3, the yearly radiation levels expected for the 1st layer (radius=22 mm), including a safety-factor of 4, are 700 krad and 1×10^{13} n_{eq}/cm^2.

Ionizing radiation such as X-rays essentially induces radiation damage in front end electronic elements consisting of silicon oxides such as transistors and isolation layers resulting in a change of threshold voltages and increased dark currents. The irradiation with hadrons (NIEL) on the other hand leads to a damage of the bulk lattice that in turn can degrade the performance of the sensor in terms of signal-to-noise ratio and charge collection efficiency. Furthermore ionising radiation in digital structures can lead to a Single Event Upset (SEU), a non permanent change of state caused by ions or electro-magnetic radiation striking a sensitive node in a micro-electronic device, or to a Single Event Latchup (SEL), a type of short circuit that triggers parasitic structures which can disrupt proper functioning of the element, or possibly even can lead to its destruction. To simulate the impact of the expected radiation level in the ALICE ITS systematic irradiation tests using X-rays, protons and neutrons are carried out throughout 2012 and onwards on various sensor, analog and digital test structures in order to:

– Study their performance, stability and annealing behavior before and after X-ray and hadron (neutrons and protons) irradiation as basis for a recommendation of a technology to be chosen as baseline for the development of future ITS prototype detectors;

– Gain experience in the operation of new ITS structures under realistic operational conditions;

– Provide further input for simulation studies on the expected detector performance under upgrade run conditions.

To disentangle the various radiation-induced effects 3 types of structures are currently under investigation:

– Basic structures (diodes and transistors): 2 test structures were designed and implemented in TowerJazz 0.18 μm CMOS technology in order to study basic operational parameters such as threshold voltage, transconductance, and dark current as a function of radiation type and dose as well as of the layout. Test structures containing various types of NMOS and PMOS transistors and capacitors for different epitaxial thicknesses have already been produced in earlier runs and are available for radiation tests (RAL structures). Special test structures (TID_TJ180) consisting of various transistor types as well as breakdown diodes were developed and produced in addition in the first half of 2012 (ALICE_ITS_TJ180).

– Digital structures: a test chip for dedicated SEU tests has been designed and implemented in TowerJazz 0.18 μm CMOS technology (SEU_TJ180) consisting of various RAM structures and shift registers to test the stability and reliability of switching states during irradiation with charged particles.

– Full sensor structures (including analog and digital front end electronics): MIMOSA32 prototype matrices were produced in TowerJazz 0.18 μm CMOS technology containing both analog and digital elements that allow the characterization of full sensor prototypes under irradiation and test beam conditions.

A more detailed description of the prototype structures and preliminary results of irradiation tests carried out so far is given in the following section.

4.3.4.2 Testbeam

Operation and performance tests of prototype matrices in a high momentum particle beam are an integral part of the qualification procedure. First test beams have been carried out using non-irradiated and irradiated MIMOSA32 test matrices. First results of these tests are reported in the following Section 4.3.4.4. Another test beam period is foreseen for October 2012 at the CERN SPS in the EUDET telescope [112] to measure MIMOSA32 chips. The readout will be performed using the dedicated ALICE ITS readout system described in Section 4.3.4.3. First integration tests of the different data acquisition systems have been carried out successfully and presently preparations for the mechanical integration are underway.

In July 2012 two Timepix chips [113] have been tested in the T10 beam area at the PS. Objective of such tests was to study the suitability of Timepix modules as compact and mobile beam monitoring device for test beam purposes. Timepix is derived from the Medipix2 chip which was developed for single photon counting applications and consists of a 256 $\times$ 256 55 μm matrix of 55 μm $\times$ 55 μm pixels. The tests have been successfully completed and one Timepix system is now available to be used as beam monitor either for SEU tests or for the upcoming beam test in late 2012.

During the LHC shutdown in 2013/14 test beams will be carried out outside of CERN. One option under investigation is the possibility to carry out test beams at DESY. In the coming years the need for beam time will substantially increase as it is an essential ingredient for the validation and selection of the technology to be adopted. Test beams will remain an important part of the activity as part of the Q&A procedure beyond the R&D phase also during the production of the final detector.

4.3.4.3 Test Setups

A versatile readout system has been developed for the ITS upgrade. This system will be used for the readout of different prototype chips in laboratory tests and test beams. The readout system consists of a principal readout card (ZRC), an auxiliary card, and a web user interface.

Presently being used by the ALICE Zero Degree Calorimeters [114], the ZRC (ZDC Readout Card) is a general purpose card that provides an interface to the ALICE DATE (ALICE Data Acquisition and Test Environment) via DDL (Detector Data Link) interface or Ethernet. Through mezzanine boards, the ZRC card can be interfaced with up to 4 various application specific auxiliary cards, which are the interface between the ZRC and the proximity (or carrier) board on which the pixel sensor is housed. The ZRC is also equipped with a NIM-LVDS I/O mezzanine card to interface with the ALICE trigger system or to receive and process external trigger signals.

The user can configure the readout system through a web interface which communicates with the Ethernet interface on the ZRC. The configuration data are sent from the ZRC to the auxiliary card and also to the pixel sensor. After initializing the readout, the data coming from the pixel sensor are received by the

auxiliary card and then sent to the ZRC card, which performs an event building by combining data from the sensors, attaches a common data header and then sends the event to ALICE DATE. The system can be configured to work with a trigger or in a continuous mode.

One test system is currently at CERN to test MIMOSA32 pixel sensor prototypes. Further test-systems will be distributed to other users in the coming weeks.

4.3.4.4 Prototype Results

4.3.4.4.1 Irradiation Tests - TID_TJ180 Structure A set of test structures has been submitted for production in February 2012 in order to evaluate different aspects of the TowerJazz 0.18 μm CMOS technology. Radiation tolerance is tested using the CMOS structures of the TID_TJ180 block that is shown in Figure 4.13.

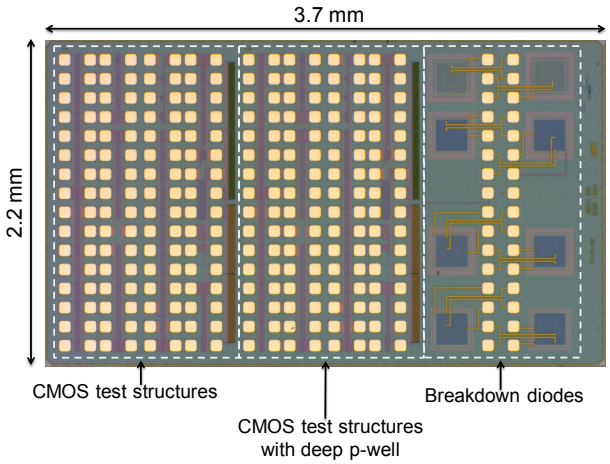

Figure 4.13: Picture of the TID_TJ180 test structure indicating the dimensions and the individual blocks.

The TID_TJ180 structure consists of the following blocks:

- CMOS transistors with different sizes, different gate oxide thicknesses and threshold voltage options. Other devices like resistors, FOXFETs (Field OXide Field Effect Transistor), diodes and capacitors are also implemented.
- CMOS test structures containing the structures of the first block but with a deep pwell (DPW) layer.
- Breakdown diodes containing 8 matrices of nwell diodes to measure the diode breakdown voltage and depletion layer capacitance in reverse bias. This block is organized in regular structures of 16 $\times$ 8 pad matrices, each of which can be tested individually in a probe station.

First irradiation tests of PMOS and NMOS structures were carried out using a X-ray system at CERN. Figure 4.14 shows I_d as a function of V_{gs} measured on an NMOS transistors before and after irradiation up to 10 Mrad. A shift of the threshold voltage can clearly be recognized for an irradiation level 10 times higher than expected in the ALICE ITS. Figure 4.15 shows the shift of the threshold voltage ΔV_{th} as a function of the irradiation dose, indicating a threshold voltage shift of about 10 - 20mV at the expected radiation level for layer 1 of about 700 krad for the minimum size NMOS and PMOS devices. These values are within the expected intrinsic process mis-match of the technology. As proven with other deep-submicron technologies the threshold values of the ELT (Enclosed Layout Transistor) devices are unchanged up to 10 Mrad TID. Similarly, the radiation induced leakage current is very small even up to the highest measured dose. At 10 Mrad, after 24 hours of annealing, threshold shift values recover

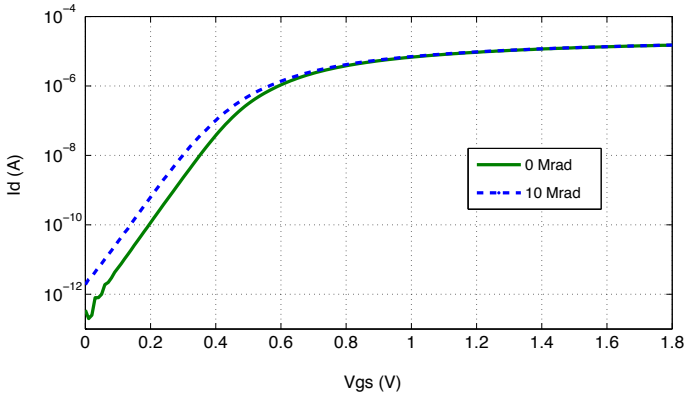

Figure 4.14: Drain current as function of the gate-source voltage of a minimum size NMOS transistor measured before X-ray irradiation and after irradiation up to 10 Mrad.

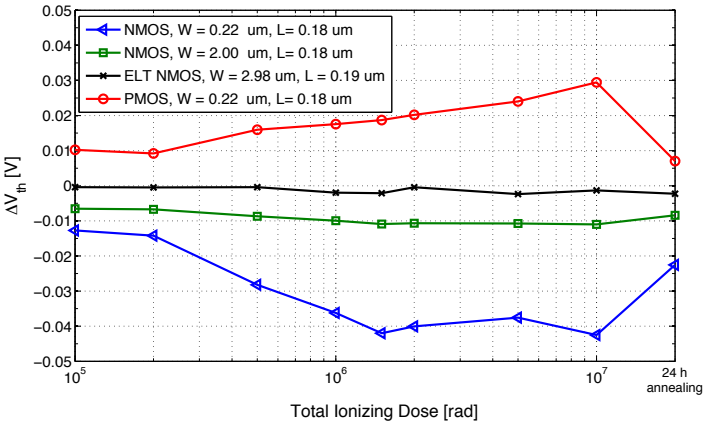

Figure 4.15: Threshold voltage shift as function of TID of PMOS and NMOS transistors with and without ELT layout.

significantly as can be seen in Figure 4.15. A similar effect is observed for the radiation induced leakage current.

4.3.4.4.2 Irradiation Tests - RAL Structures A dedicated test setup has been developed to characterize 0.18 μm TowerJazz CMOS test structures designed by RAL [2] before and after irradiation with X-rays. The structures contain a set of PMOS and NMOS transistors, capacitors and special structures to test the nwell isolation behavior [55, p.89].

In total 10 dies produced with a 5.5 μm epitaxial layer have been mounted on dedicated carrier cards. The structures are not protected against electrical discharge and were partly destroyed during setup and preparation. Consequently only a subset of the produced structures was available for irradiation tests that were carried out using the same X-ray irradiation system as for the TID_TJ180 structures.

The irradiation was carried out in pre-defined steps of 100 krad, 200 krad, 500 krad, 1 Mrad, 2 Mrad and 5 Mrad. Few samples were are also irradiated up to 10 Mrad. Each chip has been tested before irradiation and immediately after each irradiation step. After the maximum dose step the chips were stored at room temperature and remeasured after 24 hours and 1 week of annealing. First results of I_d as a function of V_{gs} for 2 of these PMOS structures are shown in Figure 4.16 showing the shift of I_d towards higher V_{gs} after 10 Mrad. The shift of the threshold voltage ΔV_{th} as a function of the irradiation dose

[2] Rutherford Appleton Laboratory, Didcot, UK

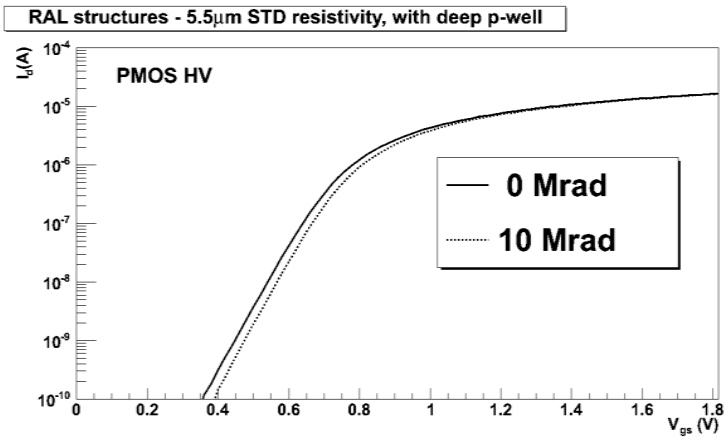

Figure 4.16: Drain current as function of the gate-source voltage of a PMOS transistor measured before X-ray irradiation and after irradiation up to 5 Mrad.

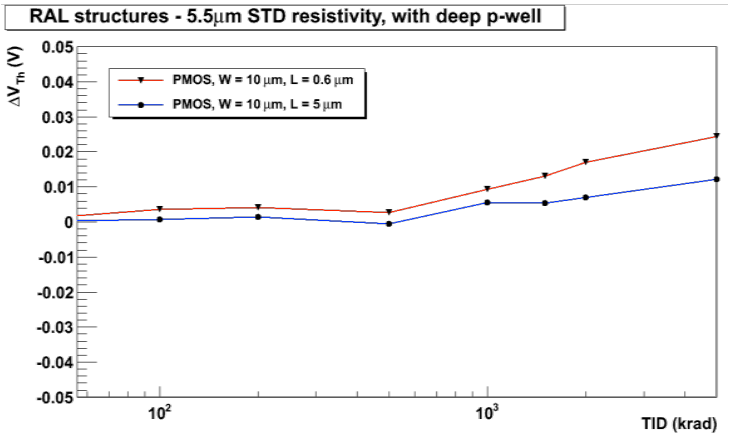

Figure 4.17: Threshold voltage shift as function of TID of two PMOS transistors irradiated up to 5 Mrad.

remains in the order of 20-30 mV up to 5 Mrad. Figure 4.17 shows the observed threshold shift of two PMOS transistors irradiated up this dose. The results are compatible with those obtained on TID_TJ180 structures and are within the precision of the measurement setup.

4.3.4.4.3 SEU Structure The SEU_TJ180 block, shown in Figure on the right, has been designed to evaluate the Single Event Upset (SEU) sensitivity of the 0.18 μm TowerJazz CMOS technology. Figure 4.18 shows a picture of the structure indicating the dimensions. The SEU_TJ180 has been designed to work with a frequency of up to 10 MHz; the three modules that it contains are implemented using 1.8 V CMOS IP cells, and they share the main clock and some signals such as data IO and addressing ports. This chip was submitted to TowerJazz in February 2012 and it was delivered by the foundry at the beginning of July 2012.

The total size of this block is 4.9 mm $\times$ 4.4 mm and it consists of 3 the following modules:

- SP_RAM block containing an array of 16 single port RAM memories 1024 $\times$ 16 bits;
- DP_RAM block containing an array of 8 dual port RAM memories 2048 $\times$ 16 bits;
- SR block with a 16 bit 2048 stages shift register.

Currently 2 different test setups for the SEU_TJ180 structure are under construction:

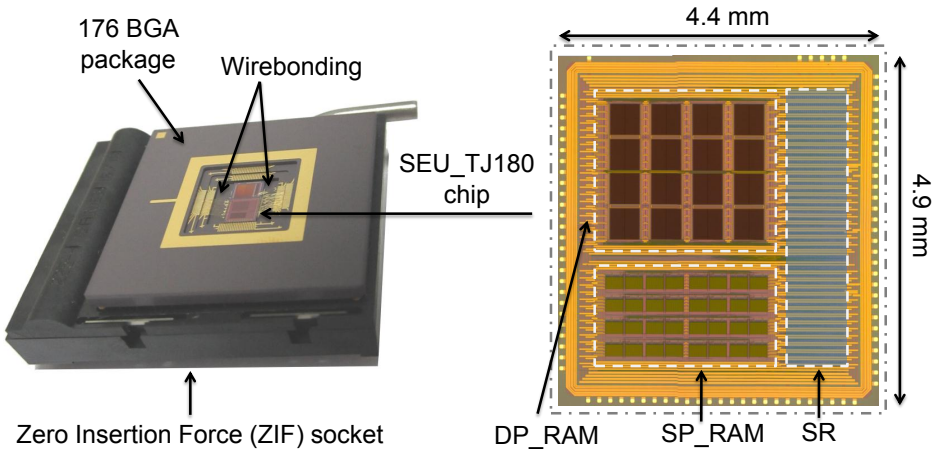

Figure 4.18: Picture of the SEU_TJ180 structure indicating the dimensions and different blocks (right) and picture of one SEU_TJ180 structure mounted on the test socket (left).

- The readout system described in Section 4.3.4.3 will be used to read out the SEU structures before and after irradiation with protons from different beam sources.
- NPI Prague has developed a test system consisting of a SEU device kit board, a FPGA board for connectivity via USB and a board for the acquisition of analog data. Test measurements using this system will be carried out using mono-energetic α-sources and proton beams from a cyclotron. A dedicated GUI allows for a convenient operation and analysis of the test data.

Objectives of the test measurements are to identify the distribution of SEU across the test structures and the evaluation of the SEU cross section as a function of proton energy. The mapping of SEU can also be measured using picosecond infrared lasers. First results of the test measurements are expected by end of October 2012.

4.3.4.4.4 MIMOSA32 In winter 2011 a first chip was manufactured in the 0.18 μm TowerJazz technology, based on a high-resistivity, 18 μm thick, epitaxial layer. Various pixel designs were implemented in the chip to compare their charge collection properties and investigate the radiation tolerance of the technology.

The former were first studied with an ^{55}Fe source, looking at the chip response to the 5.9 keV X-rays it emits. Figure 4.19 displays the distribution of the charge collected by pixels containing a deep pwell hosting two PMOS transistors polarised with the 1.8 V reference voltage of the process. The figure shows the charge collected in the seed pixel of the clusters (left) and in the set of 4 pixels in a cluster which collects most of the charge. The figure on the left exhibits a small peak at large charge values, which originates from those X-rays impinging the chip in the vicinity of a sensing diode, which thus collects its full charge (about 1640 e^-). For the most common case, the charge is shared among several pixels forming a cluster, the seed pixel collecting typically 40-50% of the total cluster charge. The right panel of the figure shows that nearly all the cluster charge is concentrated in 4 pixels, confirming the limited diffusion of the charges due to the high resistivity of the epitaxial layer.

The figure shows also the distributions measured after an exposure of the chip to a TID of 3 Mrad. No significant degradation is observed, indicating that the yearly dose expected in the ITS innermost layers ($\leq$ 1 Mrad) should not modify the sensor charge collection properties. There is in particular no indication of a parasitic charge collection node generated by the deep pwell.

The pixel noise was measured to be in the range of 15-20 e^- ENC at room temperature (20°C), depending

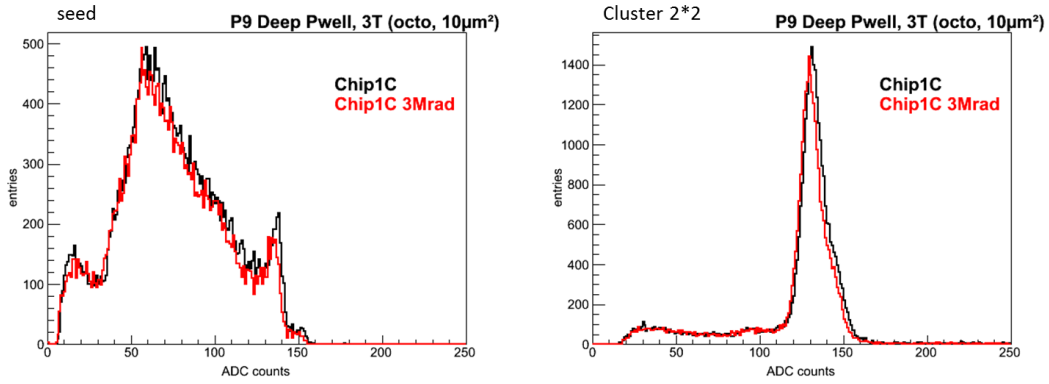

Figure 4.19: Measurement of MIMOSA32 (deep pwell) before (black curve) and after (red curve) 3 Mrad TID.

on the pixel type, and exhibited no significant change after a 3 Mrad TID.

Beam tests were performed in summer 2012 at the CERN-SPS with 60-120 GeV particles, which allowed evaluating the chip detection performances at two different coolant temperatures (T_c =15°C and 30°C), before and after a combined radiation load of 1 Mrad and 10^{13} n_{eq}/cm^2. The study is based on 6 different MIMOSA32 dies, tested individually on a beam telescope composed of four pairs of microstrip detectors. The detection performances (e.g. signal charge collected, pixel noise, signal-to-noise ratio (SNR), hit cluster properties, detection efficiency) were derived from a total sample of about 50,000 tracks reconstructed in the beam telescope and traversing the pixel array under test.

Five different pixel variants were investigated. Three variants featured a square geometry with a 20 μm pitch, one of them hosting the deep pwell mentioned earlier. The two remaining variants address an "elongated" geometry based on 20 × 40 μm^2 large pixels. The designs of the latter differ by their charge sensing system, made of a single sensing diode in one case and of a pair of interconnected diodes in the other case. For the sake of radiation tolerance and single point resolution, the pixel pattern was staggered. As compared to the square pixels, the sensing diodes feature a reduced area (9 μm^2 instead of 10.9 μm^2) in order to maintain the capacitive noise at an acceptable level when interconnecting the diodes.

The hits reconstructed in the square pixels exhibited a typical cluster charge of ∼1100-1200 electrons, essentially concentrated in 2 to 4 pixels, about 40-50 % of the charge being collected by the seed pixel. Figure 4.20 displays the distribution of the charge collected by the cluster seed pixel in the deep pwell case. The measurements were performed at T_c = 30°C before and after irradiation. The latter originates no visible effect on the charge collection efficiency, but increases the noise by more than 50%.

The noise values observed reproduce those measured in the laboratory ($\lesssim$ 20 e^-ENC before irradiation and $\lesssim$ 30 e^-ENC after irradiation, at T_c = 30°C). The SNR varies accordingly from 30-35 (MPV) before irradiation, depending on the pixel variant, to 20-25 for the aforementioned combined radiation load. The detection efficiency, which is about 100% before irradiation, remains nearly unchanged after irradiation (e.g. the deep pwell pixels exhibits still a detection efficiency of 99.87 ± 0.07%(stat)). Its measured SNR before and after irradiation is shown in Figure 4.21.

Similar measurements were performed with the elongated pixels. Because of the lower sensing node surface and density, the seed pixel was only collecting ∼400 electrons (MPV) in case of the single-diode pixel. This value raised to ∼550 electrons in case of double-diode pixels. These values decreased slightly after irradiation (see Figure 4.22, while the noise was observed to increase significantly.

The corresponding SNR MPV measurements are displayed in Figure 4.22 (right) for the single-diode pixel, zooming the lowest values of the distribution, where detection inefficiencies would manifest themselves. The SNR amounts to ∼22 before irradiation and drops to ∼11 after irradiation. The detection

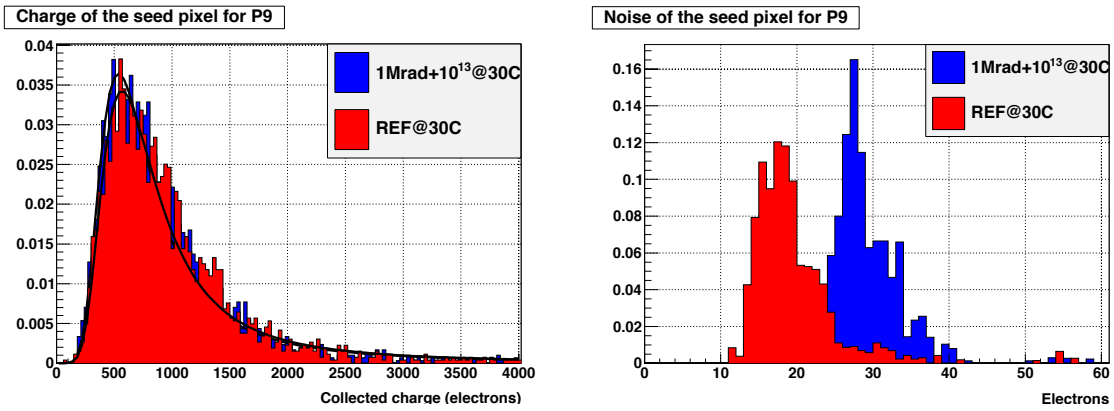

Figure 4.20: MIMOSA32 deep pwell pixel beam test results: charge collected by the seed pixel of the reconstructed clusters (left) and pixel noise (right) at T_c = 30°C. The results are shown before (red) and after (blue) irradiating the sensor with 1 Mrad and $1 \times 10^{13} n_{eq}/cm^2$.

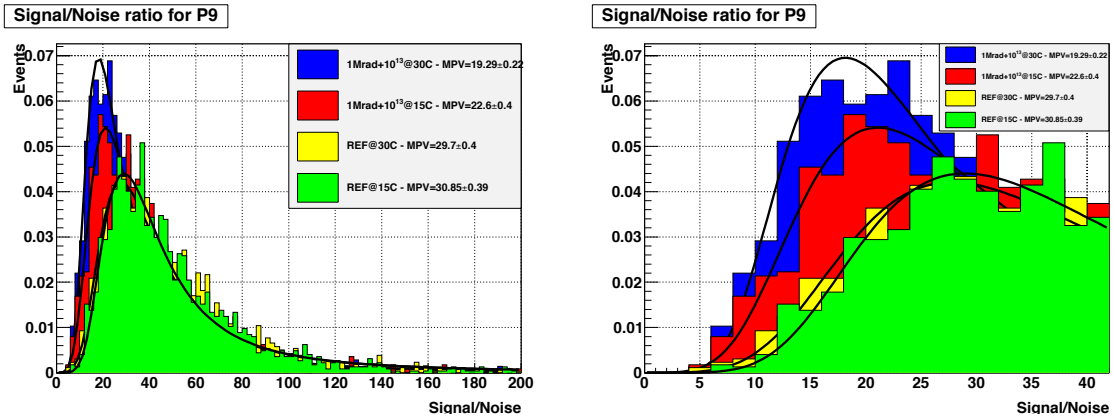

Figure 4.21: MIMOSA32 deep pwell pixel beam test results: seed pixel SNR at T_c = 15°C and 30°C, before (yellow and green) and after (red and blue) irradiating the sensor with 1 Mrad and $1 \times 10^{13} n_{eq}/cm^2$. The distribution on the right is a zoom on the low value range of the full distribution shown on the left.

efficiency decreases accordingly from about 100% before irradiation to about 98% after. The latter value increases to about 99.5% when reducing the coolant temperature to 15°C. Overall, the double-diode pixels exhibit very similar performances.

Accounting for the modest optimisation of the single-diode elongated pixel design and for the high irradiation load and operating temperature considered, the results obtained with this pixel geometry are very promising and allow taking this approach as a baseline for the MISTRAL pixel design.

4.3.4.5 Hybrid Pixel Assemblies

For hybrid pixel detectors the chip and the sensor will be optimized separately. A key issue is the reduction of the thickness of the two components down to a target thickness of 50 μm for the ASIC and 100 μm for the silicon sensor. A study was started together with IZM Berlin to develop a process to achieve such thicknesses for a hybrid pixel detector using standard bump bonding technology with Sn-Ag bumps. The first dummy assemblies using the present ALICE pixel layout (8192 pixels per chip of 50 μm $\times$ 425 μm) have been produced with the final thicknesses. A thorough inspection of the sensor and chip edges did not reveal any cracks or other potentially fatal mechanical damages. A SEM (Scanning Electron Microscope) inspection of the assemblies allowed to precisely measure the thicknesses of the samples and to inspect the bump connections on the edges by inspecting the side of the assemblies. On the first set of assemblies delivered, individual open connections on the corner of the

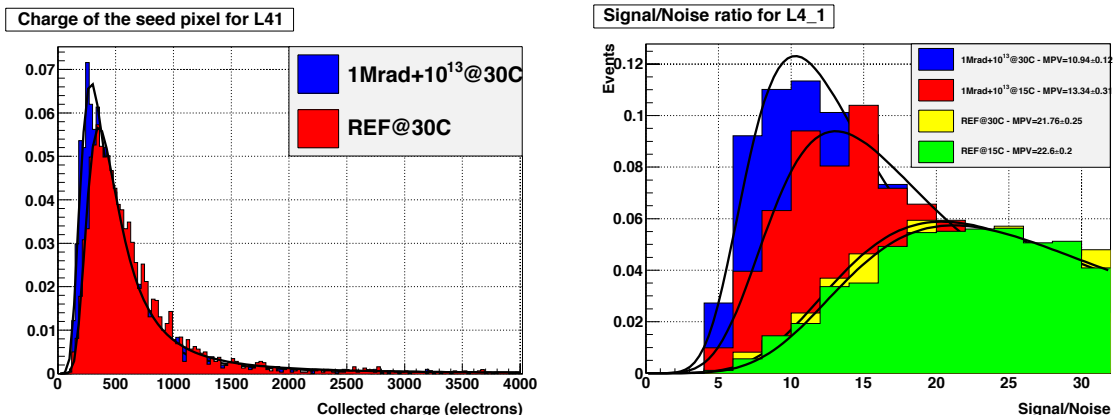

Figure 4.22: MIMOSA32 single-diode elongated pixel beam test results: charge collected by the seed pixel (left) at $T_c = 30°$ and seed pixel SNR at $T_c = 15°C$ and $30°C$, before (yellow and green) and after (red and blue) irradiating the sensor with 1 Mrad and $1 \times 10^{13} n_{eq}/cm^2$. The SNR distribution is a zoom on the low value range of the full distribution.

assemblies were observed. After adjusting the bump bonding parameters and tuning of the laser power for carrier release the second set of delivered assemblies exhibited fully connected edges. Figure 4.23 shows a SEM image of one assembly. The side view shows the sandwich structure of the chip and the sensor with the bump connections in between. The pitch between the bumps is 50 μm.

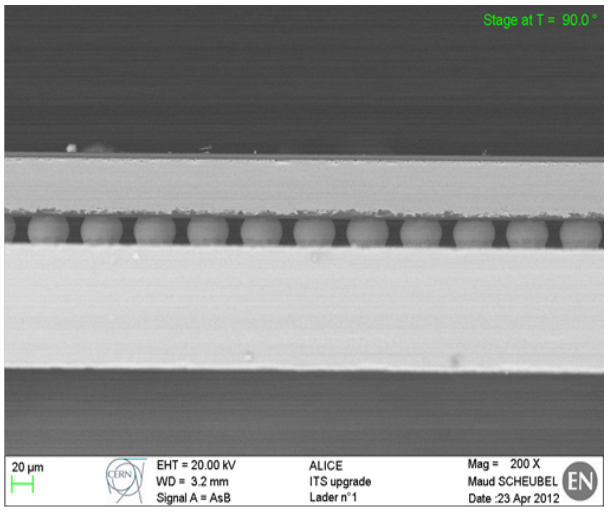

Figure 4.23: SEM image of an assemblies produced by IZM. The chip thickness is 50 μm and the sensor thickness is 100 μm.

A first set of 13 sensor wafers using epitaxial silicon wafers and an edgeless layout have been produced by FBK Trento. The wafers have an epitaxial layer thickness of 90 μm. The wafer contains several single chip sensors compatible with the ALICE pixel chip layout and a large number of test diodes with varying edge geometries. All of the structures have a etched trench at the edge. Some structures have added a single guard ring between the active region and the trench. Several distances between the active region and the trench have been implemented to allow for a systematic study of the optimum configuration. The wafers have been completed processing in May 2012. First tests on the different test structures are presently ongoing.

4.3.4.6 *Thinning Tests*

The monolithic silicon pixel chips need to be thinned to 50 μm in order to meet the material budget requirements. Thinning and dicing are therefore an essential part of the production procedure. While thinning to 50 μm is a service provided by industry, the large size of the dies are not standard in industry. Furthermore, compared to industrial applications the number of wafers needed for the ITS is low.

The first set of dummy wafers with a die size of 15 mm $\times$ 30 mm has been successfully thinned to 50 μm in early 2012. Discussions with the commercial supplier on how to optimize the process flow have led to the proposal to use a Dice-Before-Grind (DBG) approach for the next set of dummy wafers. In addition 2 MIMOSA20 [115] wafers have been sent for thinning and dicing. These wafers are fully processed CMOS wafers and will allow to verify the thinning process with real wafers.

Furthermore, an additional set of patterned dummy wafers was sent for thinning to have components available for interconnection tests and to build dummy modules for mechanical and cooling tests. This set of 25 wafers with the specifications of TowerJazz has been procured and has been sent for metallization and patterning. The first 5 wafers with Aluminum traces have been delivered and were sent for dicing and thinning to 50 μm. The patterned dummy chips will be available for interconnection and module tests in autumn 2012. Figure 4.24 shows the patterned wafers before thinning and dicing.

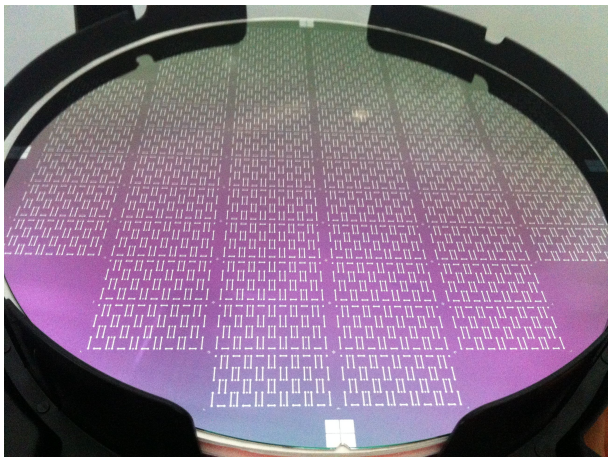

Figure 4.24: Patterned silicon wafer for interconnection tests before thinning and dicing.

4.3.4.7 *Bus Cable and Interconnection*

A flex cable design using a single polyimide layer with one layer of Aluminum as conductor has been prepared to produce dummy modules. The flex cable dimension is 28.08 cm $\times$ 1.5 cm and it is equipped with a daisy chain structure. The pattern corresponds to the connection scheme designed for dummy chips, assuming 100 contacts per die of 3 cm $\times$ 1.5 cm. The polyimide used for the production of the cables is 50 μm thick with one Aluminum layer of 25 μm. The pads are exposed to a very thin Au flash to protect them from oxidation. Figure 4.25 shows a picture of one of the flex cables produced. A total set of 20 flex cables has been produced. Special care was laid on the production steps which ensure the planarity of the flex cable.

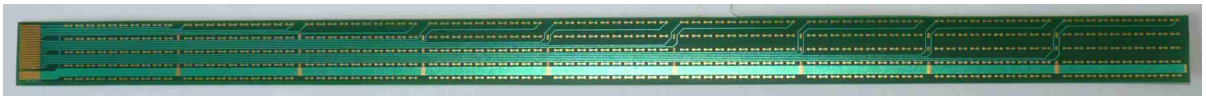

Figure 4.25: Picture of one polyimide flex cable.

In parallel to the production of the flex cable a design was made to produce dummy chips with the corresponding connection pattern.

Several types of alternative interconnections are being investigated for the connection between the chip and the flex cable based on BGA type connections distributed over the full surface of the chip. The CERN workshop produced a set of dummy chips and bus pieces made of metallized polyimide that allow to test different interconnection techniques.

First test have been successfully carried out using standard BGA balls of 500 μm diameter and a standard furnace. Figure 4.26 shows one chip polyimide foil equipped with BGA balls and the bus cable with the holes placed on top of it. Further improvements in the mechanical tools used and in the procedure of the soldering are currently being carried out. However, balls of this dimension present too large a contribution to the material budget for a final module. BGA balls of smaller diameter are being acquired at the moment and the design of the polyimide foils is being adapted.

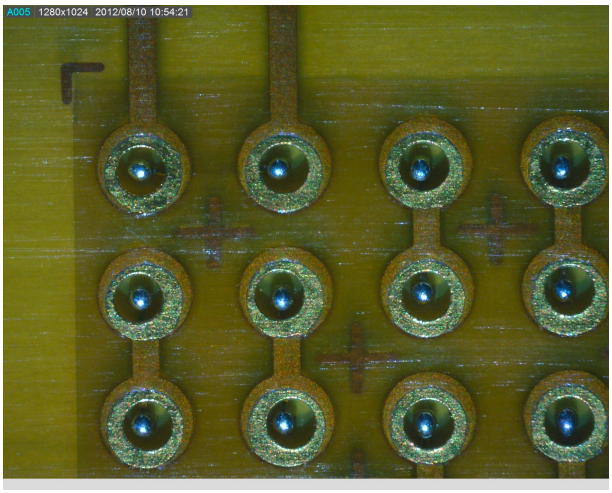

Figure 4.26: Chip polyimide foil equipped with 500 μm BGA balls and bus polyimide placed on top of it before the final reflow step.

As an alternative to the standard BGA type connections plastic core BGA balls are considered for their lower material budget. Discussions are ongoing with the supplier of these type of balls at the moment. The compatibility in terms of radiation resistance of plastic core BGA balls still needs to be proven.

Traditionally BGA contacts are soldered using a furnace heated up to around 200 °C. This implies that the full structure, in the case of the ALICE ITS the full pixel module, is undergoing a temperature step. Considering the different thermal expansion of the polyimide of the bus and the silicon dies this will lead to stress induced in the module. As the components used are also very thin an additional risk of damage has to be considered. Laser soldering uses a well defined laser beam to heat up the solder ball for a short duration, without exposing the rest of the module to the temperature step. First test have been successfully carried out using polyimide foils as described above. Figure 4.27 shows four images of the soldering sequence using a laser soldering head. The complete soldering step duration is 500 ms with a peak temperature of 280 °C. Further tests are in preparation with the aim to reduce the solder volume.

4.4 Strip Detector Technologies

The silicon micro-strip technology guarantees a good spatial precision and offers a great PID capability, introducing limited material budget. It can be equipped with relatively low power consumption front-end electronics and due to its competitive cost can be used to cover large sensitive areas. Thanks to these features, and taking into account its limited granularity, the strip detectors are considered as an optimal option for the outer layers of the ITS Upgrade.

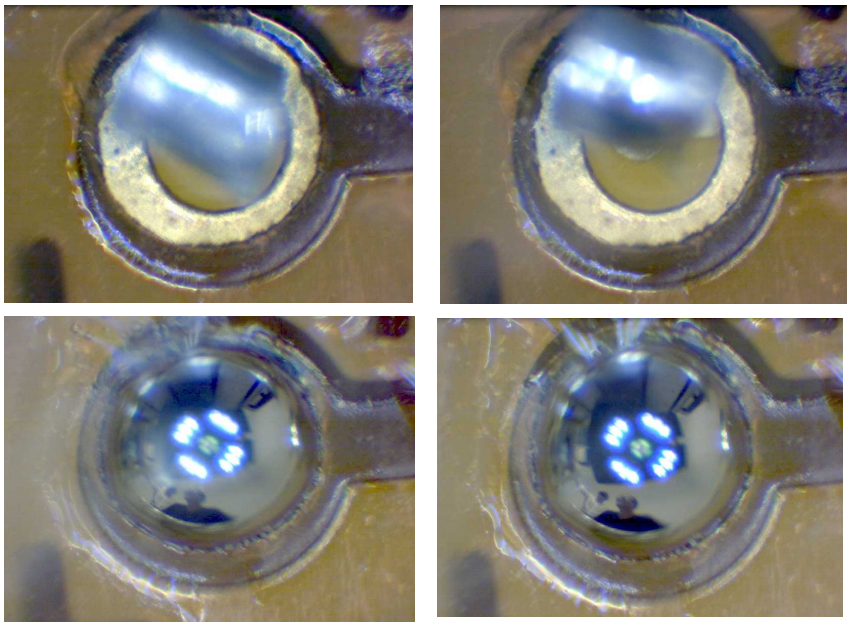

Figure 4.27: Sequence of laser soldering of one contact using a chip polyimide foil and a bus polyimide foil. The sequence starts with the top left image. The final connection is visible in the bottom right image.

4.4.1 Strip Sensor Layout

The present ITS Silicon Strip Detector (SSD) design is optimized for the present LHC conditions and ALICE physics goals. Although the available strip detector technologies are rather mature, the construction of a new strip detector will benefit from past experience, leading to better reliability and uniformity of several components and thus to a significantly improved overall performance in real operating conditions. In addition, appropriate modifications made on each component design will allow the requirements suggested by the new physics aims, the expected experimental conditions and the position of the detector in the new tracker to be met.

The upgraded strip detector will be based on 300 μm thick, double-sided micro-strip sensors with a 35 mrad stereo angle between the strips on opposite sides, in order to keep an acceptable rate of ambiguities in track reconstruction. Given the prospect of a smaller distance between the strip layers and the interaction vertex and taking into account the increased particle multiplicity foreseen at the nominal LHC energy, we considered a redesign of the current SSD sensor with a decrease in the cell size in order to keep the occupancy low.

The simplest way to achieve this goal is to halve the strip length while keeping the same sensor dimensions: each sensor-side accommodates two arrays of 768 strips of 20 mm length, for a total number of 3072 strips per sensor. The strips are cut in half by inserting a narrow gap (a few μm wide) between them. This gives no efficiency loss for particle hit detection. The sensor layout appears in Figure 4.28.

This layout modification results in a factor of two lower occupancy, better ghost hit rejection and lower strip capacitance, which has a beneficial effect on the signal-to-noise ratio. Dedicated simulations suggest the feasibility of using strip detectors to build the intermediate layers of the ITS, keeping the occupancy, the efficiency and the purity at the present level, or better, even in increased multiplicity conditions. On the other hand, the new design doubles the readout channel density, with important effects on the global power dissipation and on the requirements of the cooling system. It also makes the sensor to front-end chip connection and the module assembly more challenging.

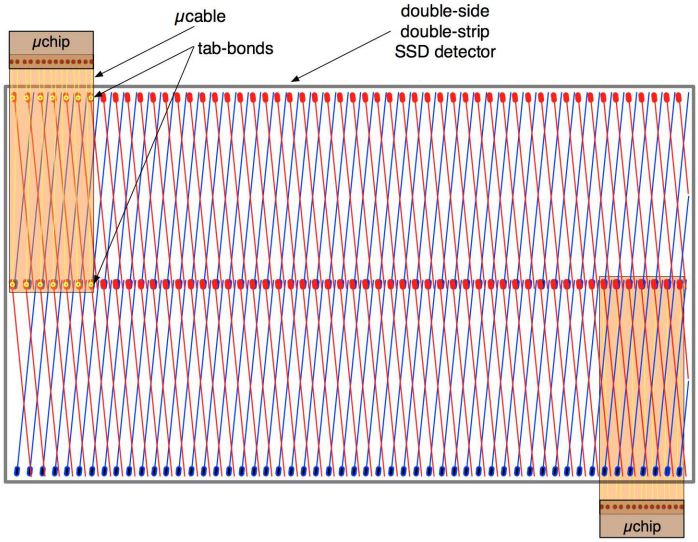

Figure 4.28: Schematic view of the new strip sensor layout. Two rows of 768 strips are arranged on each side (in red and blue for the front and back side). The dots represent the corresponding bonding pads.

4.4.2 Interconnections and Module Layout

The present SSD module uses low-mass polyimide-based cables with aluminum conductors for the electrical connections between the sensor and the front-end chip [116]. This technology is still considered the most suitable for this kind of detector layout, thanks to its greater flexibility with respect to the standard wire bonding technique. It allows the positioning of both hybrid circuits (reading p- and n-sides) on the same side of the sensor, by folding around the sensor edge the micro-cables connected to the opposite side.

In the present SSD, cables made of 10 μm polyimide foil with 14 μm thick aluminum traces are used to connect the front-end chip to the sensor on the input side and to the hybrid circuit on the output side. The length of the input traces connecting the chip to the detector is 11 mm, with a fan-out to adapt the input layout (128 input pads in one row with 80 μm pitch) to the sensor pitch (95 μm). The trace width is 36 μm.

The recent technology development offers now the possibility to realize cables with a smaller inter-trace pitch, down to 42.5 μm, and to connect and readout a doubled number of strips arranged on two separated rows, preserving the low material budget and a compact detector layout. First prototypes of (10+10) μm thick aluminum-polyimide adhesive-less foiled dielectric cables connecting 128 strips, with minimum inter-trace pitch of 42.5 μm and trace width of about 22 μm, have been manufactured. The geometrical characteristics for the sample designed to connect the p- and n-side of the sensor, with the corresponding two different dimensions, are listed in Table 4.5. The traces are arranged in order to match two rows of bonding pads with a pitch of 95 μm on the sensor side (contacting two groups of 64 half-length strips), and the two staggered rows of pads on the front-end chip, each with a pitch of 85 μm. A second cable version compatible with a 256-channels front-end chip has been developed and manufactured, with slightly more relaxed parameters (44.5 μm minimum inter-trace pitch).

In parallel, the hybrid circuit used to accommodate the chips, drive out the signals and provide the services is being designed with the same aluminum-polymide cable technology as used in the present SSD, in two symmetric layouts corresponding to the two sides of the sensor. The power and interconnecting cable (also called *flex*) will be glued onto a stiffener, made of five-layer carbon-fibre material. The flex is a two-layer bus used for power, digital i/o and analog outputs. The interconnections between the two layers are made by TAB (Tape Automatic Bonding) bonded vias.

Table 4.5: Microcable dimensions and arrangement

Cable Area	To-Hybrid	To-Chip (*Output Pads*)	To-Chip (*Input Pads*)	Transmitting Area	To-Sensor
Trace Pitch [μm]	130	130	42.5	47.5	47.5
Trace Width [μm]	$\sim$ 80	$\sim$ 48	$\sim$ 30	$\sim$ 22	$\sim$ 30
Trace Quantity	43	43	128	128	128
Bonding Pad Placement	One Row	One Row	Two Rows (Staggered)	- -	Two Rows (Staggered)

The front-end module of the upgraded strip detector is shaped in a very compact layout in order to guarantee a continuous sensitive area once integrated in the tracker layers. The flexibility of the interconnections should allow the arrangement of the front-end electronics of the whole module on the downstream side with respect to the incident particles, leaving sufficient space to accommodate the supports and the cooling services. Different options for the module layout are are being studied. Figure 4.29 shows a possible arrangement of the cables and the hybrids, before and after folding them on the sensor. At present, this option seems to allow the simplest assembly procedure and the most comfortable placement of the chips, optimizing at the same time the cable dimensions and the hybrid layout. A specific program of

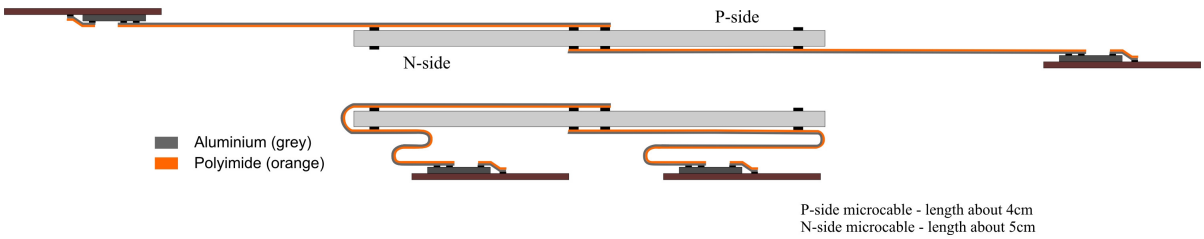

Figure 4.29: Schematic view of the strip module, in the open (top) and folded (bottom) configurations.

test and quality control will be organized to carry out a complete static characterization of the sensors. The assembly procedure will foresee electrical and functionality tests at each processing step, allowing faulty component rejection and possible reworking before the final integration in the complete module. First strip module prototypes will be tested with beam particles to study the performance, the efficiency and the spatial resolution of the strip detector once the full chain is integrated in the module.

4.4.3 Prototype Development

A set of dummy strip sensors with the described geometric characteristics has been manufactured at FBK Trento in spring 2012. As showed in Figure 4.30, a narrow gap of 5 μm is inserted at the middle of the sensor to cut in half the strips. Each strip can be contacted from the pads placed at the edge and at the middle of the sensor, allowing a flexible design of the module layout.

The same production supplied a series of dummy chips, reproducing dimensions and bonding pad positions of the 128- and 256-channel versions of the final front-end ASIC: the dimensions of the two chip versions are 5.9 cm $\times$ 6.25 cm and 11.85 cm $\times$ 6.25 cm respectively; in both versions the input bonding pads are arranged on two staggered rows.

Since the single-point TAB technique becomes extremely challenging at small trace width and pitch, it is planned to use the dummy silicon components and the manufactured cables to test and verify the possible solutions for module interconnection and assembly. The first attempt to TAB-bond cables with 42.5 μm trace pitch has been carried out at the SE SRTIIE Kharkov with a manual ultrasonic bonder. The micro-cable prototypes have been framed with modified Yamaichi frames and successfully bonded to both the dummy chip versions. The existing equipment previously used to test the SSD components

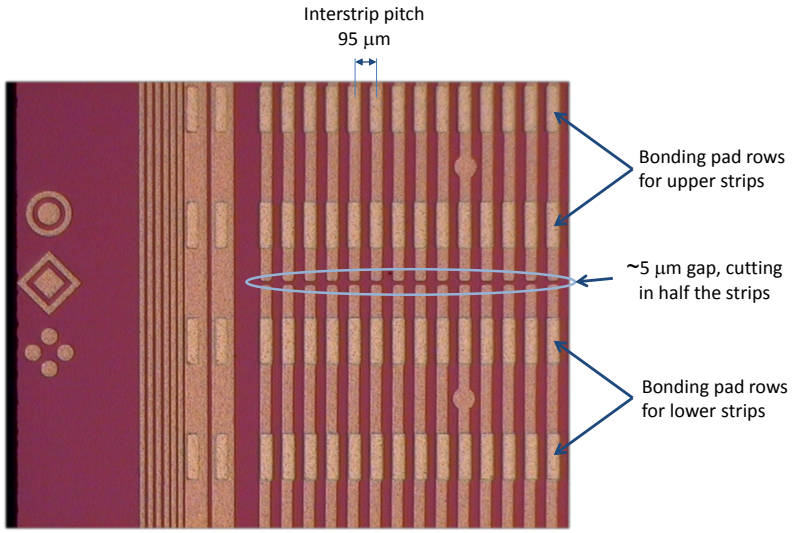

Figure 4.30: Dummy strip sensor detail: narrow horizontal gap cutting in half the strips.

is being modified according to the new cable layout in order to perform a complete electrical test and to assess the quality of the assembly procedure. The assembly of the first complete dummy module assembly is planned for autumn 2012.

4.4.4 Front-end Electronics for Strip Detectors

A new front-end chip for Silicon Strip Sensors will incorporate on board the analog to digital conversion, today performed outside the front-end ASIC. The ASIC will deliver to the back-end electronics digitized data serialized on a few high speed differential links. To accommodate more channels on chip, one could explore the use of commercial flip chip technologies as an alternative to standard wire bonding. The front-end chip will be designed in the same process (0.13 μm or 0.18 μm) chosen for the pixel sensors. This will minimize the use of different technologies in the project and will favor expertise exchange and building block re-use among the different subsystems. The requirements for the front-end ASIC for the strips are reported in table 4.6.

The key difference between a new front-end and the existing HAL25 will be the data digitization directly on chip. The requirements on total dose are easily accommodated by modern CMOS technologies without enclosed layout transistors. A Single Event Upset tolerant design will be adopted in the control

Table 4.6: Strip FE requirements

ASIC Specification	HAL25 (present SSD)	Upgrade Chip
Input Pitch	80 μm	44 μm
ASIC Size	3.65 mm $\times$ 11.90 mm	6 mm $\times$ 6 mm
Noise (5 pF load)	400 e^-	400 e^-
Peaking Time	1.4 - 2.2 μs	1 - 2 μs
Power per Channel	500 μW	500 μW
Total Number of Channels	128	128
Digitization	Off Chip	On Chip
Radiation Level	30 krad	30 krad
Technology	CMOS 0.25 μm	CMOS 0.13 - 0.18 μm

path. The front-end ASIC will interface to the outside world with fully differential digital I/O (LVDS or SLVS). Several approaches can be used for the on chip digitization of the analogue information. The spectacular progress recently made in the domain of analog to digital converters allows a design of an extremely low power and fast ADC. Successive approximation converters with 40 Msamples per second, 2 mW of power, 0.04 mm^2 of area and resolution of 10 bits are today state of the art, so the integration of one ADC per channel can be envisaged.

In the inner strip layer, the hit density will be about 0.9 tracks/cm^2. Including charge sharing, this will lead to an event rate of no more than 5 kHz per strip. A charge amplifier followed by a slow shaper (with shaping times in the μs range) can then be used to combine low noise with low power consumption. The amplifier output is sampled and digitized by a 10 bit ADC. The binary data stream is then inspected to look for peaks. Given the low data rate, if a peak is found on one channel, the samples corresponding to the same position of the peak in the other channels can also be transmitted. This would offer enough information to apply common mode correction algorithms in the readout FPGA, where further signal processing can be done before the data are sent to the DAQ for mass storage. With the assumed event rate, such a scheme would require a bandwidth of 150 Mbit/s to transmit 128 channels in 10 μs, well in time to comply with the readout requirement of 50 kHz. A sampling frequency of 5 MHz will be sufficient in the ADC, leading to and estimated power consumption of 200 μW for the converter. Taking into account pre-amplification, processing and data transmission, the power consumption could be kept below 1 mW per channel. A lower power alternative is to digitize the amplitude information with a Time-over-Threshold scheme. With such a technique, however, the information to correct for common mode fluctuations would be lost.

The design of the front-end chip will start only after a final decision on the use of the strip sensors will be made. It is foreseen to have a short period (3-4 months) of behavioral simulations to choose the most suitable architecture before starting the design of the circuit. After that the design of a small prototype will be undertaken. This first ASIC will contain already the full processing chain, but only a limited number of channels to reduce the development costs. After this first step, one will proceed with the design of the final circuit. The full development cycle of the ASIC is expected to last two years.

4.5 Summary

The implementation studies for the ITS upgrade are considering two layout options. The first option, referred to as Layout 1, plans to equip all seven layers with monolithic pixels. Layout 2 uses pixels (either monolithic or hybrid) for the inner 3 layers and double sided silicon strip detectors for the 4 outer layers.

An R&D program has been launched to study the various technical options, such as choice of technology and architecture. The TowerJazz CMOS 0.18 μm process has been selected for further investigation offering the unique feature of integrating in the pixel full CMOS electronics with low capacitance sensing diodes. Dedicated test structures have been designed and produced to study the radiation hardness (TID, SEU, NIEL) for the ALICE ITS upgrade and measurements are presently being carried out. A prototype pixel matrix (MIMOSA32) has been produced and first results from test beam and laboratory tests are reported in this chapter.

An important aspect of the implementation will be the layout of the modules for the inner and outer pixel layers. First proposals for the data and power connection schemes have been worked out and are under investigation. Special emphasis is laid on the design and interconnection of a low mass bus cable which will provide power and data connections.

Progress has also been made in the development of hybrid pixel assemblies and strip detectors. Specifically a production of thin hybrid assemblies with a total thickness of 150 μm has been demonstrated

using dummy components. Furthermore, silicon strip sensors for the ALICE ITS upgrade have been designed and first prototypes have been produced, which will be used for module assembly and TAB-bonding tests.

The main objectives in the coming months are the completion of the radiation hardness studies of the TowerJazz structures and performance tests of pixel sensor prototypes, both in laboratory and test beam. Furthermore, the studies on the module layout and the data and power transmission scheme will be continued. Integral to this study is the production of a low mass bus cable for the pixel layers and the choice of interconnection technology. Based on this first prototype modules for pixel and strip layers will be designed and produced.

Chapter 5

Mechanical Layout, Services and Integration

5.1 Introduction and System Overview

The ITS upgrade consists in replacing the current detector with an entirely new one consisting of 7 layers of silicon tracking detectors. Three inner layers close to the beampipe and four outer layers on larger radius are arranged in a cylindrical volume around the beampipe. The new ITS layout, described in Figure 5.1 and in Table 5.1, provides a natural geometrical grouping of the three inner and four outer layers in two separate barrels (Inner Barrel and Outer Barrel)each of these with slightly different requirements. There are two design options currently being considered: 1) 7 layers all based on pixel detectors , 2) 3 inner layers equipped with pixel and 4 outer layers with strip detectors. The mechanical design for the Inner Barrel and Outer Barrel will follow different approaches, as will be shown in the following chapter.

5.2 Upgrade Design Constraints

5.2.1 External Constraints: Detector Layout, Beampipe and Installation

Relevant requirements for the detector impact parameter resolution is the position of the innermost layer. This inner layer has to be at a minimum radial distance from the beam axis and as close as possible to the beampipe wall. These requirements have motivated the ALICE collaboration to investigate the possibility of reducing the beampipe outer radius, from the present 29.8 mm to less then 20.0 mm, and to locate the first detector layer at 2 mm from the beampipe wall. Placing the silicon detector so close to the fragile beryllium beampipe represents a delicate task for the mechanical design and integration. This task is made even more challenging by the requirement of a layout that allows for a rapid access to the ITS modules during the yearly LHC shutdown (3-4 month time). The new ITS inner layers have to be translated approximately 3 meters along the beampipe to allow this accessibility. This translation is needed to move the ITS out of the inner bore of the TPC in which the detector is housed [55]. The requirement of extracting the ITS inner layers within a short period of time, which excludes the possibility of displacing the surrounding detectors, sets severe constraints on the design and on the installation procedure of the new ITS.

5.2.2 Internal Constraints: Detector Sensors, Power Dissipation and Material Budget

The above considerations on the external boundary conditions to the design of the detector have to be combined with the internal constraints which are defined by the tracking performance requirements. These requirements are different for the internal and external layers and are reported in Table 5.1. The

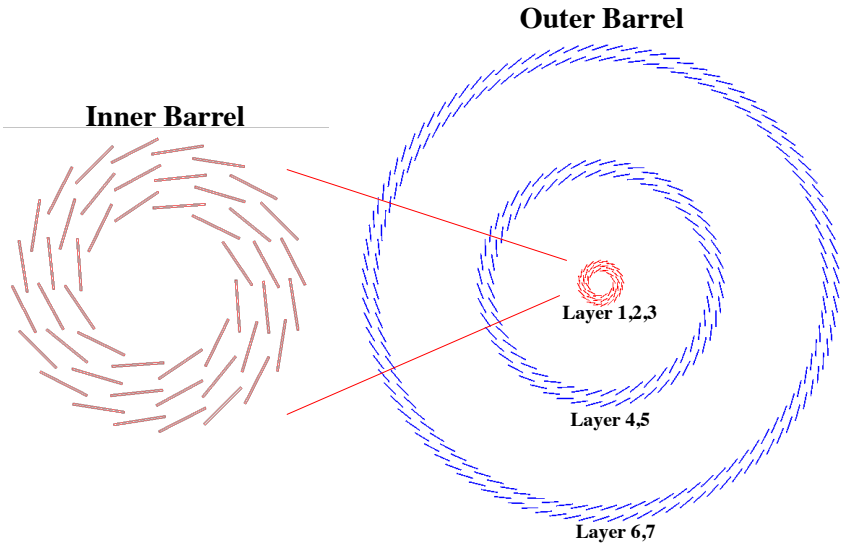

Figure 5.1: Schematic layout of the new ITS.

Table 5.1: Requirements for the ITS upgrade

Parameters	Inner Barrel	Outer Barrel
Beampipe outer radius (mm)	20	-
Beampipe wall tickness (mm)	0.8	-
Detector Technology	Pixel	Pixel−Strip
Number layers	3	4
Mean radial positions (mm)	22, 28, 36	200, 220, 410, 430
Stave length in z (mm)	270, 270, 270	843, 843, 1475, 1475
Power consumption (W/cm^2)	$0.3 \div 0.5$	≤ 0.5 mW/strip
Total material budget per layer (% of X_0)	≈ 0.3	≤ 1.0
Working temperature (°C)	≈ 30	≈ 30

fundamental requirement that strongly affects the detector design is the material budget, which for the inner layers is set to a very demanding value of 0.3 % of X_0. This value drives the following criteria: 1)Sensors choice (silicon pixel with a thickness of 50 μm),2) The detector technology (oriented towards MAPS), 3)The signal and electrical bus design, 4) The mechanical support structure design and materials, 5)The design of the cooling system. The frame inside which this material budget request has to be located is defined by a modest radiation environment, by a moderately low heat dissipation, 0.3-0.5 W/cm^2, by an operative temperature of 30°C with a 5°C temperature gradient along a detection plane, and by a small overall detector size limited to 27 cm in length for the inner layers. These conditions allow to design a light mechanical structure without compromising the stiffness.

5.3 Detector Layout

A dedicated simulation has been performed to optimize the arrangement of the detector modules in cylindrical layers around the beampipe (Section 3.5). The radial positions of all layers are optimized to reach the maximum pointing resolution, tracking efficiency and momentum resolution in the available space between the new beampipe and the TPC. The longitudinal extension of each layer is determined by the requirement of a pseudo-rapidity coverage of $|\eta| < 1.22$ over 90 % of the luminous region. This simulation resulted in seven layers distributed at different radii, with the three inner ones very close to the beam line and the innermost layer only 2 mm away from the wall of the beampipe. In this simulation

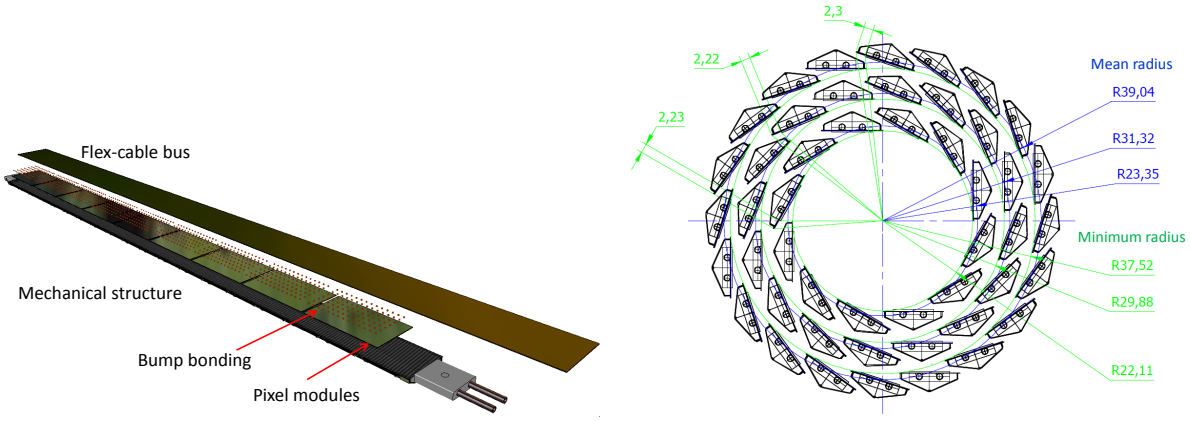

Figure 5.2: Sketch of the building blocks constituting a generic stave (left) and front view of their positioning around the beampipe to form the Inner Barrel (right).

the overlap regions for the sensors have been also taken into account in order to avoid dead zones. The full azimuthal coverage plus 200 μm of additional overlap in the sensitive area has to be guaranteed by the mechanical layout. No overlap along the longitudinal direction has been foreseen to simplify the assembly.

Modularity Concept: Stave, Layer, Half Barrel, Inner and Outer Barrel

The ITS mechanical design is conceived as a two-barrel structure: Inner Barrel and Outer Barrel. The design effort has been concentrated so far on the Inner Barrel due to the more stringent requirements in terms of material budget. The Inner Barrel has a modular structure consisting of 3 concentric layers, each segmented in the azimuthal direction in modules referred to as ”staves”.

The stave is the smallest operable part of the detector (Figure 5.2). Two pixel technologies are being considered: monolithic and hybrid. In the case of monolithic pixel detectors, a stave is formed by 9 silicon pixel chips (15 mm $\times$ 30 mm $\times$ 50 μm thick) aligned in z to form a detection area of 15 mm $\times$ 270 mm, which are flip-chip bump bonded on a flex-cable bus. The latter incorporates also the interface to the data link. In the example of hybrid pixel detectors, a number of front-end chips are bump bonded to a silicon sensor to form an assembly called ”ladder”. A few of these assemblies are aligned in z to cover the same detection area as for the stave based on monolithic pixel chips. The ladders are mounted on a flex-cable via wire-bonding or Through Silicon Vias (TSV). The electronics circuit that performs the readout of the pixel chips, or front-end chips in the case of hybrid pixel detectors, and implements the interface to the off-detector electronics, not shown in the schematics, will be either mounted on the stave, at its edge, or on a separate unit connected to one or more staves via electrical cables. The stave includes a carbon fiber support structure, which provides a light and stiff frame for the sensors and the electrical bus. Additionally this support integrates the cooling interface to remove the dissipated heat.

This modular structure allows performing a complete characterization of each stave before the next step of integration. The staves are assembled in a layer by mounting them on two light carbon wheels that provide the support at the two ends. The three inner layers are then coupled together by two carbon end caps, which are connect to each other by a cylindrical sandwich shell located outside the third layer. This shell provides the torsional stiffness to the assembly. The barrels themselves come in two halves in order to be able to integrate them around the beampipe (Figure 5.3).

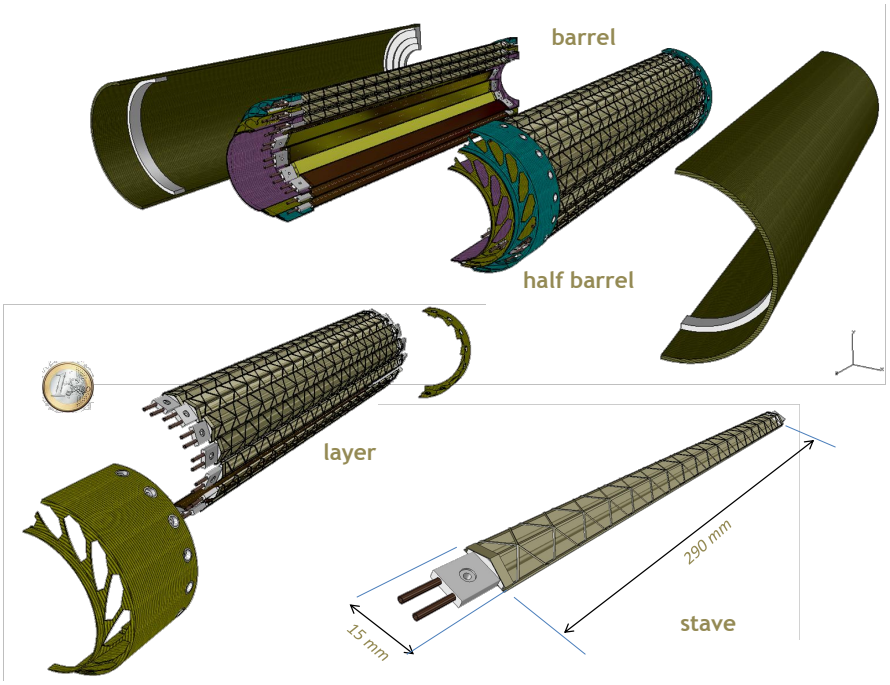

Figure 5.3: Drawings of the three innermost layers of the new ITS: from single stave to barrel.

5.4 Beampipe

The beampipe layout affects the ITS performance and integration. Few critical parameters can be easily identified: radius wall, thickness, material and sag.

Beampipe Radius, wall Thickness and Material

The reduction of the beampipe diameter in the center of the ALICE detector is one of the main objectives in view of improved impact parameter resolution (see Section 3.9.4). Current studies indicate that it should be possible to arrive at a beampipe inner radius of 17.2 mm, compared to the present value of 29 mm. Estimates for the linear sum of fabrication tolerance, survey precision and alignment uncertainties amount to 5.1 mm, resulting in a minimum clearance of 12.1 mm radius with respect to the nominal beamline. The LHC aperture is quoted in terms of the so called n_1 parameter, which is a function of this mechanical clearance as well as the position along the beam line due to the varying beta function. The 12.1 mm clearance corresponds to an aperture of $n_1 = 13.9$ at the ALICE interaction point for nominal injection optics. Beyond a distance of 2 m from the interaction point the minimal aperture requirement of $n_1 > 10$ is violated and a larger beampipe radius is foreseen. Therefore, in the current layout we assume a conical or cylindrical beampipe with larger diameter beyond a distance of 1 m from the IP. The wall thickness of the central Beryllium beampipe section is assumed to be 0.8 mm. Using a smaller value of 0.5 mm is challenging due to possible issues with gas tightness and mechanical stability. The wall thickness and material for the beampipe section beyond 1 m from the IP will be decided by background simulations and practical considerations. Since the machine parameters for the high luminosity heavy ion running are not yet defined and since ALICE wants to operate this detector configuration during the HL-LHC era after LS3, a conservative number of 19.2 mm for the beampipe inner radius is assumed until further studies of LHC optics confirm the feasibility of the 17.2 mm radius.

Beampipe Sag and Installation

The present central part of the beampipe is 4.8 m long with about 4 m inside the TPC. In order to comply with the access requirements discussed previously, the new ITS will slide along the beampipe to reach

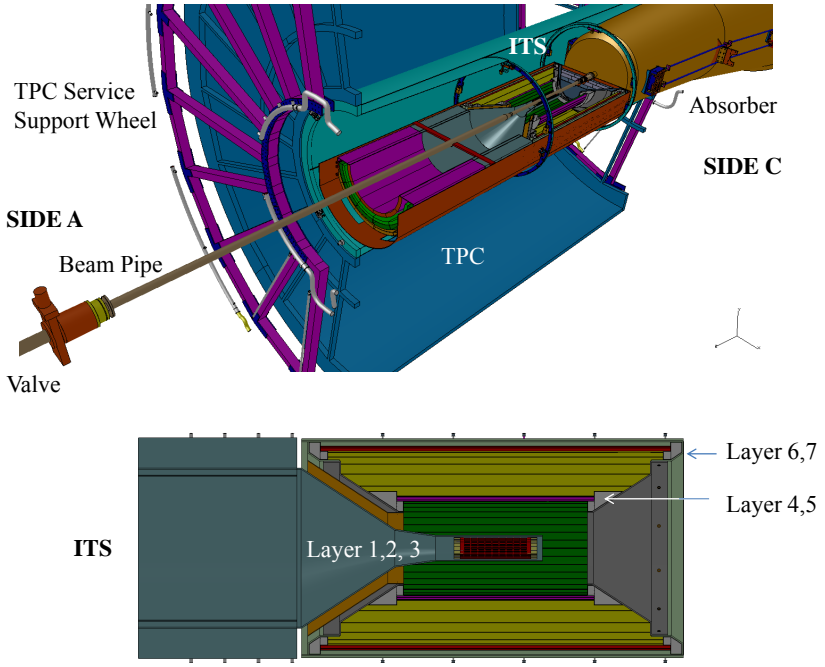

Figure 5.4: New ITS positioned inside the TPC (top) and new layout (bottom).

its final position inside the TPC. The central part of the beampipe is limited on one side by the large hadronic absorber, which penetrates into the TPC preventing the access, and on the opposite side by a large vacuum valve (see Figure 5.4). The connection to the contiguous beampipe sections is made via bellows to avoid induced displacements. The extension of the length of the beampipe, up to 5.5 m, and the relocation of the vacuum valve, about 1.5 m apart from the TPC, are necessary to allow the positioning of the new ITS around the beamipipe before it is translated towards the final position.

A study has been carried out in order to evaluate the minimum number of supports necessary to contain the sag, which has to be sufficiently small to allow the installation of the new ITS at 2 mm radial distance from the beampipe wall. These studies results show a large deflection if the beampipe is supported only at the two extremities. The maximum sag in the middle of an unsupported length of 5.07 m (corresponding to the 5.5 m overall length) is 2.8 mm for a beampipe with 19.2 mm inner radius and 0.8 mm wall thickness. This deflection creates the necessity to add an intermediate support in oder to reduce the sag to 0.07 mm. The beampipe sag reduces its aperture and therefore the possibility to reduce its inner diameter. In addition a beampipe stiff layout will provide a higher first natural frequency, which is also an LHC requirement to avoid structural resonances. However an intermediate support complicates the installation procedure. Since the ITS is inserted from one side, it has to pass through the beampipe intermediate support when sliding along the beampipe to reach the final position. The beampipe integration is a delicate procedure that covers its installation inside the TPC and the connection to the LHC ring.

5.5 ITS Installation

The layout and installation procedure of the new ITS are constrained by the ALICE layout [3], the time available for the installation and by the requirement in terms of fast accessibility. The last requirement is particularly challenging considering that an access to the current ITS would require about seven months till the ALICE nominal configuration is restored. The services of the current ITS are connected to either side of the TPC. On the side of the hadronic assorber (C-side) the services are not accessible without moving the TPC. The latter has to be displaced by about 4 meters to the parking position, along the beam axis in the direction opposite to the hadronic absorber (A-side), in order to provide access to the

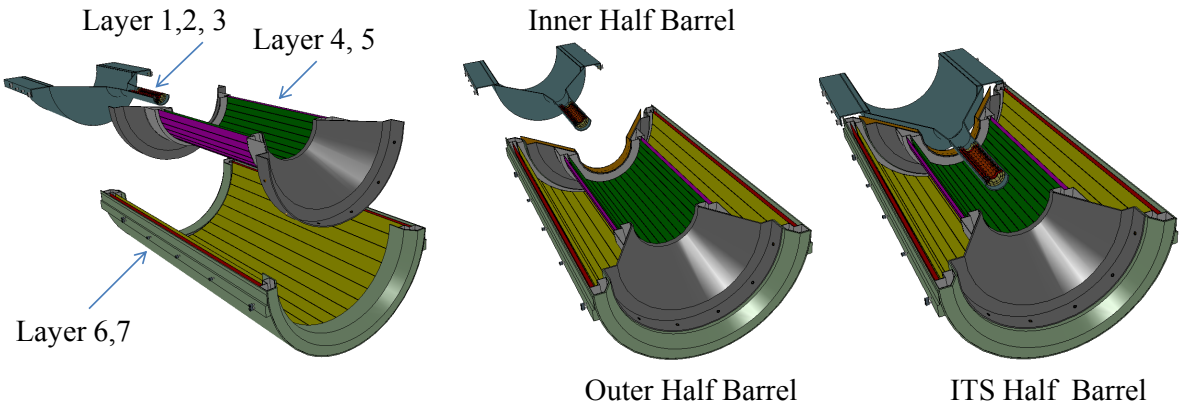

Figure 5.5: ITS modular mechanical structure.

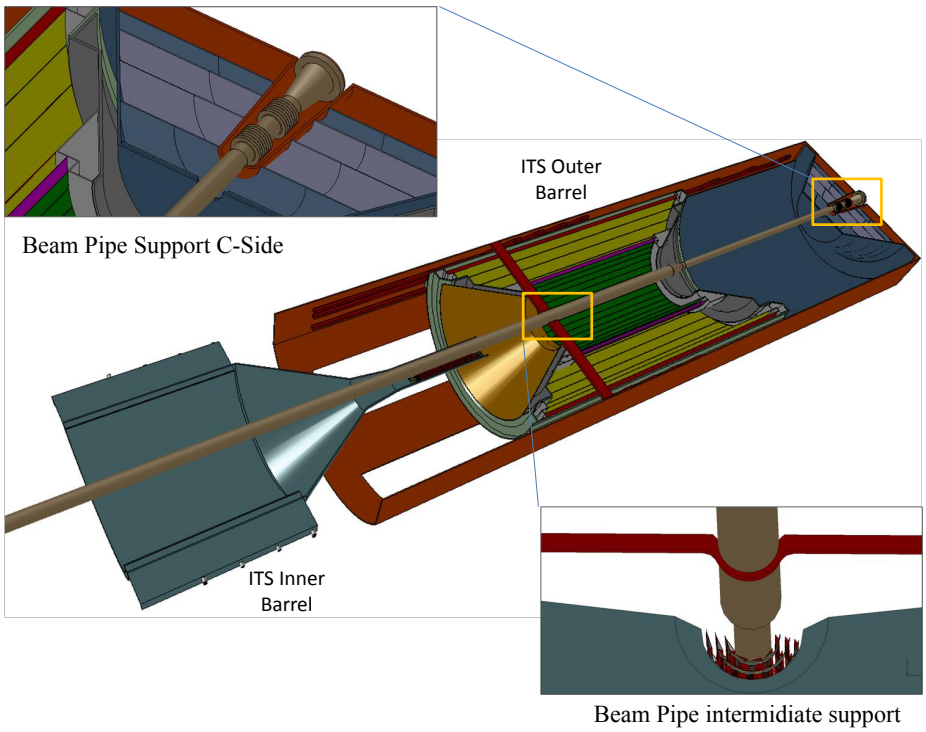

Figure 5.6: ITS half-barrel insertion inside the TPC. A detail of two beampipe supports is also shown. The third support is outside the TPC (not shown).

services patch panels. Moving the TPC in the parking position and back in place is a complex and lengthy operation which requires the 7 months previously referred to. Therefore, the requirement of faster accessibility calls for a new detector layout, with the services connected only on the A-side, as well as a new installation concept. A first feasibility study will be discussed in the following section.

5.5.1 Detector Barrel Installation

With reference to Figure 5.4, the new ITS will be inserted from the A-side and guided along the beam axis in the cylindrical volume between the TPC and the beampipe, without the need of displacing the TPC.

For installation purposes the ITS is divided in two concentric barrels: Inner Barrel and Outer Barrel (see Figure 5.5). Each barrel comes in top and bottom halves, which will be separately mounted around the

beampipe. The insertion of each half barrel has to take into account two main geometrical constraints:

– the beampipe intermediate support, which consists of an horizontal carbon bar placed inside the TPC, is in the way of the ITS translation towards the nominal position (Figure 5.6);

– the innermost layer has to be placed at 2 mm from the beampipe wall.

To overcome these constraints each ITS half barrel is inserted in the TPC starting from the parking position, which is shifted in the radial direction, to allow the necessary clearance with respect to the beampipe and its intermediate support. The translation towards the final positioning is controlled by a guiding system. These guides are designed such a way to keep the axis of the barrel always parallel to the beam axis. This is in order to avoid interference during the installation. In the last centimeters of the translation along the z-axis the half barrel approaches the beampipe with a radial movement to reach the final position.

The installation concept described above allows for an independent and fast extraction of the Inner Barrel and Outer Barrel. The barrels guiding system and the beampipe supports are fixed to a common support cage, which is in turn attached to the TPC (see Figure 5.6). The relative radial position between the ITS layers and the beampipe is guaranteed by the machining accuracy of the common support. The half barrels accurate positioning in z is provided by precise mechanical stops engaged at the end of the translation. In order to minimize the material budget in the detection area, the Inner Barrel is a cantilever structure supported only at one end outside the Outer Barrel acceptance (see Figure 5.7). The Outer Barrel has no intermediate mechanical structures amongst the four detection layers, as the assembly is stiffened by a cylindrical composite sandwich shell outside the last layer. The connection of the layers to the external structural shell is obtained by two conical carbon end-pieces located at the extremities of the detection area. The Outer Barrel is designed to allow each half to be opened in two concentric parts, each constituted by the assembly of layers 4-5 and layers 6-7 (see Figure 5.5). This allows the access to individual staves.

5.5.2 Service Installation

In order to be able to extract the ITS without displacing the TPC, all ITS services should come from A-side. In case it is necessary to route some of the services to the C-side, for example the cables that distribute the low-voltage power to the detector outer layers, they should be implemented so they can be connected and disconnected remotely. A remote connection mechanism is used for the distribution of the high-voltage power in the current ALICE TPC. This is based on a connector consisting of a crown of flexible contacts that provides the electrical connection to the corresponding part in the detector power rod.

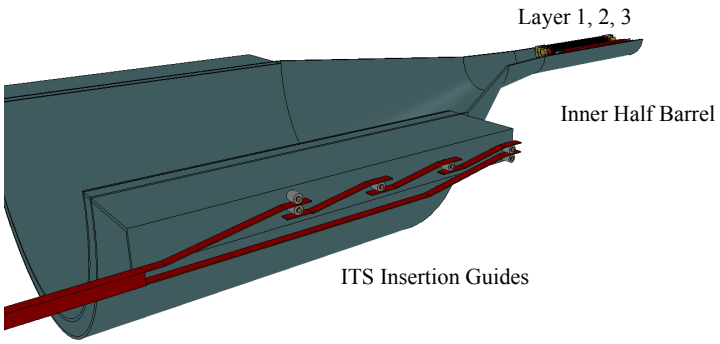

Figure 5.7: Concept of the ITS Outer Barrel insertion: detector and services.

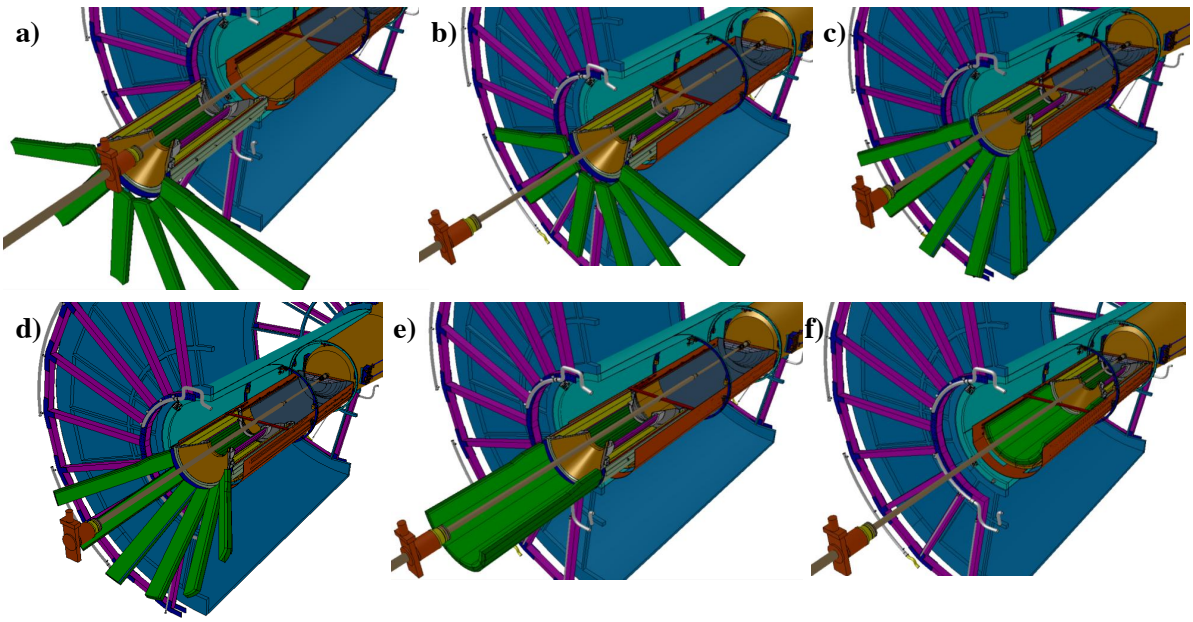

Figure 5.8: Concept of the ITS barrel insertion: detector and services.

In the following section we further discuss some basic guidelines that will need to be adopted for the layout of the new ITS services. The services will be grouped per detector half-barrel, since they will be installed together with the half-barrel as a single object and they will be routed from the detector to a patch panel located in an accessible area outside the TPC. Inside the TPC cone, the services carriers will form half cone jutting from the ITS to the TPC Service Support Wheel. As shown schematically in Figure 5.8, when the ITS is mounted around the beampipe in its parking position, the beampipe vacuum valve interferes with service carriers. In order to avoid such interference, the services carriers will be opened radially with respect to the beam line, and will be progressively closed to reach the final conical arrangement while the detector is translated towards the interaction point. The installation sequence of the Outer Barrel is shown in Figure 5.8.

5.6 R&D on Mechanical Support Structure

In this section we will discuss the studies that have been carried out to identify and characterize materials, processes and technologies suitable for the construction of the new ITS mechanical support structure. Such a support structure must, as discussed in Section 5.2, fulfill stringent requirements in terms of minimum mass and highest stiffness. The design of the mechanical support is inherently linked to the layout of the cooling system that will be adopted to remove the heat dissipated by the on-detector electronics. This cooling system may be integrated or even embedded in the mechanical structure.

The different mechanical layouts which have been investigated can be divided in two groups that refer to two different cooling concepts under study: *cold plates* and *cooling pipes*. In the *cold plates* concept the cooling is provided by a refrigerant fluid (monophase or biphase) flowing in a microchannels structure, which is either in a silicon (microchannel section area 0.04 mm^2) or in a polyimide (microchannel section area 0.16 mm^2) substrate. The plate is in thermal contact with the front-end electronics while the mechanical structure has to support the sensors with the bus and the *cold plates*. In the *cooling pipes* option the cooling is provided by a refrigerant fluid (monophase or biphase) flowing in 1.5 mm outer diameter tube (0.035 mm wall thickness). The tube is embedded in the mechanical structure to which the sensors are glued. Heat is transferred from the sensors to the pipes by the high thermal conductive structure.

Table 5.2: Lists of carbon fibers used for the prototypes.

Composite type	Composite material	Young modulus (GPa)	Tensile strength (GPa)	Density	Thermal conductivity (W/m K)	Dimension (mm)
Unidirectional prepreg	K13D2U-2k	560	2.2	115 g/m^2	$\approx$ 450	0.07
Impregnated thread	M60J-3K	365	2.9	0.15 g/m	$\approx$ 95	D = 0.3
Impregnated thread	M55J-6K	340	2.1	0.32 g/m	$\approx$ 100	D = 0.5
Fabric (0/90)	T300	-	-	207 g/m^2	-	0.12
CF Paper	FGS003	-	-	48 g/m^2	$\approx$1000	0.03
Carbon fleece	-	-	-	8 g/m^2	-	0.02

5.6.1 Materials

The natural choice for a material with an high specific stiffness properties and low Z is Carbon Fiber Reinforced Plastics (CFRP). CFRP offer the possibility to create the material at the same time of the structure and then to tailor its structural properties in the maximum stressed directions.

In the case of the *cold plate* the specific stiffness and the low Z are the parameters driving the design. Therefore, the choice is oriented to the use of High Modulus carbon fiber with a Young modulus larger than 300 GPa (see Table 5.2). For the *cooling pipes* solution, the carbon fiber has to instead comply with the requirements in terms of specific stiffness and high thermal conductivity. This restricts the material choice and adds new constraints. High thermal conductivity fiber is usually associated with larger fiber diameter and larger stiffness, which implies added difficulties to shape and bend the fibers into the desired shape. In particular, this limitation complicates the winding of the fibers around the cooling pipes which is needed to maximize the heat exchange between the cold source (refrigerant in the pipe) and the cooling bridge (carbon fiber). The choice of the material for the cooling pipes to be embedded in the structure is driven by the requirement on the low material thickness and on the high thermal conductivity properties through the tubes wall thickness. The compromise among these conflicting requirements is in the use of a plastic tube with a thin wall. Polyimide small diameter pipes, ASIN B0013H0ZC1, [117] (1.5 mm outer diameter) with thin wall ($\approx 35\,\mu$m) have been used for the prototypes and other materials are under investigation. Different CFRP materials types have been considered in this design and prototyping phase: prepreg unidirectional and bidirectional (0/90), or wet tow. The carbon fibers used in the prototypes in combination with different epoxy resins are listed in Table 5.2. The materials thermal conductivity along the fiber direction is reported in the table.

5.6.2 Production Processes

The first dummy structures have been manufactured using two standard processes for composite materials production: ”manual lay-up” and ”filament winding”. In both processes a mandrel has been produced and used for the manual stratification of the pre-impregnated lamina or for the winding of the carbon rowing. Several tests have been performed to obtain the best stratification sequence and the minimum winding angles for the rowing. After the stratification or winding processes the CFRP structure undergoes a polymerization process which consists in applying a pressure load by counter-mould then exposing the structure to thermal cycle in an oven. The production is conceived as a single assembling with a unique curing process, in order to reduce the weight of the glue that has a large impact on the final weight. Mandrels and processes have been developed up to a level that demonstrates the feasibility of the various structures under consideration. Further improvements that will be beneficial both for the overall mass of the structure and the accuracy of its shapes will be done at a later stage.

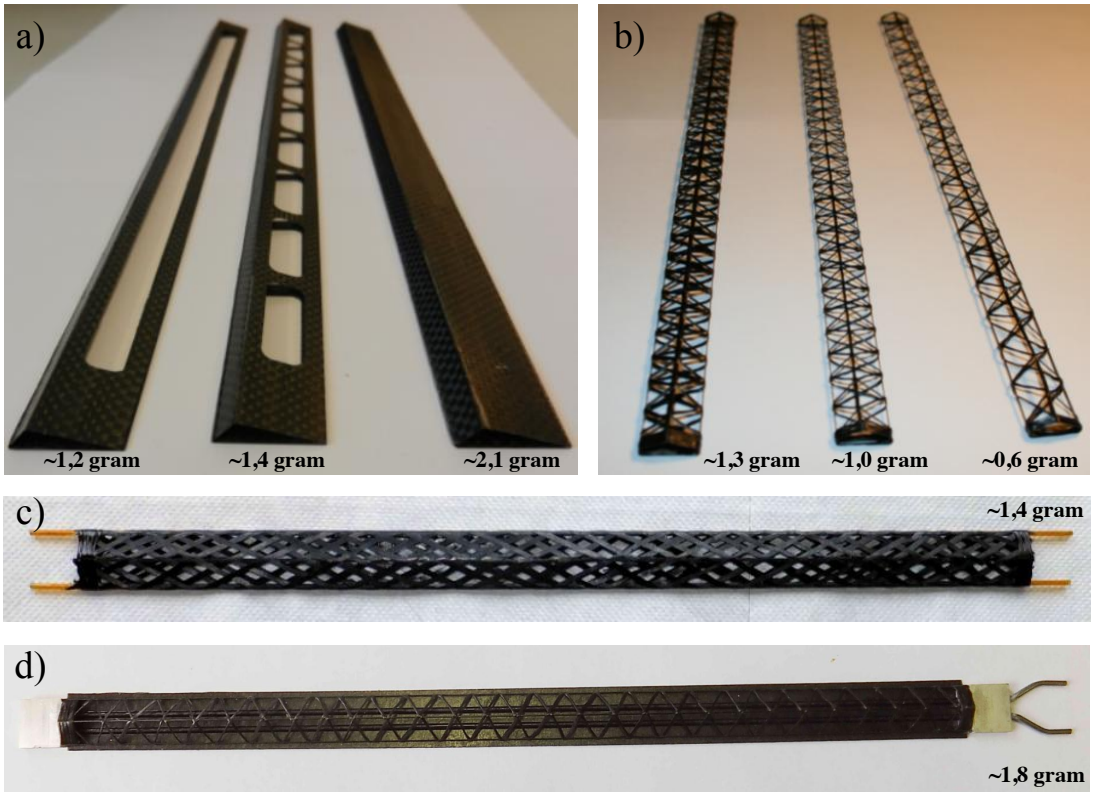

Figure 5.9: Pictures of the stave structures which are presented in this document for the two cooling options. For the *cold plate* concept two structures are being considered a) Open shell structure, b) Wound truss structure; while for the *cooling pipe* option other two structures are being considered c) Wound truss structure with pipes and d) Wound truss structure plus a plate with embedded pipes. The different prototypes have been manufactured trying to optimize the process and to reduce the material.

5.6.3 Stave Prototypes: Mechanical Structure

Different prototypes of the mechanical structure for the two stave concepts, *cold plate* and *cooling pipes*, have been produced and are discussed in the following.

5.6.3.1 Cold Plate Option

Two designs have been developed for this option: a light shell structure and a filament wound truss structure.

Open Shell Structure

This structure, 290 mm long, has a triangular section and a 120 μm thick wall. It is made by one (0/90) cross ply fabric of carbon fiber T300 prepreg [118]. A series of windows are opened in the structure, after the polymerization cycle, in order to reduce the material in front of the sensors. The structure with the best compromise between stiffness and weight (short openings) weighs $\approx$ 1,4 grams. It provides good stiffness and easy assembling and handling.

Wound Truss Structure

This structure is completely open. It is obtained by winding a carbon rowing around a mandrel with a winding angle and a number of helixes optimized to reduce the material budget. The wound struc-

ture has been developed as a simple support in alternative to the open shell structure, for the *cold plate* cooling concept. The material used is carbon fiber M55J 6K (6000 filament with 5 μm diameter) [118]. Each carbon filament has a section of 0.198 mm^2. The fibers are wound with an angle of 60 deg with respect the stave axis. The structure weighs $\approx$ 1.3 grams with optimum stiffness comparable to a continuous aluminum shell with the same wall thickness and section (see Figure 5.12). After an appropriate optimization of the manufacturing process, using M60J 3k (3000 filaments) [118] and a winding angle of 45 deg it was possible to reduce the weight of the structure to $\approx$0,6 grams while preserving a good stiffness. However, the reduced mass of the structure has to be balanced against aspects related to the handling of the material and assembly of the structure.

5.6.3.2 Cooling Pipes Option

For this cooling option two design concepts have been developed and prototyped: wound truss structure with pipes and wound truss structure combined to a carbon plate with embedded pipes.

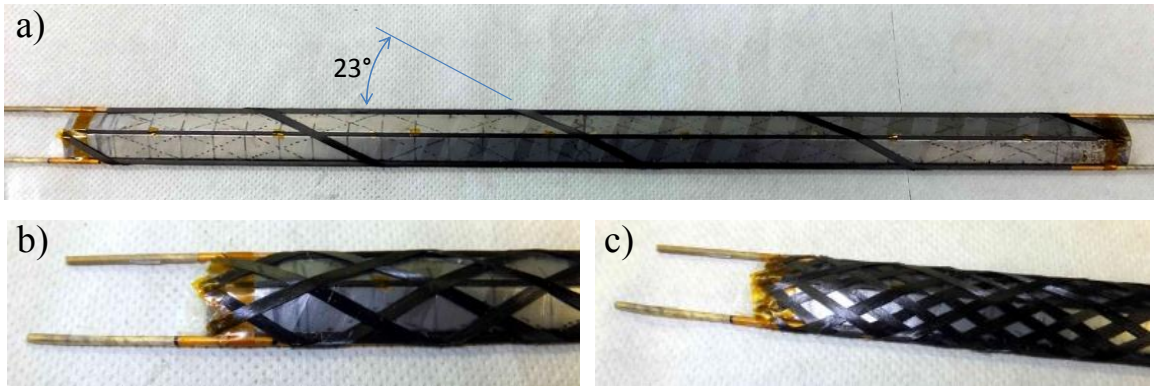

Figure 5.10: Production steps of a wound truss structure with pipes

Wound Truss Structure with Pipes

For the *cooling pipes* solution, the polyimide tubes (1.5 mm outer diameter and 35 μm wall thickness) have been embedded in the structure. The tubes are placed at the two corners of the triangular mandrel and the winding is done over the tubes without any additional glue. For this application the same technique described for the wound truss structure has been used, but the M55j fiber has been replaced with a better thermal conductive carbon fiber: K13D2U ($\approx$ 450 W/mK) [119]. K13D2U has been used as unidirectional prepreg 1.5 mm wide, 0.07 mm thick. The bending radius of this fiber is reduced with respect to the prototype done with the M55j due to the larger Young modulus and the filament diameter of 10 μm. A wider winding angle, $\approx$ 23 deg with respect to the stave axis, was used to avoid that fibers break during the production process while the number of helixes was increased (see Figure 5.10). The thermal performance of the structure was tuned by decreasing the step of the winding and enhancing the thermal contact between the fibers and the polyimide tubes through a ply of high conductive graphite paper (CF Paper [120]) wrapped around the pipes. The structure has a total weight of 1.4 grams and represents a trade-off among minimum material, stiffness and high thermal conductivity. This structure is particularly appealing if the detector has very low power consumption, in which case a wider winding step and an evaporative coolant could be considered to further reduce the material budget. With such a structure a value close to the 0.1 % of X_0 could be achieved if monolithic pixel sensors are produced on a large silicon surface covering the entire stave surface and no external electrical bus is needed.

Sample size 19 mm x 100 mm

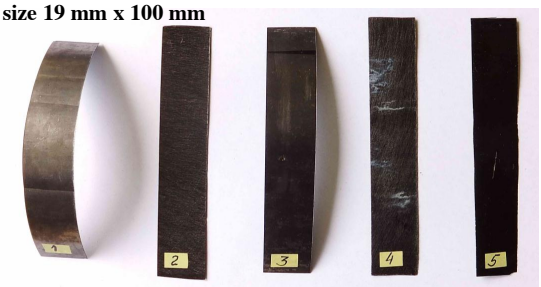

Lay up samples	1	2	3	4	5
	CF Prepreg	C Fleece	Mylar	C Fleece	CF Prepreg
	CF Paper	CF Prepreg	CF Prepreg	CF Prepreg	
		CF Paper	CF Paper	C Fleece	
		C Fleece	Mylar		
thick (mm)	0.09	0.14	0.11	0.12	0.07
Weight (gram)	0.33	0.40	0.37	0.31	0.20

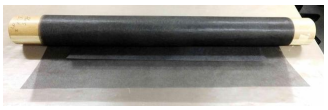

C Fleece

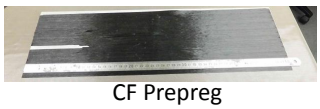

CF Prepreg

CF Paper

Figure 5.11: Carbon plate lay up optimization: samples with different materials and stacking sequence. The option number 2 has been chosen for the prototyping of the wound truss structure plus carbon plate with embedded pipes.

Wound Truss Structure plus Carbon Plate with Embedded Pipes

The layout of this structure is conceived such to provide a thermal bridge between the two polyimide cooling tubes (1.5 mm outer diameter, 35 μm wall thickness) by means of an unidirectional ply of high thermal conductivity carbon fiber (K13D2U, 70 μm thick) oriented in the direction normal to the axis of the tubes. The tubes are glued on top of the carbon ply and the thermal contact is enhanced by a thermal graphite foil (30 μm thick) that wraps the tubes and that is glued to the K13D2U lamina. These tubes are placed in the center of the structure to reduce the thermal gradient along the width. For structural reason an additional thin ply of carbon fleece (20 μm thick) is added on the top and bottom sides of the plate. An optimization study has been carried out to obtain a low-mass balanced lay up for the plate that embeds the tubes. A filament wound top cover, obtained with the same technology described as above, is glued on top of the thermal plate to stiffen the assembly (Figure 5.11).

5.6.4 Structural Test

The prototype structures described up to now show an optimum stiffness to mass ratio. A bending test was performed on few samples of the different structures and the stiffness properties were evaluated. This was done by applying a lumped mass to the center of the structure, simply supported at the two ends with an unsupported length of 270 mm. The load-deflection curves are compared in fig 5.12. A Finite Element Model (FEM) was developed and tuned based on this test results. The FEM was then used to predict the sag of the structure under the distributed weight of the sensors and the electrical bus (5 grams) with a load factor of 2. This model was also used to evaluate the first natural frequency of the structure. As an example the structural behavior of the wound truss structure with pipes is shown in Figure 5.13.

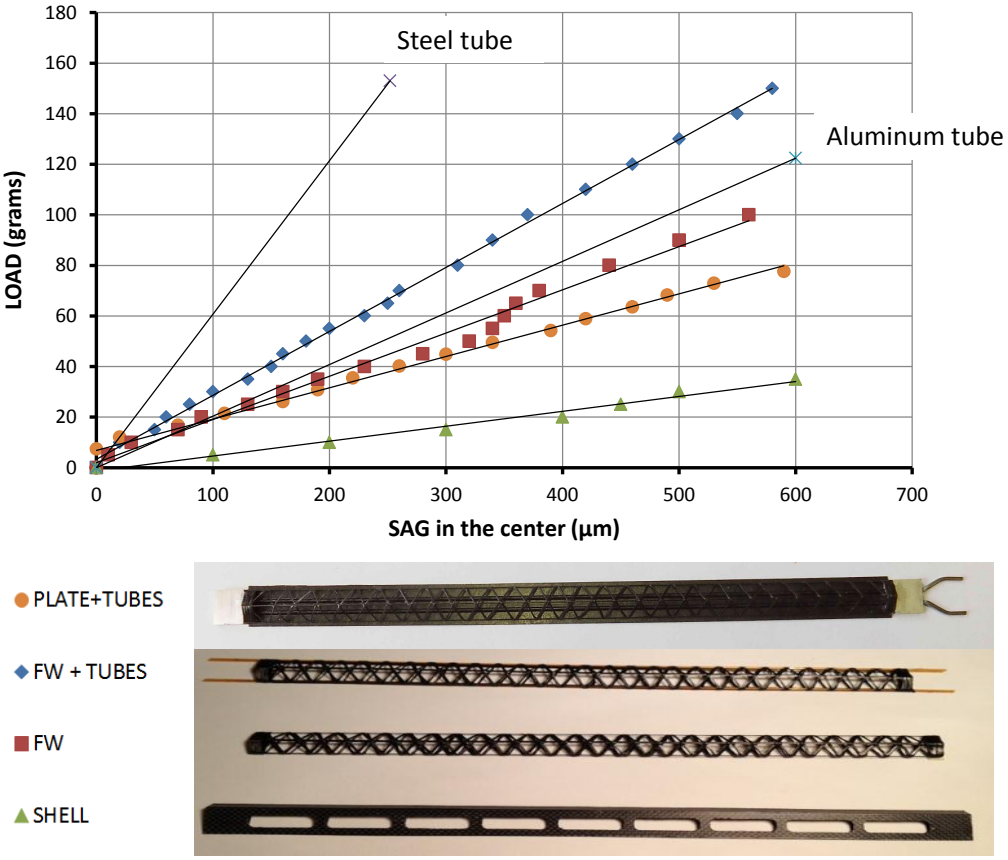

Figure 5.12: Bending test results performed on the four prototype structures. A tube made in aluminum and one in steel with an equivalent section have been added to the plot as reference.

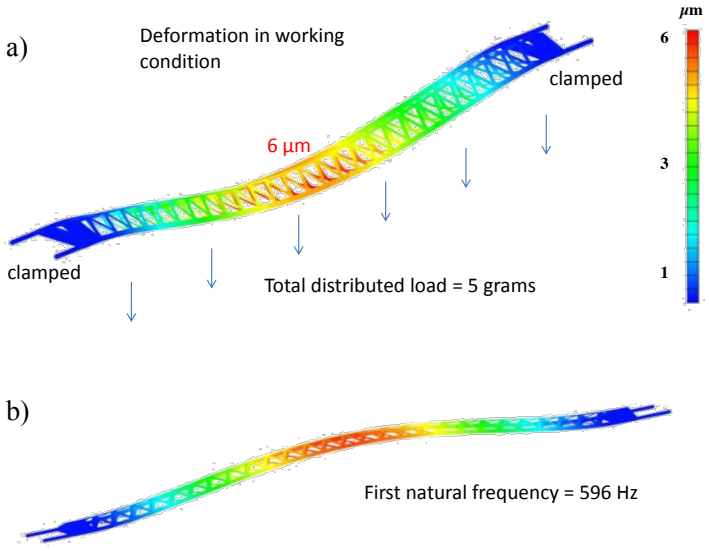

Figure 5.13: a) Structure deformation under a distributed load of 5 grams (load factor = 2) simulating the expected working condition. b) Structure first natural frequency and modal shape.

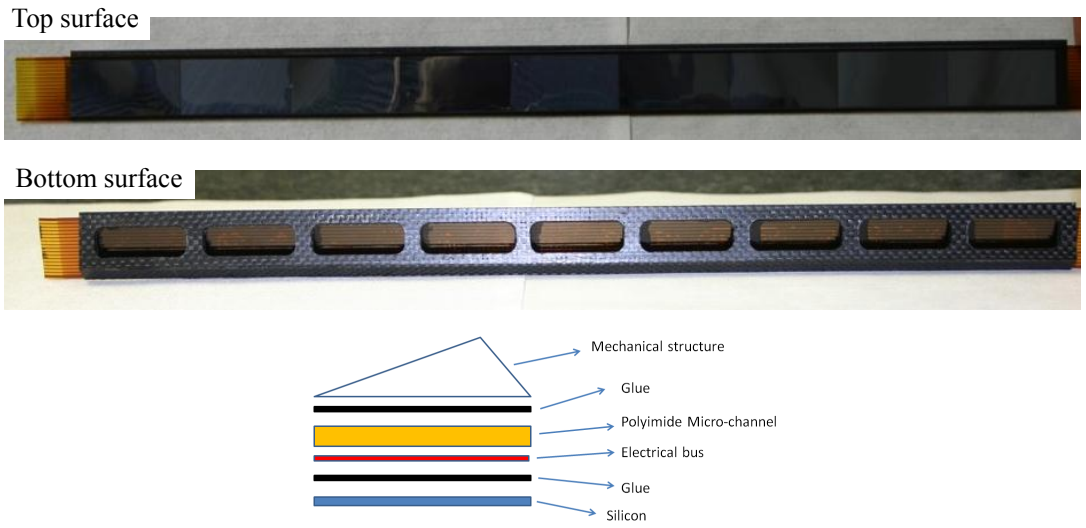

Figure 5.14: Pictures of the top and bottom surfaces of the stave prototype based on polyimide microchannel plate glued on a carbon fiber support (open shell structure). A schematic description of the components that form the stave is shown in the bottom.

5.7 Stave Prototypes: Assembly

Two of the four support structures described in Section 5.6.3 have been used to produce the first stave prototypes with dummy sensors. One structure was used for each of the two cooling options. These prototypes have been developed with the following objectives:

- develop experience with the manipulation of very thin and fragile components (the dummy silicon chips);
- realize the fist support and jig tools needed for the assembly of the different components;
- study various glue dispensing techniques;
- verify the overall mechanical accuracy and stability of the stave;
- perform a test of the cooling system and a thermal characterization of the stave.

The two prototypes have been equipped with nine blank silicon pieces 50 μm thick and 15 mm $\times$ 30 mm large placed in thermal contact with the cooling element. An heater made in polyimide is glued on top of the blank silicon pieces to provide the expected power consumption.

5.7.1 Cold Plate Stave Assembly

The first prototype is shown in Figure 5.14. The assembly procedure is done in two steps. The nine dummy silicon chips are first glued on the polyimide microchannel plate and then the microchannel plate is glued on the carbon fiber support. During the first step the glue has to be uniformly dispensed along the polyimide surface to guarantee the adequate thermal contact between the silicon and the cooling unit. This assembly has been performed using a Coordinate Measuring Machine (CMM) (Mitutoyo Crysta Apex 9166 [121]). The same CMM machine was used to produce all the modules of the present pixel detector [122, 123]. An adhesive mask is aligned and placed on the microchannel plate to confine the glue while the required thickness (100 μm for these prototypes) is guaranteed by the precise movement of the CMM machine, which removes the excess of glue dispensed by hand. The nine silicon chips are first aligned and held by vacuum on a dedicated jig and then precisely placed on the microchannel plate.

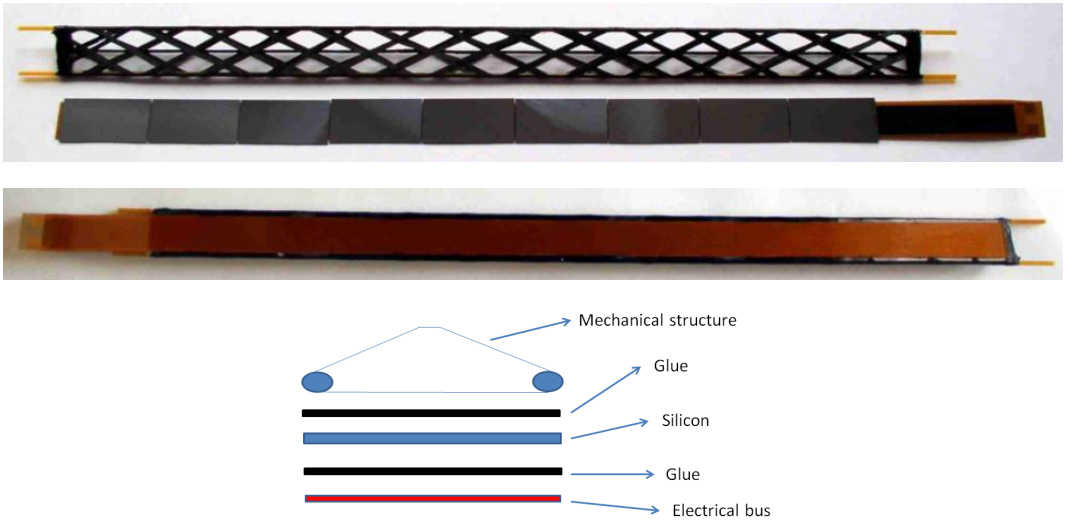

Figure 5.15: Pictures of the assembly prototype based on silicon chips with polymide heater, glued on a carbon fiber mechanical support with integrated polyimide tubes. A schematic description of the components that form the stave is shown on the bottom.

During the glue curing phase (24 h), both the silicon chips and the microchannel plate are kept flat by the jigs. The second part of the procedure consists in gluing the opposite side of the microchannel plate on the carbon fiber support. A picture of this prototype is shown in Figure 5.14. For this first prototype the glue was dispensed along the mechanical support using a mask as in the previous step, but to minimize the material budget we are considering the use of dots of glue dispensed by a syringe. One of the ongoing R&D activities on the polyimide microchannel plate is the integration of the electrical bus in its cover layer.

5.7.2 Cooling Pipes Stave Assembly

The second prototype is shown in Figure 5.15. In this case we have a similar a two-step assembly procedure. The first step involves gluing the nine silicon chips on a thin heater made of polyimide, which simulates the electrical bus and provides the expected power consumption. In the second step this assembly is glued on the carbon support structure built with fiber filaments wound around the polyimide tubes. The first assembling step is performed dispensing a layer of glue 100 μm thick using an adhesive mask on top of the poliymide heater held in position by a vacuum system. The silicon pieces are placed one after the other by a manual pick-and-place machine. A glue dispenser machine is being equipped with a microscope and a pick-and-place tool to automatize this part of the procedure. The next step is to dispense a calibrated layer of glue on the mechanical structure. This part of the procedure is very important since has to guarantee a good thermal contact between the silicon and the cooling element. Different techniques will be evaluated for the glue dispensing, as for example films, mask or syringe. The structure of this prototypes was bathed into a calibrated layer of glue and then placed in contact with the silicon. This technique accounts for the non planarity of the structure but reduces the control on the thickness of the dispensed glue.

5.8 Cooling

Several cooling schemes fully integrated in the support structure and based on different refrigerant media (air, liquid and two-phase) have been studied.

An air-cooling system has the advantage of not introducing any extra material (i.e. pipes and liquid) in the detector sensitive volume. The effectiveness of such implementation depends on the airflow velocity and

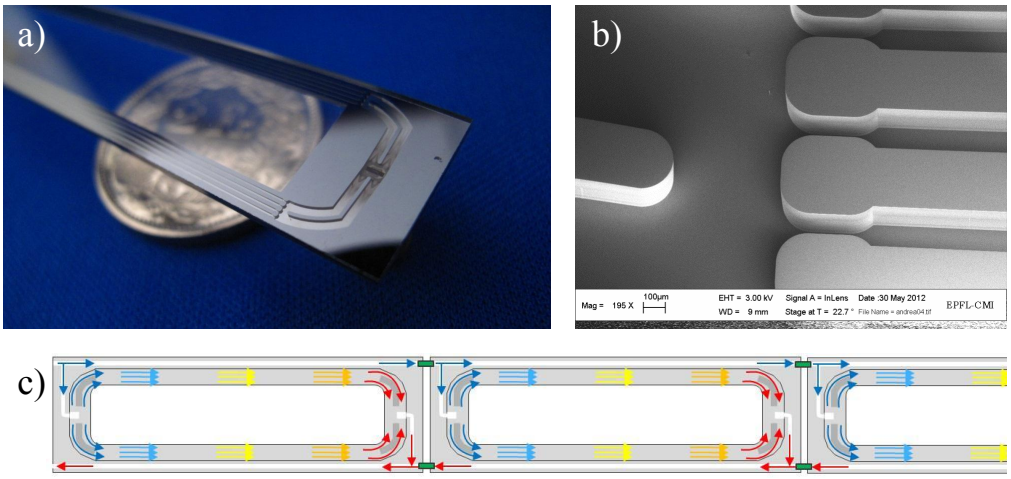

Figure 5.16: a) Picture of a silicon microchannel frame. For the prototyping phase the cover layer is produced in pirex to allow the visual inspection. b) Zoom of the inlet manifold and c) sketch of frames interconnection.

on the possibility to guide the flow over the dissipating elements. The preliminary simulations discussed in [55], showed that operating the detector at a mean temperature of 35° with a power consumption ranging from 0.3 to 0.5 W/cm^2 requires an air speed of 10 to 20 m/s. These results are valid under the assumption of an ideal airflow along the ITS layers. The implementation of such concept and the stiffening of the structure to prevent the mechanical vibration at the calculated air speed, put severe constrains on the mechanical design with an impact on the material budget. Therefore, the air-cooling scheme is not competitive in terms of material budget with the other cooling schemes under consideration and discussed below. Should the R&D on the pixel chip result in a power density significantly lower than 0.3 W/cm^2, the air-cooling scheme could become attractive and new studies will have to be carried out.

The other cooling schemes under consideration will be discussed in this section with a special focus on the *cold plate* and *cooling pipe* concept.

5.8.1 Cooling Scheme based on a Cold Plate

This *cold plate* scheme is based on a polyimide or silicon substrate, within which a cooling fluid flows through a set of parallel cooling channels (microchannels).

Silicon Microchannels

The solution of microchannels etched on a silicon substrate is described in this section. This is actually an option considered for the NA62 Experiment at CERN [124]. This cooling technique [125] is being studied within the framework of the Cooling Project of the PH-DT group at CERN, in cooperation with the Microsystems Laboratory of EPFL [126] in Lausanne and CSEM [127] in Neuchatel.

The silicon microchannel plates optimized for the NA62 experiment are based on a 4-inch wafer (101.6 mm). This means that three plates would be required to equip each stave (270 mm length) of the ALICE ITS inner layers. The preliminary criteria adopted to choose the size of the silicon microchannels (200 μm $\times$ 200 μm) are based on the studies published by Prof. J. Thome from the EPFL in Lausanne [128].

The first prototypes of low material budget micro-fabricated silicon cooling plates have been built in the class 100 clean-room of the Center of MicroNanoTechnology at EPFL in Lausanne. The process is carried out on a Czochralski silicon wafer polished on both sides. The main characteristics of the substrate are: 4 inches diameter, 380 μm thickness and 0.1 - 0.5 Ω·cm p-type. The microchannels are covered with a silicon layer 50 μm thick. The two silicon layers are pressed at room temperature and

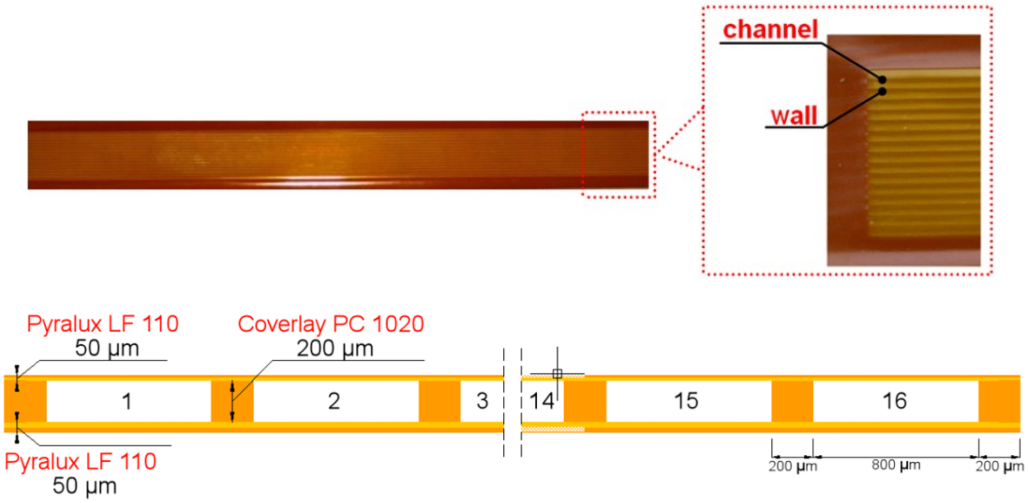

Figure 5.17: Picture of a polyimide MCHS prototype: 16 channels with a cross section of 0.8 $\times$ 0.2 mm, and walls of 0.2 mm between adjacent channels. A sketch of the cross section is shown in the bottom.

afterwards annealed at high temperature. The possibility to have the silicon microchannels only at the long edge of the stave is being considered. In this case an opening is etched in the middle of the frame which sits in front of the detector sensitive area (sideline microchannel structure).

The first prototypes of a sideline microchannel structure have been recently produced (see Figure 5.16) following the aforementioned procedure, including the extra etching step needed to create the opening in the structure. A dedicated R&D program is being carried-out to interconnect the three frames required to build a stave (see sketch in Figure 5.16). The test performed so far, focused on thermal characterization of the single frame, confirmed the high potentiality of this cooling concept applied to the ALICE requirements. Nevertheless further developments are necessary to bring this concept to the same maturity of the others and to have a complete integrated system that could be fully characterized at the stave level.

Polyimide Microchannels

Polyimide based Micro-Channels Heat Sink (MCHS) [129] represents an interesting possibility to cool down the pixel stave using single phase cooling. The MCHS, showed in Figure 5.17 is a multilayer polyimide composite made with a layer of Pyralux LF110 [130, 131] at the bottom, a Photoimageable PC 1020 [131, 132] layer in the middle and a Pyralux LF7001 [130, 131] layer glued on the top. The multilayer PC 1020, which is 200 μm thick, is glued on the LF110. The rectangular pattern which defines the channels is created with a photolithography process at 180°C and the foil of LF7001 is hot pressed on the top of the substrate to cover the channels. The full structure is then thermally cured at 180°C for 10 hours in order to achieve its ultimate end-use properties.

The MCHS structure is glued on a carbon-fiber structure which is used to rigidify the stave and to support it onto the two carbon-fiber wheels. The advantage of the polyimide substrate is the high radiation length (29 cm). The estimated mean material budget ranges from 0.085% of X_0 to 0.13% of X_0 if water or C_6F_{14} is used as coolant respectively. This estimate does not include the carbon fiber support structure.

An analytical thermo-fluid dynamic study has been carried out to find the best microchannel section (800 μm $\times$ 200 μm) fulfilling the operational requirements. Mechanical tests have been performed on the MCHS prototypes to verify the leak tightness. The pressure inside the MCHS was raised up to 10 bars without showing delamination. The polyimide compatibility with water is also being verified in a long term test. One of the first prototypes was pressurized with argon at 2 bar and submerged in water. This test is running for nine months and the structure has yet to show any leak.

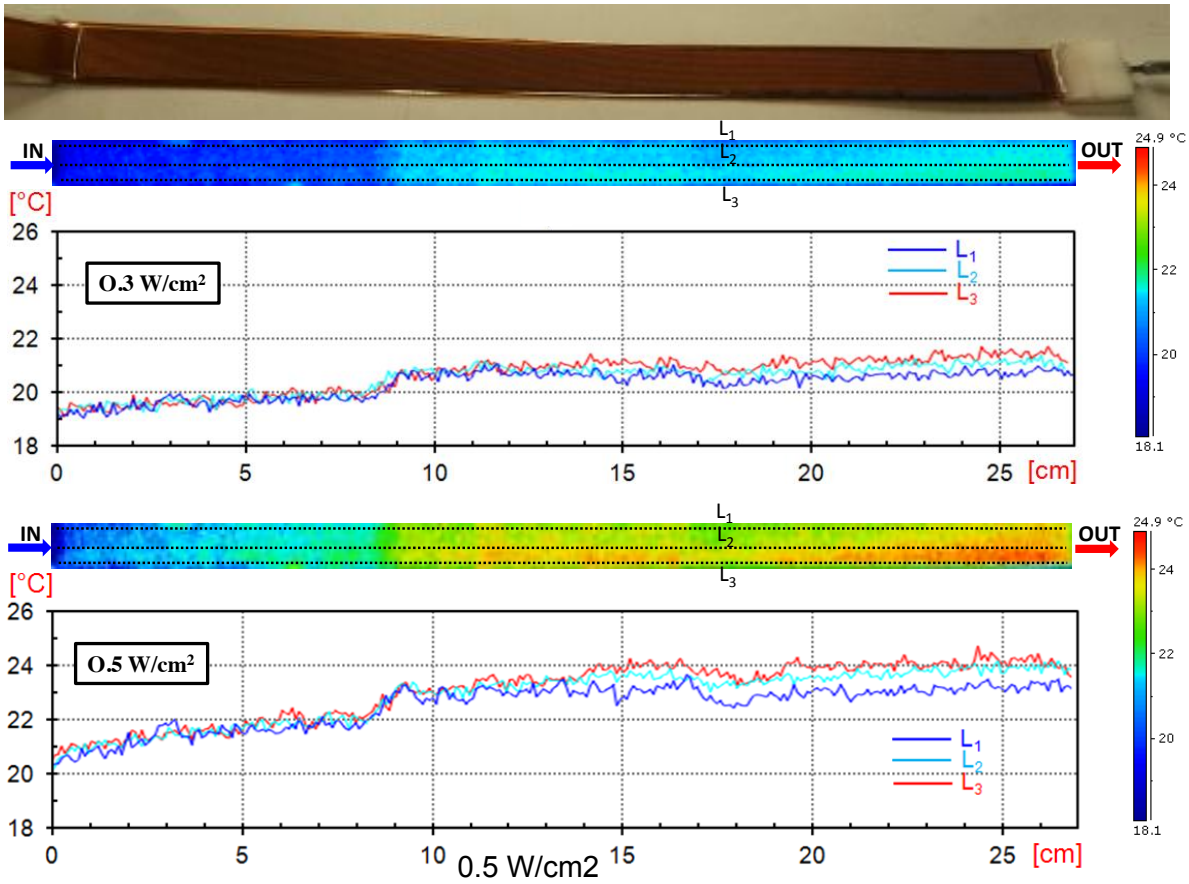

Figure 5.18: Thermographic images and temperature profiles of the heater surface glued on the polyimide microchannel plate. The power consumption applied is 0.3 and 0.5 W/cm^2 top and bottom plots respectively, with the water flow rate of 4.8 l/h.

The thermal behavior of the microchannels has been tested. A kapton heater 15 mm $\times$ 270 mm was glued onto the MCHC to emulate the expected electronics heat flux. Water was used as coolant in single phase at about 15°C at the inlet. The test was performed at different flow rates (from 2 l/h to 4.8 l/h) showing different pressure drops between inlet and outlet (from 262 mbar to 620 mbar). Two values of heat flux were considered: 0.3 and 0.5 W/cm^2. The temperature distribution above the heated surface was measured with a thermal infrared camera. Two PT100 in thermal contact with the heater at the inlet and outlet were used as reference.

Figures 5.18 shows the thermographic images of the heater during the test with water flow at 4.8 l/h and an heat flux at 0.3 (on top) and 0.5 W/cm^2 (on bottom). In the same figure the temperature distributions along three lines L1/2/3 are reported. The temperature increases uniformly along the flow direction in both tests. The peak temperature is located closer to the outlet and is 21.7°C at 0.3 W/cm^2 and 24.7°C at 0.5 W/cm^2. with an average working temperature of 20.5°C and 22.5°C respectively. The measured thermal gradient on the surface is 2.7°C at 0.3 W/cm^2 and 4.7°C at 0.5 W/cm^2. Good performance can be obtained also at lower flow rate. In particular at 2 l/h with a heat flux of 0.3 W/cm^2 the average temperature is less then 23°C with a maximum value of 25.4°C.

5.8.2 Cooling Pipes Option: Cooling Elements Description and Test

This solution is suitable both for single phase or evaporative cooling concept . As first approach water was used as fluid, keeping the coolant study as a further optimization step. The two polyimide tubes embedded in the mechanical structure are interconnected at one extremity in order to have the inlet and

outlet on the same side. Two different prototypes described in Section 5.6.3.2 have been tested: a) Wound truss structure with pipes and uniform carbon plate b) Wound truss structure with pipes.

Wound Truss Structure with a uniform Carbon Plate

This structure (see Figure 5.19) is tested by applying a polyimide heater glued on top of the carbon plate that simulates the heat dissipated by the detector. The produced heat is carried by the carbon plate to the embedded pipes where it is removed by the water flow. In this path there are two thermal critical interfaces: the first is between the heater and the carbon plate (assembly level as described in Section 5.7) and the second is between the carbon plate and the embedded pipes (structure construction level detailed in Section 5.6.3).
The results of the thermal tests performed on this structure are shown in Figure 5.20. The thermographic pictures of the heater surface show the temperatures measured with a water flow rate of 8 l/h, water temperature at the inlet of 14.8°C and with an applied power density of 0.3 W/cm^2 and 0.5 W/cm^2. The structure shows slightly warmer areas in the central region, and a possible explanation of these warmer areas could be the reduced thermal contact between the plate and the pipe in that region. This thermal contact could be enhanced by optimizing the production process or by squeezing the tubes on the carbon conductive plate (option under investigation). The test showed that the maximum temperature of the heater stays below 25°C with a power density of 0.3 W/cm^2 and below 30°C with a power density of 0.5 W/cm^2. The temperature profile is quite uniform along the stave and the maximum temperature gradient with the higher power consumption (0.5 W/cm^2) is below 7°C even considering the hotspots. The structure also showed good behavior with a reduced flow rate. An increase of about 2 degrees for both the power consumptions was measured at a flow rate of 3 l/h. Such a small flow rate will guarantee a low pressure drop and a low water velocity in the pipes enhancing the system reliability.

Wound Truss Structure with Pipes

For the test of this structure 9 pieces of blank silicon were glued on the filament wound structure. A polyimide heater was glued on top of the silicon pieces to emulate the power consumption. The dissipated heat goes thorough the silicon and is carried to the cooling pipes via the carbon fiber strips. The thermal contact is enhanced by a graphite foil wrapped all around the pipes (see Figure 5.22).

The thermal results obtained with this structure are shown in Figure 5.22. The test has been carried out using the flow rate of 8 l/h with the water temperature at the inlet of 14.8°C. The power density applied is 0.3 W/cm^2. The measured temperature profile stays below ≈33°C. The temperature profile is quite uniform although there is a temperature drop at the two extremities (close to the hydraulic connectors) which brings to maximum temperature non uniformity around ≈6°C. As expected the hotter zone is located in the center of the structure between the two tubes. A similar test was performed with the power density of 0.5 W/cm^2. In this case the maximum temperature was around 45°C.

This structure was designed to be a compromise between thermal and mechanical performance and the test showed its capability to fulfill the lowest ITS requirements in terms of power consumption (≈0.3 W/cm^2).

5.9 Material Budget

The material budget estimated for the stave prototypes as mentioned above is reported in this section. The stave prototypes to which this estimate applies fulfill the mechanical and thermal requirements of the new ITS, although further studies and optimization are still needed.
The following considerations are based on two main assumptions: monolithic silicon chips 50 μm thick

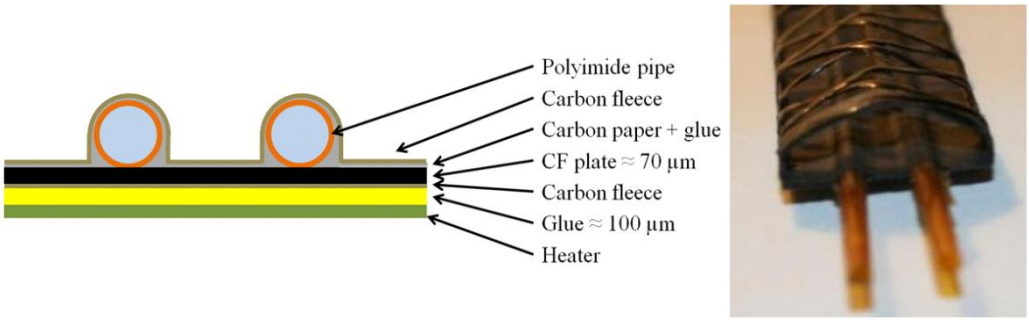

Figure 5.19: Picture of the wound truss structure with uniform carbon plate and polyimide tubes (right) and schematic section view (left).

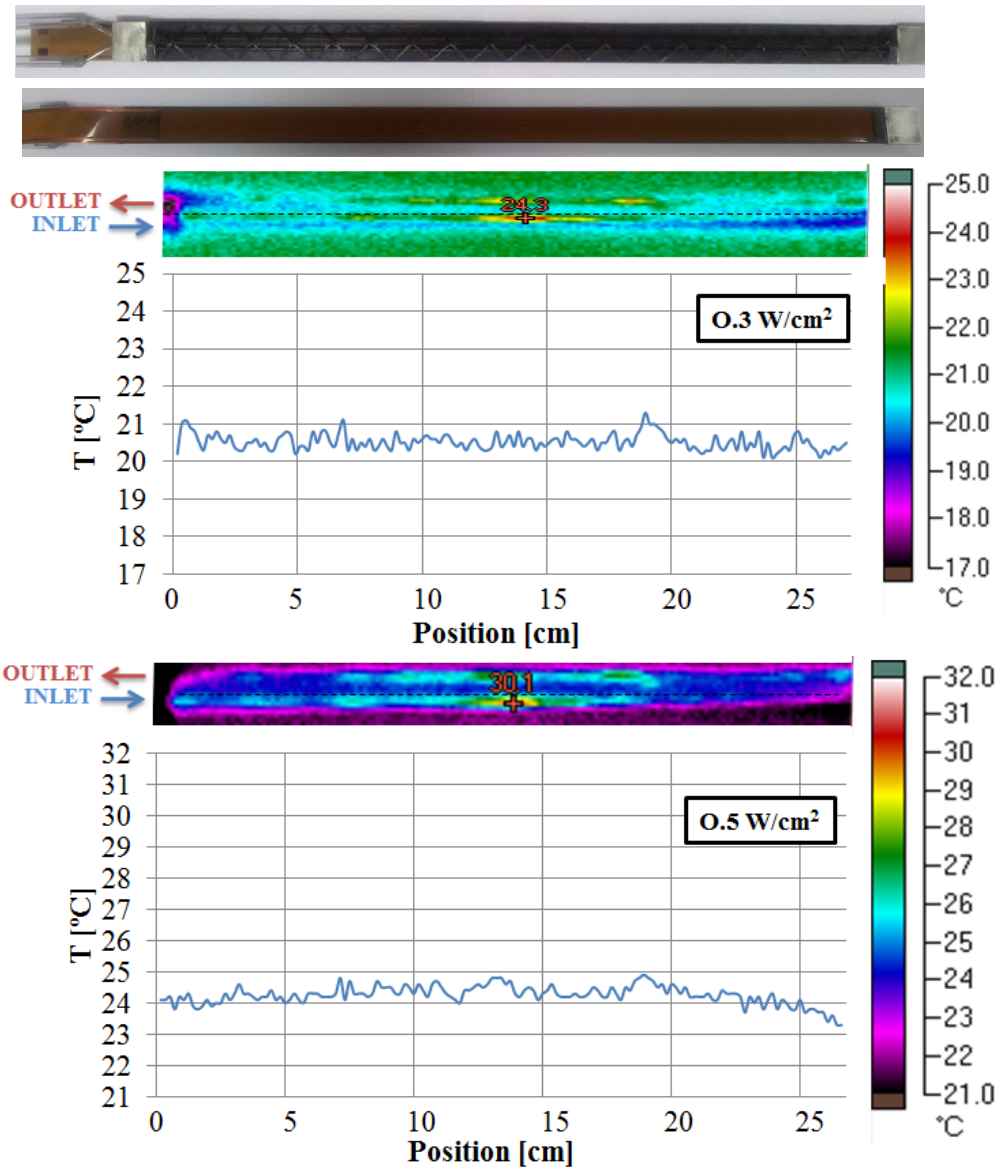

Figure 5.20: Thermographic images of the heater surface with water flow rate of 8 l/h and power consumption of 0.3 W/cm^2 (on top) and 0.5 W/cm^2 (on bottom). The temperature profile is taken along the center the structure. The warmest spot temperatures are outlined on top of the thermographic images.

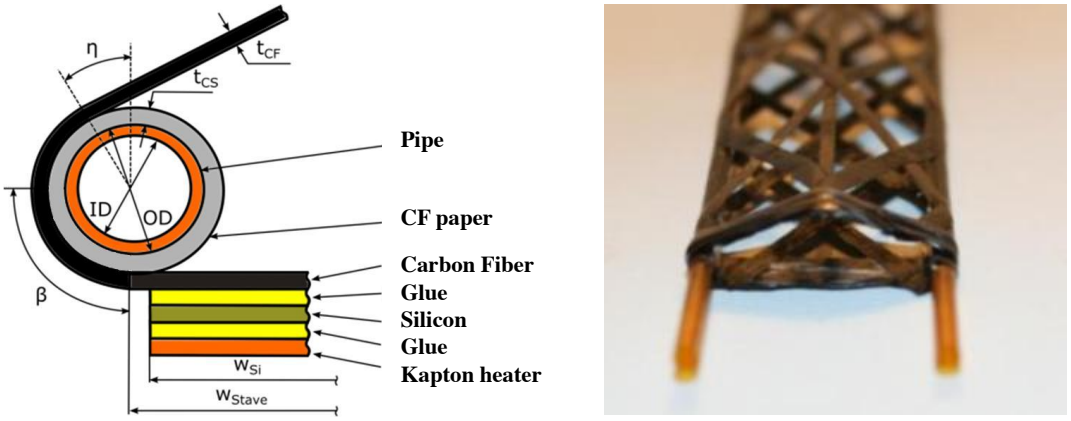

Figure 5.21: Picture of the wound truss structure with pipes (right) and schema of the section view (left).

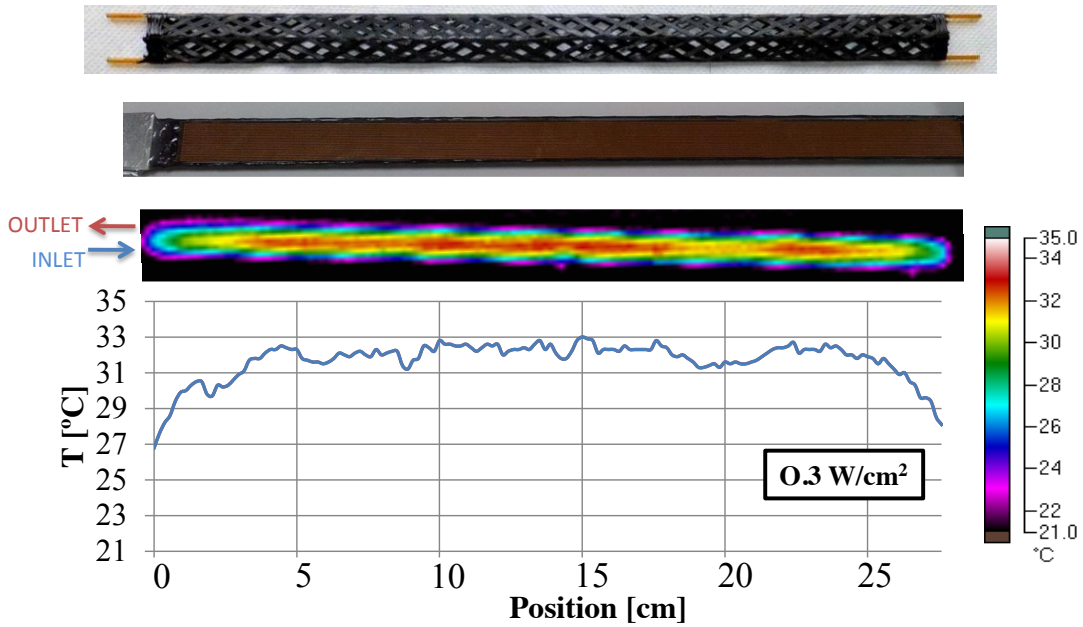

Figure 5.22: Thermographic images of the heater surface with water flow rate of 8 l/h and power consumption of 0.3 W/cm^2. The temperature profile is taken along the center the structure.

and a double layer electrical bus, similar to the one produced for the HFT project in STAR [109]. The different materials considered and their contribution in percentage to the overall material budget are listed in the Tables 5.3, 5.4 and 5.5. A sketch of the mechanical structure used to build these prototypes is shown on the top of each table.

5.9.1 Cold Plate Prototype: Material Budget Estimate

The estimate reported in this section applies to the open shell structure with the polyimide microchannels (see Section 5.6.3).

The material budget for the mechanical structure considers that a part of the stave surface (22 %) is covered with one layer of carbon fiber 120 μm thick, a part (43 %) with two layers and the rest (35 %) is uncovered. On top of this structure the polyimide microchannels plate is glued. The top and bottom cover layers of the microchannels are 50 μm thick while the walls between the microchannels are 200 μm

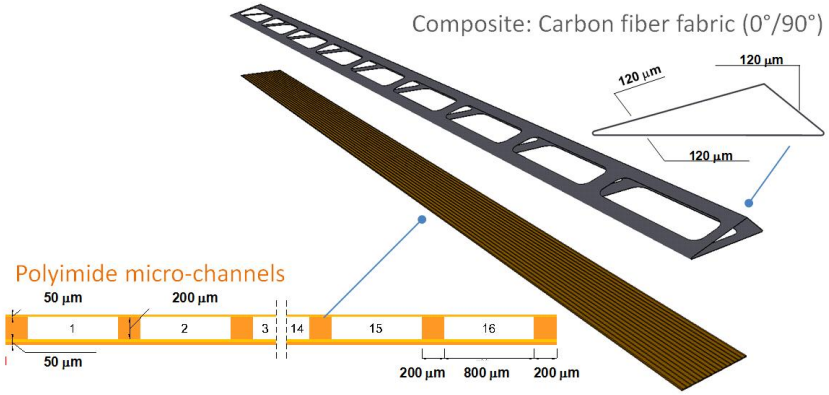

Figure 5.23: Mechanical structure and polyimide microchannels sections.

Table 5.3: MCHS cold plate prototype: list of components and their contribution to the mean material budget estimate.

Material	Surface (%)	Tickness (μm)	X_0 (cm)	X/X_0 (%)	Contribution to the total X/X_0 (%)
CFRP	22	120	25	0.011	3.5
CFRP	43	240	25	0.043	13.7
Glue (CFRP - microchannel plate)	20	100	44.4	0.005	1.5
Polyimide microchannels walls	21	200	28.6	0.015	4.9
Polyimide microchannels covers	100	100	28.6	0.035	11.6
Water	79	200	36.1	0.044	14.5
Electrical bus	100	-	-	0.075	25.0
Glue (bus - silicon)	100	100	44.4	0.022	7.5
Silicon	100	50	9.36	0.054	17.8
Total				≈ 0.30	

wide and 200 μm thick. The microchannels are 200 mm $\times$ 800 μm filled with water. Two layers of glue (100 μm thick) at the interface of the microchannels with the mechanical structure and with the silicon detectors have been considered.

The mean value of the material budget is approximately 0.30 X/X_0. An equivalent estimate is obtained if a filament wound support structure is considered instead of the open shell structure.

5.9.2 Cooling Pipes Prototype: Material Budget Estimate

In the two following sections we quote the material budget for two prototypes corresponding to the *cooling pipe* concept.

Wound Truss Structure with Pipe and a uniform Carbon Plate

This prototype has shown good thermal performance (see Section 5.8.2) thanks to the carbon fiber plate 140 μm thick with embedded polyimide tubes. This structure is further stiffened by a wound truss structure build with the carbon fiber M60J. The wall of the polyimide tube is 35 μm thick and water is considered as coolant. On top of the mechanical structure we are considering 2 layers of glue 100 μm thick, plus silicon and a double layer electrical bus. The mean value of the material budget is approximately 0.31 X/X_0 that is quite similar to the one for the *cold plate* prototype.

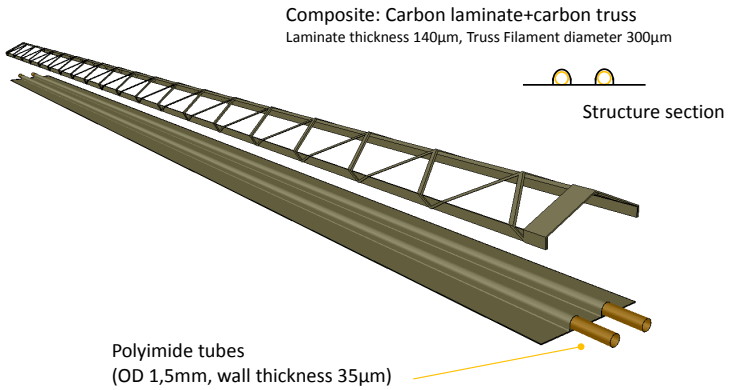

Figure 5.24: Wound truss structure combined to a carbon plate with embedded polyimide tubes.

Table 5.4: Wound truss structure with uniform carbon plate prototype: list of components and their contribution to the mean material budget estimate.

Material	Surface (%)	Tickness (μm)	X_0 (cm)	X/X_0 (%)	Contribution to the total X/X_0 (%)
CFRP filament	35	100	25	0.014	4.6
Carbon plate	100	140	25	0.056	18.2
Polyimide Tubes	19	70	28.6	0.005	1.5
Water	19	1450	36.1	0.06	19.3
Glue (CFRP - silicon)	100	100	44.4	0.022	7.3
Silicon	100	50	9.36	0.054	17.4
Glue (silicon - bus)	100	100	44.4	0.022	7.3
Electrical bus	100	-	-	0.075	24.4
Total				≈ 0.31	

Wound Truss Structure with Pipes

The second prototype being considered is the carbon fiber wound structure with embedded polyimide tubes. The CFRP material budget reported in Table 5.5 accounts for the percentage of surface covered by both top and bottom carbon fibers. The wall of the polyimide tube is 35 μm thick and the water has been considered as coolant. In addition we accounted for 2 layers of glue 100 μm thick assuming a coverage of 50% for the layer between the structure and the silicon.

The mean value for this prototype is approximately $0.26\,X/X_0$. It is important to point out that this structure is slightly lighter than the previous two but it has reduced thermal performance. The R&D activity on this structure is important because it will allow us to further contain the material budget if a chip with a power density lower than of $0.3\,W/cm^2$ will be used to build the new detector.

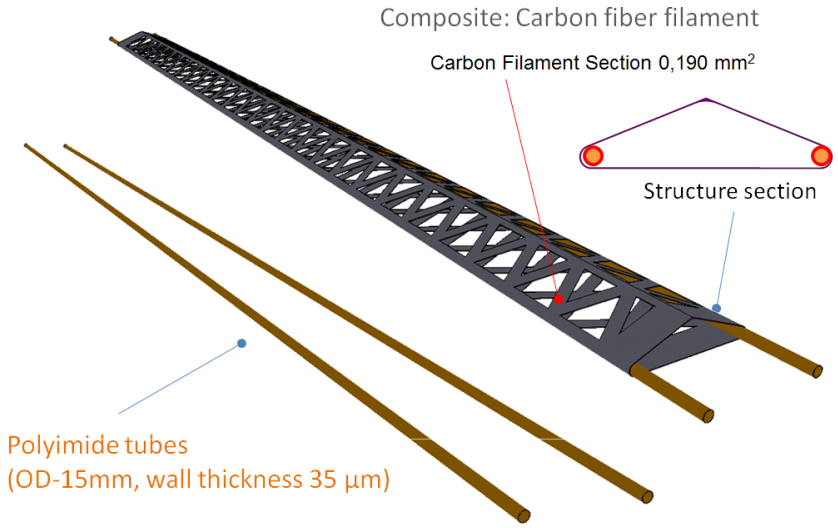

Figure 5.25: Mechanical structure with embedded cooling pipes layout.

Table 5.5: Wound truss structure with pipe prototype: list of components and their contribution to the mean material budget estimate.

Material	Surface (%)	Tickness (μm)	X_0 (cm)	X/X_0 (%)	Contribution to the total X/X_0 (%)
CFRP filament	100	70	25	0.035	12.6
Polyimide Tubes	19	70	28.6	0.005	1.8
Water	19	1450	36.1	0.06	22.8
Glue (CFRP - silicon)	50	100	44.4	0.01	4.4
Silicon	100	50	9.36	0.054	20.7
Glue (silicon - bus)	100	100	44.4	0.022	8.7
Electrical bus	100	-	-	0.075	29.0
Total				≈ 0.26	

Chapter 6

Project Organization, Cost Estimate and Time Schedule

6.1 Project Organization

The development of the new ITS is part of the current ALICE ITS Project, which is organized according to the ALICE Collaboration rules and constitution. In addition to the Institutes already members of the ITS Project, several new Institutes have joined the ITS Collaboration to participate in the development and construction of the new detector and are actively participating in the R&D studies. Very few Institutes who are currently members of the ITS project will not participate in the development of the new ITS. Nevertheless, these Institutes have confirmed their commitments to the maintenance and operation of the present ITS. The Institutes that intend to contribute to the ITS upgrade project are listed in Table 6.1.

The contributions and responsibilities of the participating Institutes, as well as the manpower and funding resources, are being discussed and will be defined in the MoU that will be set up at the time of the Technical Design Report which is planned for end 2013. Some Funding Agencies have already in 2011 and 2012 allocated relevant resources for the R&D activities and have committed themselves for 2013.

All institutes taking part in the ITS project have specific expertise and past experience in the development, construction and running of silicon trackers. Several institutes have long standing expertise in ASIC design, construction of detector ladder and support mechanics, manufacturing of composite materials, integration and characterization of hybrid pixel and microstrip detectors. The world leading experts for the development of monolithic pixel detectors are also part of the ITS collaboration.

6.2 Cost Estimate

At the present stage several technologies are being considered for the implementation of the ITS detector. The technology that will be adopted for the implementation of the different detector layers, will be chosen to best suit the detector requirements within the boundaries set by the available funds and the project time line. In terms of performance and cost the use of monolithic pixel detectors would be suitable for all layers, while the hybrid pixel detectors may become prohibitive as the radius increases due to cost reasons. However, a limitation to the use of monolithic pixel detectors for the innermost layers may arise from the level of radiation that can be tolerated by the selected technology. Moreover, it could turn out that a few microstrip layers at large radii is mandatory for particle identification if the charge signal delivered by the thin sensor layer of monolithic pixel detectors does not provide enough resolution. Based on the above considerations it can be reasonably assumed that the ITS will be based at most on two silicon detector technologies.

Table 6.1: Expression of interest to the ITS detector upgrade, subject to funding

Country Funding Agency	City	Institute
CERN	Geneva	European Organization for Nuclear Research
China	Wuhan	Institute of Particle Physics, Central China Normal University (CCNU)
Czech Republic	Řež u Prahy	Nuclear Physics Institute of the ASCR
France IN2P3	Strasbourg	Institut Pluridisciplinaire Hubert Curien, Université Louis Pasteur, IN2P3-CNRS
Italy INFN	Bari	Sezione INFN e Dipartimento dell'Università e del Politecnico di Bari
Italy INFN	Cagliari	Sezione INFN e Dipartimento di Fisica dell'Università di Cagliari
Italy INFN	Catania	Sezione INFN e Dipartimento di Fisica dell'Università di Catania
Italy INFN	Frascati	Laboratori Nazionali di Frascati (LNF)
Italy INFN	Legnaro	Laboratori Nazionali di Legnaro (LNL)
Italy INFN	Padova	Sezione INFN e Dipartimento di Fisica e Astronomia dell'Università di Padova
Italy INFN	Roma	Sezione INFN e Dipartimento di Fisica dell'Università "La Sapienza" di Roma
Italy INFN	Torino	Sezione INFN e Dipartimento di Fisica dell'Università di Torino
Italy INFN	Trieste	Sezione INFN e Dipartimento di Fisica dell'Università di Trieste
Korea	Seoul	Yonsei University
Pakistan	Islamabad	Faculty of Sciences, COMSATS, Institute of Information Technology
Russia	St. Petersburg	Institute of Physics, St. Petersburg State University
Slovakia	Košice	Slovak Academy of Sciences, IEP
UK STFC	Birmingham	University of Birmingham
UK STFC	Warrington	STFC Daresbury Laboratory
UK STFC	Chilton	Rutherford Appleton Laboratory
Ukraine	Kharkov	Ukrainian Academy of Sciences, KIPT-KFTI
Ukraine	Kharkov	Scientific Research Technological Institute of Instrument Engineering SRTIIE
Ukraine	Kiev	Bogolyubov Institute for Theoretical Physics (BITP)

In the following we give a cost estimate for the two design options under study:

- Option 1: 7 layers of monolithic pixel detectors, which would provide excellent standalone tracking efficiency and p_{t} resolution, but limited PID capability.
- Option 2: a combination of 3 innermost layers of hybrid pixel detectors and 4 outermost layers of strip detectors, which would provide better PID capability but worse standalone tracking efficiency and momentum resolution.

The cost breakdown for the two detectors options is reported in Table 6.2. The costs associated to the activities described in the table should be understood in terms of CORE values: material costs, excluding Institutes personnel costs and basic infrastructures. CORE estimates include detector components and production costs, as well as industrial or outsourced manpower for production, installation and integration. It should also be noticed that the R&D activities are not included.

6.3 Time Schedule

The ALICE upgrade is planned to be in operation after Long Shutdown 2 (LS2) and has a programme that will extend till the high luminosity LHC (HL-LHC) era after Long Shutdown 3 (LS3). The current LHC schedule foresees LS2 to take place in 2018 and LS3 to start in 2022. The upgrade of the TPC

Table 6.2: Cost estimates for the ALICE Inner Tracking System

ITS option 1[a]	
Item	Cost[MCHF]
Silicon	2.0
Thinning, dicing and mounting	1.0
MCM	1.0
Kapton cables	1.0
Cables, connectors and patch panels	2.0
Mechanics and cooling	1.5
On-detector low-voltage regulation	0.5
Power supply	1.0
Total	**10.0**

ITS option 2[b]	
Item	Cost[MCHF]
Double side detector	8.0
Front-end electronics	4.0
Readout	0.8
Assembly tools	0.8
Cables and optical fibers	0.8
Cooling	0.2
Mechanics	0.6
Power supply	0.8
Total	**16.0**

[a] ITS option 1 = 7 layers of monolithic pixels
[b] ITS option 2 = 3 layers (inner) of hybrid pixels and 4 layers (outer) of strips

Table 6.3: ITS upgrade timeline

Year	**Activity**
2012 – 2014	**R&D**
2012	finalization of detector specifications
	evaluation of detector technologies (radiation and beam tests)
	first prototypes of sensors, ASICS, and ladders (demonstrators)
2013	selection of technologies and full validation
	engineering design for sensors, ASICs, ladders, data links
	engineering design for support mechanics and services
	Technical Design Report
2014	final design and validation
2015 – 2018	**Construction and Installation**
2015 – 2016	production, construction and test of detector modules
2017	assembly and pre-commissioning in clean room
2018	installation in the cavern

defines the installation strategy and schedule. The installation of the new TPC components (readout chambers and electronics) has to take place on the surface in the SXL2 cleanroom at P2, and therefore the TPC must be removed from the cavern during this time. In order to maximize the time available for the installation of the new TPC readout chambers and electronics, the removal of the TPC will take place at the beginning of the shutdown period. The reinstallation takes place towards the end of this shutdown

period, in a time which is still compatible with the following ITS installation and commissioning. While the TPC is on the surface, the upgrade of the other detectors, related services and infrastructure work will also be performed. We currently envisage two installation scenarios based on different assumptions for the duration of LS2, respectively of 18 months (Scenario 1) and 14 months (Scenario 2). In Scenario 1 the complete upgrade takes place in an LS2 of at least 18 months. Whereas in Scenario 2, the TPC and the ITS are removed during the 'End of Year Technical Stop' 2016/2017, ALICE does not operate in 2017 and the upgrade installation happens in an LS2 of at least 14 months. A temporary beampipe is installed inside the ALICE detector for the 2017 LHC run. The installation schedules for these two scenarios differ essentially for how long the TPC can be in the SXL2 cleanroom, which is much longer in Scenario 2, whereas for the ITS a period of 3 month is foreseen for the installation and commissioning. The ITS upgrade timeline is given in Table 6.3.

List of Figures

List of Tables

References

[1] ALICE Collaboration, *ALICE: Physics Performance Report, Volume I*, J. Phys. **G30**, 1517 (2004), doi:10.1088/0954-3899/30/11/001.

[2] *ALICE Memorandum of Understanding, ALICE RRB-D 00-41, and related addenda.*

[3] ALICE Collaboration, *The ALICE experiment at the CERN LHC*, Journal of Instrumentation **3**, S08002 (2008), doi:10.1088/1748-0221/3/08/S08002.

[4] *Physics Publications of the ALICE Collaboration in Refereed Journals.*

[5] L. Musa and K. Safarik, CERN Report No. CERN-LHCC-2012-012. LHCC-I-022, 2012 (unpublished).

[6] STAR Collaboration, *The STAR Heavy Flavor Tracker, Conceptual Design Report*, submitted to DOE at CD1 review, 2009.

[7] M. Mangano, P. Nason and G. Ridolfi, *Heavy-quark correlations in hadron collisions at next-to-leading order*, Nuclear Physics B **373**, 295 (1992), doi:10.1016/0550-3213(92)90435-E.

[8] ALICE Collaboration, K. Aamodt *et al.*, *Two-pion Bose-Einstein correlations in central Pb-Pb collisions at sqrt($s_N N$) = 2.76 TeV*, Phys.Lett. **B696**, 328 (2011), arXiv:1012.4035, doi:10.1016/j.physletb.2010.12.053.

[9] The ALICE Collaboration, K. Aamodt *et al.*, *Elliptic flow of charged particles in Pb-Pb collisions at 2.76 TeV*, Phys.Rev.Lett. **105**, 252302 (2010), arXiv:1011.3914.

[10] The ALICE Collaboration, B. Abelev *et al.*, *Charged-particle multiplicity density at mid-rapidity in central Pb-Pb collisions at* $\sqrt{s_{NN}} = 2.76$ *TeV*, Phys.Rev.Lett. **105**, 252301 (2010), arXiv:1011.3916, doi:10.1103/PhysRevLett.105.252301.

[11] M. Capeans *et al.*, *ATLAS Insertable B-Layer Technical Design Report*, CERN-LHCC-2010-013. ATLAS-TDR-019, 2010.

[12] K. Gill, *CMS Pixel Upgrade, CERN PH Seminar;*, https://indico.cern.ch/conferenceDisplay.py?confId=168135, 2012.

[13] R. Rapp and v. H. Hendrik, *in Quark-Gluon Plasma 4 (R.C. Hwa and X.N.Wang, eds.), World Scientific (Singapore)*, Phys.Lett. **B664**, 111 (2010), arXiv:0903.1096.

[14] R. Rapp, J. Wambach and H. van Hees, *The Chiral Restoration Transition of QCD and Low Mass Dileptons*, 0901.3289, arXiv:0901.3289.

[15] PHENIX Collaboration, A. Adare *et al.*, *Enhanced Production of Direct Photons in* Au + Au *Collisions at* $\sqrt{s_{NN}} = 200$ GeV *and Implications for the Initial Temperature*, Phys. Rev. Lett. **104**, 132301 (2010), doi:10.1103/PhysRevLett.104.132301.

[16] K. Eskola, H. Paukkunen and C. Salgado, *EPS09: A New Generation of NLO and LO Nuclear Parton Distribution Functions*, JHEP **0904**, 065 (2009), arXiv:0902.4154, doi:10.1088/1126-6708/2009/04/065.

[17] D. Caffarri et al. (ALICE Collaboration), Quark Matter 2012, Washington D.C, August 2012, http://qm2012.bnl.gov, [link].

[18] J. Aichelin, P. Gossiaux and T. Gousset, *Radiative and Collisional Energy Loss of Heavy Quarks in Deconfined Matter*, 1201.4192, arXiv:1201.4192.

[19] J. Uphoff, O. Fochler, Z. Xu and C. Greiner, *Open heavy flavor in Pb+Pb collisions at sqrt(s)=2.76 TeV within a transport model*, 1205.4945, arXiv:1205.4945.

[20] V. Greco, H. van Hees and R. Rapp, *Heavy-quark kinetics at RHIC and LHC*, 0709.4452, arXiv:0709.4452.

[21] STAR Collaboration, J. Adams *et al.*, *Azimuthal anisotropy in Au+Au collisions at s(NN)**(1/2) = 200-GeV*, Phys.Rev. **C72**, 014904 (2005), arXiv:nucl-ex/0409033, doi:10.1103/PhysRevC.72.014904.

[22] B. Abelev et al. (STAR Collaboration), *Mass, quark-number, and sqrt s(NN) dependence of the second and fourth flow harmonics in ultra-relativistic nucleus-nucleus collisions*, Phys.Rev. **C75**, 054906 (2007), arXiv:nucl-ex/0701010, doi:10.1103/PhysRevC.75.054906.

[23] M. Krzewicki et al. (ALICE Collaboration), *Elliptic and triangular flow of identified particles at ALICE*, 1107.0080, arXiv nucl-ex/1107.0080, 2011., arXiv:1107.0080.

[24] V. Greco, C. Ko and R. Rapp, *Quark coalescence for charmed mesons in ultrarelativistic heavy-ion collisions*, Physics Letters B **595**, 202 (2004), doi:10.1016/j.physletb.2004.06.064.

[25] F. Noferini et al. (ALICE Collaboration), Quark Matter 2012, Washington D.C, August 2012, http://qm2012.bnl.gov, [link].

[26] I. Belikov et al. (ALICE Collaboration), *K^0_s and Λ production in Pb–Pb collisions with the ALICE experiment*, 1109.4807, arXiv hep-ex/1109.4807, 2011., arXiv:1109.4807.

[27] M. Aggarwal et al. (STAR Collaboration), *Strange and Multi-strange Particle Production in Au+Au Collisions at $\sqrt{s_{NN}}$ = 62.4 GeV*, Phys.Rev. **C83**, 024901 (2011), arXiv:1010.0142, doi:10.1103/PhysRevC.83.024901.

[28] M. He, R. J. Fries and R. Rapp, *Heavy-Quark Diffusion and Hadronization in Quark-Gluon Plasma*, Phys.Rev. **C86**, 014903 (2012), arXiv:1106.6006, doi:10.1103/PhysRevC.86.014903.

[29] Y. Oh, C. M. Ko, S. H. Lee and S. Yasui, *Heavy baryon/meson ratios in relativistic heavy ion collisions*, Phys.Rev. **C79**, 044905 (2009), arXiv:0901.1382, doi:10.1103/PhysRevC.79.044905.

[30] S. Lee, K. Ohnishi, S. Yasui, I. Yoo and C. Ko, *Λ_c Enhancement from Strongly Coupled Quark-Gluon Plasma*, Phys. Rev. Lett. **100**, 222301 (2008), doi:10.1103/PhysRevLett.100.222301.

[31] F. Becattini, *Production of Multiply Heavy Flavored Baryons from Quark Gluon Plasma in Relativistic Heavy Ion Collisions*, Phys. Rev. Lett. **95**, 022301 (2005), doi:10.1103/PhysRevLett.95.022301.

[32] G. Innocenti et al. (ALICE Collaboration), Quark Matter 2012, Washington D.C, August 2012, http://qm2012.bnl.gov, [link].

[33] M. He, R. J. Fries and R. Rapp, *$\mathbf{D_s}$-Meson as Quantitative Probe of Diffusion and Hadronization in Nuclear Collisions*, 1204.4442, arXiv:1204.4442.

[34] I. Kuznetsova and J. Rafelski, *Heavy flavor hadrons in statistical hadronization of strangeness-rich QGP*, Eur.Phys.J. **C51**, 113 (2007), arXiv:hep-ph/0607203, doi:10.1140/epjc/s10052-007-0268-9.

[35] M. He, R. J. Fries and R. Rapp, *Thermal Relaxation of Charm in Hadronic Matter*, Phys.Lett. **B701**, 445 (2011), arXiv:1103.6279, doi:10.1016/j.physletb.2011.06.019.

[36] P. Levai and R. Vogt, *Thermal charm production by massive gluons and quarks*, Phys.Rev. **C56**, 2707 (1997), 19 pages in Latex and 9 Postscript figures Report-no: LBNL-39984, arXiv:hep-ph/9704360, doi:10.1103/PhysRevC.56.2707.

[37] P. Braun-Munzinger and K. Redlich, *Charmonium production from the secondary collisions at LHC energy*, Eur.Phys.J. **C16**, 519 (2000), ps file 11 p, arXiv:hep-ph/0001008, doi:10.1007/s100520000356.

[38] B.-W. Zhang, C.-M. Ko and W. Liu, *Thermal charm production in a quark-gluon plasma in Pb-Pb collisions at s**(1/2)(NN) = 5.5-TeV*, Phys.Rev. **C77**, 024901 (2008), 8 pages, 8 figures, arXiv:0709.1684, doi:10.1103/PhysRevC.77.024901.

[39] J. Uphoff, O. Fochler, Z. Xu and C. Greiner, *Heavy quark production at RHIC and LHC within a partonic transport model*, Phys.Rev. **C82**, 044906 (2010), arXiv:1003.4200, doi:10.1103/PhysRevC.82.044906.

[40] A. Andronic, P. Braun-Munzinger, K. Redlich and J. Stachel, *Evidence for charmonium generation at the phase boundary in ultra-relativistic nuclear collisions*, Phys.Lett. **B652**, 259 (2007), arXiv:nucl-th/0701079, doi:10.1016/j.physletb.2007.07.036.

[41] X. Zhao and R. Rapp, Phys.Lett. **B664**, 253 (2008), arXiv:0712.2407.

[42] Y.-p. Liu, Z. Qu, N. Xu and P.-f. Zhuang, Phys.Lett. **B678**, 72 (2009), arXiv:0901.2757.

[43] ALICE Collaboration, B. Abelev *et al.*, *J/psi production at low transverse momentum in Pb-Pb collisions at sqrt(sNN) = 2.76 TeV*, 1202.1383, arXiv:1202.1383.

[44] Y. Dokshitzer and D. Kharzeev, *Heavy-quark colorimetry of QCD matter*, Phys. Lett. B **519**, 199 (2001), doi:10.1016/S0370-2693(01)01130-3.

[45] N. Armesto, C. Salgado and U. Wiedemann, *Medium-induced gluon radiation off massive quarks fills the dead cone*, Phys. Rev. D **69**, 114003 (2004), doi:10.1103/PhysRevD.69.114003.

[46] S. Wicks, W. Horowitz, M. Djordjevic and M. Gyulassy, *Heavy quark jet quenching with collisional plus radiative energy loss and path length fluctuations*, Nucl.Phys. **A783**, 493 (2007), arXiv:nucl-th/0701063, doi:10.1016/j.nuclphysa.2006.11.102.

[47] N. Armesto, A. Dainese, C. Salgado and U. Wiedemann, *Testing the color charge and mass dependence of parton energy loss with heavy-to-light ratios at BNL RHIC and CERN LHC*, Phys. Rev. D **71**, 054027 (2005), doi:10.1103/PhysRevD.71.054027.

[48] W. Horowitz and M. Gyulassy, *Heavy quark jet tomography of Pb + Pb at LHC: AdS/CFT drag or pQCD energy loss?*, Phys.Lett. **B666**, 320 (2008), arXiv:0706.2336, doi:10.1016/j.physletb.2008.04.065.

[49] J. Albacete, Y. Kovchegov and A. Taliotis, *Modeling Heavy Ion Collisions in AdS/CFT*, JHEP **0807**, 100 (2008), arXiv:0805.2927, doi:10.1088/1126-6708/2008/07/100.

[50] ALICE Collaboration, B. Abelev *et al.*, *Suppression of high transverse momentum D mesons in central Pb-Pb collisions at* $\sqrt{s_{NN}} = 2.76$ *TeV*, 1203.2160, arXiv:1203.2160.

[51] A. Grelli et al. (ALICE Collaboration), Quark Matter 2012, Washington D.C, August 2012, http://qm2012.bnl.gov, [link].

[52] S. Sakai et al. (ALICE Collaboration), Quark Matter 2012, Washington D.C, August 2012, http://qm2012.bnl.gov, [link].

[53] ALICE Collaboration, B. Abelev *et al.*, *Production of muons from heavy flavour decays at forward rapidity in pp and Pb-Pb collisions at* $\sqrt{s_{NN}} = 2.76$ *TeV*, 1205.6443, arXiv:1205.6443.

[54] CMS Collaboration, S. Chatrchyan *et al.*, *Suppression of non-prompt J/psi, prompt J/psi, and Y(1S) in PbPb collisions at sqrt(sNN) = 2.76 TeV*, 1201.5069, arXiv:1201.5069.

[55] ALICE Collaboration, *Conceptual Design Report for the Upgrade of the ALICE ITS*, CDR-0, version released on the 6th of March (http://aliceinfo.cern.ch/ITSUpgrade/node/9), 2012.

[56] R. Rapp, *Theory of Soft Electromagnetic Emission in Heavy-Ion Collisions*, Acta Phys.Polon. **B42**, 2823 (2011), arXiv:1110.4345, doi:10.5506/APhysPolB.42.2823.

[57] R. Rapp and J. Wambach, *Low mass dileptons at the CERN SPS: Evidence for chiral restoration?*, Eur.Phys.J. **A6**, 415 (1999), arXiv:hep-ph/9907502, doi:10.1007/s100500050364.

[58] NA60 Collaboration, R. Arnaldi *et al.*, *Evidence for the production of thermal-like muon pairs with masses above 1-GeV/c**2 in 158-A-GeV Indium-Indium Collisions*, Eur.Phys.J. **C59**, 607 (2009), arXiv:0810.3204, doi:10.1140/epjc/s10052-008-0857-2.

[59] NA60 Collaboration, R. Arnaldi *et al.*, *NA60 results on thermal dimuons*, Eur.Phys.J. **C61**, 711 (2009), arXiv:0812.3053, doi:10.1140/epjc/s10052-009-0878-5.

[60] NA60 Collaboration, S. Damjanovic, R. Shahoyan and H. J. Specht, *NA60: In hot pursuit of thermal dileptons*, CERN Cour. **49N9**, 31 (2009).

[61] H. van Hees and R. Rapp, *Dilepton Radiation at the CERN Super Proton Synchrotron*, Nucl.Phys.

A806, 339 (2008), arXiv:0711.3444, doi:10.1016/j.nuclphysa.2008.03.009.

[62] S. Borsnyi *et al.*, *Is there still any mystery in lattice QCD? Results with physical masses in the continuum limit III*, Journal of High Energy Physics **2010**, 1 (2010), 10.1007/JHEP09(2010)073.

[63] S. Weinberg, *Precise Relations between the Spectra of Vector and Axial-Vector Mesons*, Phys. Rev. Lett. **18**, 507 (1967), doi:10.1103/PhysRevLett.18.507.

[64] T. Das, V. S. Mathur and S. Okubo, *Low-Energy Theorem in the Radiative Decays of Charged Pions*, Phys. Rev. Lett. **19**, 859 (1967), doi:10.1103/PhysRevLett.19.859.

[65] R. Chatterjee, D. K. Srivastava, U. Heinz and C. Gale, *Elliptic flow of thermal dileptons in relativistic nuclear collisions*, Phys. Rev. C **75**, 054909 (2007), doi:10.1103/PhysRevC.75.054909.

[66] T. Sjöstrand, S. Mrenna and P. Skands, *PYTHIA 6.4 Physics and Manual*, JHEP **05**, 026 (2006), arXiv:hep-ph/0603175.

[67] K. Hagiwara *et al.*, *Review of Particle Physics*, Physical Review D **66**, 010001+ (2002).

[68] X. Wang and M. Gyulassy, *HIJING: A Monte Carlo model for multiple jet production in p p, p A and A A collisions*, Phys. Rev. **D44**, 3501 (1991), doi:10.1103/PhysRevD.44.3501.

[69] M. Cacciari, M. Greco and P. Nason, *The p_t spectrum in heavy flavor hadroproduction*, JHEP **9805**, 007 (1998), arXiv:hep-ph/9803400.

[70] ALICE Collaboration, B. Abelev *et al.*, *Measurement of charm production at central rapidity in proton-proton collisions at $\sqrt{s} = 7$ TeV*, JHEP **1201**, 128 (2012), arXiv:1111.1553, doi:10.1007/JHEP01(2012)128.

[71] A. Dainese et al. (ALICE collaboration), *Heavy-flavour production in Pb-Pb collisions at the LHC, measured with the ALICE detector*, 1106.4042, arXiv nucl-ex/1106.4042, 2011, arXiv:1106.4042.

[72] A. Abulencia et al. (CDF Collaboration), *Measurement of the ratios of branching fractions $B(B_s^0 \to D_s^- \pi^+)/B(B^0 \to D^- \pi^+)$ and $B(B^+ \to \overline{D}^0 \pi^+)/B(B^0 \to D^- \pi^+)$*, Phys.Rev.Lett. **96**, 191801 (2006), arXiv:hep-ex/0508014, doi:10.1103/PhysRevLett.96.191801.

[73] S. Ricciardi et al. (LHCB Collaboration), *Studies of b-hadron decays to charming final states at LHCb*, 1110.3249, arXiv hep-ex/1110.3249, 2011., arXiv:1110.3249.

[74] ALICE Collaboration, C. Bianchin *et al.*, *Measurement of D^0 v_2 in Pb-Pb collisions at $\sqrt{s_{NN}} =$ 2.76 TeV with ALICE at the LHC*, 1111.6886, arXiv:1111.6886.

[75] ALICE Collaboration, B. Abelev, *Measurement of charm production at central rapidity in proton-proton collisions at sqrt(s) = 2.76 TeV*, 1205.4007, arXiv:1205.4007.

[76] ALICE Collaboration, B. Abelev *et al.*, *Ds meson production at central rapidity in proton–proton collisions at sqrt(s) = 7 TeV*, 1208.1948, arXiv:1208.1948.

[77] ATLAS Collaboration, CERN Report No. ATL-PHYS-PUB-2011-012, 2011 (unpublished).

[78] LHCb Collaboration, CERN Report No. LHCb-CONF-2010-013, 2010 (unpublished).

[79] PHENIX Collaboration, A. Adare *et al.*, *Detailed measurement of the e^+e^- pair continuum in $p+p$ and Au + Au collisions at $\sqrt{s_{NN}} = 200$ GeV and implications for direct photon production*, Phys. Rev. C **81**, 034911 (2010), doi:10.1103/PhysRevC.81.034911.

[80] ALICE Collaboration, B. Abelev *et al.*, *Neutral pion and η meson production in proton-proton collisions at $\sqrt{s} = 0.9$ TeV and $\sqrt{s} = 7$ TeV*, 1205.5724, arXiv:1205.5724.

[81] R. Averbeck *et al.*, *Reference Heavy Flavour Cross Sections in pp Collisions at $\sqrt{s}$ = 2.76 TeV, using a pQCD-Driven $\sqrt{s}$-Scaling of ALICE Measurements at $\sqrt{s}$ = 7 TeV*, 1107.3243, arXiv:1107.3243.

[82] E. Crescio et al., *Performance of the ITS stand-alone tracker in pp collisions*, ALICE-INT-2009-046, 2009.

[83] PHOBOS Collaboration, *Identified hadron transverse momentum spectra in Au+Au collisions at*

$\sqrt{s_{NN}} = 62.4$ *GeV*, Phys. Rev. C **75**, 024910 (2007), doi:10.1103/PhysRevC.75.024910.

[84] G. Schneider, *Installation of the central beryllium beam pipe in the ALICE experiment*, EDMS: 1113439, 2011.

[85] ALICE Collaboration, *Charged-Particle Multiplicity Density at Midrapidity in Central Pb-Pb Collisions at* $\sqrt{s_{NN}}$ *= 2.76 TeV*, Phys. Rev. Lett. **105**, 252301 (2010), doi:10.1103/PhysRevLett.105.252301.

[86] A. Alscher, K. Hencken, D. Trautmann and G. Baur, *Multiple electromagnetic electron-positron pair production in relativistic heavy-ion collisions*, Phys. Rev. A **55**, 396 (1997), doi:10.1103/PhysRevA.55.396.

[87] K. Hencken, G. Baur and D. Trautmann, *Production of QED pairs at small impact parameter in relativistic heavy ion collisions*, Phys. Rev. C **69**, 054902 (2004), doi:10.1103/PhysRevC.69.054902.

[88] K. Hencken, Y. Kharlov and S. Sadovsky, *Ultraperipheral Trigger in ALICE*, ALICE-INT-2002-11, 2002.

[89] S.Sadovsky, K.Hencken and Yu.Kharlov, *Generator for e+e pairs in PbPb collisions at LHC*, ALICE-INT-2002-27, 2002.

[90] O. S. Brning *et al.*, *LHC Design Report* (CERN, Geneva, 2004).

[91] *AliRoot: ALICE Off-line framework for simulation, reconstruction and analysis*, http://aliceinfo.cern.ch/Offline.

[92] A. Mastroserio, S. Rossegger, C. Terrevoli and et al., *Simulation tools for the ITS upgrade*, ALICE Internal Note (under preparation), 2012.

[93] P. Billoir, *Track fitting with multiple scattering: A new method*, Nuclear Instruments and Methods in Physics Research **225**, 352 (1984), doi:DOI:10.1016/0167-5087(84)90274-6.

[94] R. Fruehwirth, *Application of Kalman filtering to track and vertex fitting*, Nuclear Instruments and Methods in Physics Research Section A: Accelerators, Spectrometers, Detectors and Associated Equipment **262**, 444 (1987), doi:DOI:10.1016/0168-9002(87)90887-4.

[95] E. Bruna, E. Crescio and M. Masera, *Response functions for particle Identification in the Inner Tracking System*, ALICE-INT-2006-004, 2006.

[96] ATLAS Pixel Collaboration, *ATLAS pixel detector: Running experience*, PoS VERTEX 2009 001.

[97] M. Deveaux et al., *Radiation tolerance of a column parallel CMOS sensor with high resistivity epitaxial layer*, Journal of Instrumentation **6** (2011), doi:10.1088/1748-0221/6/02/C02004.

[98] ALICE Collaboration, *Production of pions, kaons and protons in pp collisions at* $\sqrt{s}$ *= 900 GeV with ALICE at the LHC*, Eur. Phys. J. **71**, 1655 (2011), doi:10.1140/epjc/s10052-011-1655-9.

[99] A. Morsch and B. Pastircak, *Radiation in ALICE Detectors and Electronics Racks*, ALICE-INT-2002-028, 2002.

[100] B. Pastircak, J. Vrlakova, A. Morsch and M. Tavlet, *Radiation zoning calculations for ALICE experiment update*, ALICE-INT-2009-008, 2009.

[101] J. C. e. a. J. Ballin, R. Coath, *Design and performance of a CMOS study sensor for a binary readout electromagnetic calorimeter*, Journal of Instrumentation **6** (2011).

[102] e. a. L. Ratti, *Monolithic pixel detectors in a 0.13 µm CMOS technology with sensor level continuous time charge amplification and shaping*, NIM-A **568**, 159 (2006).

[103] e. a. I. Peric, *Particle Detectors in High Voltage CMOS Technologies-New Achievements*, NIM-A **650**, 158 (2011).

[104] A. G. M. W. R. Coath, J. Crooks and R. Turchetta, *Advanced pixel architectures for scientific image sensors*, TWEPP-09: Topical Workshop on Electronics for Particle Physics, Paris, France ,

57 (2009).

[105] A. R. et. al, *The front-end system of the silicon drift detectors of ALICE*, NIM-A **541**, 267 (2005).

[106] C. Fuentes *et al.*, *Power distribution with custom DC-DC converters for SLHC trackers*, in *Nuclear Science Symposium Conference Record (NSS/MIC), 2009 IEEE*, pp. 1300 –1305, 2009, doi:10.1109/NSSMIC.2009.5402359.

[107] J. A. et al., *The ALICE TPC, a large 3-dimensional tracking device with fast readout for ultra-high multiplicity events*, Nucl. Instr. and Meth. A **622**, 316 (2010).

[108] B. J. (Editor), *Ultra-thin chip technology and applications* (Springer, Berlin, Germany, 2011).

[109] L. Greiner *et al.*, *A MAPS based vertex detector for the STAR experiment at RHIC*, Nuclear Instruments and Methods in Physics Research Section A: Accelerators, Spectrometers, Detectors and Associated Equipment **650**, 68 (2011), doi:10.1016/j.nima.2010.12.006.

[110] S. Seddiki, *Open charm physics with the CBM experiment*, QGP-France 2010, 2010.

[111] I. V. et al., *A reticle size CMOS pixel sensor dedicated to the STAR HFT*, Journal of Instrumentation , C01102 (2012).

[112] I. Gregor, *Summary of One Year Operation of the EUDET CMOS Pixel Telescope*, presented at the LCWS08 conference (2009), doi:arXiv:0901.0616.

[113] X. L. et. al, *Timepix, a 65k programmable pixel readout chip for arrival time, energy and/or photon counting measurements*, NIM-A **581** (2007).

[114] S. S. et al., *The Readout System for the ALICE Zero Degree Calorimeters*, IEEE Trans. Nucl. Sci. 52 **58**, 1759 (2011).

[115] C. C. et al., *MIMOSA 20 user manual*, 2007.

[116] M. Bregant et al, *Assembly and validation of the ALICE silicon microstrip detector*, Nuclear Instruments and Methods in Physics Research Section A **570**, 312 (2007), doi:10.1016/j.nima.2006.09.031.

[117] Amazon Supply, *www.AmazonSupply.com*, 2012.

[118] Toray Carbon Fibers America, Inc., *www.toraycfa.com*, 2012.

[119] Mitsubishi Chemical Holdings America, *www.mitsubishichemical.com*, 2012.

[120] Amec Thermasol Heat Management and Thermal Control Solutions, *www.amecthermasol.co.uk*, 2012.

[121] Mitutoyo U.S.A., *http://www.mitutoyo.com*, 2012.

[122] V. Manzari, *Assembly, construction and testing of the ALICE silicon pixel detector*, Nuclear Instruments and Methods in Physics Research Section A: Accelerators, Spectrometers, Detectors and Associated Equipment **570**, 241 (2007), doi:10.1016/j.nima.2006.09.028.

[123] R. Santoro, *Status of the ALICE silicon pixel detector*, Nuclear Instruments and Methods in Physics Research Section A: Accelerators, Spectrometers, Detectors and Associated Equipment **581**, 330 (2007), doi:10.1016/j.nima.2007.07.138.

[124] NA62 Collaboration, *NA62 Technical design document*, Doc. N. NA62-10-07, 2010.

[125] A. Mapelli et al, *Low material budget microfabricated cooling devices for particle detectors and front-end electronics*, Nucl. Phys. B (Proc. Suppl.) **215**, 349 (2011).

[126] *CMI-EPFL, Center of Micronanotechnology, Ecole Polytechnique Federale de Lausanne*, 2011.

[127] *CSEM, http://www.csem.ch/site/default.asp*, 2011.

[128] J. R. Thome et al., *Two-Phase Cooling of Targets and Electronics for Particle Physics Experiments*, Proceedings of TWEPP 2009, Paris (France) , 366 (2009).

[129] R. De Oliveira *et al.*, *Development of a polyimide microchannel on-detector cooling system for the ITS upgrade*, ALICE Internal Note 2012-001, 2012.

[130] *Pyralux, LF Coverlay,http://www2.dupont.com/Pyralux/en_US/products/*

adhesives_films/LF/LF_films.html, 2011.

[131] *Pyralux, product properties, http://www2.dupont.com/Pyralux/en_US/assets/downloads/pdf/PyraluxProductProperties.pdf*, 2011.

[132] *Pyralux, PC Photoimageable Coverlay, http://www2.dupont.com/Pyralux/en_US/products/adhesives_films/PC/pyralux_pc.html*, 2011.

A The ALICE Collaboration

B. Abelev[71] , J. Adam[37] , D. Adamová[78] , A.M. Adare[128] , M.M. Aggarwal[82] , G. Aglieri Rinella[33] , M. Agnello[102 ,88] , A.G. Agocs[127] , A. Agostinelli[27] , Z. Ahammed[123] , N. Ahmad[17] , A. Ahmad Masoodi[17] , S.A. Ahn[64] , S.U. Ahn[40 ,64] , I. Aimo[22] , M. Ajaz[15] , A. Akindinov[50] , D. Aleksandrov[94] , B. Alessandro[102] , A. Alici[98 ,12] , A. Alkin[3] , E. Almaráz Aviña[60] , J. Alme[35] , T. Alt[39] , V. Altini[31] , S. Altinpinar[18] , I. Altsybeev[124] , C. Andrei[74] , A. Andronic[91] , V. Anguelov[87] , J. Anielski[58] , C. Anson[19] , T. Antičić[92] , F. Antinori[99] , P. Antonioli[98] , L. Aphecetche[108] , H. Appelshäuser[56] , N. Arbor[67] , S. Arcelli[27] , A. Arend[56] , N. Armesto[16] , R. Arnaldi[102] , T. Aronsson[128] , I.C. Arsene[91] , M. Arslandok[56] , A. Asryan[124] , A. Augustinus[33] , R. Averbeck[91] , T.C. Awes[79] , J. Äystö[42] , M.D. Azmi[17 ,84] , M. Bach[39] , A. Badalà[105] , Y.W. Baek[66 ,40] , R. Bailhache[56] , R. Bala[85 ,102] , R. Baldini Ferroli[12] , A. Baldisseri[14] , F. Baltasar Dos Santos Pedrosa[33] , J. Bán[51] , R.C. Baral[52] , R. Barbera[26] , F. Barile[31] , G.G. Barnaföldi[127] , L.S. Barnby[96] , V. Barret[66] , J. Bartke[111] , M. Basile[27] , N. Bastid[66] , S. Basu[123] , B. Bathen[58] , G. Batigne[108] , M. Battistin[33] , B. Batyunya[62] , J. Baudot[61] , C. Baumann[56] , R. Bavontaweepanya[109] , I.G. Bearden[76] , H. Beck[56] , N.K. Behera[44] , I. Belikov[61] , F. Bellini[27] , R. Bellwied[117] , E. Belmont-Moreno[60] , G. Bencedi[127] , S. Beole[22] , I. Berceanu[74] , A. Bercuci[74] , Y. Berdnikov[80] , D. Berenyi[127] , A.A.E. Bergognon[108] , D. Berzano[22 ,102] , L. Betev[33] , A. Bhasin[85] , A.K. Bhati[82] , J. Bhom[121] , L. Bianchi[22] , N. Bianchi[68] , J. Bielčík[37] , J. Bielčíková[78] , A. Bilandzic[76] , S. Bjelogrlic[49] , F. Blanco[117] , F. Blanco[10] , D. Blau[94] , C. Blume[56] , M. Boccioli[33] , S. Böttger[55] , A. Bogdanov[72] , H. Bøggild[76] , M. Bogolyubsky[47] , L. Boldizsár[127] , M. Bombara[38] , J. Book[56] , H. Borel[14] , A. Borissov[126] , F. Bossú[84] , C. Bortolin[33] , J.A. Botelho Direito[33] , M. Botje[77] , E. Botta[22] , E. Braidot[70] , P. Braun-Munzinger[91] , M. Bregant[108] , T. Breitner[55] , T.A. Broker[56] , T.A. Browning[89] , M. Broz[36] , R. Brun[33] , E. Bruna[22 ,102] , G.E. Bruno[31] , D. Budnikov[93] , H. Buesching[56] , S. Bufalino[22 ,102] , P. Buncic[33] , O. Busch[87] , Z. Buthelezi[84] , D. Caballero Orduna[128] , D. Caffarri[28 ,99] , X. Cai[7] , H. Caines[128] , E. Calvo Villar[97] , P. Camerini[24] , V. Canoa Roman[11] , G. Cara Romeo[98] , W. Carena[33] , F. Carena[33] , N. Carlin Filho[114] , F. Carminati[33] , A. Casanova Díaz[68] , J. Castillo Castellanos[14] , J.F. Castillo Hernandez[91] , E.A.R. Casula[23] , V. Catanescu[74] , T. Caudron[33] , C. Cavicchioli[33] , C. Ceballos Sanchez[9] , J. Cepila[37] , P. Cerello[102] , B. Chang[42 ,130] , N. Chankhunthot[109] , S. Chapeland[33] , J.L. Charvet[14] , S. Chattopadhyay[95] , S. Chattopadhyay[123] , I. Chawla[82] , M. Cherney[81] , C. Cheshkov[33 ,116] , B. Cheynis[116] , V. Chibante Barroso[33] , D.D. Chinellato[117] , P. Chochula[33] , M. Chojnacki[76 ,49] , S. Choudhury[123] , P. Christakoglou[77] , C.H. Christensen[76] , P. Christiansen[32] , T. Chujo[121] , S.U. Chung[90] , C. Cicalo[101] , L. Cifarelli[27 ,33 ,12] , F. Cindolo[98] , J. Cleymans[84] , F. Coccetti[12] , F. Colamaria[31] , D. Colella[31] , A. Collu[23] , G. Conesa Balbastre[67] , Z. Conesa del Valle[33] , M.E. Connors[128] , G. Contin[24] , J.G. Contreras[11] , T.M. Cormier[126] , Y. Corrales Morales[22] , P. Cortese[30] , I. Cortés Maldonado[2] , M.R. Cosentino[70] , F. Costa[33] , M.E. Cotallo[10] , E. Crescio[11] , P. Crochet[66] , E. Cruz Alaniz[60] , R. Cruz Albino[11] , E. Cuautle[59] , L. Cunqueiro[68] , A. Dainese[28 ,99] , H.H. Dalsgaard[76] , A. Danu[54] , E. Da Riva[33] , I. Das[46] , D. Das[95] , S. Das[4] , K. Das[95] , A. Dash[115] , S. Dash[44] , S. De[123] , G.O.V. de Barros[114] , A. De Caro[29 ,12] , G. de Cataldo[104] , C. Decosse[33] , J. de Cuveland[39] , A. De Falco[23] , D. De Gruttola[29] , H. Delagrange[108] , A. Deloff[73] , N. De Marco[102] , E. Dénes[127] , S. De Pasquale[29] , A. Deppman[114] , G. D Erasmo[31] , R. de Rooij[49] , M.A. Diaz Corchero[10] , D. Di Bari[31] , T. Dietel[58] , C. Di Giglio[31] , S. Di Liberto[100] , A. Di Mauro[33] , P. Di Nezza[68] , R. Divià[33] , Ø. Djuvsland[18] , A. Dobrin[126 ,32] , T. Dobrowolski[73] , B. Dönigus[91] , O. Dordic[21] , O. Driga[108] , A.K. Dubey[123] , A. Dubla[49] , L. Ducroux[116] , W. Dulinski[61] , P. Dupieux[66] , A.K. Dutta Majumdar[95] , D. Elia[104] , D. Emschermann[58] , H. Engel[55] , B. Erazmus[33 ,108] , H.A. Erdal[35] , B. Espagnon[46] , M. Estienne[108] , S. Esumi[121] , D. Evans[96] , G. Eyyubova[21] , D. Fabris[28 ,99] , J. Faivre[67] , D. Falchieri[27] , A. Fantoni[68] , M. Fasel[91 ,87] , R. Fearick[84] , D. Fehlker[18] , L. Feldkamp[58] , D. Felea[54] , A. Feliciello[102] , B. Fenton-Olsen[70] , G. Feofilov[124] , J. Ferencei[37] , A. Fernández Téllez[2] , A. Ferretti[22] , A. Festanti[28] , J. Figiel[111] , M.A.S. Figueredo[114] , S. Filchagin[93] , D. Finogeev[48] , F.M. Fionda[31] , E.M. Fiore[31] , E. Floratos[83] , M. Floris[33] , S. Foertsch[84] , P. Foka[91] , S. Fokin[94] , E. Fragiacomo[103] , A. Francescon[33 ,28] , U. Frankenfeld[91] , U. Fuchs[33] , C. Furget[67] , M. Fusco Girard[29] , J.J. Gaardhøje[76] , M. Gagliardi[22] , A. Gago[97] , M. Gallio[22] , D.R. Gangadharan[19] , P. Ganoti[79] , C. Garabatos[91] , E. Garcia-Solis[13] , C. Gargiulo[33] , I. Garishvili[71] , J. Gerhard[39] , M. Germain[108] , C. Geuna[14] , M. Gheata[54 ,33] , A. Gheata[33] , B. Ghidini[31] , P. Ghosh[123] , P. Gianotti[68] , M.R. Girard[125] , P. Giubellino[33] , E. Gladysz-Dziadus[111] , P. Glässel[87] , M. Goffe[61] , R. Gomez[113 ,11] , M. Gomez Marzoa[33] , E.G. Ferreiro[16] , L.H. González-Trueba[60] , P. González-Zamora[10] , S. Gorbunov[39] , A. Goswami[86] , S. Gotovac[110] , L.K. Graczykowski[125] , R. Grajcarek[87] , A. Grelli[49] , C. Grigoras[33] , A. Grigoras[33] , V. Grigoriev[72] , A. Grigoryan[1] , S. Grigoryan[62] , B. Grinyov[3] , N. Grion[103] , P. Gros[32] , J.F. Grosse-Oetringhaus[33] , J.-Y. Grossiord[116] , R. Grosso[33] , F. Guber[48] , R. Guernane[67] , B. Guerzoni[27] , M. Guilbaud[116] , K. Gulbrandsen[76] , H. Gulkanyan[1] , T. Gunji[120] , A. Gupta[85] , R. Gupta[85] , R. Haake[58] , Ø. Haaland[18] , C. Hadjidakis[46] , M. Haiduc[54] , H. Hamagaki[120] , G. Hamar[127] , B.H. Han[20] , L.D. Hanratty[96] , A. Hansen[76] , Z. Harmanová-Tóthová[38] , J.W. Harris[128] , M. Hartig[56] , A. Harton[13] ,

D. Hatzifotiadou[98] , S. Hayashi[120] , A. Hayrapetyan[33 ,1] , S.T. Heckel[56] , M. Heide[58] , H. Helstrup[35] , A. Herghelegiu[74] , G. Herrera Corral[11] , N. Herrmann[87] , B.A. Hess[122] , K.F. Hetland[35] , B. Hicks[128] , B. Hippolyte[61] , Y. Hori[120] , P. Hristov[33] , I. Hřivnáčová[46] , C. Hu[61] , M. Huang[18] , T.J. Humanic[19] , D.S. Hwang[20] , R. Ichou[66] , S. Igolkin[33] , P. Ijzermans[33] , R. Ilkaev[93] , I. Ilkiv[73] , H. Illemanns[33] , M. Inaba[121] , E. Incani[23] , P.G. Innocenti[33] , G.M. Innocenti[22] , M. Ippolitov[94] , M. Irfan[17] , C. Ivan[91] , V. Ivanov[80] , A. Ivanov[124] , M. Ivanov[91] , O. Ivanytskyi[3] , A. Jachołkowski[26] , P. M. Jacobs[70] , H.J. Jang[64] , M.A. Janik[125] , R. Janik[36] , P.H.S.Y. Jayarathna[117] , S. Jena[44] , D.M. Jha[126] , R.T. Jimenez Bustamante[59] , P.G. Jones[96] , H. Jung[40] , A. Junique[33] , A. Jusko[96] , A.B. Kaidalov[50] , S. Kalcher[39] , P. Kaliňák[51] , T. Kalliokoski[42] , A. Kalweit[57 ,33] , J.H. Kang[130] , V. Kaplin[72] , A. Karasu Uysal[33 ,129 ,65] , O. Karavichev[48] , T. Karavicheva[48] , E. Karpechev[48] , A. Kazantsev[94] , U. Kebschull[55] , R. Keidel[131] , P. Khan[95] , S.A. Khan[123] , M.M. Khan[17] , K. H. Khan[15] , A. Khanzadeev[80] , Y. Kharlov[47] , B. Kileng[35] , B. Kim[130] , J.S. Kim[40] , J.H. Kim[20] , D.J. Kim[42] , D.W. Kim[40 ,64] , T. Kim[130] , S. Kim[20] , M.Kim[40] , M. Kim[130] , S. Kirsch[39] , I. Kisel[39] , S. Kiselev[50] , A. Kisiel[125] , J.L. Klay[6] , J. Klein[87] , C. Klein-Bösing[58] , M. Kliemant[56] , A. Kluge[33] , M.L. Knichel[91] , A.G. Knospe[112] , M.K. Köhler[91] , C. Kobdaj[109] , T. Kollegger[39] , A. Kolojvari[124] , M. Kompaniets[124] , V. Kondratiev[124] , N. Kondratyeva[72] , A. Konevskikh[48] , V. Kovalenko[124] , M. Kowalski[111] , S. Kox[67] , G. Koyithatta Meethaleveedu[44] , J. Kral[42] , I. Králik[51] , F. Kramer[56] , A. Kravčáková[38] , T. Krawutschke[87 ,34] , M. Krelina[37] , M. Kretz[39] , M. Krivda[96 ,51] , F. Krizek[42] , M. Krus[37] , E. Kryshen[80] , M. Krzewicki[91] , Y. Kucheriaev[94] , T. Kugathasan[33] , C. Kuhn[61] , P.G. Kuijer[77] , I. Kulakov[56] , J. Kumar[44] , P. Kurashvili[73] , A. Kurepin[48] , A.B. Kurepin[48] , A. Kuryakin[93] , S. Kushpil[78] , V. Kushpil[78] , H. Kvaerno[21] , M.J. Kweon[87] , Y. Kwon[130] , P. Ladrón de Guevara[59] , I. Lakomov[46] , R. Langoy[18] , S.L. La Pointe[49] , C. Lara[55] , A. Lardeux[108] , P. La Rocca[26] , R. Lea[24] , M. Lechman[33] , K.S. Lee[40] , S.C. Lee[40] , G.R. Lee[96] , I. Legrand[33] , J. Lehnert[56] , R. Lemmon[106] , M. Lenhardt[91] , V. Lenti[104] , H. León[60] , I. León Monzón[113] , H. León Vargas[56] , Y. Lesenechal[33] , P. Lévai[127] , S. Li[7] , J. Lien[18] , R. Lietava[96] , S. Lindal[21] , V. Lindenstruth[39] , C. Lippmann[91 ,33] , M.A. Lisa[19] , H.M. Ljunggren[32] , P.I. Loenne[18] , V.R. Loggins[126] , V. Loginov[72] , D. Lohner[87] , C. Loizides[70] , K.K. Loo[42] , X. Lopez[66] , E. López Torres[9] , G. Løvhøiden[21] , X.-G. Lu[87] , P. Luettig[56] , M. Lunardon[28] , J. Luo[7] , G. Luparello[49] , C. Luzzi[33] , R. Ma[128] , K. Ma[7] , D.M. Madagodahettige-Don[117] , A. Maevskaya[48] , M. Mager[57 ,33] , D.P. Mahapatra[52] , A. Maire[87] , M. Malaev[80] , I. Maldonado Cervantes[59] , L. Malinina[62 ,,ii] , D. Mal'Kevich[50] , P. Malzacher[91] , A. Mamonov[93] , L. Manceau[102] , L. Mangotra[85] , V. Manko[94] , F. Manso[66] , C. Mansuy[33] , V. Manzari[104] , Y. Mao[7] , A. Mapelli[33] , M. Marchisone[66 ,22] , J. Mareš[53] , G.V. Margagliotti[24 ,103] , A. Margotti[98] , A. Marín[91] , C. Markert[112] , M. Marquard[56] , D. Marras[23] , I. Martashvili[119] , N.A. Martin[91] , P. Martinengo[33] , M.I. Martínez[2] , A. Martínez Davalos[60] , G. Martínez García[108] , Y. Martynov[3] , A. Mas[108] , S. Masciocchi[91] , M. Masera[22] , A. Masoni[101] , L. Massacrier[108] , A. Mastroserio[31] , A. Matyja[111 ,108] , C. Mayer[111] , J. Mazer[119] , G. Mazza[22] , M.A. Mazzoni[100] , F. Meddi[25] , A. Menchaca-Rocha[60] , J. Mercado Pérez[87] , M. Meres[36] , Y. Miake[121] , L. Milano[22] , J. Milosevic[21 ,,iii] , A. Mischke[49] , A.N. Mishra[86 ,45] , D. Miśkowiec[91] , C. Mitu[54] , S. Mizuno[121] , J. Mlynarz[126] , B. Mohanty[123 ,75] , L. Molnar[127 ,33 ,61] , L. Montaño Zetina[11] , M. Monteno[102] , E. Montes[10] , T. Moon[130] , M. Morando[28] , D.A. Moreira De Godoy[114] , S. Moretto[28] , A. Morreale[42] , A. Morsch[33] , V. Muccifora[68] , E. Mudnic[110] , S. Muhuri[123] , M. Mukherjee[123] , H. Müller[33] , M.G. Munhoz[114] , S. Murray[84] , L. Musa[33] , J. Musinsky[51] , A. Musso[102] , B.K. Nandi[44] , R. Nania[98] , E. Nappi[104] , C. Nattrass[119] , T.K. Nayak[123] , S. Nazarenko[93] , A. Nedosekin[50] , M. Nicassio[31 ,91] , M.Niculescu[54 ,33] , B.S. Nielsen[76] , T. Niida[121] , S. Nikolaev[94] , V. Nikolic[92] , S. Nikulin[94] , V. Nikulin[80] , B.S. Nilsen[81] , M.S. Nilsson[21] , F. Noferini[98 ,12] , P. Nomokonov[62] , G. Nooren[49] , N. Novitzky[42] , A. Nyanin[94] , A. Nyatha[44] , C. Nygaard[76] , J. Nystrand[18] , A. Ochirov[124] , H. Oeschler[57 ,33] , S. Oh[128] , S.K. Oh[40] , J. Oleniacz[125] , A.C. Oliveira Da Silva[114] , C. Oppedisano[102] , A. Ortiz Velasquez[32 ,59] , A. Oskarsson[32] , P. Ostrowski[125] , J. Otwinowski[91] , K. Oyama[87] , K. Ozawa[120] , Y. Pachmayer[87] , M. Pachr[37] , F. Padilla[22] , P. Pagano[29] , G. Paić[59] , F. Painke[39] , C. Pajares[16] , S.K. Pal[123] , A. Palaha[96] , A. Palmeri[105] , V. Papikyan[1] , G.S. Pappalardo[105] , W.J. Park[91] , A. Passfeld[58] , B. Pastirčák[51] , C. Pastore[104] , D.I. Patalakha[47] , V. Paticchio[104] , B. Paul[95] , A. Pavlinov[126] , T. Pawlak[125] , T. Peitzmann[49] , H. Pereira Da Costa[14] , E. Pereira De Oliveira Filho[114] , D. Peresunko[94] , C.E. Pérez Lara[77] , D. Perini[33] , D. Perrino[31] , W. Peryt[125] , A. Pesci[98] , V. Peskov[33 ,59] , Y. Pestov[5] , P. Petagna[33] , V. Petráček[37] , M. Petran[37] , M. Petris[74] , P. Petrov[96] , M. Petrovici[74] , C. Petta[26] , S. Piano[103] , M. Pikna[36] , P. Pillot[108] , O. Pinazza[33] , L. Pinsky[117] , N. Pitz[56] , D.B. Piyarathna[117] , M. Planinic[92] , M. Płoskoń[70] , J. Pluta[125] , T. Pocheptsov[62] , S. Pochybova[127] , P.L.M. Podesta-Lerma[113] , M.G. Poghosyan[33] , K. Polák[53] , B. Polichtchouk[47] , W. Poonsawat[109] , A. Pop[74] , S. Porteboeuf-Houssais[66] , V. Pospíšil[37] , B. Potukuchi[85] , S.K. Prasad[126] , R. Preghenella[98 ,12] , F. Prino[102] , C.A. Pruneau[126] , I. Pshenichnov[48] , G. Puddu[23] , C. Puggioni [23] , V. Punin[93] , M. Putiš[38] , J. Putschke[126] , E. Quercigh[33] , H. Qvigstad[21] , A. Rachevski[103] , A. Rademakers[33] , T.S. Räihä[42] , J. Rak[42] , A. Rakotozafindrabe[14] , L. Ramello[30] , A. Ramírez Reyes[11] , R. Raniwala[86] , S. Raniwala[86] , S.S. Räsänen[42] ,

B.T. Rascanu[56] , D. Rathee[82] , K.F. Read[119] , J.S. Real[67] , K. Redlich[73 ,iv], R.J. Reed[128] , A. Rehman[18] , P. Reichelt[56] , M. Reicher[49] , R. Renfordt[56] , A.R. Reolon[68] , A. Reshetin[48] , F. Rettig[39] , J.-P. Revol[33] , K. Reygers[87] , L. Riccati[102] , R.A. Ricci[69] , T. Richert[32] , M. Richter[21] , P. Riedler[33] , W. Riegler[33] , F. Riggi[26 ,105] , A. Rivetti[22] , M. Rodríguez Cahuantzi[2] , A. Rodriguez Manso[77] , K. Røed[18 ,21] , D. Rohr[39] , D. Röhrich[18] , R. Romita[91 ,106] , F. Ronchetti[68] , P. Rosnet[66] , S. Rossegger[33] , A. Rossi[33 ,28] , C. Roy[61] , P. Roy[95] , A.J. Rubio Montero[10] , R. Rui[24] , R. Russo[22] , E. Ryabinkin[94] , A. Rybicki[111] , S. Sadovsky[47] , K. Šafařík[33] , R. Sahoo[45] , P.K. Sahu[52] , J. Saini[123] , H. Sakaguchi[43] , S. Sakai[70] , D. Sakata[121] , A.B. Saleem[15] , C.A. Salgado[16] , J. Salzwedel[19] , S. Sambyal[85] , V. Samsonov[80] , X. Sanchez Castro[61] , L. Šándor[51] , A. Sandoval[60] , M. Sano[121] , G. Santagati[26] , R. Santoro[33 ,12] , J. Sarkamo[42] , E. Scapparone[98] , F. Scarlassara[28] , R.P. Scharenberg[89] , C. Schiaua[74] , R. Schicker[87] , C. Schmidt[91] , H.R. Schmidt[122] , S. Schuchmann[56] , J. Schukraft[33] , T. Schuster[128] , Y. Schutz[33 ,108] , K. Schwarz[91] , K. Schweda[91] , G. Scioli[27] , E. Scomparin[102] , P.A. Scott[96] , R. Scott[119] , G. Segato[28] , I. Selyuzhenkov[91] , S. Senyukov[61] , J. Seo[90] , S. Serci[23] , E. Serradilla[10 ,60] , A. Sevcenco[54] , A. Shabetai[108] , G. Shabratova[62] , R. Shahoyan[33] , N. Sharma[82 ,119] , S. Sharma[85] , S. Rohni[85] , I. Sgura[104] , K. Shigaki[43] , K. Shtejer[9] , Y. Sibiriak[94] , E. Sicking[58] , S. Siddhanta[101] , T. Siemiarczuk[73] , D. Silvermyr[79] , C. Silvestre[67] , G. Simatovic[59 ,92] , G. Simonetti[33] , R. Singaraju[123] , R. Singh[85] , S. Singha[123 ,75] , V. Singhal[123] , B.C. Sinha[123] , T. Sinha[95] , B. Sitar[36] , M. Sitta[30] , T.B. Skaali[21] , K. Skjerdal[18] , R. Smakal[37] , N. Smirnov[128] , R.J.M. Snellings[49] , W. Snoeys[33] , C. Søgaard[76 ,32] , R. Soltz[71] , H. Son[20] , J. Song[90] , M. Song[130] , C. Soos[33] , F. Soramel[28] , I. Sputowska[111] , M. Spyropoulou-Stassinaki[83] , B.K. Srivastava[89] , J. Stachel[87] , I. Stan[54] , I. Stan[54] , G. Stefanek[73] , M. Steinpreis[19] , E. Stenlund[32] , G. Steyn[84] , J.H. Stiller[87] , D. Stocco[108] , M. Stolpovskiy[47] , P. Strmen[36] , A.A.P. Suaide[114] , M.A. Subieta Vásquez[22] , T. Sugitate[43] , C. Suire[46] , R. Sultanov[50] , M. Šumbera[78] , X. Sun[7] , T. Susa[92] , T.J.M. Symons[70] , A. Szanto de Toledo[114] , I. Szarka[36] , A. Szczepankiewicz[111 ,33] , A. Szostak[18] , M. Szymański[125] , J. Takahashi[115] , J.D. Tapia Takaki[46] , A. Tarantola Peloni[56] , A. Tarazona Martinez[33] , A. Tauro[33] , G. Tejeda Muñoz[2] , A. Telesca[33] , C. Terrevoli[31] , J. Thäder[91] , D. Thomas[49] , R. Tieulent[116] , A.R. Timmins[117] , D. Tlusty[37] , C. Tobon Marin[33] , A. Toia[39 ,28 ,99] , H. Torii[120] , L. Toscano[102] , V. Trubnikov[3] , D. Truesdale[19] , W.H. Trzaska[42] , T. Tsuji[120] , A. Tumkin[93] , R. Turchetta[107] , R. Turrisi[99] , T.S. Tveter[21] , J. Ulery[56] , K. Ullaland[18] , J. Ulrich[63 ,55] , A. Uras[116] , J. Urbán[38] , G.M. Urciuoli[100] , G.L. Usai[23] , M. Vajzer[37 ,78] , M. Vala[62 ,51] , L. Valencia Palomo[46] , S. Vallero[87] , J. Van Beelen[33] , P. Vande Vyvre[33] , J. Van Hoornen[33] , M. van Leeuwen[49] , L. Vannucci[69] , A. Vargas[2] , R. Varma[44] , M. Vasileiou[83] , A. Vasiliev[94] , V. Vechernin[124] , M. Veldhoen[49] , M. Venaruzzo[24] , E. Vercellin[22] , S. Vergara[2] , R. Vernet[8] , M. Verweij[49] , L. Vickovic[110] , G. Viesti[28] , J. Viinikainen[42] , Z. Vilakazi[84] , O. Villalobos Baillie[96] , Y. Vinogradov[93] , A. Vinogradov[94] , L. Vinogradov[124] , T. Virgili[29] , Y.P. Viyogi[123] , A. Vodopyanov[62] , S. Voloshin[126] , K. Voloshin[50] , G. Volpe[33] , B. von Haller[33] , I. Vorobyev[124] , D. Vranic[91] , J. Vrláková[38] , B. Vulpescu[66] , A. Vyushin[93] , B. Wagner[18] , V. Wagner[37] , R. Wan[7] , D. Wang[7] , Y. Wang[7] , Y. Wang[87] , M. Wang[7] , D. Wang[7] , K. Watanabe[121] , M. Weber[117] , J.P. Wessels[33 ,58] , U. Westerhoff[58] , J. Wiechula[122] , J. Wikne[21] , M. Wilde[58] , G. Wilk[73] , A. Wilk[58] , M.C.S. Williams[98] , B. Windelband[87] , M. Winter[61] , L. Xaplanteris Karampatsos[112] , C.G. Yaldo[126] , Y. Yamaguchi[120] , H. Yang[14 ,49] , S. Yang[18] , P. Yang[7] , S. Yasnopolskiy[94] , J. Yi[90] , Z. Yin[7] , I.-K. Yoo[90] , J. Yoon[130] , W. Yu[56] , X. Yuan[7] , I. Yushmanov[94] , V. Zaccolo[76] , C. Zach[37] , C. Zampolli[98] , S. Zaporozhets[62] , A. Zarochentsev[124] , P. Závada[53] , N. Zaviyalov[93] , H. Zbroszczyk[125] , P. Zelnicek[55] , I.S. Zgura[54] , M. Zhalov[80] , H. Zhang[7] , X. Zhang[70 ,66 ,7] , F. Zhou[7] , Y. Zhou[49] , D. Zhou[7] , H. Zhu[7] , J. Zhu[7] , J. Zhu[7] , X. Zhu[7] , A. Zichichi[27 ,12] , A. Zimmermann[87] , G. Zinovjev[3] , Y. Zoccarato[116] , M. Zynovyev[3] , M. Zyzak[56]

Affiliation notes

[i] Deceased
[ii] Also at: M.V.Lomonosov Moscow State University, D.V.Skobeltsyn Institute of Nuclear Physics, Moscow, Russia
[iii] Also at: University of Belgrade, Faculty of Physics and "Vinča" Institute of Nuclear Sciences, Belgrade, Serbia
[iv] Also at: Institute of Theoretical Physics, University of Wroclaw, Wroclaw, Poland

Collaboration Institutes

[1] A. I. Alikhanyan National Science Laboratory (Yerevan Physics Institute) Foundation, Yerevan, Armenia
[2] Benemérita Universidad Autónoma de Puebla, Puebla, Mexico
[3] Bogolyubov Institute for Theoretical Physics, Kiev, Ukraine

[4] Bose Institute, Department of Physics and Centre for Astroparticle Physics and Space Science (CAPSS), Kolkata, India
[5] Budker Institute for Nuclear Physics, Novosibirsk, Russia
[6] California Polytechnic State University, San Luis Obispo, California, United States
[7] Central China Normal University, Wuhan, China
[8] Centre de Calcul de l'IN2P3, Villeurbanne, France
[9] Centro de Aplicaciones Tecnológicas y Desarrollo Nuclear (CEADEN), Havana, Cuba
[10] Centro de Investigaciones Energéticas Medioambientales y Tecnológicas (CIEMAT), Madrid, Spain
[11] Centro de Investigación y de Estudios Avanzados (CINVESTAV), Mexico City and Mérida, Mexico
[12] Centro Fermi - Museo Storico della Fisica e Centro Studi e Ricerche "Enrico Fermi", Rome, Italy
[13] Chicago State University, Chicago, United States
[14] Commissariat à l'Energie Atomique, IRFU, Saclay, France
[15] COMSATS Institute of Information Technology (CIIT), Islamabad, Pakistan
[16] Departamento de Física de Partículas and IGFAE, Universidad de Santiago de Compostela, Santiago de Compostela, Spain
[17] Department of Physics Aligarh Muslim University, Aligarh, India
[18] Department of Physics and Technology, University of Bergen, Bergen, Norway
[19] Department of Physics, Ohio State University, Columbus, Ohio, United States
[20] Department of Physics, Sejong University, Seoul, South Korea
[21] Department of Physics, University of Oslo, Oslo, Norway
[22] Dipartimento di Fisica dell'Università and Sezione INFN, Turin, Italy
[23] Dipartimento di Fisica dell'Università and Sezione INFN, Cagliari, Italy
[24] Dipartimento di Fisica dell'Università and Sezione INFN, Trieste, Italy
[25] Dipartimento di Fisica dell'Università 'La Sapienza' and Sezione INFN, Rome, Italy
[26] Dipartimento di Fisica e Astronomia dell'Università and Sezione INFN, Catania, Italy
[27] Dipartimento di Fisica e Astronomia dell'Università and Sezione INFN, Bologna, Italy
[28] Dipartimento di Fisica e Astronomia dell'Università and Sezione INFN, Padova, Italy
[29] Dipartimento di Fisica 'E.R. Caianiello' dell'Università and Gruppo Collegato INFN, Salerno, Italy
[30] Dipartimento di Scienze e Innovazione Tecnologica dell'Università del Piemonte Orientale and Gruppo Collegato INFN, Alessandria, Italy
[31] Dipartimento Interateneo di Fisica 'M. Merlin' and Sezione INFN, Bari, Italy
[32] Division of Experimental High Energy Physics, University of Lund, Lund, Sweden
[33] European Organization for Nuclear Research (CERN), Geneva, Switzerland
[34] Fachhochschule Köln, Köln, Germany
[35] Faculty of Engineering, Bergen University College, Bergen, Norway
[36] Faculty of Mathematics, Physics and Informatics, Comenius University, Bratislava, Slovakia
[37] Faculty of Nuclear Sciences and Physical Engineering, Czech Technical University in Prague, Prague, Czech Republic
[38] Faculty of Science, P.J. Šafárik University, Košice, Slovakia
[39] Frankfurt Institute for Advanced Studies, Johann Wolfgang Goethe-Universität Frankfurt, Frankfurt, Germany
[40] Gangneung-Wonju National University, Gangneung, South Korea
[41] Gauhati University, Department of Physics, Guwahati, India
[42] Helsinki Institute of Physics (HIP) and University of Jyväskylä, Jyväskylä, Finland
[43] Hiroshima University, Hiroshima, Japan
[44] Indian Institute of Technology Bombay (IIT), Mumbai, India
[45] Indian Institute of Technology Indore, Indore, India (IITI)
[46] Institut de Physique Nucléaire d'Orsay (IPNO), Université Paris-Sud, CNRS-IN2P3, Orsay, France
[47] Institute for High Energy Physics, Protvino, Russia
[48] Institute for Nuclear Research, Academy of Sciences, Moscow, Russia
[49] Nikhef, National Institute for Subatomic Physics and Institute for Subatomic Physics of Utrecht University, Utrecht, Netherlands
[50] Institute for Theoretical and Experimental Physics, Moscow, Russia
[51] Institute of Experimental Physics, Slovak Academy of Sciences, Košice, Slovakia
[52] Institute of Physics, Bhubaneswar, India
[53] Institute of Physics, Academy of Sciences of the Czech Republic, Prague, Czech Republic

[54] Institute of Space Sciences (ISS), Bucharest, Romania
[55] Institut für Informatik, Johann Wolfgang Goethe-Universität Frankfurt, Frankfurt, Germany
[56] Institut für Kernphysik, Johann Wolfgang Goethe-Universität Frankfurt, Frankfurt, Germany
[57] Institut für Kernphysik, Technische Universität Darmstadt, Darmstadt, Germany
[58] Institut für Kernphysik, Westfälische Wilhelms-Universität Münster, Münster, Germany
[59] Instituto de Ciencias Nucleares, Universidad Nacional Autónoma de México, Mexico City, Mexico
[60] Instituto de Física, Universidad Nacional Autónoma de México, Mexico City, Mexico
[61] Institut Pluridisciplinaire Hubert Curien (IPHC), Université de Strasbourg, CNRS-IN2P3, Strasbourg, France
[62] Joint Institute for Nuclear Research (JINR), Dubna, Russia
[63] Kirchhoff-Institut für Physik, Ruprecht-Karls-Universität Heidelberg, Heidelberg, Germany
[64] Korea Institute of Science and Technology Information, Daejeon, South Korea
[65] KTO Karatay University, Konya, Turkey
[66] Laboratoire de Physique Corpusculaire (LPC), Clermont Université, Université Blaise Pascal, CNRS–IN2P3, Clermont-Ferrand, France
[67] Laboratoire de Physique Subatomique et de Cosmologie (LPSC), Université Joseph Fourier, CNRS-IN2P3, Institut Polytechnique de Grenoble, Grenoble, France
[68] Laboratori Nazionali di Frascati, INFN, Frascati, Italy
[69] Laboratori Nazionali di Legnaro, INFN, Legnaro, Italy
[70] Lawrence Berkeley National Laboratory, Berkeley, California, United States
[71] Lawrence Livermore National Laboratory, Livermore, California, United States
[72] Moscow Engineering Physics Institute, Moscow, Russia
[73] National Centre for Nuclear Studies, Warsaw, Poland
[74] National Institute for Physics and Nuclear Engineering, Bucharest, Romania
[75] National Institute of Science Education and Research, Bhubaneswar, India
[76] Niels Bohr Institute, University of Copenhagen, Copenhagen, Denmark
[77] Nikhef, National Institute for Subatomic Physics, Amsterdam, Netherlands
[78] Nuclear Physics Institute, Academy of Sciences of the Czech Republic, Řež u Prahy, Czech Republic
[79] Oak Ridge National Laboratory, Oak Ridge, Tennessee, United States
[80] Petersburg Nuclear Physics Institute, Gatchina, Russia
[81] Physics Department, Creighton University, Omaha, Nebraska, United States
[82] Physics Department, Panjab University, Chandigarh, India
[83] Physics Department, University of Athens, Athens, Greece
[84] Physics Department, University of Cape Town and iThemba LABS, National Research Foundation, Somerset West, South Africa
[85] Physics Department, University of Jammu, Jammu, India
[86] Physics Department, University of Rajasthan, Jaipur, India
[87] Physikalisches Institut, Ruprecht-Karls-Universität Heidelberg, Heidelberg, Germany
[88] Politecnico di Torino, Turin, Italy
[89] Purdue University, West Lafayette, Indiana, United States
[90] Pusan National University, Pusan, South Korea
[91] Research Division and ExtreMe Matter Institute EMMI, GSI Helmholtzzentrum für Schwerionenforschung, Darmstadt, Germany
[92] Rudjer Bošković Institute, Zagreb, Croatia
[93] Russian Federal Nuclear Center (VNIIEF), Sarov, Russia
[94] Russian Research Centre Kurchatov Institute, Moscow, Russia
[95] Saha Institute of Nuclear Physics, Kolkata, India
[96] School of Physics and Astronomy, University of Birmingham, Birmingham, United Kingdom
[97] Sección Física, Departamento de Ciencias, Pontificia Universidad Católica del Perú, Lima, Peru
[98] Sezione INFN, Bologna, Italy
[99] Sezione INFN, Padova, Italy
[100] Sezione INFN, Rome, Italy
[101] Sezione INFN, Cagliari, Italy
[102] Sezione INFN, Turin, Italy
[103] Sezione INFN, Trieste, Italy
[104] Sezione INFN, Bari, Italy

[105] Sezione INFN, Catania, Italy
[106] Nuclear Physics Group, STFC Daresbury Laboratory, Daresbury, United Kingdom
[107] STFC Rutherford Appleton Laboratory, Chilton, United Kingdom
[108] SUBATECH, Ecole des Mines de Nantes, Université de Nantes, CNRS-IN2P3, Nantes, France
[109] Suranaree University of Technology, Nakhon Ratchasima, Thailand
[110] Technical University of Split FESB, Split, Croatia
[111] The Henryk Niewodniczanski Institute of Nuclear Physics, Polish Academy of Sciences, Cracow, Poland
[112] The University of Texas at Austin, Physics Department, Austin, TX, United States
[113] Universidad Autónoma de Sinaloa, Culiacán, Mexico
[114] Universidade de São Paulo (USP), São Paulo, Brazil
[115] Universidade Estadual de Campinas (UNICAMP), Campinas, Brazil
[116] Université de Lyon, Université Lyon 1, CNRS/IN2P3, IPN-Lyon, Villeurbanne, France
[117] University of Houston, Houston, Texas, United States
[118] University of Technology and Austrian Academy of Sciences, Vienna, Austria
[119] University of Tennessee, Knoxville, Tennessee, United States
[120] University of Tokyo, Tokyo, Japan
[121] University of Tsukuba, Tsukuba, Japan
[122] Eberhard Karls Universität Tübingen, Tübingen, Germany
[123] Variable Energy Cyclotron Centre, Kolkata, India
[124] V. Fock Institute for Physics, St. Petersburg State University, St. Petersburg, Russia
[125] Warsaw University of Technology, Warsaw, Poland
[126] Wayne State University, Detroit, Michigan, United States
[127] Wigner Research Centre for Physics, Hungarian Academy of Sciences, Budapest, Hungary
[128] Yale University, New Haven, Connecticut, United States
[129] Yildiz Technical University, Istanbul, Turkey
[130] Yonsei University, Seoul, South Korea
[131] Zentrum für Technologietransfer und Telekommunikation (ZTT), Fachhochschule Worms, Worms, Germany

Acknowledgements

The Collaboration wishes to thank the following persons for their contribution to the preparation of this CDR: M. He, R. J. Fries and R. Rapp, Cyclotron Institute and Department of Physics and Astronomy, Texas A&M University; M. Cacciari, LPTHE Paris and CNRS; H. Mugnier, J. Rousset, et P. Chalmet of MIND Microtechnologies in Archamps, and the Departement de la Haute Savoie for supporting MIND to collaborate on monolithic detectors;